Advancements in the Calibration of the FlashCam Camera for Imaging Air Cherenkov Telescopes and a New Analysis of HESS J1729-345

Dissertation

der Mathematisch-Naturwissenschaftlichen Fakultät

der Eberhard Karls Universität Tübingen

zur Erlangung des Grades eines

Doktors der Naturwissenschaften

(Dr. rer. nat.)

vorgelegt von

Fabian Leuschner

aus Rottweil

Tübingen

2024

Gedruckt mit Genehmigung der Mathematisch-Naturwissenschaftlichen Fakultät der Eberhard Karls Universität Tübingen.

Tag der mündlichen Qualifikation:	31.07.2024
Dekan:	Prof. Dr. Thilo Stehle
1. Berichterstatter/-in:	Prof. Dott. Andrea Santangelo
2. Berichterstatter/-in:	Prof. Dr. Klaus Werner

Abstract

FlashCam (FC) is a novel camera design for imaging air Cherenkov telescopes (IACTs). FC is designated to be used in the Medium-Sized Telescopes (MSTs) of the southern array of the upcoming Cherenkov Telescope Array (CTA). In 2019, a fully functional advanced prototype of an FC camera was installed into the 28 m CT5 telescope of the High Energetic Stereoscopic System (H.E.S.S.). This thesis covers several topics related to the calibration of FC, both for the existing camera within H.E.S.S., and for future installations of the camera in CTA.

An LED-based pulse emitter, currently used for flatfield measurements in H.E.S.S., is characterized to investigate its suitability as an on-site calibration unit for FC in CTA-South. Such a calibration unit should ideally be able to homogeneously illuminate the camera over the full dynamic range of FC, which goes beyond the design requirements of the current device. Laboratory measurements and simulations of the camera's response to the light pulses show that the current device cannot handle the needs of FC in an MST. The updated requirements for a calibration unit are derived from these investigations.

Following the installation of FC into CT5, the Monte-Carlo (MC) simulation chain of H.E.S.S. had to be validated. MC simulations are critical to the analysis of IACT data, so the simulation configuration must match the actual conditions. This thesis' author was part of a small team that validated the simulations for the HAP analysis chain of H.E.S.S. The work of this team led to a significant improvement in the reconstruction of the energy flux of astronomical sources. Here, the MC validation process is presented step by step, with the author's contributions highlighted.

With the validated analysis configuration in hand, a pending step in the FC science verification could be addressed. The example of the supernova remnant HESS J1731-347 demonstrates the ability of the FC-equipped CT5 to correctly reconstruct the key parameters of a moderately extended source. The analysis of HESS J1731-347 triggered a study into the energy dependence of the neighboring source HESS J1729-345, using archival data from the CT1-4 telescopes of H.E.S.S. The main result of this study is that HESS J1729-345 actually consists of two spatially separated sources. One is only detected significantly at energies below 1 TeV, and is spatially aligned with a possible star-forming region more than 1 kpc away from HESS J1731-347. The other is fainter and is only detected significantly above 1 TeV. This second source is spatially coincident with a molecular cloud that is suspected to interact with escaping particles from HESS J1731-347, a hypothesis supported by the results of this work.

Zusammenfassung

FlashCam (FC) ist ein neuartiges Kameradesign für abbildende Luftschauer-Tscherenkov Teleskope (IACTs). FC ist für den Einsatz in den mittelgroßen Teleskopen (MST) des südlichen Arrays des künftigen Cherenkov Telescope Array (CTA) vorgesehen. 2019 wurde ein voll funktionsfähiger, fortgeschrittener Prototyp einer FC Kamera in das 28 m CT5 Teleskop des High Energy Stereoscopic System (H.E.S.S.) eingebaut. Die vorliegende Arbeit behandelt verschiedene Aspekte der Kalibration von FC, sowohl für die bestehende Kamera in H.E.S.S. als auch für zukünftige Installationen der Kamera im CTA.

Die Eigenschaften eines LED-basierten Lichtpulserzeugers, der gegenwärtig für Flatfield Messungen in H.E.S.S. verwendet wird, werden charakterisiert, um zu untersuchen, ob er dazu geeignet ist, als Kalibrationsgerät für FC in CTA-Süd zu dienen. Ein solches Kalibrationsgerät sollte in der Lage sein, die Kamera über ihren vollen dynamischen Bereich homogen zu beleuchten, was über den Einsatzzweck des vorliegenden Lichtpulserzeugers hinausgeht. Labormessungen und Simulationen der Kamerareaktion auf die Lichtpulse zeigen, dass der vorliegende Lichtpulserzeuger nicht in der Lage ist, die Anforderungen von FC in einem MST zu erfüllen. Aus diesen Untersuchungen werden die benötigten Eigenschaften eines solchen Kalibrationsgeräts abgeleitet.

In Folge des Einbaus von FC in CT5 musste die Monte-Carlo (MC) Simulationskette von H.E.S.S. validiert werden. MC Simulationen spielen eine wesentliche Rolle bei der Analyse von IACT Daten. Es ist deshalb von großer Bedeutung, dass die Simulationen mit den realen Bedingungen übereinstimmen. Der Autor der vorliegenden Arbeit war Teil eines kleinen Teams, das die MC Simulationen für die HAP Analysekette von H.E.S.S. validierte. Die Arbeit dieses Teams führte zu signifikanten Verbesserungen in der Rekonstruktion des Energieflusses astronomischer Quellen. Der Prozess der MC Validation wird in der vorliegenden Arbeit schrittweise präsentiert, wobei die Beiträge des Autors hervorgehoben werden.

Die validierte Analysekonfiguration erlaubte es, einen ausstehenden Schritt der wissenschaftlichen Verifizierung von FC anzugehen. Am Beispiel des Supernova Überrests HESS J1731-347 kann die Fähigkeit von CT5 mit FC als Kamera gezeigt werden, die wichtigsten Parameter einer moderat ausgedehnten Quelle zu rekonstruieren. Die Analyse von HESS J1731-347 stieß eine Studie der benachbarten Quelle HESS J1729-345 an, die unter Verwendung von H.E.S.S.-Archivdaten der Teleskope CT1-4 auf ihre Energieabhängigkeit hin untersucht wurde. Das wichtigste Ergebnis

dieser Studie ist die Erkenntnis, dass HESS J1729-345 nicht eine einzelne Quelle ist, sondern aus zwei räumlich getrennten Quellen besteht. Eine der beiden Quellen kann nur bei Energien unter 1 TeV signifikant detektiert werden. Ihre Position am Himmel stimmt mit einer möglichen Sternentstehungsregion überein, die mehr als 1 kpc von HESS J1731-347 entfernt liegt. Die andere Quelle ist schwächer und kann nur bei Energien über 1 TeV signifikant detektiert werden. Sie überschneidet sich räumlich mit einer Molekülwolke, von der vermutet wird, dass sie mit hochenergetischen Teilchen interagiert, die aus HESS J1731-347 herausgeschleudert werden. Diese Hypothese wird durch die Ergebnisse der vorliegenden Arbeit gestützt.

Contents

I

Very High Energy Gamma-ray Astronomy

I.1 Introduction: A window to extreme environments

Astronomy can be considered the oldest science in human history. Stone-, Copper-, and Bronze Age peoples such as the Egyptians, the Babylonians, the Inka and some of which we do not even know the names like the builders of Stonehenge or the creators of the Nebra Sky Disk tried to understand the apparent movement of the Sun, the Moon, the planets and the stars. For thousands of years, astronomy only dealt with visible light in the wavelength band the atmosphere is transparent to and that can be perceived by the human eye. In the early twentieth century, however, scientists discovered an ionizing radiation whose intensity increases with the height above the ground ("Höhenstrahlung", German for "high-altitude radiation"). This altitude dependence led to the conclusion that the origin of this radiation must be cosmic ([Hes26]), thus it has been named *cosmic rays* (CRs). Over the course of the century, it became evident that the majority of the radiation measured consists of charged particles rather than photons. The term cosmic rays was however kept.

In the past decades, the flux of CRs has been measured with multiple ground- and space-based instruments. A spectrum combining the results of multiple instruments is depicted in Figure I.1 and the explanation of its features follows [Tju20].

It turned out that the CR spectrum above 10 GeV can well be described by a powerlaw of the form $\Phi \propto E^{-\Gamma}$ with a relatively stable powerlaw index Γ. At the low energy end, i.e., $\lesssim 10\,\mathrm{GeV}$, the spectrum flattens out which is believed to be mainly due to ionization processes of the interstellar medium (ISM). Further, CRs in that energy range are modulated by the solar magnetic field, as measurements of the Voyager satellites after leaving the Heliosphere have confirmed. At $E_{\mathrm{knee}} \sim 10^6\,\mathrm{GeV}$ is the *knee*, where the spectrum softens from $\Gamma \approx 2.7$ to ≈ 3.1, before hardening again at the *ankle*, at $E_{\mathrm{ankle}} \approx 5 \times 10^9\,\mathrm{GeV}$. Then, the measured powerlaw index changes to $\Gamma \approx 2.5 - 2.8$, depending on the instrument that conducted the measurement. The last feature to be mentioned is the cutoff at high energies, around $E_{\mathrm{cut}} = 4 \times 10^{10}\,\mathrm{GeV}$. Additionally, minor features have been found or are discussed such as the *hip* at $\sim 100\,\mathrm{GeV}$, the *iron knee* ($\approx 8 \times 10^7\,\mathrm{GeV}$) and the *second knee* ($\approx 3 \times 10^8\,\mathrm{GeV}$).

The interpretation of the main features, knee, ankle and cutoff is briefly outlined. Knee and

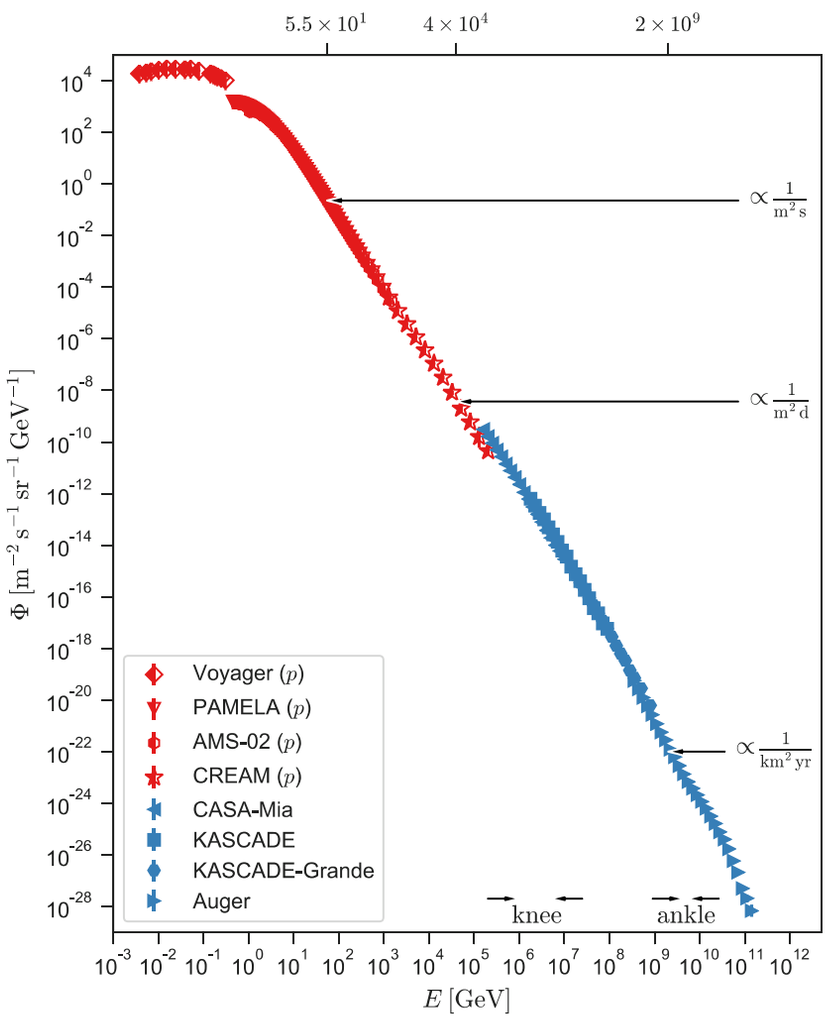

Figure I.1: All-particle spectrum of cosmic rays. The red, left filled data points describe the proton flux only, neglecting other nuclei. This is, because protons dominate the spectrum below 10^4 GeV and thus many of the used experiments only provide proton fluxes. The results are unweighted, features at the transition of different instruments (e.g., between Voyager and PAMELA) can be due to different calibrations. Image source: [Tju20].

ankle are assumed to be related: CRs with $E < E_{\text{knee}}$ are believed to be of galactic origin, while CR particles with $E > E_{\text{ankle}}$ are assumed extragalactic. The steepest part of the CR spectrum in between the two features then can be interpreted as a transition region, in which the galactic proportion starts to decrease, but the extragalactic proportion is not yet dominant. Subsequently, the second knee might be due to two different source types within the galactic population. The interpretation that beyond the ankle, CRs are of extragalactic origin is based on the Larmor radius of the CRs:

$$r_g = \frac{1\,\text{pc}}{Z} \frac{E[\text{PeV}]}{B[\mu\text{G}]} \tag{I.1}$$

For particles beyond the spectral ankle – the exact energy depending on the atomic number Z – Equation I.1 evaluates to a radius larger than the galaxy, indicating that the ambient galactic magnetic field is unable to confine CRs of these energies ([Bel13]). Vice versa, it can be concluded that CRs with $E < E_{\text{knee}}$ are of galactic origin. From the CR spectrum and its lack of features below the knee it can be concluded that galactic CRs are produced in a (limited) number of source classes that share a similar mechanism.

For the cutoff, two theories currently exist: either, CRs are limited by the Greisen-Zatsepin-Kuzmin (GZK) limit (see, e.g., [Gre66]). The GZK limit describes an interaction of CRs of energies above 5×10^{10} GeV with photons of the cosmic microwave background (CMB), producing pions. An alternative explanation is that there is an maximum energy that can be reached in the acceleration mechanisms. However, both approaches are compatible with current measurements and a final conclusion cannot be drawn.

The main question that arises from this spectrum is that of the origin of CRs. It needs powerful engines to accelerate particles to the measured energies[1]. However, studying CRs alone cannot answer the question of their origin: magnetic fields in the galaxy, the solar system, and even around the Earth deflect them proportional to their charge and anti-proportional to their energy. As a result, their arrival directions are almost isotropically distributed for energies up to $\sim 10^{10}$GeV and tracing back their distinct sources is impossible ([Aab17]).

Particles that are not deflected by cosmic magnetic fields are photons. When very high energetic (VHE) CRs interact with particles or electromagnetic fields, they can produce VHE gamma-rays ([Tju20]). The gamma-ray production rate depends on the ambient particle density, field strength, and the density of CRs themselves. I.e., most gamma-rays are expected to be produced at the (supposedly) dense sites of CR acceleration. Observing these VHE gamma-rays opens a window through which the most energetic accelerators in our galaxy can be identified and studied. This chapter briefly introduces the physical mechanisms that are involved in the acceleration of CRs and in the production of gamma-rays in Section I.2, before discussing different source classes that have been discovered so far in Section I.3. Finally, Section I.4 leads to the next chapter by explaining the process by which gamma-rays can be detected.

[1] For comparison: the most powerful accelerator built on Earth so far, the Large Hadron Collider (LHC), accelerates particles "only" to 14 TeV.

I.2 Mechanisms of CR acceleration and gamma-ray production

I.2.1 Acceleration of CRs

The process presented is summarized briefly to provide a basic understanding. A more complete picture including all the necessary derivations of equations can be found in [Lon11], which is also used as the main source for the information provided here. In 1949, Enrico Fremi proposed a mechanism to accelerate CRs within the galaxy by means of collisions with so-called magnetic mirrors ([Fer49]), i.e., moving irregularities in the interstellar magnetic field. It results in a mean energy gain $\Delta E \propto (V/c)^2$, with V being the velocity of the magnetic mirror and c the vacuum speed of light. The mechanism is referred to as *second-order Fermi acceleration* due to the quadratic occurrence of V/c. It fulfills one key requirement to account for the observed cosmic ray spectrum: It results in a power-law over wide ranges in energy. However, the mechanism is insufficient in that way that there are not enough interstellar clouds which additionally are rather slow, so, the mechanism only provides a slow gain in CR energy. When restricting the scope of action of the mechanism to turbulent regions, for example, the shells of supernova remnants (SNR), the gain in energy is more efficient ([Lon11]). Nevertheless, also restricting the picture to such regions, the mechanism proposed by Fermi does not suffice to confine the spectral index to a range between 2 and 3. Therefore, an advanced mechanism is needed that is more uniform and ideally results in a powerlaw spectrum of the observed form.

Since the 1970s, astrophysical discussions on the acceleration of CRs are dominated by strong shock waves. This process is called *diffuse shock acceleration* (DSA). A. R. Bell introduced DSA in a physics based approach, investigating the behavior of the accelerated particles ([Bel78]). The explanations in [Lon11] that are summarized here follow Bell's thoughts. The setup is a shock moving through an ambient medium at highly supersonic velocity $V \gg c_s$, with c_s being the speed of sound in that medium. Further, it is assumed that the medium consists of a flux of high energy particles, moving at velocities close to the speed of light and in particular much larger than V. This setup can be caused by supernova explosions and might be present in the successive SNRs. The high energetic particles can cross the shock without taking much notice of it, as their Larmor radius is much larger than the thickness of the shock front. Behind and in front of the shock front, the velocity distribution of the high energy particles is isotropic, due to scattering. Figure I.2 yields sketches showing the setup in the frame of rest of the shock front, the region behind it, and the region in front of it.

It turns out to be most convenient to treat the basic setting DSA in the rest frame of the shock (Figure I.2, left panel). In front of the shock (*upstream*) and behind it (*downstream*), there are two different densities of gas, ρ_u and ρ_d. The equation of continuity requires $\rho_\mathrm{u} v_\mathrm{u} = \rho_\mathrm{d} v_\mathrm{d}$, with v_u and v_d being the velocity of a particle entering the shock from upstream and leaving it towards downstream, respectively. In a strong shock, $\rho_\mathrm{d}/\rho_\mathrm{u} = 4$ can be assumed for a monoatomic or ionized medium and therefore $v_\mathrm{u} = 4 v_\mathrm{d}$. Further, it is $v_\mathrm{u} = V$, as we are in the frame of rest of the shock and the velocity of the ISM particles can be neglected compared to V in the frame of a neutral observer. Hence, in the rest frame of the shock, particles from the upstream region

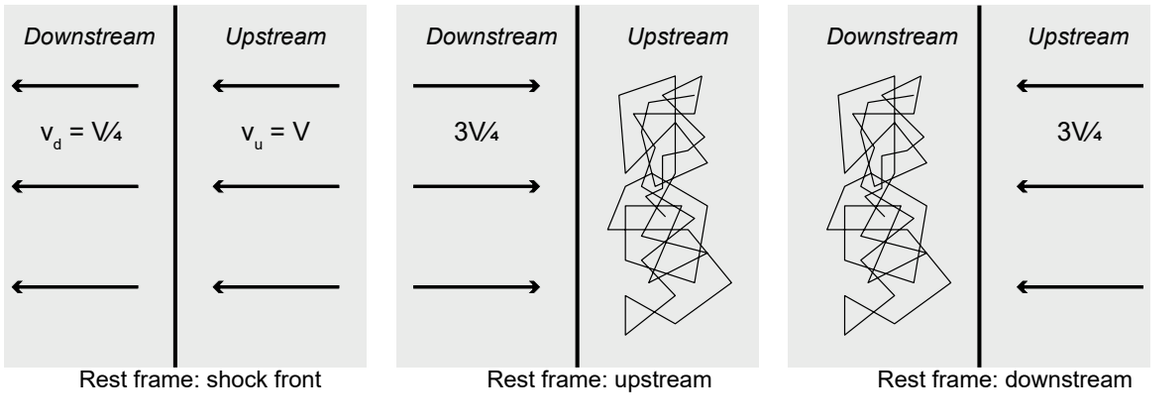

Figure I.2: Velocities in DSA, as seen from different frames of rest. For a neutral observer, the shock moves with velocity V from left to right; from the downstream region with density ρ_d and particle velocities v_d into the upstream region with ρ_u and v_u. Figure created based on [Lon11].

approach at $v_\mathrm{u} = V$ and particles in the downstream region move away at $v_\mathrm{d} = V/4$.

For an observer in the rest frame of the upstream medium (Figure I.2, center panel), the downstream medium approaches at a velocity of $v = \frac{3}{4}V$, and on the contrary, in the rest frame of the downstream medium (Figure I.2, right panel), the upstream medium approaches at the same $v = \frac{3}{4}V$. In both rest frames, the particles within the medium move in a random walk with high energy but mean velocity 0. Considering now a test particle in the upstream region: the velocity in that region is isotropic and the particle moves randomly, but is on average at rest with its surrounding. When the shock approaches, it will cross the shock front head-on, increasing its energy slightly. Then, in the downstream medium, the test particle will scatter multiply without energy loss, randomizing the direction of its velocity. As the particles move randomly with velocities much faster than the propagation velocity of the shock, the test particle might at some point cross the shock front head-on, back towards the upstream region, again gaining a small amount of energy. In the upstream region, the test particle will once more scatter and randomize its direction without energy loss.

This process is repeated until the particle leaves the accelerator which happens at probability $1 - P = \frac{V}{c}$. Therefore, the probability of a particle to remain in the acceleration region can be defined as

$$P = 1 - \frac{V}{c} \tag{I.2}$$

When crossing the shock front, the particle's energy changes to

$$E' = \gamma_v \left(E + p_x v\right) \tag{I.3}$$

due to the velocity v of the gas on the other side of the shock. As the particles are relativistic, but the shock is not, it is $\gamma_v = 1$, $E = pc$ and the component of the test particle's momentum perpendicular to the shock front $p_x = \frac{E}{c}\cos(\theta)$, where θ is the angle under which the particle crosses the shock. Rewriting Equation I.3 as

$$E' = E + pv\cos(\theta) \tag{I.4}$$

immediately delivers the energy gain of an individual crossing under the angle θ

$$\Delta E = pv\cos(\theta) \qquad \frac{\Delta E}{E} = \frac{v}{c}\cos(\theta). \tag{I.5}$$

Normalizing and integrating over all angles θ gives the average energy gain of one crossing of the shock front

$$\left\langle \frac{\Delta E}{E} \right\rangle_{\text{cross}} = \frac{2}{3}\frac{v}{c} \underbrace{=}_{v=\frac{3}{4}V} \frac{1}{2}\frac{V}{c}. \tag{I.6}$$

As illustrated in Figure I.2, particles only drop out of the acceleration process in the downstream region[2]. So, the process outlined above can be considered to always consist of two crossings and increases the energy of a particle on average by

$$\left\langle \frac{\Delta E}{E} \right\rangle_{\text{proc}} = \frac{V}{c}. \tag{I.7}$$

In reference to the second order Fermi acceleration, this mechanism is also referred to as first order Fermi mechanism.

One can define β via $E \equiv \beta E_0$ as the factor by which the energy increases per process cycle. Then,

$$\beta = \frac{E}{E_0} = 1 + \frac{U}{c} \tag{I.8}$$

and after k process cycles, the energy of a test particle that has started with E_0 is

$$E = \beta^k E_0. \tag{I.9}$$

If N_0 is the number of particles initially in the accelerator, after k cycles

$$N = P^k N_0 \tag{I.10}$$

is the number of particles left, with the probability of a particle to remain in the accelerating region P from Equation I.2. Combining Equation I.9 and Equation I.10 yields

$$\frac{\ln(N/N_0)}{\ln(E/E_0)} = \frac{\ln P}{\ln \beta} \tag{I.11}$$

which leads to the relation

$$\frac{N}{N_0} = \left(\frac{E}{E_0}\right)^{\ln P/\ln\beta}. \tag{I.12}$$

[2]Particle escape in the upstream region is possible as a stochastic process and does occur. However, it occurs in both directions, is sub-dominant compared to the particle release due to the moving shock and is therefore not considered in the calculations.

It can be recognized that N in Equation I.12 is indeed $N(\geq E)$, as all these particles have reached energy E and the fraction P of them is expected to remain in the accelerator. Thus, Equation I.12 can be reformulated in the infinitesimal form

$$N(E)\mathrm{d}E = \text{const.} \cdot E^{(\ln P/\ln \beta)-1}\mathrm{d}E. \tag{I.13}$$

With Equation I.2 and Equation I.8, it is

$$\frac{\ln P}{\ln \beta} = -1 \tag{I.14}$$

and thus

$$N(E)\mathrm{d}E \propto E^{-2}\mathrm{d}E. \tag{I.15}$$

This is a powerlaw for $N(E)$ with a spectral index of 2, being close to the observed ≈ 2.7 of the CR spectrum. In young SNRs, DSA results in acceleration of particles up to $E_{\mathrm{max}} \sim 10^5\,\mathrm{GeV}$ ([Lon11]).

Both these results, the spectral index and E_{max} are close to the observations, but still yield a non-negligible gap. However, the DSA mechanism has been seen as a promising approach to explain the galactic CR spectrum. Further theoretical studies found that E_{max} can be adapted due to magnetic field amplification. This term describes an amplification of the magnetic field in the acceleration region around a shock due to the accelerated CRs themselves. Simulations show that the amplification might be sufficiently strong to allow CR energies to the knee of the CR spectrum (see e.g. [Bel13] for a review). Further, shocks that do not move parallel to the magnetic field and in particular chaotic magnetic fields allow modifications to the spectral index of -2 derived in Equation I.15. The possible modifications are sufficient to explain the observed CR spectrum. Also, a dependence of the emitted CR spectrum on the age of an SNR has been suggested and is supported by observations, e.g. of SN1987A and Cassiopeia A (again, [Bel13] provides a review). Thus, the DSA mechanism with the named adaptions is deemed sufficient to explain the galactic CR spectrum up to its knee. Beyond that feature, collective phenomena such as superbubbles and galactic winds are discussed ([Vie22]). For extragalactic CRs with energies beyond the ankle of the CR spectrum, larger and more powerful engines are necessary and are available, as for example the jets of active galactic nuclei (AGN, [Aar17]).

I.2.2 Gamma-ray production

The production of gamma-rays follows directly from the acceleration of CRs, as outlined in Section I.1. The CRs scatter with ambient particles, photons, or interact with the ambient magnetic field. All these processes may lead to the emission of gamma-rays. The probabilities for this emission to happen is maximal where the density of CRs is maximal, in dense environments, and in the presence of strong magnetic fields. On the other hand, gamma-rays are – as far as is known today – not produced by any thermal processes, e.g., the radiation of stars. Therefore, gamma-rays are an excellent tracer for the sources of CRs and allow to study the non-thermal

universe.

Typically, two emission processes are distinguished: *Hadronic emission*, that is dominated by protons, and *leptonic emission* that is mostly due to electrons.

Hadronic gamma-ray emission

When hadronic CRs collide with ambient matter, pions of all charges (π^0, π^+, π^-) are produced ([Tju20]). In the case of hadrons as energetic as the GZK limit, even interactions with CMB photons are possible that lead via the Delta resonance (Δ^+) to positive or uncharged pions. The same holds for less energetic hadrons interacting with higher energetic photons than those in the CMB. These pions decay promptly. In the case of $\pi^{+/-}$, the products are correspondingly charged muons ($\mu^{+/-}$) and eventually $e^{+/-}$, seconded by ν_μ, $\bar{\nu_\mu}$, ν_e, and $\bar{\nu_\mathrm{e}}$. While these neutrinos follow direct paths and can in principle be used as tracers of CRs, their detection and subsequent source identification is challenging with contemporary detectors (see [Abb23]). Contrary, uncharged pions decay into two photons,

$$\pi^0 \rightarrow \gamma\gamma, \tag{I.16}$$

each carrying approximately $E_{\pi^0}/2$. The spectrum of gamma-rays produced by a hadronic CR primary with energy E_CR peaks at about $0.1E_\mathrm{CR}$ ([Hin09]).

Leptonic gamma-ray emission

Leptonic CRs, mostly electrons and positrons, are accelerated to very high energies as well. There are three major processes through which leptons can radiate gamma-rays and lose energy thereby: bremsstrahlung, synchrotron radiation and the inverse Compton effect. It is useful to compare the dominance of these processes by means of their cooling time $\tau = \frac{E_\mathrm{e}}{\mathrm{d}E/\mathrm{d}t}$. All three processes are extensively described in various textbooks and reviews, for example [Hin09], [Lon11], [Ryb04], and [Tju20]. The following passage is a summary based on these sources.

Bremsstrahlung gamma-rays are emitted when the leptons pass another charged particle, i.e., a nucleus. For bremsstrahlung, τ_br is energy independent, as $\frac{\mathrm{d}E}{\mathrm{d}t} \propto E_\mathrm{e}$. For the production of VHE gamma-rays, however, this process is negligible.

Of higher importance is the emission of *synchrotron radiation*. The loss timescale of that process shows strong dependence on the mass of a particle and inverse dependence to the ambient B-field, as well as on the energy:

$$\tau_\mathrm{syn} \propto \frac{m^4}{EB^2}. \tag{I.17}$$

This allows three conclusions: Firstly, the E^{-1}-dependence shows that synchrotron emission is dominant over bremsstrahlung at sufficiently high energies, as τ_syn becomes smaller with increasing energy of a particle. Secondly, the B^{-2}-term implies a non-negligible modification of the electron CR spectrum in the case of sufficiently strong magnetic fields. Especially the B-field amplification suggested as a modification of the DSA mechanism to allow highest energies can

limit the lepton acceleration and potentially lead to a cutoff in the lepton spectrum. Finally, the m^4 dependence of τ_{syn} leads to a strong suppression of synchrotron radiation from protons compared to leptons, in the order of $\sim 10^{-13}$ ($\sim 10^{-10}$ in the relativistic limit). Therefore, the described possible cutoff does not affect the hadron CR spectrum.

If the B-fields are not too strong, or, if the injection energy of leptons is sufficiently large, *inverse Compton* (IC) *scattering* dominates the leptonic gamma-ray emission. Basis of the process is the energy transfer from high energetic, charged particles such as CR electrons to low energy photons, e.g. from star light, radio emission or the CMB. There are two different regimes to be covered separately for IC scattering. If $\frac{4E_{\mathrm{e}}E_{\mathrm{T}}}{m^2c^4} << 1$, with E_{e} being the initial electron and E_{T} the initial target energy, IC scattering must be treated in the Thomson regime. The energy loss rate of an $e^{+/-}$ is given in the Thomson regime by

$$\left(\frac{\mathrm{d}E}{\mathrm{d}t}\right)^{\mathrm{Th}}_{\mathrm{IC}} = \frac{4}{3}\sigma_{\mathrm{T}} c u_{\mathrm{rad}} \beta^2 \gamma^2, \tag{I.18}$$

with the energy density of the ambient radiation field, u_{rad}. This is very similar to a description for the synchrotron energy loss rate, and correspondingly, the cooling time behaves like

$$\tau^{\mathrm{Th}}_{\mathrm{IC}} \propto \frac{m^4}{E u_{\mathrm{rad}}}. \tag{I.19}$$

Extreme cases of IC scattering are covered by the Klein-Nishina regime, namely if $\frac{4E_{\mathrm{e}}E_{\mathrm{T}}}{m^2c^4} >> 1$. This is at "electron energies around 300 TeV, 10 TeV and 30 GeV for scattering off CMB, IR from dust and visible light, respectively" ([Hin09]). Then, the γ^2 dependence from Equation I.18 is replaced by a $\ln\gamma$ dependence, resulting in

$$\tau^{\mathrm{KN}}_{\mathrm{IC}} \propto \frac{m^4}{u_{\mathrm{rad}}} \frac{E}{\ln E}. \tag{I.20}$$

Comparing the two cooling times for the different cases of IC radiation, Equation I.19 and Equation I.20, the change in energy dependence is striking. While in the Thomson regime, τ follows E^{-1} it goes in the Klein-Nishina regime as $E/\ln E$. In the relativistic limit in which the Klein-Nishina regime is important, this can be approximated as $E/\ln E \sim E$. However, while IC induced radiation is capable of producing more energetic gamma-rays, synchrotron cooling already dominates over IC cooling at typical B-field strength in the ISM. Note that alike for synchrotron radiation, $\tau_{\mathrm{IC}} \propto m^4$. This proportionality effectively suppresses IC radiation for hadrons.

Differentiation of hadronic and leptonic gamma-ray emission

The spectra of gamma-ray observations can help to investigate whether detected gamma-rays originate from hadronic or leptonic processes, or whether both are present within a source. Understanding the origin of gamma-rays from a specific source is necessary to limit the parameter space of that source and in particular of the acceleration and emission region, for example the strength of the B-field. Figure I.3 shows simulated spectra of leptonic (upper panel) and hadronic

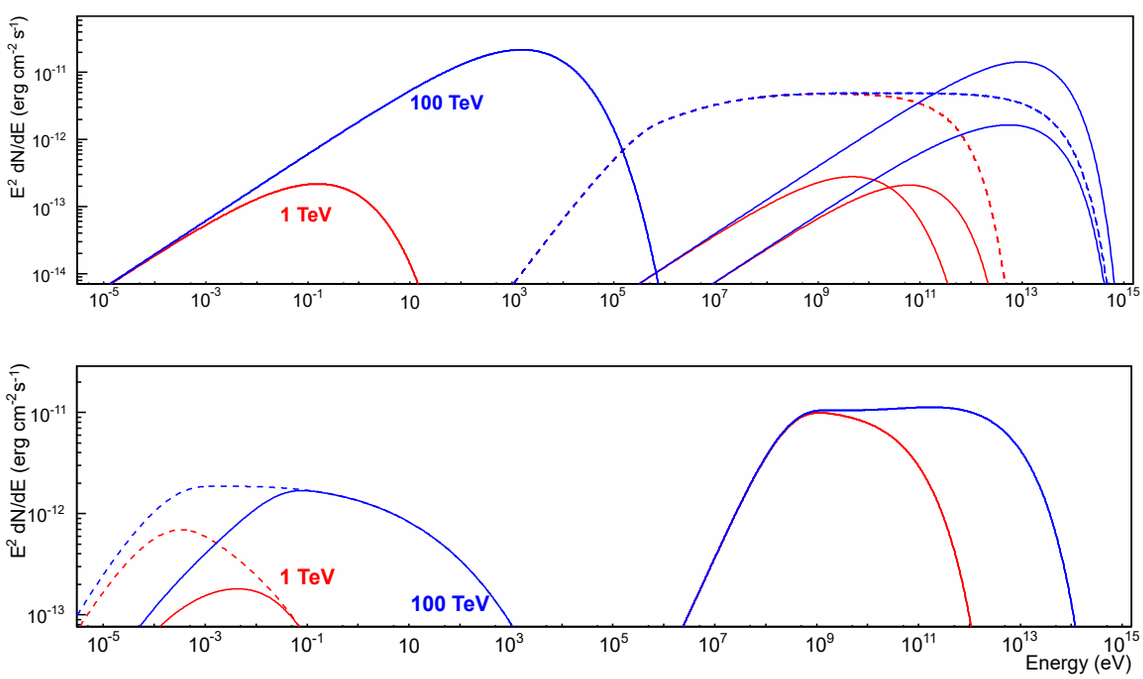

Figure I.3: Simulated SEDs for radiation from cutoff-powerlaw-distributions of particles: $\frac{\mathrm{d}N}{\mathrm{d}E} \propto E^{-2} \exp -\frac{E}{E_{\mathrm{cut}}}$; $E_{\mathrm{cut}} = 1\,\mathrm{TeV}$ (red) and $=100\,\mathrm{TeV}$ (blue). *Upper panel*: electrons emitting synchrotron and IC radiation, from left to right (low to high energies): on the CMB ($k_B T = 2.35 \times 10^{-4}\,\mathrm{eV}$), on infrared light from dust ($k_B T = 0.02\,\mathrm{eV}$) and on visible light, e.g., from stars ($k_B T = 1.5\,\mathrm{eV}$). Dashed: Bremsstrahlung, which is in actual observations suppressed due to the more effective cooling of synchrotron and IC radiation. *Lower panel*: gamma-rays from π^0-decay and synchrotron radiation from secondary leptons. Steady injection over $10^4\,\mathrm{yr}$ (dashed: $10^5\,\mathrm{yr}$) is assumed. More details on the setting are given in the main text. Image source: [Hin09].

(lower panel) emission scenarios in the gamma-ray band. Note that the emission in the radio- to X-ray bands also in the lower panel is leptonic, caused by secondary leptons. The simulated source is at a distance of 1 kpc and yields a matter density of 100 H atoms per cm^3. The radiation fields applied for the leptonic emission have a strength of 0.26 $\frac{eV}{cm^3}$ for CMB and infrared light and of 1 $\frac{eV}{cm^3}$ for visible light. Further, for the leptonic emission a B-field of 3 µG has been assumed and a total particle energy of 10^{47} erg has been simulated. For the hadronic emission, the values are 30 µG for the B-field and 10^{48} erg for the total particle energy.

The two scenarios therefore are not for direct comparison, but give an impression of the shape of the spectrum that is expected by a leptonic or hadronic emission scenario, and in particular of spectral features that can be expected from the one or the other. Note that the leptonic emission scenarios only consider synchrotron/IC emission at one of the given radiation fields at a time, while in actual observations, scattering will take place at all radiation fields simultaneously. The expected spectrum therefore is an overlap of the three spectra given and possible others.

VHE gamma-ray observations of the kind discussed in this thesis are in the energy range of $\sim$ 0.01 to 100 TeV. Consequently, they are able to precisely measure the cutoffs in the π^0-decay spectra and potentially also the cutoffs in the synchrotron/IC spectra (except that for CMB alone), depending on the input energy[3]. The shape of the hadronic emission spectrum is dominated by an unmodified powerlaw in VHE gamma-rays, in case of the blue curve over multiple decades in energy, before showing a steep cutoff. The powerlaw index in VHE gamma-rays is always similar to or larger than that of the particle spectrum. On the other hand, spectra of the leptonic emission show a steady powerlaw from MeV on that are harder than the assumed particle spectrum. They peak at $0.01 - 0.1 E_{\mathrm{cut}}$ of the particle spectrum and yield a sharp cutoff towards higher energies. However, with VHE gamma-ray observations alone, it is often not feasible to distinguish leptonic and hadronic emission unambiguously. Multiwavelength observations, e.g. in the radio band to search for the secondary synchrotron emission emerging in a hadronic emission scenario can help, as well as GeV observations. Even then, the differentiation between the emission scenarios remains challenging, as bright emission from both, hadrons and leptons remains a possibility.

I.3 Source classes

As at the time of writing, only twenty-five years have passed since the detection of the first VHE gamma-ray source ([Wee89]). In these years, the field has grown to not less than 257 firmly detected sources (and counting) that are listed in the TeVCat[4] catalog of VHE gamma-ray sources. About one third of these sources (90) has not been identified in other wavelengths so far. However, several source classes with up to $\sim$ 30 objects have been identified. Most of the unidentified sources are located in a dense environment on the sky in which multiple optical or other counterparts are in question.

[3] Note that the B-field in the simulation is assumed for the ISM without any amplification. A higher B-field would lead to more efficient cooling and an earlier cutoff.

[4] http://tevcat.uchicago.edu/. Accessed March 6th, 2024.

In the following, a brief overview of the most prominent source classes is given. The overview is divided in two sections, Section I.3.1 on galactic sources, and Section I.3.2 on extragalactic sources. For further reading, the reviews on VHE gamma-ray catalogs by de Naurois ([de 21]), generally on VHE gamma-ray sources by Bose et al. ([Bos22]) and exemplarily on the H.E.S.S. experiment and its scientific highlights by Pühlhofer et al. ([Püh24]) are suggested.

I.3.1 Galactic sources

Naturally, galactic sources (i.e., sources inside our galaxy) are easier to detect, to resolve, and therefore to study than their counterparts in other galaxies. As of now, the most numerous galactic source classes that have been detected are (shell-type) SNRs, pulsar wind nebulae (PWN) and binary systems (which can be divided in different source classes themselves).

SNRs have already before their detection been thought of as prime candidates of high VHE gamma-ray luminosity (e.g., [Dru94]). Their shocks are assumed to be the main accelerator of galactic CRs. However, a direct observational proof that SNRs do accelerate protons remained elusive until 2013, when a pion decay feature has been observed in the GeV spectrum of the SNRs IC443 and W44, measured by the Fermi satellite ([Ack13]). In VHE gamma-rays, about thirty SNRs are detected, many with a resolved shell structure in which DSA is assumed to happen. The origin of the emission can in most cases not exclusively be explained with hadronic processes, but neither with a pure leptonic approach. Mainly two methods turned out to be promising to identify SNRs in which hadrons are accelerated to TeV (and possibly PeV) energies: The first has already been outlined in Paragraph I.2.2: a connection of the TeV spectrum with that in lower energies, especially at MeV-GeV may allow to identify the mechanism of gamma-ray production. The other promising technique is applicable if the SNR is close to a molecular cloud. It is mostly agreed upon that if SNR shells accelerate CRs, those with the highest momentum leave the acceleration region first ([Ptu08]). In case a molecular cloud is nearby, they can enter and interact with that cloud, before the shock has reached it. Emission from such a cloud is therefore a sign for hadron acceleration. This technique has been applied by the H.E.S.S. collaboration successfully to the SNR W28 ([Aha08a]). Also, the SNR HESS J1731-347 is a candidate to interact with a molecular cloud, which is further discussed in Chapter VI.

PWN are the oldest source class of VHE gamma-rays, as the 1989 in VHE gamma-rays detected Crab nebula is a PWN. The Crab nebula is also the brightest persistent source in VHE gamma-rays and therefore serves as standard candle for this field of astronomy. A PWN is a nebula surrounding a pulsar, luminous in a broad range of wavelengths from radio to gamma-rays. It is known by now, that the emission from a PWN is due to synchrotron and IC radiation of electrons from the pulsar wind that are accelerated by relativistic shocks. Thus, PWN are accelerators of CR electrons. If the PWN is located in a dense environment, e.g., a star forming region, electrons that escape the PWN itself might form a PWN halo. They are fainter, but much more extended sources than normal PWN, which often can barely be spatially resolved.

Binary systems turn out to emit gamma-rays as well, given the right conditions. More than ten sources are known that emit VHE gamma-rays at least temporarily. The majority of these

are compact objects with massive O- or B-type companions. As the only identified compact objects are pulsars, it would be an obvious solution to associate the VHE gamma-ray emission of a binary system to pulsar wind interacting with the massive star wind (in case no other emission processes are identified). However, being a black hole cannot be excluded for all compact objects which would contradict the wind interaction theory at least in these cases. Special cases among VHE gamma-ray emitting binary systems are microquasars, colliding wind binaries and classical novae. Microquasars are characterized by relativistic jets from accelerated material accreting onto the compact object. As of now, only one microquasar, SS 433, is known to emit VHE gamma-rays ([Aha24]). The observations match a leptonic emission process due to a standing shock $\sim 100\,\mathrm{pc}$ away from the compact object. The model is in agreement with electron acceleration to $> 200\,\mathrm{TeV}$.

Colliding wind binaries, such as η Car act on much closer distances. The system consists of two massive stars ($\approx 100\ M_\odot$ and $\approx 30\ M_\odot$) and was found to emit VHE gamma-rays close to periastron, when the stellar winds of the two stars interact. A hadronic emission scenario is preferred in the community to explain the emission of the colliding wind binary and also the VHE gamma-ray data tends towards that scenario ([Abd20]). However, with the currently published results the leptonic scenario cannot be ruled out.

Classical novae are transient sources. They consist of a white dwarf that accretes matter from a massive companion star until ejecting its outer layer in a thermonuclear explosion. The 2021 outburst of the classical nova system RS Ophiuchi has been the first to be detected in VHE gamma-rays ([Aha22b]). The emission scenario is hadronic, due to interaction of the ejecta material with the stellar wind of the companion star.

There are more galactic sources of VHE gamma-rays but going into details for all of them is not within the scope of this work. The interested reader is referred to the reviews given above and the references therein.

I.3.2 Extragalactic sources

Extragalactic TeV gamma-ray astronomy differs from its galactic counterpart in the first place in the portion of the sky to be observed. Due to the smaller angular extension of the galactic plane compared to the extragalactic sky, it has been possible to obtain meaningful surveys of the galactic plane (see e.g., [Abd18b] and [Abe18]). For the extragalactic sky, however, this has not yet been feasible as current generation instruments are not sufficient to scan the entire sky within a reasonable time frame and obtain meaningful sensitivity simultaneously. Thus, extragalactic observations are limited to persistent or transient targets of which it is believed that they emit VHE gamma-rays. These targets can roughly be divided into two groups: galactic gamma-ray emitters and stellar phenomena.

Galactic sized emitters are mostly AGN of various orientation, such as for example blazars, quasars, or BL Lac objects. Following the widely accepted unification model for AGNs ([Ant93] and subsequent works), they yield a large ($\sim$ kpc), relativistic jet of charged particles that extends into the intergalactic medium (IGM). Within these jets VHE gamma-rays are produced,

the detection of whose helps to understand various phenomena. Firstly, the strength and if possible the localization of the gamma-ray emission allows to draw direct conclusions on the jets and their most powerful acceleration regions (e.g., [Acc09b]). While the majority of sources in our galaxy does not show temporal variability, AGNs often do. Bright flares of VHE gamma-ray emission allow to constrain the physical size of the corresponding particle acceleration region, as causal information can at maximum travel at the speed of light. Such flares have been seen in multiple AGNs, among them the first ever detected extragalactic source, Markarian 421 ([Ahn16]). Furthermore, from AGN observations information on the extragalactic background light (EBL) can be obtained. EBL is a background of infrared and optical photons and supposed to be approximately uniform in the intergalactic space. It consists of the integrated light ever emitted in the universe ([Bos22]). Studies in the spectrum and intensity of the EBL are therefore of high interest for cosmology. VHE gamma-rays yield sufficiently high energy to interact with EBL photons and undergo pair-production ($\gamma\gamma \rightarrow e^- e^+$). The resulting electrons and positrons might emit light in various processes (e.g., bremsstrahlung, synchrotron emission, annihilation) but the initial VHE photon and its direction information will not be recreated. This process drastically suppresses VHE photons on large distances, forming an energy- and luminosity dependent horizon. However, comparing the spectra of distant ($z \gtrsim 1$) AGN – mostly blazars – with models allows to draw conclusions on the EBL intensity and spectrum, as done for example with the H.E.S.S. experiment in [Abd17b].

Stellar sized phenomena in extragalactic sources describe VHE gamma-rays that are supposed to be emitted in events induced by objects of stellar size. Due to the large distances to other galaxies, such events can barely be detected, yet even be spatially resolved. Thus, the majority of extragalactic stellar sized VHE gamma-ray emitters are gamma-ray bursts (GRBs)[5]. GRBs are very luminous outbreaks of gamma-rays that over-shine for $\sim 1\,\mathrm{s}$ the entire universe. However, due to their rapid luminosity attenuation, it took until 2018 to observe GRBs for the first time in VHE gamma-rays ([Abd19]). A special case in extragalactic observations is the Large Magellanic Cloud (LMC). As a satellite galaxy of the Milky Way, it is sufficiently close that current VHE gamma-ray telescopes can resolve individual sources. Subsequently, the H.E.S.S. experiment has detected and resolved four individual sources in the LMC. In the regard of common observations, the LMC can almost be treated like a distant part of the Milky Way itself. Of special interest in the LMC is SN 1987A. It is the closest observed supernova since Kepler's supernova in 1604. While for Kepler's supernova a SNR has been detected in VHE gamma-rays ([Aha22a]), no VHE gamma-ray emission has been reported from SN 1987A so far. Ongoing observations on that source position might in future allow to draw a finer picture of SNR evolution.

I.4 Detecting gamma-rays on earth

The previous sections have shown that there are many science cases which make the study of VHE gamma-rays interesting. This section will go into details how they can be detected on Earth.

[5] Although the nature of GRBs has not been fully understood yet, the time frame on which they occur allows to classify them as stellar sized.

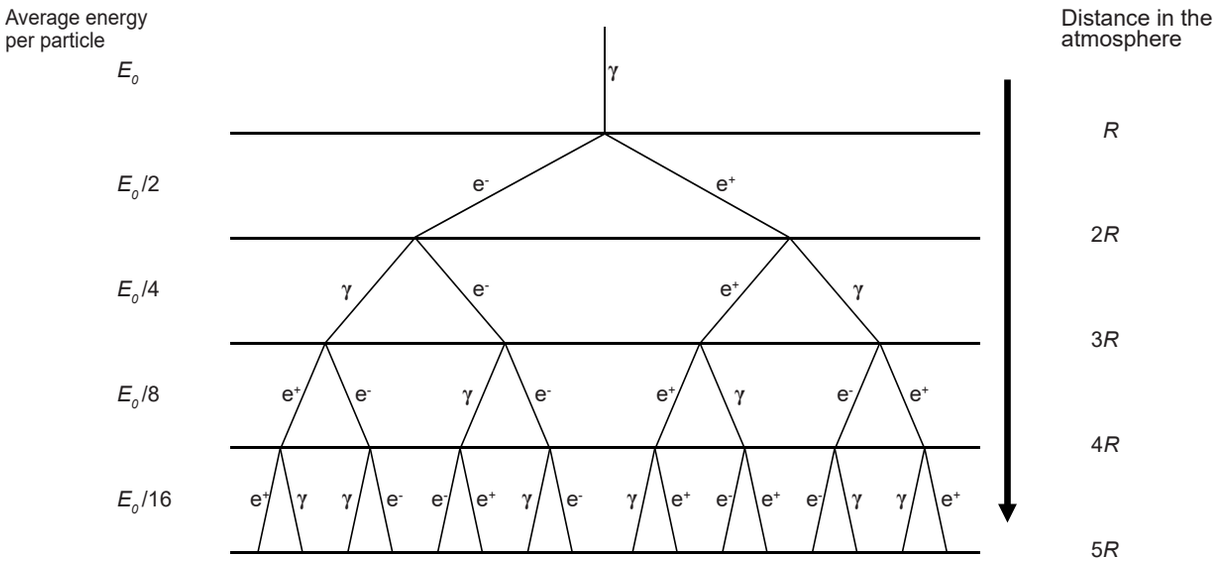

Figure I.4: Model of an extended air shower, induced by a photon. Image created based on [Lon11].

Focus will be put on the physical processes behind such detections. Technical details concerning the instruments will be discussed in Chapter II.

I.4.1 The challenge of low fluxes

There are two major challenges in observing VHE gamma-rays: Firstly, the atmosphere is opaque to light of wavelengths shorter than the optical band [Gia68] and secondly, the flux of VHE photons is extremely low. For example, even the brightest non-transient source, the Crab nebula, has above 1 TeV a photon flux of only $\sim 2 \times 10^{-11} \frac{1}{\mathrm{cm}^2\,\mathrm{s}}$ [Aha06b] corresponding to about 1 photon per year and square-meter.

This leads on first sight to an unresolvable contradiction in choosing the observation technique: The opaqueness of the atmosphere suggests observations with space-missions, while the low flux makes them unpractical, as the collection area of a space-telescope is limited to a few m^2 due to the rocket carrying the spacecraft. The solution found in VHE gamma-ray astronomy is to observe secondary (Cherenkov) light produced by extended air showers (EAS). The physics of EAS and of the Cherenkov effect will be explained in the next two sections. Technical aspects on how observations can actually be conducted will be described in detail in Chapter II.

I.4.2 Extended Air Showers

A good description on how EAS are initiated is given in [Lon11]. This section summarizes the detailed explanation given there.

When a VHE photon penetrates the atmosphere, the dominant interaction mechanism is electron-positron pair-production. As both particles in the resulting e^--e^+-pair are still highly relativistic ($E \gg m_e c^2$), their dominating energy losing mechanism is the emission of bremsstrahlung.

Moreover, in this energy range the radiation length ξ_0 of e^- and e^+ emitting bremsstrahlung and that of a photon producing an e^--e^+-pair are equal. When having one of these particles, the probability of the corresponding process to happen is $\frac{1}{2}$ after path length ξ, defined by:

$$\exp\left(-\xi/\xi_0\right) = \frac{1}{2} \Leftrightarrow \xi = \xi_0 \ln(2) \equiv R \tag{I.21}$$

Combined, these effects lead to what is referred to as an electromagnetic (air-)shower: A VHE photon with initial energy E_0 penetrating the atmosphere will, on average, undergo pair-production after a distance R. The resulting e^- and e^+ in turn will produce another photon each, again on average after traveling for a distance R. On average, each particle will carry half the energy of the prior particle. That means the e^--e^+-pairs share the energy of the annihilating photons equally and the bremsstrahlung photons obtain half the energy of the e^-s and e^+s. Thus, after nR there are in total 2^n particles ($2^n/3$ of each kind) with average energy $E_0/2^n$. A sketch of such a shower is shown in Figure I.4

The average energy of the e^-s and e^+s halves with each radiation length until it eventually drops below the critical energy E_c ($= 83\,\mathrm{MeV}$ in air) at which ionization losses become the dominant process over bremsstrahlung. For the photons, Compton scattering will become more dominant than pair-production as the cross-section $\sigma_{\mathrm{pair}} \propto \ln(E_\gamma)$. This is the case at $\approx 10\,\mathrm{MeV}$ ([Kno99]). These effects determine the termination of the shower. It reaches its maximum when the average energy of the particles is about E_c. The number of distances R after the initial interaction took place until the maximum is reached, n_c, is given by

$$n_c = \frac{\ln(E_0/E_c)}{\ln(2)}. \tag{I.22}$$

With the values stated above this is $n_c = 13.6$ for a $1\,\mathrm{TeV}$ initial photon.

EAS can also be induced by a CR hadron, i.e., a proton or a more massive nucleus entering the atmosphere at sufficiently high energy. These *hadronic showers* constitute a background when observing electromagnetic EAS. Understanding their evolution allows to distinguish the two shower types. The main products of the first collision between the CR and an atmospheric nucleus are (multiple) lighter nuclei, protons and pions (charged and uncharged: π^+, π^- and π^0). The protons travel through the atmosphere, losing energy by ionization of the surrounding matter. Charged pions decay in-flight into correspondingly charged muons under emission of a neutrino ($\pi^{+/-} \to \mu^{+/-} + \nu_\mu/\bar{\nu}_\mu$). Depending on their energy, the muons can decay into electrons ($\mu^{+/-} \to \mathrm{e}^{+/-} + \nu_\mathrm{e}/\bar{\nu}_\mathrm{e} + \bar{\nu}_\mu/\nu_\mu$) which then initiate electromagnetic cascades. However, if the Lorentz factor of the muons is $\gamma \geq 20$ (corresponding to 99.87% the speed of light in vacuum), relativistic time dilation prolongs their lifetime sufficiently to travel all the way to the surface of the earth and possibly even penetrating it. The uncharged pions decay almost immediately ($\tau \sim 10^{-16}\,\mathrm{s}$), each into two VHE photons ($\pi^0 \to 2\gamma$) which each in turn initiate electromagnetic cascades as described above. Last, the nuclei with sufficient energy continue to travel through the atmosphere until they collide again with another nucleus, re-initiating the process. This is going on as long as the energy of the nuclei is sufficient for π-production: $\gtrsim 1\,\mathrm{GeV}$.

Summarizing, it can be stated that hadronic showers are much more chaotic than electro-

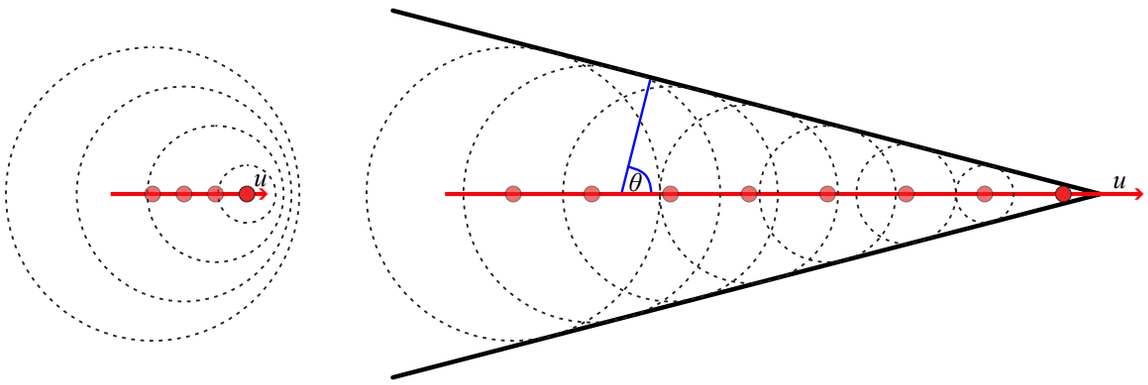

Figure I.5: Wavefronts induced by a charged particle moving with velocity u in a dielectric medium of refractive index n_r. Left: $u < \frac{c}{n_r}$, the wavefronts move faster than the particle. Right: $u > \frac{c}{n_r}$, the particle moves faster than the wavefronts. At every point within the indicated cone, two wavefronts overlap. The angle θ is the angle between $\vec{u}$ and the norm of the cone. Images created following [Ryb04].

magnetic showers. As there are more free parameters, their evolution is less predictable. On the ground level, this impacts the appearance of the two shower types and makes them distinguishable.

I.4.3 The Cherenkov effect

The previous section discusses how gamma-rays induce EAS when penetrating the Earth's atmosphere. This section focuses on a secondary effect of EAS: the emission of Cherenkov light, known as the Cherenkov effect and named after its discoverer Pavel Cherenkov. Cherenkov light flashes from gamma-ray induced EAS are the signals VHE gamma-astronomers are looking for. While the focus will be laid on the process of Cherenkov light emission in this section, the following Chapter II contains an extensive description of methods to detect Cherenkov light from EAS. The explanation of the Cherenkov effect follows that given in [Ryb04].

Figure I.5 shows a charged particle that moves with velocity $u = |\vec{u}|$ in a medium with refractive index $n_r > 1$. The black dashed circles are "information spheres" ([Ryb04]) that originate in prior positions of the particle, denoted by the red dots. The information spheres enclose the volume in the dielectric medium that is affected by the presence of a moving charge, i.e., the volume through which the electric potential of the moving, charged particle has already propagated. The wavefronts of the information spheres propagate with the speed of light in the refractive medium, $\frac{c}{n_r}$. In the left panel, u and n_r are such that $u < \frac{c}{n_r}$. Therefore, the information spheres expand faster than the particle moves forward, meaning that each point in space is only affected by one potential at the same time. In the right panel, however, it is $u > \frac{c}{n_r}$, so the particle travels superluminal in the medium and in particular faster than the potentials propagate through the medium. As can be seen, this leads to a cone in which each point is affected by two potentials originating from two different positions of the charged particle. Two potentials due to a moving charge correspond to the case of one charged particle moving in an electric field. Then, radiation is emitted. This is the Cherenkov radiation. The cone that confines the region in which Cherenkov

radiation is emitted is called the Cherenkov cone. The radiation moves outward under the angle $\theta = \cos\left(\frac{c}{n_r u}\right) = \cos\left(\frac{1}{n_r \beta}\right)$ with respect to $\vec{u}$ with the velocity $\frac{c}{n_r}$. Note that also the Cherenkov radiation is confined within the Cherenkov cone, as it expands with the same velocity.

In a gamma-ray-induced EAS, the charged particles emitting Cherenkov light are the $e^{+/-}$ that are produced in the shower. For them, $\theta \approx 1°$, which confines the emission well. In particular, compared to a hadronic EAS, the electromagnetic EAS itself is quite compact, with angles of the $e^{+/-}$ to the shower axis also on the $\sim 1°$ scale. Thus, the Cherenkov light propagates through a cone with half-opening angle $\sim \theta$ through the lower atmosphere. At typical altitudes where detectors are situated – $\sim 2000\,\mathrm{m}$ above sea level – this leads to an isotropically illuminated ring of 120 m radius [Aha04a].

The amount of Cherenkov photons in the shower (typically $\sim 100\,\frac{\mathrm{ph}}{\mathrm{m}^2}$) depends on the energy of the initial photon: the more energetic, the more photons. The direction of the initial photon corresponds to the symmetry axis of the cone. As photons do not get deflected by electromagnetic fields in space and around Earth, this direction points directly to the source of the initial photon.

This is one main reason, why it is important to distinguish between electromagnetic and hadronic EAS. Charged particles get deflected when traveling through the galaxy. Therefore, it is currently not possible to understand where they come from and what their sources are. However, gamma-rays provide an excellent window to processes in GeV, TeV and up to PeV in space.

II

Observing VHE Gamma-rays

In Chapter I a motivation is given why astronomy at TeV energies is of interest. With introducing EAS and the Cherenkov light produced by them, also a tracer for VHE gamma-rays is presented. This chapter will cover how Cherenkov light can be observed: what properties must telescopes and cameras have (Section II.1), how can the obtained data be calibrated and which conclusions can be derived from the analysis of that data (Section II.2). Due to the focus of this work, this is elaborated on the example of Imaging Air Cherenkov Telescopes (IACTs). Eventually, in Section II.3 various facilities are presented: from the beginning of IACT astronomy via the currently operating systems to the future of the field.

II.1 Imaging Air Cherenkov Telescopes

To understand the necessary properties of an IACT, one must recall the properties of the Cherenkov light cone, as given in [Aha04a]. A typical EAS induced by a 1 TeV photon creates a cone with a radius of 120 m in the optimal observing altitude of 2 km above sea level. Inside the cone, around 100 $\frac{\text{ph}}{\text{m}^2}$ are produced. In order to obtain an image covering as much of the Cherenkov cone as possible, an ideal telescope would therefore cover as much ground as possible with a giant mirror. However, a telescope with a size comparable to that of the Cherenkov cone is not realistic due to technical reasons as well as financing. Smaller telescopes can image a nearby shower from the side, creating an elliptical pattern of illuminated pixels in the camera. This leads to the problem that a single recorded Cherenkov flash gives large uncertainties on the incident particle type, direction, and energy. The solution is to construct an array of multiple IACTs, connected via high precision clocks that allow to observe and match showers in stereo mode ([Aha97]). This stereoscopic method was initially probed by the HEGRA system and found to be superior over monoscopic observations with one telescope only ([Kon99]). To apply the stereoscopic method, of course a shower needs to be detected by at least two telescopes.

The HEGRA Collaboration has studied which distances are optimal between IACTs ([Hof00]). The size of the Cherenkov cone limits the distance between two neighboring telescopes to somewhat below 150 m. While distances above 100 m are slightly favored for high source signal significances, lower telescope spacing in combination with many telescopes leads to more telescopes

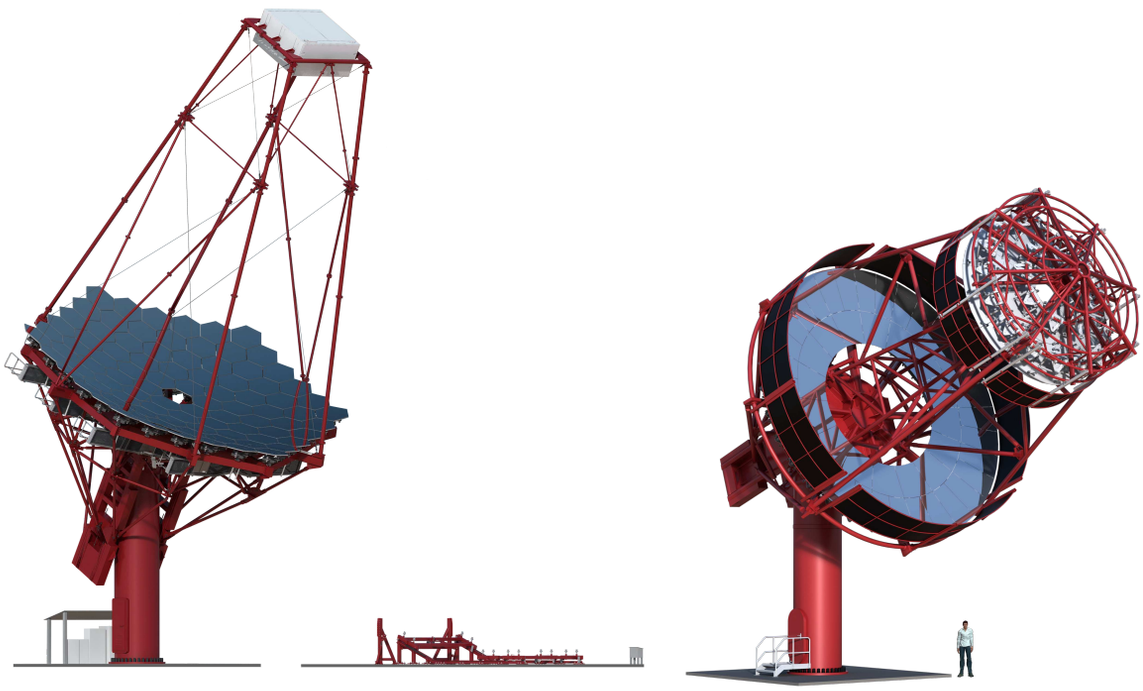

Figure II.1: Renderings of two telescopes for the upcoming CTA. Left: a DC-mounted MST. The mirror diameter will be 11.8 m. Right: a SCT with primary mirror diameter of 9.7 m and secondary mirror diameter of 5.4 m. Images not to scale. Rendering credit: G. Pérez, IAC, SMM under CC BY-NC-ND 2.0 license.

observing the same shower which improves the reconstruction quality ([Hof00]). As this also comes at cost of effective area, since the same amount of telescopes covers less area, the systems operating today use spacing of about 100 m between their telescopes (see e.g., [Aha06b])

. The necessity to construct multiple telescopes at altitudes around 2000 m above sea level with spacing of ~ 100 m between them is a strong constraint to the site of such an observatory, leaving only few spots in the world. Some of them will be mentioned in Section II.3 along with the systems operating there.

Another feature of a Cherenkov shower is its short duration. The flashes that must be recorded have durations of typically < 10 ns. At the same time, there is an optical background light, the night-sky background (NSB), that constantly glows and induces photons into the detectors at a higher rate than the actual showers ([Ben98], [Pre02], see also Chapter V). This combination is very challenging for the construction of cameras.

II.1.1 Mechanical structure

As of now, there are two approaches to build an IACT: classically a single mirror is used but recently also dual-mirror telescopes have been realized. Since the focus of this thesis lays on a camera for single mirror telescopes, these are described in more detail here. owever, at the end of this section a discussion on the advantages and disadvantages of dual mirror mountings can be found. A single-mirror IACT consists of a tessellated mirror with a camera (see Section II.1.2

and Chapter III for details) in the focal plane and support structure to hold and move both. The telescope is moveable in altitude and azimuth independently. Typical sizes are a mirror diameter of 12 m and a focal length of 16 m for observing energies $\sim$ 1 TeV ([Püh17]). The mounting typically follows the Davies-Cotton (DC) design ([Dav57]) or modifications thereof, such as the Medium-Sized Telescopes (MSTs) of the upcoming Cherenkov Telescope Array (CTA). Less commonly used, but especially for large telescopes, is a parabolic mounting. In the DC design, the mirrors are arranged on a sphere, formed by the mirror support structure. Each mirror facet has the same focal length f that is also the radius of the sphere ([Püh24]). The focal plane in the DC-mounting is at a distance of $2f$. The design provides good optical resolution for on- as well as off-axis light (i.e., light with and without an incident angle with respect to the optical axis). A rendering of a DC-mounted IACT is shown in the left panel of Figure II.1. Disadvantage of the design is that the photons arrive in the focal plane with a spread up to several ns which can be critical due to the fast timing, especially for large telescopes [Aha08b]. Therefore, a parabolic layout is used for large telescopes with (effective) mirror diameter $>$ 15 m as CT5 or the MAGIC telescopes. While the resolution for off-axis observations decreases, there is no time spread in the photon arrival times [Aha08b].

The mounting structure of an IACT is required to be exceptionally stable. The camera, which can weigh up to several tons ([Bol14]), must be moved to and held at a distance of more than 10 m from the rotation point without moving relative to the mirrors. Most IACTs are therefore made of steel to provide the necessary stability. To avoid heating up to much in the sun of the very clear observation sites, also the color of the telescope structures is important. The naive idea to paint the telescopes white would increase the reflectivity also at night, inducing unnecessarily high NSB rates. For the H.E.S.S. telescopes, the red color RAL 3016 was chosen after careful investigations as a good compromise between low background and low temperature changes. While the color absorbs blueish photons to which the detectors are most sensitive (more than a factor of five compared to red light, see Section V.3.1), it reflects red to infrared light and therefore heats up almost as little as white ([Pre02]).

In recent years, the first dual-mirror telescopes have been successfully tested. Among them are the ASTRI-Horn telescope ([Lom20]) and the the Schwarzschild-Couder Telescope (SCT, see Figure II.1, right panel for a rendering), the latter corresponding to a DC-mounted telescope of 12 m mirror diameter, with regard to the energy range covered ([Ada21]). Both of them are mounted in the Schwarzschild-Couder (SC) mounting, with a large primary and a smaller secondary mirror in the focal plane of the primary mirror. The SC-mounting provides a larger field of view (FoV) than the DC-mounting and, in particular, a better angular resolution. One reason why SC-mounted telescopes have only recently been developed is that the detector technology required to take advantage of the improved angular resolution has only matured in the last decade. The photoelectron-multiplier tubes (PMTs) that are used in all major current IACT facilities are significantly bigger than the point spread function (PSF[6]) of a (properly aligned) SC-mounted IACT [Lom20]. In SC-mounted telescopes, the detectors used are Silicon-photomultipliers (SiPMs)

[6]The PSF indicates how large a point appears in the focal plane of an instrument. It therefore is a measure for the angular resolution of a telescope.

with dimensions on the mm-scale, compared to cm-scale dimensioned PMTs ([Lom20], [Bol14]). Therefore, using the capabilities of an SC-mounted telescope is only possible since known issues of SiPM-detectors such as crosstalk and timing are sufficiently under control. However, the data taking rate of an SC-mounted telescope is much lower, making it less efficient in detecting new sources compared to a DC-mounted telescope. Because of the different structure their effective mirror area is much smaller than for DC-mounted telescopes of comparable dimensions. While a DC-mounted IACT with 12 m diameter results in an effective mirror area of 94 m^2 ([Ber03], 83% of a perfect circle), a SC-mounted IACT with 9.7 m primary reflector diameter only has an effective mirror area of 50 m^2 ([Ada21], 68% of a perfect circle). Further, the usage of SiPMs makes their cameras still slower than the PMT-based cameras of DC-mounted IACTs, due to the recovery time of the sensors. After all, the trigger rate of the SCT is about 3.5 kHz ([Pan23]), compared to more than 6 kHz expected for the MSTs of CTA.

Therefore, one must state that SC-mounted IACTs are already with the currently available technology superior in optical resolution. However, they suffer from the slowness of their detectors, as well as from the small effective mirror area, compared to DC-mounted IACTs of comparable size. This makes them more susceptible to NSB, which further increases the energy threshold of an SC-mounted IACT compared to a similar sized DC-mounted IACT.

II.1.2 Cameras

The cameras of IACTs must be sensitive and fast enough to record the faint and short atmospheric Cherenkov showers. Detectors of choice are therefore fast photo-multipliers, namely PMTs or SiPMs as already mentioned in Section II.1.1. Apart from that, also the readout and trigger electronics must be very fast, as must be the data transfer. Typical figures of a state-of-the-art Cherenkov camera are $\sim$ 2000 PMT pixels or $\sim$ 10000 SiPM pixels that are read out at trigger rates of several kHz. This leads to data rates of multiple Gbit/s. Processing must be equally fast, as the cameras trigger directly on the incoming data that is sampled with a frequency of few ns. In summary, the invention of microelectronics and in particular modern computers at the end of the last century was a necessary condition for the development of modern IACTs.

Cameras for IACTs do not need to resolve the energy of the light they detect, as the energy information of the incident photon is contained in the number of Cherenkov photons. Therefore, the cameras must be very sensitive and able to count the individual photons in a shower. Further, the geometrical properties of a shower must be recorded to reconstruct its direction, distance, and to distinguish between hadronic and electromagnetic showers. For that, the cameras need to be pixelated. The pixels themselves consist of a single PMT or a SiPM and consequently have dimensions of mm to cm. To reduce the impact of dead space between sensors, Winston cones are deployed in front of them, and arranged such that they cover the whole camera front. Winston cones are described by an entrance window, a smaller exit window and a reflective inner surface. They collect light hitting the entrance window, guiding it to the exit window (i.e., the detector). As a side effect, the cones narrow the angle at which light reaches the detectors, minimizing stray light contamination, such as reflections from the ground.

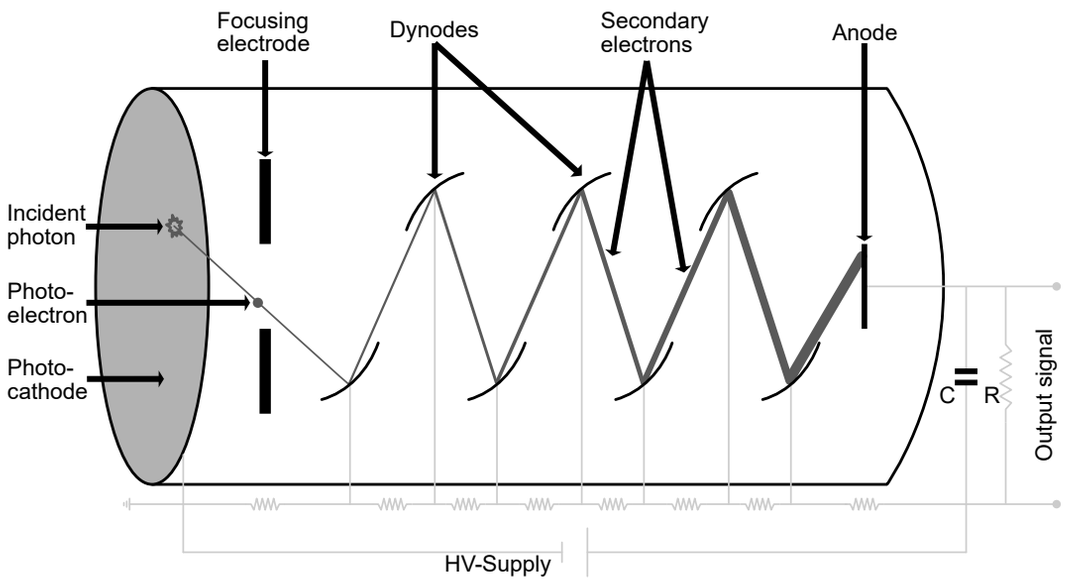

Figure II.2: Schematics of a PMT. A single photo-electron that is induced by an incident photon gets focused onto the dynodes and amplified towards the anode where it is recorded as a macroscopic current. Typical amplification is in the order of $10^6 - 10^7$.

An extensive description of a PMT-based IACT camera can be found in Section III.1. The following paragraph provides more details on the characteristics and working principle of a PMT itself and ends with a discussion about SiPMs as competing detectors.

PMTs

A PMT is a very sensitive device, capable of detecting single photons. This comes at the cost of resolving signals spatially and energetically: it only counts photons, regardless of the impact position on the PMT entrance window and without obtaining information on their wavelengths. Figure II.2 shows a sketch with the main elements of a PMT. On the left is the entrance window with the photo-cathode at which one photon induces via the photo-electric effect one (primary) photo-electron (pe). A focusing electrode guides the pe to the first of a series of dynodes at increasing high voltage. At each dynode, the incoming electron(s) are multiplied (indicated by increasing thickness of the lines in Figure II.2) until they eventually hit the anode at the rear end of the PMT. The signal to be recorded is the output current of the anode ([Ham17]). Its amplitude is proportional to the number of pe induced at the photo-cathode. The gain of the device, i.e. the conversion factor from a pe to signal current, is determined by the voltage across the PMTs and by the number of dynodes. Typical order of magnitude for the gain is $10^6 - 10^7$. In principle, PMTs can be designed with any number of dynodes, with more dynodes providing higher gain and therefore clearer signals. However, PMTs with more dynodes are more complex to construct and therefore more expensive, which is an important point in the construction of PMT-based IACT cameras. In fact, the PMTs contribute about 40% to the total cost of such a camera. The high voltage applied to the PMT can be varied to change the gain. It is distributed to the

dynodes via a serial connection with resistors. This leads to increasing voltage from the front to the back of the PMT, confining the secondary electrons on their path. To avoid electrostatic discharging, the interior of PMTs is in a vacuum which in turn is the reason for their typically cylindrical form.

The characteristic quantity of a PMT is its quantum efficiency (QE). It states which percentage of photons hitting the area of the photo-cathode actually induce a pe, and not get, e.g., reflected at the entrance window. The QE is a wavelength-dependent quantity, peaking at 300 to 400 nm with up to 40% for modern PMTs ([Toy13]). The wavelength range of the peak sensitivity coincides with the peak of the Cherenkov spectrum, making PMTs very suitable detectors for IACTs. For older models, also the collection efficiency (CE) is a crucial property. It defines which percentage of induced pe does actually hit the first photo-dynode and therefore can be detected as a signal. The PMTs of the H.E.S.S.-I cameras, for instance, face a mean CE of 85% ([Ber08]). However, nowadays the losses due to that are negligible thanks to CEs $> 95\%$ ([Toy13]).

Contrary, SiPMs are more robust, need less energy and are cheaper than PMTs. Their QE is higher, thus peaking with $\sim 50\%$ at 400 to 500 nm when the Cherenkov spectrum is already beyond its peak ([Kla19]). The issue of crosstalk (secondary electrons producing photons which trigger neighboring pixels) has been mostly solved by the trenching method ([Buz09]). In modern SiPMs, the cross-talk probability is down to $\sim 4\%$ ([Che19]). What remains is that the pulses of SiPMs last longer than those of PMTs. Therefore, the integration windows are longer and the signals are noisier due to higher contamination by NSB. Another disadvantage of SiPMs is their QE in red wavelengths. While PMTs have negligible QE for light beyond 550 to 600 nm, SiPMs are still efficient in detecting light up to 900 nm ([Kla19]). In this wavelength regime, the NSB-spectrum has several peaks ([Ben98]) which are ignored by PMTs but contribute to the background when using SiPMs.

These constraints imply that SiPMs perform worse in detecting events that are close to the lower threshold in energy, as the NSB is a more severe issue. Therefore, the conclusion originating from the telescope type in Section II.1.1 persists: while the spatial resolution achievable with cameras using SiPMs is better than that of cameras with PMTs, they yield in general a higher energy threshold.

II.2 Data analysis

Analysis of IACT data is different than from other types of telescopes, due to the indirect observations with the imaging Cherenkov method rather than direct observation of sources. Besides the gamma-ray background from diffuse gamma-rays, hadronic showers and muons constitute a background of triggered events and on top of all this is the optical background from NSB and electronic artifacts in the cameras. Therefore, "data analysis" includes not only the analysis of gamma-ray data, but especially a careful calibration of the obtained raw data, different than for observations in other regions of the electromagnetic spectrum. This section follows in its description the naming scheme of the community driven initiative *Data formats for gamma-ray*

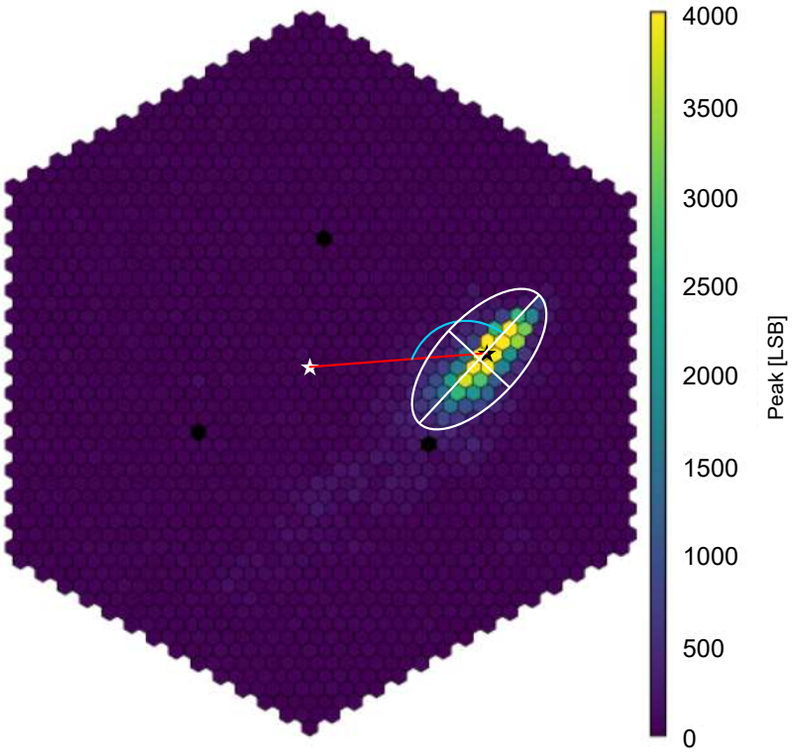

Figure II.3: The image shows a gamma-ray induced event in a FlashCam camera (see Chapter III for further information on FlashCam), generated in an MC simulation. The white ellipse is the Hillas ellipse, with its major and minor axis, i.e., the Length and Width parameter. The Size is given by the sum of all pixels' charges (in p.e.) within the ellipse. The red line is the Distance parameter, measured from the image centroid (black star) to the center of the FoV (white star) and the blue arc denotes the angle Alpha. Position and extent of all parameters has been estimated here by eye and are not to scale.

astonomy[7], adapted to the procedure for H.E.S.S. data. Data analysis can be separated into two parts: the telescope dependent *calibration* and telescope independent *high level analysis*. Section II.2.1 covers this calibration on the example of the H.E.S.S. experiment, including all the analysis from raw camera data in units of p.e. until an instrument-independent data-product is reached.The second part of the analysis is described in Section II.2.2: how to derive scientific results from individual observations. For the high level analysis, contemporary open source tools are used in this thesis.

II.2.1 Calibration

The goal of the calibration is to convert the raw telescope data into an universal data product called *event list*. Raw telescope data are the camera images: the reconstructed number of pe in each pixel of a camera integrated over a readout window of several ns, combined with a timestamp to define when this image was read out. Event lists are so-called DL3 data and contain gamma-ray candidate events with reconstructed position at the sky $\vec{p_{\mathrm{rec}}}$ and reconstructed energy E_{rec}. To obtain these from raw data, the camera images are firstly cleaned from pixels not contributing to the shower image. Then, the remaining images are parametrized and from the parameters energy and position are reconstructed consecutively. Eventually, gamma-ray candidates must be selected out of the much more numerous ($\sim 10^2$, [Aha97]) sea of CR-induced (hadronic) events. Typically, this gamma-hadron separation relies on the much more chaotic nature of hadronic

[7] Aim of the initiative is to define a common high-level data format to facilitate the analysis of data from gamma-ray instruments and to allow joint analyses of data from different instruments. See [Nig21] and https://gamma-astro-data-formats.readthedocs.io/en/v0.3/, accessed on 31st August, 2023.

showers compared to electromagnetic showers.

The other part of DL3 data is the instrument response function (IRF) in which the system response is summarized. To make the data in the event list independent of the instrument it was obtained with (and therefore usable for open source science tools), an IRF must be supplemented to the event list. The constituents of the IRF are discussed later in this section, after elaborating how to create event lists out of raw data.

Image cleaning and image parameter derivation

First step of data calibration is the *image cleaning*. Only a few pixels in a camera image contain Cherenkov light from the EAS (see Figure II.3, left panel for instance). Image cleaning refers to the removal of pixels which do not contain sufficient Cherenkov light. In the H.E.S.S. data calibration, pixels must have at least 5 p.e. and a neighbor with at least 10 p.e. or vice versa to remain in the cleaned image ([Aha06b]).

Remaining in the images is then a somewhat elliptically shaped region of illuminated pixels, the cleaned image or shower image. To derive the shower parameters and to eventually discriminate whether the shower is of hadronic or of electromagnetic origin, the second moments of the detected shower are parametrized, resulting in the image parameters. Conventionally, the Hillas parameters ([Hil85]) are used for image parametrization. Most prominent are the Width, Length, Size, Distance and Alpha ([Aha97]). Width and Length are the minor and major axis of the aforementioned ellipsis, Size is the sum of all pe in it. Distance is defined as the angular distance between the center of the FoV (i.e., the center of the camera) and the centroid of the image, the latter being denoted as $\vec{\vartheta} = (\vartheta_x, \vartheta_y)$. Eventually, Alpha is the angle between the major axis of the ellipse and the line connecting image centroid and the center of the FoV. In Figure II.3, these parameters are schematically drawn into an image of a simulated air shower.

For stereoscopic reconstruction, coincident events must be matched. Therefore, camera images are time-stamped and events occurring within $\sim 1\,\mu s$ are considered coincident[8].

While in principle the Hillas parameters in combination with geometrically reconstructed shower parameters are sufficient for the gamma-hadron separation, contemporary algorithms use more sophisticated parameters. The zeta-bdt algorithm of Ohm et al. ([Ohm09]) that will be elaborated in detail later in this section uses six parameters for their gamma-hadron separation, four of them derived from the Hillas parameters. The usually most efficient parameter for separation is the mean reduced scaled width ($MRSW$), slightly varied from that introduced in [Aha06b]. To obtain the MRSW, [Ohm09] initially calculate the scaled width (SCW) by comparing the width W_i of an image with the mean width $\langle W_i \rangle$ of a gamma-ray image of similar size and core distance ($\vec{r}$ as described in Paragraph II.2.1) , obtained from MC simulations:

$$\mathrm{SCW}_i = \frac{(W_i - \langle W_i \rangle)}{\sigma_i} \tag{II.1}$$

Here, σ_i is the spread of the distribution of the expected width ([Ohm09]). The MRSW then

[8] As the telescopes are $\sim 100\,m$ apart, small time lags are to be expected due to different travel times of light from the air showers.

is the SCW averaged over all telescopes with a weighting factor $\omega_i = \langle W_i \rangle^2 / \sigma_i^2$:

$$\mathrm{MRSW} = \frac{1}{\sum_{i \in N_{\mathrm{tel}}} \omega_i} \cdot \sum_{i \in N_{\mathrm{tel}}} (\mathrm{SCW}_i \cdot \omega_i) \tag{II.2}$$

Following the same approach, the mean reduced scaled length (*MRSL*) is obtained. Further, both parameters are also computed under the assumption of a hadronic shower, by using the mean Width and Length obtained from Off-runs, pointing at a field with no gamma-ray source. They are named mean reduced scaled width off (*MRSWO*) and mean reduced scaled length off (*MRSLO*), respectively. The two other parameters of the zeta-bdt algorithm are X_{max}, the depth of the shower maximum and the averaged spread in energy reconstruction between participating telescopes $\Delta E/E$. The former makes use of different interaction lengths of photons and hadronic particles, depending on their energy. The latter is effective because the structure of a hadronic shower makes it more likely that the energy is reconstructed differently when being watched from different viewing angles than if it was a less chaotic electromagnetic shower. Obviously, all these parameters but X_{max} can only be used in stereoscopic observations, as more than one telescope is necessary to form them.

Derivation of shower parameters

In the following, the derivation of shower parameters for runs obtained stereoscopically is first explained. The derivation of shower parameters for monoscopic observations is described at the end of the section.

An EAS can be fully described by the set $S = (a, E, \vec{\Omega}, \vec{r})$ ([Aha97]). In this notation, a is the type (electromagnetic or hadronic) of the shower, E denotes the energy of the primary particle, $\vec{\Omega} = (\Omega_x, \Omega_y, \Omega_z)$ gives the arrival direction of that particle, and $\vec{r} = (x, y)$ defines the coordinates of the shower core in the plane of the telescopes. While a (the gamma-hadron separation) and E are usually reconstructed statistically using lookup-tables generated in MC simulations, $\vec{\Omega}$ and $\vec{r}$ are determined analytically. Therefore, the uncertainties of the latter two only originate in uncertainties of the previously described parameter estimation.

The first shower parameter to be retrieved is the arrival direction $\vec{\Omega}$. For this, the shower images in the cameras are projected into the common focal plane of all telescopes taking part in the event. Then, for each pair of telescopes the intersection point of the prolonged major axes is calculated and the mean of the intersection points is the reconstructed arrival direction. The projection is schematically shown in Figure II.4. To obtain the position $\vec{r}$ of the shower core, the arrival direction is projected into the plane of the telescopes, tilted perpendicular to the optical axis. The details of these calculations are elaborated in [Aha97].

To reconstruct the energy of a shower, the derived properties Image Size and $r = |\vec{r}|$ are compared with lookup-tables for each telescope individually. To create these lookup-tables, events with varying true energies E are created at different distances from the telescopes in Monte-Carlo simulations and processed through a simulation of the telescope array. A sufficiently large number of simulated events then delivers a robust relation for E as function of Image Size and r. To

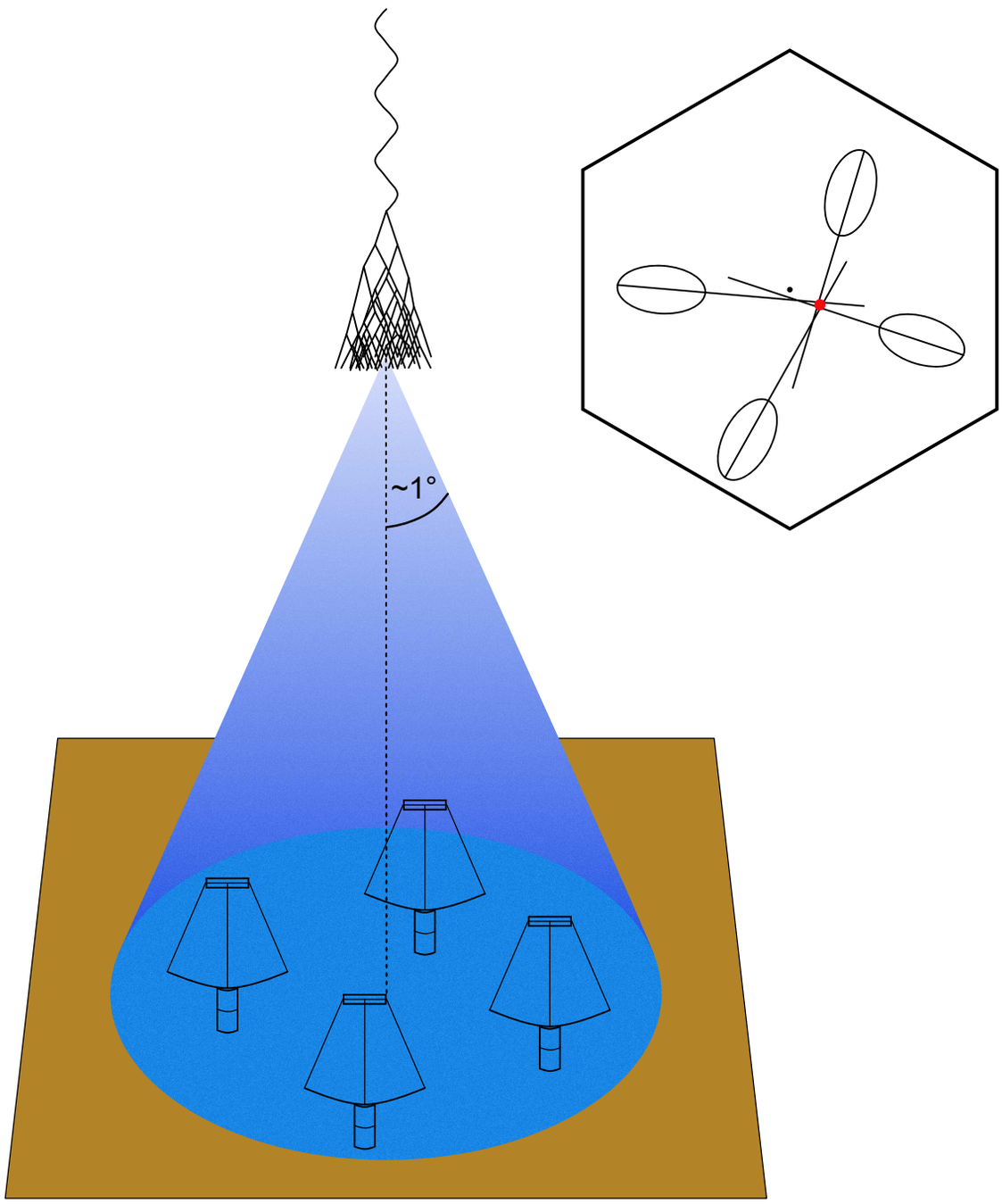

Figure II.4: Sketch of a stereoscopic shower detection and direction reconstruction. The air-shower (top) creates a Cherenkov flash (blue cone), which in turn illuminates all telescopes in its light pool (bottom). Superimposing the shower images in the cameras allows to reconstruct the direction (top right). This is done for each pair of telescopes individually. The mean of these reconstructed directions is taken as final result, denoted by the red dot. Telescopes whose image ellipses are (almost) parallel are not considered. Also, images that are very close to the center of the FoV or with small Sizes can be excluded, as their image parameters are subject to large statistical fluctuations ([Aha97]). The figure is not to scale.

account for different distances in the atmosphere to be traveled by the Cherenkov light, simulations are created at different zenith angles starting from 0° to about 65°, the maximum zenith angle under which targets are usually observed. Further, also the atmosphere and especially its transmissivity must be modeled properly, in order to obtain the correct number of Cherenkov photons reaching the telescope. As the atmospheric optical depth can change drastically, monitoring and even a correction on observation basis might be necessary. This is discussed in greater detail in Chapter V and in [Hol22]. Eventually, the estimation of the energy is performed under the assumption that the arriving particle is a gamma-ray. Hadronic showers are subsequently reconstructed with an energy of a factor 2-3 too low ([Aha97]). However, remaining hadron-induced events are (on-average) removed during gamma-hadron separation (see Paragraph II.2.1) and remainders during background estimation (see Paragraph II.2.2) and therefore do not play a role. A typical setup for MC simulations (used e.g. by the H.E.S.S. Collaboration) is CORSIKA for the event simulation and `sim_telarray` for the simulation of the telescopes (see [Ber08]).

Now, the only missing image parameter is the shower type a. It is determined during the aforementioned gamma-hadron separation that will be elaborated in the next section. Before, a possible solution for image parameter determination for monoscopic observations is presented. The approach is the MonoReco algorithm developed by Thomas Murach and collaborators for H.E.S.S. ([Mur16], [Mur17]). As pointed out in earlier works such as [Aha97], stereoscopic reconstruction strictly requires an event to be detected by two telescopes simultaneously in order to fully reconstruct it. While early, individual IACTs (e.g, the Whipple 10 m Telescope) could detect a source in the center of the FoV utilizing an excess of counts around small parameters Alpha, they were not capable of reconstructing the origin of an individual event. In the H.E.S.S. experiment, however, event-based reconstruction is used since the beginning. So, the CT5 telescope makes a monoscopic, event-based reconstruction algorithm necessary, as the majority of events detected by CT5 are not seen with the smaller CT1-4 telescopes, due to the lower energy threshold of CT5. The MonoReco algorithm uses a neural network (multilayer perceptrons) to retrieve a parameter δ, being the displacement (along the major axis of the Hillas ellipse) of the direction to be reconstructed from the image centroid $\vec{\theta}$. Image parameters to be inserted into the neural network are the Width and Length, the Size divided by the area of the Hillas ellipse (Density), the logarithm of the Size itself, and eventually the skewness and the curvature ("kurtosis") of the shower image in the camera ([Mur16]). To train the neural network, MC simulations of gamma-rays from different directions are used. The result of the analysis is an absolute value for δ. The direction into which δ must be applied is found by parameterizing the asymmetry of the shower image with its skewness [Mur16]. As briefly mentioned above, the impact parameter $\vec{r}$ can be retrieved from the reconstructed direction of the shower via a geometrical transformation only. Therefore, no special treatment in the monoscopic reconstruction is necessary. Finally, MonoReco also allows to reconstruct the energy of an event, using size, core distance and look-up tables.

Gamma-hadron separation

As pointed out above, the number of detected events initiated by hadrons outnumbers the detected gamma-ray-induced events typically by about two orders of magnitude. Therefore, it is crucial to suppress these isotropically distributed background events as good as possible. Hillas found that hadronic showers cause more irregular shapes than the well constrained ellipses coming from electromagnetic showers ([Hil85]). So, his shower parametrization robustly rejects hadronic events but is less sensitive in selecting gamma-ray like events ([Ohm09]). The drawback is that also many actual gamma-ray-induced events are removed from the analysis, which makes the detection of faint sources unnecessarily tough.

Today, more advanced approaches are in use, profiting from the increase in computing power since the 1980s when Hillas proposed his parametrization. For example the H.E.S.S. collaboration uses mainly three different methods: the *3D Model Analysis*, which compares the detected image with a three-dimensional, simulated model of the shower ([Lem06]), the semi-analytical model based *Model++ analysis* ([dN09]), and an extension of the Hillas analysis using boosted decision trees, the *zeta-bdt analysis* ([Ohm09]). The latter will be elaborated here exemplary. It also is the method used for the analyses presented in Chapter VI. Beside these, also new methods for gamma-hadron separation are under development, such as the Algorithm for Background Rejection using Image Residuals (ABRIR, [ON22]) that makes use of large IACTs (such as H.E.S.S.-CT5) and uses Cherenkov light bright enough to survive the cleaning but outside the shower image as a tracer of hadronic showers ([ON22]).

As mentioned above, the zeta-bdt analysis uses boosted decision trees to classify an event as hadronic or electromagnetic. It is introduced in [Ohm09]. A decision tree tests a series of parameters $M = [m_1, ..., m_n]$ for a binary criterion $m_g < m_{g,\mathrm{crit}}$. The parameters are ordered in descending order of separation efficiency. A decision tree is built from two sets of training data: one with signal and one with background events. Starting at the root node, the best parameter to separate signal and background events is determined together with the respective split value. For each subset, this process is repeated recursively within a branch. The recursion is stopped once further splitting does not increase the efficiency of the separation, or if the number of events within a branch reaches a preassigned minimum ([Ohm09]). The stop condition of a minimum number of events is necessary (besides the obvious condition of no more information gain) to avoid overtraining due to statistically insignificant branches ([Ohm09]). A terminated branch is called a *leaf*. It is assigned background or signal type, following the majority type of events in it. To account for statistical fluctuations in the training set, a so-called forest of two hundred decision trees is used rather than only one tree. While in the first decision tree all events got weighted equally, the events misclassified in the previous tree get higher weight in the subsequent tree. This is known as adaptive boosting.

In [Ohm09] it can be seen that the parameters and therefore also their order depend on the energy of the primary particle which induced the shower. For instance, $\mathrm{X_{max}}$ is more efficient in separating than MRSW for energies below 1 TeV, while MRSW is the most efficient parameter for showers with $E < 10\,\mathrm{TeV}$. The parameters $\mathrm{X_{max}}$ and $\Delta\mathrm{E/E}$ also depend on the zenith angle.

Therefore, simulations covering a wide range of energies must be run in sufficiently narrow zenith angle bands[9] to obtain the training sets.

The output of the boosted decision tree forest is a weighted mean of the result of all individual trees. It gives the likeliness of an event to be induced by a gamma-ray and is referred as ζ in [Ohm09]. The decision which events to keep in the end is made with *cuts*. Cuts are criteria for defining which results of a gamma/hadron separation are sufficiently certain such that the corresponding events can be assumed to have originated in an electromagnetic shower. As some parameters depend on zenith angle and energy, ζ does, too. A fixed cut on ζ leads to different cut efficiencies depending on the observational conditions, and would therefore result in a classification depending on these conditions as well ([Ohm09]). To avoid this, the γ-efficiency in each zenith angle- and energy band is predicted for all possible ζ-cuts and transformed into a new measure, the γ efficiency of an event $\epsilon(\zeta)$. In the HAP analysis chain of the H.E.S.S.-experiment, three sets of cuts are implemented for the small telescopes: originally, *standard cuts* for sufficiently bright, steep spectrum sources and *hard cuts* for weaker sources of harder spectra had been introduced ([Ohm09]). In the meantime, also *loose cuts* have been introduced to be applied on sources close to the lower energy threshold of the telescopes. The cuts on $\epsilon(\zeta)$ are 0.84 in the standard, 0.89[10] for the hard, and 0.85 in the loose configuration. Beside that, standard cuts only accept events with at least 60 p.e. image size, for hard cuts it is 160 p.e. and for loose cuts 40 p.e.. The squared angular distance between the shower direction and the assumed source position (θ^2) of an event may not be larger than $0.0125\,\mathrm{deg}^2$ or $0.01\,\mathrm{deg}^2$ for standard and hard cuts, respectively. All events that pass the applied cuts are collected in the aforementioned event list and can be used for further analysis.

Instrument Response Function

The event list contains for each event the reconstructed position and energy $\vec{p_{\mathrm{rec}}}$ and E_{rec}. However, for scientific statements, the *true* position and energy of an event, $\vec{p}$ and E are of interest. The IRF consists of three different properties: the effective area, the energy dispersion and the PSF:

$$IRF\left(\vec{p_{\mathrm{rec}}}, E_{\mathrm{rec}}|\vec{p}, E\right) = A_{\mathrm{eff}}\left(\vec{p}, E\right) \times PSF\left(\vec{p_{\mathrm{rec}}}|\vec{p}, E\right) \times E_{\mathrm{disp}}\left(E_{\mathrm{rec}}|\vec{p}, E\right) \tag{II.3}$$

The effective area corresponds to the reflector area of directly observing telescopes. It is in the order of $10^6\,\mathrm{m}^2$. Since the effective area is highly dependent on the energy of a primary it defines the energy range in which showers can be recorded. In particular, it defines an energy threshold for the telescope. Energy dispersion and PSF describe the probability distribution of energy and direction reconstruction, respectively. Technically speaking, the energy dispersion gives the probability that a gamma-ray with true energy E coming from direction $\vec{p}$ is reconstructed with energy E_{rec}. Similarly, the PSF gives the probability that a gamma-ray coming from direction

[9] Ohm et al. used seven bands from 0° to 60°. Today, twelve bands from 0° to 67° are used, with a finer grid for larger zenith angles.

[10] In [Ohm09], this value is 0.83, but has changed by the time of writing the present work.

$\vec{p}$ with energy E is reconstructed to come from direction $\vec{p_{\text{rec}}}$. Thus, they allow to estimate the statistical uncertainty of the analysis.

The IRF depends not only on the energy and the offset angle[11] of an event, but also on the observing conditions such as the zenith angle and the atmosphere. To account for the observing conditions properly, the IRF must be obtained for each observation separately. Within one observation run, the conditions are assumed to be stable. This assumption limits the maximum duration of an individual observation to $\sim 30\,\text{min}$.

Independent of the facility the data is obtained with, event lists and IRFs can be stored in the data format described in [Nig21] as FITS[12] (Flexible Image Transport System) files. These FITS files can be read by open source tools and used for instrument independent high level analysis, as will be described in the following Section II.2.2.

II.2.2 High level Analysis

While the field of gamma-ray astronomy is about to become mature, also the possibilities in terms of computing have changed since the construction of the current generation of experiments. Since in the early 2000s RAM and CPU power were quite limited compared to today, the three major facilities operating today (H.E.S.S., MAGIC and VERITAS) based not only their low-level, but also the high level analysis on the highly efficient ROOT Framework[13]. The efficiency of ROOT comes at the cost of less accessibility to new users. Python became a more interesting choice for the high level analysis in the past years. From several projects that started in the context of CTA, Gammapy ([Dei17], [Don22]) was selected as the core library for the CTA Science Tools. Thanks to the unified data format described in [Nig21], Gammapy can as well be used for the high level analysis of H.E.S.S., MAGIC, VERITAS and to some extent also for Fermi-LAT and HAWC.

Goal of the high level analysis is to obtain *science products* from the event list and IRF. Science products are sky maps, spectra, source models, etc. For that, *data reduction* must be performed, followed by estimation of the (gamma-ray) background. The reduced data is then binned, delivering first science products like spectra or sky maps. They can be used to fit models describing the observed astrophysical sources in the next step.

Data reduction and background estimation

During the Gammapy data reduction, the events are binned on a chosen geometry, selecting only the events within the energy range and from directions of interest. Geometry refers to both, a spatial map of given size and binsize and to an energy range divided by a given number of bins. The center of the map is typically the target position or the center of the on-region, in case a spectrum shall be extracted. Events that are localized outside that geometry (i.e., not in the map or not within the specified energy range) are not considered anymore. Further, events are

[11] The offset angle is the angular distance between the center of the FoV and the center of gravity of an image.
[12] https://fits.gsfc.nasa.gov/
[13] https://root.cern.ch/

rejected if the image offset from the center of the camera FoV is too large, since then the camera performance drops rapidly. A typical maximum offset chosen is 2°.

As discussed in Section II.2.1, the gamma/hadron-separation is a statistical process. Therefore, some hadrons inevitably get misclassified as gammas and constitute an homogenous background in the observation. Additionally, it is indistinguishable whether an EAS is induced by a photon or by a CR electron, which consequently contribute to the homogenous background as well. Especially near the galactic center, diffuse gamma-rays further contribute to the background. To obtain meaningful fluxes, this background must be accounted for. The common techniques are summarized in [Ber07]. Here, the ring-background and the reflected-regions-background methods will be introduced, as they will be used in Chapter VI. The ring-background method is traditionally used to derive the background for detection significances and a spatial analysis. A ring of typically 0.5° inner radius and 0.2° thickness is laid around the target position. All counts within this ring are assumed to be background. With the area of the ring, a residual background rate is calculated that is subtracted from the source position, taking into account the different exposure of the ring and the source position. For extended sources, the inner radius and the thickness can vary. To avoid contamination of the background by known (or suspected) gamma-ray sources, these positions are *masked* and thus excluded from the background estimation. In general, the background estimation method itself is not sensitive to small variations in the camera acceptance with geometry, due to the intrinsic symmetry of the ring. Vignetting, i.e., the degradation of acceptance with increasing distance to the center of the FoV, must be accounted for with corresponding acceptance models also when modeling the background. For spectral analysis, typically the reflected region background method is used. It was originally developed for *wobble observations*, where the center of the FoV is pointed slightly offset ($< 1°$) from the target. Alternating between two (or more) wobble offsets allows to eliminate the effect of vignetting and therefore, one does not rely on background acceptance models. To create off-regions, the on-region is projected on a circle. The center of this circle is the center of the FoV, its radius is the angular distance to the center of the on-region [Püh24]. Binning the number of counts after subtraction of the estimated background to a sky-map delivers an excess map, showing brighter and fainter regions, according to the analysis. However, a bright region on an excess map is not necessarily an actual source. Therefore, significance maps are produced, in which the significance of the excess in each bin is given, rather than the excess counts. Significance maps produced with Gammapy and used in Chapter VI show an estimation of the Li & Ma significance ([Li83]). Alternatively, the Li & Ma significance of a potential source can be obtained with a spectral analysis where the On-region is the assumed source. In case of point-like sources, however, the On-region must at least be as large as the gamma-ray PSF. In gamma-ray astronomy, a source usually is accepted if the derived significance is $\geq 5\sigma$. From the excess and significance maps, the morphology of an (extended) source is visible, assuming the acceptance across the map is sufficiently flat. In the course of a spectral analysis, flux points are determined, giving the collective flux from each energy bin in the whole on-region. Using these flux points, the spectrum of the source can be estimated. Numerical fitting of both, morphology and spectrum of a source, will be discussed in the next paragraph.

Fitting

The default fitting package in Gammapy is `iminuit` ([Dem20]). It is a Python interface to the C++ library Minuit2[14], a modern implementation of the widely used MINUIT minimizer-framework ([Jam75]). By means of maximum-likelihood fitting, `iminuit` matches an analytical function to a given dataset. Also least-square fits are available, as well as the possibility to provide a custom cost-function. However, maximum-likelihood fits are suitable for IACT data and the commonly used default method ([Don22]).

The datasets are the flux points and the excess maps produced during data reduction. Analytical functions may be the spectral models describing the flux points (e.g., a powerlaw of the form $\mathrm{d}N/\mathrm{d}E = N_0(E/E_0)^{-\Gamma}$) or spatial models, describing a 2D or 3D geometrical distribution of intensity.Models used in this work are introduced in Chapter VI. There are several models pre-implemented in Gammapy together with an easy accessible interface to introduce custom models.

An advantage of the `iminuit` package and the underlying MINUIT framework over other fitting routines is the estimation of (statistical) uncertainties. It is done with the HESSE and the MINOS algorithms. While the former is used in Gammapy as error estimator, the latter is more exact for highly non-linear models to be fitted ([Jam75]). The statistical uncertainties calculated during fitting correspond to 1σ, i.e., a confidence level of 68% ([Dem20]). These are also the uncertainties stated for the model parameters in Chapter VI.

The fitted models or individual parameters of them can eventually be interpreted to draw conclusions on the observed system. The shape of the spectrum may be compared to expectations from different theories and simulations and the spatial extension (or position) can be aligned with observations in other bands of the electromagnetic spectrum. In Section VI.4, such a fitting and interpretation process is performed. The surrounding of an SNR is modeled spectrally and spatially, and the results are used to locate and explain the origin of this emission.

II.3 Facilities

The following sections aim at describing some of the most influential facilities in IACT astronomy. Section II.3.1 gives an overview of the beginning of the field at the Whipple Observatory and how the HEGRA telescopes established the stereoscopic method. Following to that, Section II.3.2 describes the H.E.S.S. experiment in a bit greater detail, as big parts of this work are based on that array of IACTs. The future of the entire field is the CTA which will be introduced in Section II.3.3. Further operating or planned IACT facilities are listed in Section II.3.4. The rather short description of these compared to H.E.S.S. and CTA is not intended as a ranking, but is due to the focus of this thesis, which is on work with H.E.S.S. and developments for CTA.

[14] https://root.cern.ch/root/htmldoc/guides/minuit2/Minuit2.html

II.3.1 The origins

The first ever confirmed observation of TeV gamma-rays using an IACT was accomplished with the 10-m reflector of the Whipple Observatory, Arizona in 1989 [Wee89]. With a, compared to today's standards, archaic camera of just 37 pixels they detected the Crab Nebula with at a 9σ significance level. In 81 h40 min of observations, obtained between December 1986 and February 1988, they received 1173 excess counts over 651801 OFF-counts. While the uncertainties where much higher than today ("a factor of 1.5 (...) in both flux and energy", [Wee89]), they noted that the emission appears to be continuous. This makes the Crab Nebula until today the standard candle in TeV astronomy [Hes08].

While the observations at the Whipple Observatory gave birth to the Imaging Atmospheric Cherenkov Technique, a crucial step towards its maturing over the past ~ 20 yr was done with the High Energy Gamma Ray Astronomy (HEGRA) Cherenkov telescopes. The first telescope of HEGRA was completed in 1992 at the Roque de los Muchachos Observatory on the Canary island La Palma. From 1998 on, the system operated in its full extension stage with five identical telescopes (see [Kon99]). The telescopes had a $8.5\,\mathrm{m}^2$ reflector and a camera of 271 pixels, each. They were arranged in the corners of a square of 100 m side length, with the fifth telescope in the center of the square. Already during construction, the system was intended to operate stereoscopically. In 1996, the first ever detection of the Crab Nebula using the stereoscopic method was reported ([Koh96]). Three years later, it was proven that the stereoscopic method is superior over monoscopic observations ([Kon99]). In 2002, HEGRA was shut down to free the manpower for the construction and operation of H.E.S.S. and MAGIC, instruments of the second generation of IACTs.

II.3.2 H.E.S.S.

The H.E.S.S. collaboration operates five IACTs in the Khomas Highlands of Namibia at an elevation of 1800 m, near the Gamsberg ([Püh24]). The first four of these telescopes (named CT1-4) have been operational since 2003. CT1-4 are arranged at the corners of a square of 120 m side length. Each of them has a reflector of 12 m diameter and a camera with 960 pixels. Their design aims at energies above 100 GeV. In 2012, the fifth telescopes (CT5) was completed in the center of the square, which marks the transition from H.E.S.S. phase I to H.E.S.S. phase II. CT5 has a parabolic mirror whose dimensions correspond to a spherical mirror of 28 m diameter, making H.E.S.S. CT5 the largest optical[15] telescope in the world. The camera of CT5 originally consisted of 2048 pixels. All H.E.S.S. cameras use PMTs as light detectors. The installation of CT5 increased the number of events triggered significantly, as the large collection area effectively reduced the energy threshold of the whole system below 100 GeV. However, the original CT1-4 cameras were unable to follow these trigger rates due to their readout dead-time [Püh24]. Therefore, in 2015 and 2016, the cameras of CT1-4 were upgraded with new electronics, reducing the dead-time significantly ([Gia17]). The upgraded electronics is based on the NECTAr technology

[15] As IACTs detect the blueish Cherenkov light emitted in air showers, they may be called "optical telescopes", although their science case is TeV gamma-rays

originally developed for usage in CTA (see [Nau12] for more information on the NECTAr technology). CT1-4 with upgraded cameras are referred to as HESS1U. In 2019, also CT5 got an upgrade. The camera was exchanged with a fully functional prototype of a FlashCam (see Chapter III for more information on FlashCam). This upgrade increased the stability of the system and its capabilities for science operations ([Bi22, Püh21]).

Thanks to its location close to the Tropic of the Capricorn, the H.E.S.S. experiment can observe the center of the Milky Way close to the zenith every night. This allowed to survey the entire galactic plane ([Abd18b]) and made H.E.S.S. the IACT experiment that has detected the most TeV sources so far. However, with H.E.S.S. also extragalactic sources can be seen. Most notable is the blazar PKS 2155-304, about which the H.E.S.S. Collaboration has published more than a dozen papers (see the latest [Abd17a] and citations therein).

At the time of writing this thesis, H.E.S.S. is in its second extension phase after the initially planned end of operations in 2019. The chances to continue operations longer than the planned end in the second half of 2024 are good, as no facility south of the equator will competitive in sensitivity to gamma-rays before the end of the decade ([Püh24]).

II.3.3 CTA

The upcoming CTA is the next generation IACT facility ([Hof24]). It will operate IACTs of three different sizes in the northern hemisphere on the Canary Island of La Palma, at the site of the former HEGRA and current MAGIC telescopes and in Paranal, Chile, in the southern hemisphere near ESO's VLT and ELT. The three different telescope sizes are to cover energies over five orders of magnitude, from 0.2 to 300 TeV.

Large-Sized Telescopes (LSTs) implement a parabolic mirror of 23 m diameter to detect the faintest Cherenkov flashes from showers that are initiated by photons of 20 to 150 GeV (full system sensitivity). Their light carbon fibre structure allows fast positioning and optimizes the LSTs for searching galactic and extragalactic transients. A first prototype LST – which will be used as LST-1 in the final array – was inaugurated at La Palma in 2018 and is since then in an extensive testing, commissioning and science verification process. Preliminary results of this process are given in [Maz22]. Technical details of the LST are described in [Cor19].

The MSTs will cover the core energy range of CTA from 0.1 to 5 TeV (see e.g. [Bra23], [Püh17]). MSTs are built in a modified DC layout upon a steel structure. Their reflector is about 12 m in diameter, making them similar telescopes as H.E.S.S. CT1-4. A novelty for IACTs will be the positioner tower (see Figure II.1, left panel), holding the azimuth and elevation drives and acting as a protective storage for electrical components of the MSTs and their cameras. The tower will have a diameter of 2 m and a height of 9 m. As cameras, MSTs will have FlashCams (see Chapter III) in the southern hemisphere array and NectarCAMs (see [Gli16]) in the northern hemisphere array. While the first complete NectarCAM is still under testing in the lab, the first complete FlashCam is already in use in H.E.S.S. CT5. However, the core element of the NectarCAM readout-electronics, the NECTAr-Chip ([Nau12]), is running in the HESS1U-cameras and has proven its stability there. In Berlin-Adlershof, a prototype MST has been operated to

prove that the telescope structure and both cameras provide basic functionality [Hof24]. As an alternative approach, also SC-mounted telescopes are developed with a size comparable to MSTs, the SCTs ([Ada21]). Since their development lays behind the MSTs, they are not foreseen in the initial layout of the two CTA sites, but might be built in a future enhancement stage of CTA ([Hof24]).

For the highest energies (5 to 300 TeV), CTA will deploy Small-Sized Telescopes (SSTs, [Whi22]) at its southern hemisphere site. They will be SC-mounted with an effective mirror area of $\sim 5\,\mathrm{m}^2$, only. From different suggestions, the ASTRI-Horn telescope structure design and the CHEC-S camera were chosen for the SSTs of CTA (see [Arc21], [Zor19] and references therein). The SC mounting in combination with a SiPM camera results in the highest angular resolution of all IACTs that will be built initially within CTA.

Construction of CTA has started at both sites. At the time of writing this thesis, planned start of operations for CTA are the late 2020s. Besides the already running LST-1, also *pathfinders* for MSTs will be built sooner (planned for 2025), allowing to possibly optimize details of the telescope design and the deployment procedure. In the first stage, CTA will consist of 4 LSTs and 5 MSTs in the northern array and 14 MSTs and 37 SSTs in the south (*alpha configuration*). With additional, already granted funding 2 or 3 LSTs and 5 SSTs will be added to the southern array ([Hof24]). The planned, final enhancement stage of the two CTA sites would consist of 4 LSTs and 15 MSTs in the north and 4 LSTs, 25 MSTs and 70 SSTs in the south (*omega configuration*). However, funding for this is not yet guaranteed and technical as well as scientific developments might change the needs of instrumentation.

CTA is planned to be operated as (the first) open gamma-ray observatory, accepting observing proposals from the whole scientific community. Additional to that, 40% of the total observing time within the first ten years is reserved to follow the CTA key science projects (see [Con19]). With CTA, the field of ground-based, imaging gamma-ray astronomy is about to become mature. Thanks to the unprecedented sensitivity of the telescope systems, hundreds of new sources will be detected, once both arrays are completed.

II.3.4 Other IACT facilities

There are other, major IACT facilities that should not go unmentioned, although they are not part of the work conducted within this thesis. Currently in operation are the Major Atmospheric Gamma Imaging Cherenkov Telescope (MAGIC) and the Very Energetic Radiation Imaging Telescope Array System (VERITAS). Another planned facility is the ASTRI Mini-Array, which has been developed as part of the CTA development but will be operated independently. This section briefly introduces these facilities.

MAGIC consists of two parabolic telescopes of 17 m mirror diameter each. It is located at the Roque de Los Muchachos Observatory on the Canary Island of La Palma, the former HEGRA and future CTA-North site. Actually, the CTA-North array will be constructed around the MAGIC telescopes while those remain observing, according to current planning. The first telescope has been operational since 2004, the second since 2009. In 2012, MAGIC underwent a major upgrade

to unify the two telescopes for easier and better stereoscopic observations. Technical details and the performance of the system operating since then are summarized in [Ale16a] and [Ale16b]. Main design goal of the MAGIC telescopes is a low energy threshold of about 50 GeV and fast repointing, with a slewing rate of $7°/s$[16].

VERITAS is located at the Whipple Observatory in the USA. It consists of four telescopes with a 12 m diameter, DC-mounted dish each, arranged in an irregular quadrangle. The first telescope was completed in 2004. After an intensive testing and commissioning phase ([Hol06]), the three other telescopes were built in 2006. As suggested by the dimensions of the telescopes, VERITAS covers a similar energy range as the H.E.S.S. phase I array, but with a somewhat smaller FoV and in the North: from about 100 GeV to < 30 TeV ([Han24]). VERITAS is the first IACT array that exploits intensity interferometry observations ([Abe20]). During bright moon-phases when standard IACT operations are impossible, they use the large collection area of the IACTs and their baseline of about 100 m to measure the diameter of bright stars in the optical wavelength band ([HB67]). It is a promising method to reduce the time in which IACTs cannot conduct any scientific operations.

ASTRI-Horn is the telescope proposal for the SSTs of CTA upon which the structure of the final SSTs is based. Funding from the Brazilian, Italian and South African government was granted to built pathfinder telescopes at the CTA-South array. However, the availability of these funds does not match the time-schedule of CTA. In order not to let the funding lapse, the ASTRI-Mini Array will be built, as described in [Scu22]. It will consist of nine SC-mounted telescopes with an effective area of about $5\,m^2$ each, located at the Teide Astronomical Observatory, on the Canary Island of Tenerife, in visual range to the Roque de Los Muchachos Observatory. Core program for the ASTRI Mini-Array will be observations of gamma-rays from ~ 1 to 100 TeV. At the time of writing this thesis (2024), scientific operations are planned to start in 2025.

[16] see https://magic.mpp.mpg.de/newcomers/technical-implementation/, accessed on 26th October, 2023

III

FlashCam: a camera for the Medium-Sized-Telescopes of CTA

III.1 A fully digital camera for Imaging Air Cherenkov Telescopes

III.1.1 The FlashCam concept

The FlashCam concept was presented at the 4th Heidelberg International Symposium on High Energy Gamma-Ray Astronomy in 2008 for the first time ([Her08]). While being meant as a concept purely for the electronics of cameras for IACTs (mainly for CTA), "FlashCam" (FC) became a standing term for a specific camera built upon that concept within the next decade. As of today, 2023, FC is foreseen to be the camera for the MSTs of CTA-S ([Hof24]). Furthermore, since 2019 a FlashCam is installed in the CT5 telescope of the H.E.S.S. experiment in Namibia ([Püh21]).

The FC concept is unique within Cherenkov cameras, as it features fully digital signal processing and is organized in small modules that facilitate mass production and are easily accessible for maintenance ([Püh24]). Due to the modular concept, FC follows a horizontal layout with three different levels: the photon detector plane (PDP), the readout electronics (ROS) and the data acquisition (DAQ). Figure III.1 shows schematically this layout and the connections between the different levels. Another unique feature is that only one readout channel is used per pixel, contrary to two (high- and low gain) as for most IACT cameras. The fully digital approach in signal processing allows the camera still to cover a dynamic range of < 1 to 3000 p.e. ([Püh15]). In the upcoming two paragraphs, the components of FC and its working principle are explained in detail. Section III.1.2 covers the hardware of the camera, including the camera mechanics and auxiliary systems. In Section III.1.3 it is presented how the digital signal processing of FC works in detail.

III.1.2 Hardware

The three levels of FC's horizontal layout mentioned above serve as an efficient pipeline for data-taking. Single photons are detected basis by the PDP on a pixel-by-pixel basis. The resulting signals are processed and buffered by the ROS, where a trigger decision is also made. If the camera is triggered, all signals are sent to the DAQ for further processing. Finally, the results

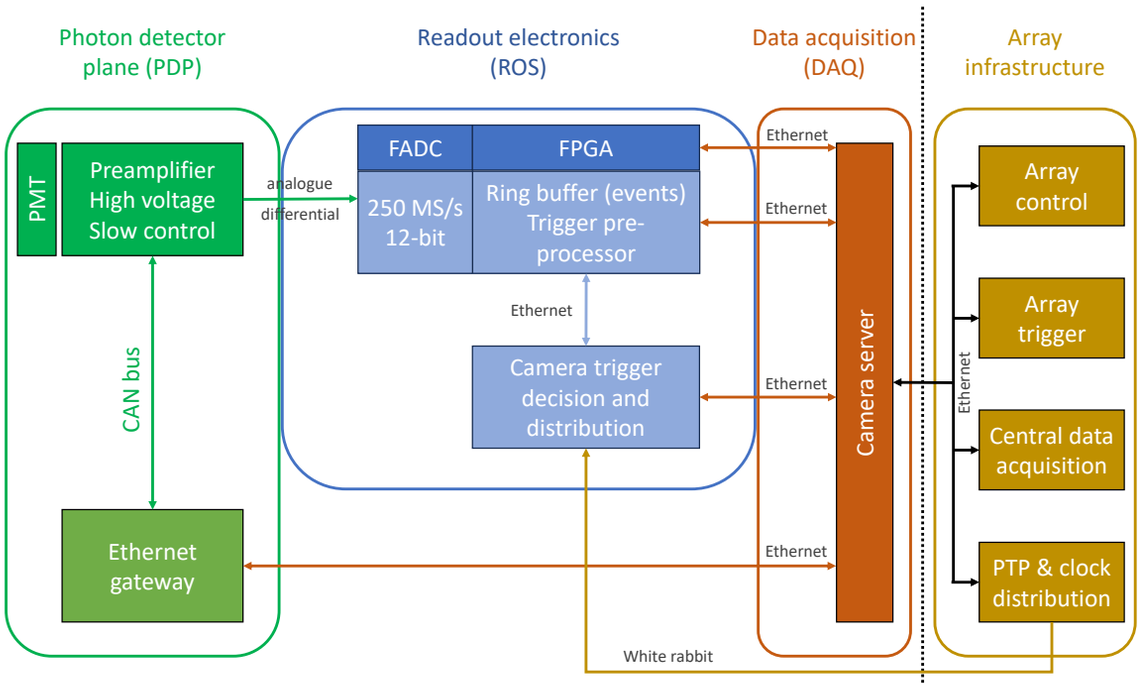

Figure III.1: Organization chart of a camera following the FC concept. The highlighted frames represent the three layers of an FC camera, as well as the central control level of the array the camera is installed in. The chart is adapted from [Püh19].

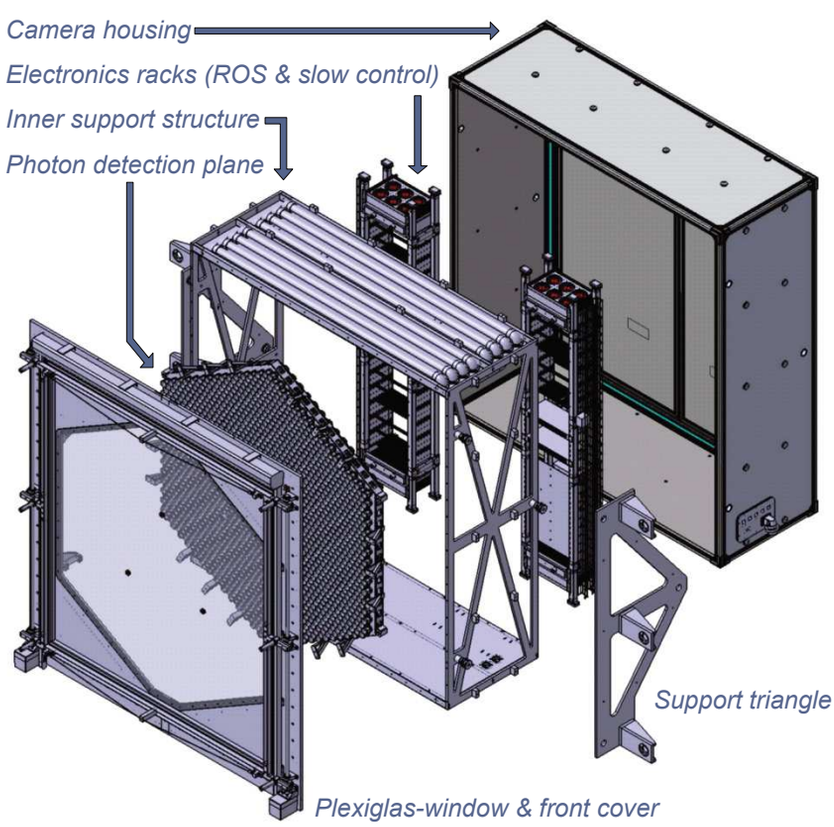

Figure III.2: Exploded view of a FlashCam camera body. Visible are the PDP, the racks for electronics (here without FADC modules) with cooling fans on top, as well as the camera housing and support structures. Not shown are the pipes of the cooling system. The camera server will not be hosted inside the camera body but in a separate shelter. Picture taken from [Püh24].

are transferred to the central infrastructure of the observatory. In the following, the hardware configuration of an FC for the MSTs of CTA-S is described, which is identical to the fully functional advanced prototype used in the large telescope of the H.E.S.S. experiment (FC@CT5). The information is summarized from [Püh15], [Püh19] and [Püh24].

The PDP consists of 147 PDP-modules, each of them holding twelve pixels and support electronics for high voltage (HV) supply and slow control. This results in 1758 pixels for data taking, three masked pixels for calibration and three posts to hold a Plexiglas front cover. The latter protects the pixels from mechanical damage and shields them from UV radiation well below 300 nm. The front cover with the Plexiglas window is shown leftmost in Figure III.2 The parallelogram-shaped PDP-modules are arranged such that the complete PDP forms a regular hexagon. Foreseen photo-detectors for the usage in the MSTs of CTA-S are PMTs with a diameter of 0.18°, resulting in a camera FoV of 7.7°. For possible upgrades in the future, the usage of SiPMs is in principle possible and currently under investigation. In front of the PMTs, Winston cones are placed to minimize both, the loss of photons due to pixel spacing and contamination through stray-light. Additionally, each pixel features a preamplifier that employs a non-linear amplification scheme. It amplifies signals below ~ 250 p.e. linearly and saturates in a controlled way for higher amplitudes. In saturation, the integrated signal can be described with a quasi-logarithmic function of the input charge ([Püh19]). This amplification scheme allows a very good resolution of low-amplitude signals, while still being able to handle signals up to and exceeding 3000 p.e..

The PDPs are DC-coupled. Therefore, a constant baseline current is set which damps the electronic noise and makes the data-taking procedure more stable. As changes in the NSB induce a correlated change of the baseline-level, it is used to monitor the NSB level as well. However, for later signal-processing the baseline-level must be subtracted again.

The signals generated in the PDP are routed via cat 6 Ethernet cables to the ROS for further processing. The ROS consists of eighty-four FADC-modules, twelve Trigger-modules and one Master-module. All modules are based on a common motherboard design, equipped with different piggy-backs which assign them their functionality. Core of the motherboards is a field programmable gate array (FPGA), which runs different code depending on the type of module. The FADC-modules are equipped with either one or two piggybacks, holding twelve flash analog-to-digital converters (FADCs) each. This allows each module to continuously digitize the signals from twelve or twenty-four pixels, respectively, each at a rate of 250 MHz. The FPGA of the FADC-modules serves as a ring buffer for these digitized signals.
If the camera triggers, the corresponding time window – a so-called *trace* – is read out from the ring buffer and sent to the camera DAQ. Typical length of a trace is 128 ns. The camera is capable to handle trigger rates up to 30 kHz dead time free. Trigger decisions are formed in the Trigger-modules, each of which collects information from seven FADC-modules. The camera triggers whenever the summed charge in one of the 588 overlapping nine-pixel-patches exceeds a given threshold. A mechanism is implemented to avoid single pixels with very high signals accidentally trigger the camera. Thanks to the re-programmable FPGAs, other trigger schemes could be incorporated as well. When occuring, the trigger signals are distributed via the Master-

module over the whole camera. At the same time, it sends a signal to the DAQ that there is a trigger in this camera which subsequently can be distributed to the entire array. Vice versa, array trigger signals are received, processed, and distributed via the DAQ and the Master-module as well.

The ROS is connected to the camera DAQ via four 10 $\frac{\text{Gbit}}{\text{s}}$ Ethernet fibers for data transfer and two additional ones for slow control and monitoring. The DAQ itself consists of an off-the-shelf computer, the camera server. It receives the traces read out and processes them. This means that parameters like the maximum or the width are derived from the trace and buffered before being sent to the array wide data acquisition. More details on FC's signal processing are given in Section III.1.3. The camera server also is responsible for communication between the array control and the camera like receiving and processing commands or sending monitoring information. Further, it controls the support systems of the camera. Among them are smoke and humidity detectors and a climate-control system. The latter consists of two components. Firstly, there is an active water cooling system with a thermo-circulator installed outside. It provides stable temperatures inside the camera body and effectively transports the heat produced by the ROS outside the camera body. The second component of the climate control system is a ventilation system creating a light overpressure inside the camera. In case of leaks in the ceiling, this prevents remaining moisture from evaporating and major amounts of dust from entering the camera. The total power consumption of the camera and its support systems is about 6 kW.

III.1.3 Pulse reconstruction

The reconstruction of pulses in FC is rather complex due to the non-linear behavior of the pre-amplifier. The goal is to calculate the number of pe, i.e., the charge Q induced in a pixel. The pulse reconstruction can be divided in two distinct steps: first is the digital trace processing, happening directly on the camera server, second is the actual charge reconstruction from the trace parameters. In CTA it is foreseen to perform this step at the centralized computing cluster at the CTA-S Observatory site. For FC@CT5 it is done only in Europe. The description of the process below is implemented in the FC used in H.E.S.S.-CT5. For CTA, the reconstruction algorithm will most likely be adapted. However, the requirements for the reconstruction performance are still not finalized.

Start point of the digital trace processing are the raw traces from the FADCs, containing the ADU counts in bins of 4 ns. These traces get upsampled: by means of a gliding average filter the traces are smoothed and the sample frequency is increased from 250 MHz to 1 GHz. Next, the derivation of the upsampled traces is computed numerically. The result is referred to as differentiated trace. Eventually, the upsampled and the differentiated traces are added up with a weighting factor, (partially) canceling the undershoot of the differentiation. This last operation is the digital counterpart of an analog pole-zero cancellation, therefore, the final trace is called the pz-corrected trace. Figure III.3 illustrates these steps on the example of three pulses of different intensity (i.e., different charges initially induced). The traces of these are shown in each of the three different steps of digital signal processing.

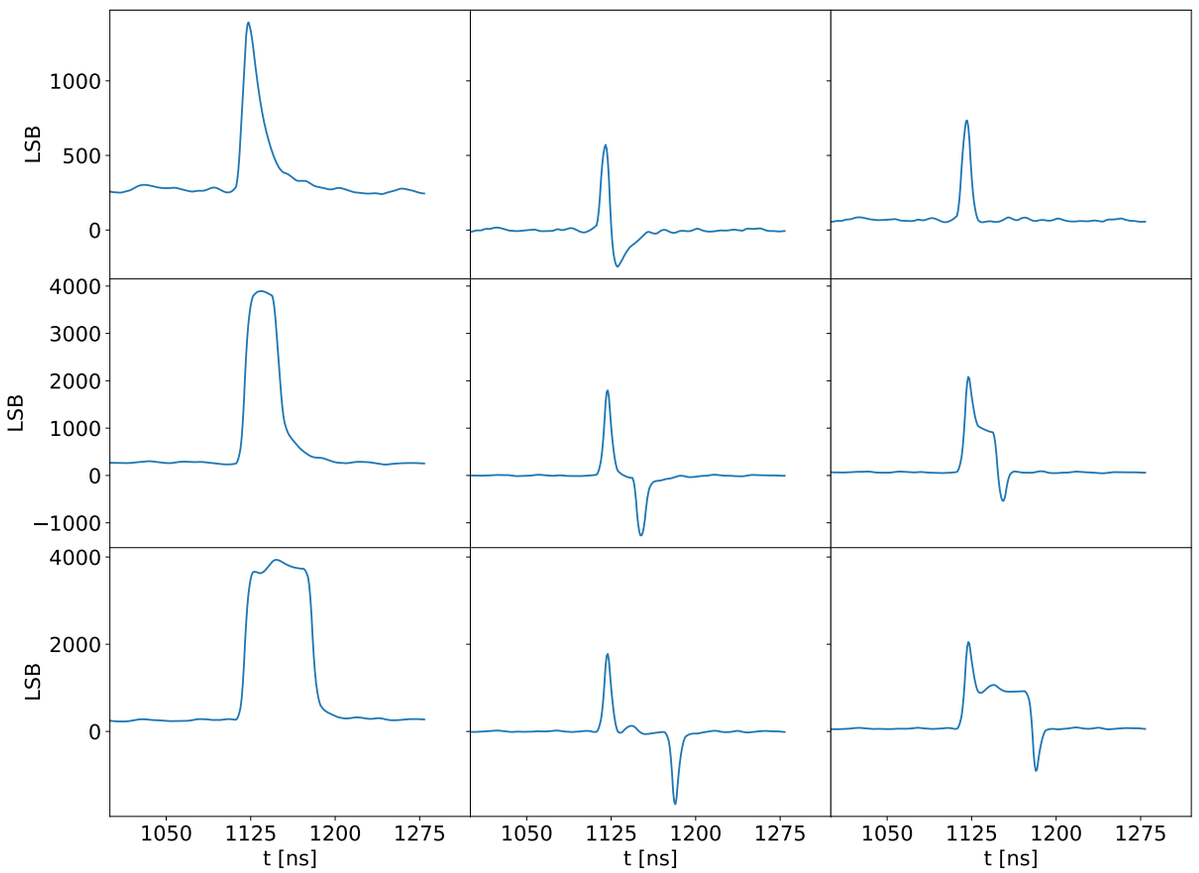

Figure III.3: The steps of digital signal processing. Columns, left to right: Upsampled, differentiated and pz-corrected traces. Rows, top to bottom: Traces recorded in the lab from pulses of about 100 p.e., 450 p.e., and 900 p.e., respectively ("linear, transition and non-linear regime"). Note that the upsampled (and consequently also the pz-corrected) traces have a background level > 0, due to the baseline-shift.

From each trace recorded, multiple parameters are saved. Important for the reconstruction explained in the following are

- A_{1200}, the integral of the baseline subtracted upsampled trace above 1200 ADU.
- T_{d}, the time between the global maximum and the global minimum of the differentiated trace.
- $xmax$, the maximum of the upsampled or the pz-corrected trace, respectively (x is then replaced by either u or pz).
- $xbgmax$, the respective background of the upsampled or the pz-corrected trace.

The three intensities used in Figure III.3 are instances of the three regimes used in the reconstruction of FC signals: the linear, the non-linear and the transition regime. These regimes are determined by the behavior of the pre-amplifier. In the linear regime (signals below 250 p.e.), the induced charges and the amplitudes of the pulses are linearly connected (for short, single-peak pulses as appearing in Cherenkov astronomy). This is no longer the case in the non-linear and the transition regime due to the controlled saturation of the preamplifier. Therefore, other calibration curves with more parameters are necessary. These parameters are either camera-wide parameters, representing the average behavior of all pixels or pixel-wise parameters to correct for deviations from the average in individual pixels.

In the linear regime, the charge can be reconstructed with $xmax$, taking into account the respective background $xbgmax$ as shown in Equation III.1. The background is induced by the baseline-shift which leads to a constant number of counts, even in absence of any signal.

$$Q = \frac{xmax - xbgmax}{g_{\mathrm{x}}} \tag{III.1}$$

g_{x} is the pixel-wise gain of the corresponding quantity. It is derived from single pe measurements (SPE measurements, see [Bel93] for more details) for $umax$ (g_{u}) and describes how many adu-counts correspond to 1 p.e. in the upsampled trace. In practice, $pzmax$ is chosen over $umax$ for reconstruction as it is sharper (c.f. Figure III.3) and therefore, faintest signals can be resolved with higher accuracy. The corresponding gain g_{pz} is derived from g_{u} via the mean between 30 and 150 p.e. of $R_{\mathrm{u/pz}} = \frac{umax}{pzmax}$:

$$g_{\mathrm{pz}} = \frac{g_{\mathrm{u}}}{R_{\mathrm{u/pz}}} \tag{III.2}$$

It is necessary to take $xbgmax$ into account for the background in Equation III.1, rather than the average baseline-shift of the trace: The peak $xmax$ is obtained as the maximum within (the peaking) 4 ns window of a trace[17]. As this approach favors selecting the value with the maximum background fluctuation within the window, using the average baseline-shift of the trace would on large scales cause a positive bias in the reconstructed charge Q. $xbgmax$, however, is the maximum

[17] This window corresponds to one sample. Which sample to chose is determined from the time of the trigger.

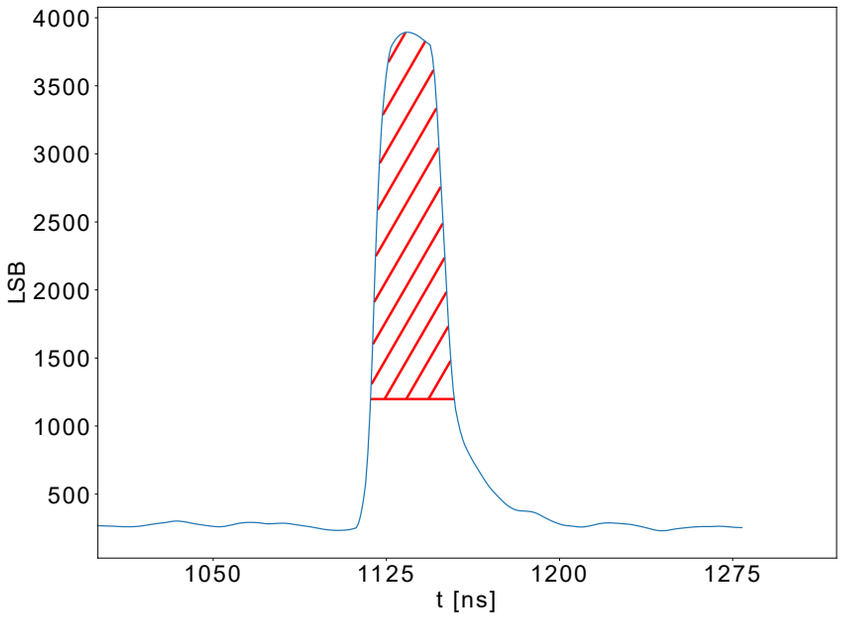

Figure III.4: Graphical illustration of the A_{1200} parameter. It is defined as the area under the baseline-corrected (not shown), upsampled trace above a threshold of 1200 ADU (red-shaded area). Mathematically this corresponds to the integral of the trace after subtracting the average baseline + 1200 ADU and setting all negative values to 0. Again, note that the baseline-subtraction is not shown here.

within a 4 ns-window right before the pulse is measured (16 to 20 ns before the position of the maximum) and therefore cancels this bias out.

For very high input intensities (>500 p.e. with the current pre-amplifier settings, see the bottom row of Figure III.3), the linear relation does not hold anymore. As the pre-amplifier then is in saturation, the amplitude is constant, regardless of the induced charge. However, the duration of the pulse T_d increases with growing intensity. Using masked pixels[18], a calibration curve following Equation III.3 for a reconstructed $umax_\mathrm{rec}$ can be constructed.

$$umax_\mathrm{rec} = \mathrm{e}^{c_{1,2}T_\mathrm{d}+s_{1,2}\cdot bls+b_{1,2}} \tag{III.3}$$

Here, $c_{1,2}$ and $s_{1,2}$ are camera-wide calibration parameters, $b_{1,2}$ is a pixel-wise correction. The indices 1 and 2 refer to the first and the second non-linear regime, as the powerlaw describing it breaks around 1400 p.e.. bls denotes the baseline-shift of the trace which accounts for the background. $umax_\mathrm{rec}$ is the maximum of the baseline subtracted upsampled trace under the assumption that the camera response was linear for all intensities. The relation of $umax_\mathrm{rec}$ and the induced charge Q is linear per definition with g_u that is found during the laboratory calibration.

$$Q = \frac{umax_\mathrm{rec}}{g_\mathrm{u}} \tag{III.4}$$

Note that g_u would also be the gain of $umax$ for reconstruction in the linear regime.

While both approaches – the linear relation of $pzmax$ and the exponential relation of T_d – meet the CTA benchmark[19] in their respective regimes, the transition between them needs to be covered separately. So, the transition regime (middle row in Figure III.3) is introduced for pulses

[18] Masked pixels are pixels whose FoV is artificially reduced, such that their response is in the linear regime while it is in the non-linear regime for the rest of the camera.

[19] The term "benchmark" is used, as at the time of writing, no formally approved CTA requirements are available.

that are not in the linear regime anymore but which cannot be resolved with sufficient accuracy in the non-linear regime. It relies on the area of the baseline-subtracted, upsampled trace above 1200 ADU, A_{1200}, as sketched in Figure III.4. From A_{1200}, $umax_{\mathrm{rec}}$ is obtained again such that the charge can be derived as in Equation III.4. The relation between $umax_{\mathrm{rec}}$ and A_{1200} itself is linear:

$$umax_{\mathrm{rec}} = k_{\mathrm{A}} A_{1200} + b_{\mathrm{A}} \tag{III.5}$$

Here, b_{A} is a camera-wide constant and k_{A} a pixel-wise parameter. Investigations whether A_{1200} might also be the better variable to describe the non-linear regime found that it gets unstable when the signal intensity approaches 1000 p.e. with the current pre-amplifier settings. Therefore, in FC@CT5 the three regimes are in use as described above. At the time of writing, a paper with more detailed analyses and conclusions on the reconstruction is in preparation ([Bi24]), as well as an internal documentation for CTA with more extended studies.

III.2 Usage in H.E.S.S.

In October 2019, a fully functional advanced prototype of an FC was installed into the large CT5 telescope of the H.E.S.S. experiment ([Püh21], [Bi22]). Only two days after installation into the telescope, the Crab nebula was detected with high significance at its actual position, demonstrating basic functionality of the camera after installation [Hof22]. The new combination FC@CT5 underwent an extensive technical commisioning program to ensure full functionality while the H.E.S.S.-I array continued standard science operations. Subsequently, CT5 joined the four smaller telescopes again for observations. Within the next couple of months, science verification observations of various sources were scheduled alongside the normal science operations to ensure the full functionality of FC@CT5. At the same time, the technical performance of FC was carefully monitored. Both, the science verification and the technical performance were presented at the International Cosmic Ray Conference 2021 ([Püh21], [Bi22]). The results are summarized below.

In laboratory measurements prior to the installation to CT5 the technical performance of FC was found to work up to expectations and fulfilling all requirements set by CTA ([Wer17], [Püh19]). In [Bi22], it is shown that the performance also in the field is stable and up to expectations during the first year of operation the paper covers: In that time, the availability of the camera was $> 98\%$. The cooling system, assumed to be one of the most critical parts ([Wer17]), maintained the optimal camera-internal temperature of 26 to 32 °C with a standard deviation per pixel < 0.1 °C within one observation run. Over the entire first year, the standard deviation of the temperature within one pixel was between 1.1 °C and 1.6 °C.

Using the flatfield (FF) unit installed in CT5, FF coefficients were obtained. The FF coefficients are a pixel-wise quantity. For each pixel, they give the ratio of the reconstructed charge to the median charge over the entire camera ([Bi22]). Thus, they are a measure of the homogeneity of the camera response which is very good with a standard deviation of 5.2% in the FF coefficients

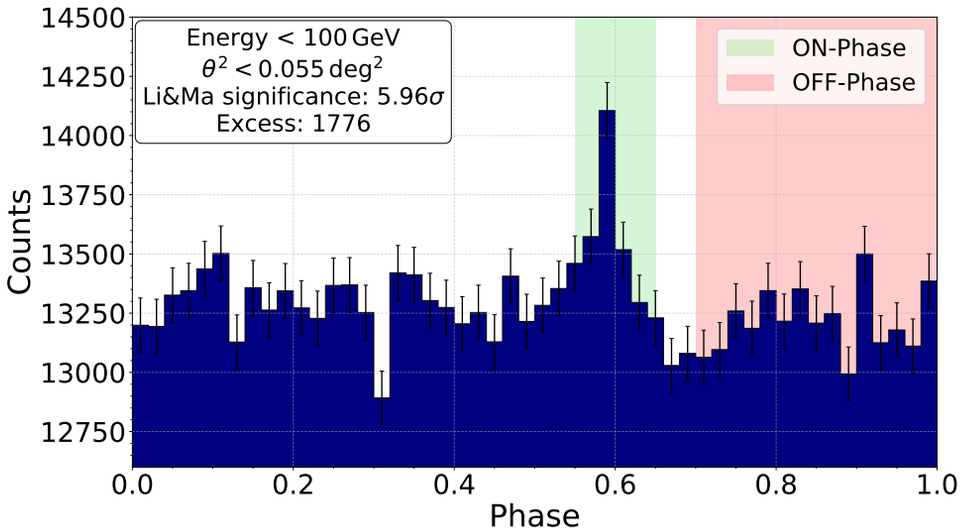

Figure III.5: Phasogram of the Vela pulsar, obtained with FC@CT5. To obtain the data below 100 GeV, a special set of cuts optimized for lower energies is applied. Image taken from [Püh21].

between the pixels. FF coefficients are obtained twice per month, allowing solid monitoring. Over the first year of observations, the variation of most pixels is less than 3% [Bi22]. Eventually, also the gain of the camera is monitored using the FF unit. A gain loss of up to 4% in combination with an increase of the gain spread (the relative standard deviation) from 2.5% to 4% is reported [Bi22]. Gain loss is a normal aging phenomenon of PMTs and can be countered by increasing the high voltage applied to them.

Three months after installation of the camera, the reconstruction of charges in the non-linear regime was tested with intensity sweep runs. For that, the illumination level of the camera by the FF unit is increased from the normal value of FF runs (130 p.e.) to more than 2000 p.e.. The reconstruction from the intensity sweep runs agrees with the laboratory calibration, obtained with masked pixels. The resolution exceeds the CTA benchmark ([Bi22]). More details on flatfielding in IACT astronomy, the FF unit used in H.E.S.S., and a study on FF simulations are given in Chapter IV. Eventually, also the timing and the stability of the trigger rate are discussed in [Bi22]. The timing accuracy between the pixels varies by $\sim \pm 0.5$ ns and can be corrected for. Negligible variations within single pixels < 0.1 ns remain. The trigger rate is found to be stable over the entire year at zenith-corrected ~ 2.7 kHz[20]. During observation runs, dead time significantly < 0.1 ns is reported and fully attributed to the backend software. Apart from that, the system is running smoothly and fully up to expectations.

It was not only verified that FC works as planned technically, but also that the obtained data is of good quality. The science verification of FC@CT5 as described in [Püh21] addresses six tasks:

1. Verify that simulations and actual data match in low-level analysis by observing bright point-sources.

2. Verify the pointing and the pointing model.

3. Verify the gamma-ray PSF derived from simulations.

[20] Due to limitations in the H.E.S.S. DAQ it is not possible to reach FC's expected maximum trigger rates of up to 30 kHz.

4. Ensure a flat background in the FoV during observations.

5. Measure and reconstruct correctly the spectrum of a reference gamma-ray point-source.

6. Measure and reconstruct correctly the phasogram of a pulsed reference source.

To complete these tasks, observations of the Crab Nebula (task 1-5), the BL Lac object PKS 2155-304 (task 1-4) and the Vela pulsar (task 6) were obtained. Additionally, data from the intermediate BL Lac object PKS 0903-57 is used (task 2-4), as this source underwent a strong outburst starting April 1, 2020. Another point that is not addressed in the science verification presented here is the analysis of an extended source. This was done on the example of the SNR HESS J1731-347 with observations conducted in 2020 and 2021. The results of that step are presented in detail in Chapter VI.

The analyses in [Püh21] are conducted with a preliminary configuration of HAP. HAP is the first standard H.E.S.S. software that was adapted to analyse FC@CT5 data. In the version used for [Püh21], still some uncertainties were present. Resolving them led to a validation of the entire MC simulation chain of HAP, which is outlined in [Leu23] and reported in more detail in Chapter V, as well as in the PhD theses of J. Schäfer ([Sch23]) and Simon Steinmassl ([Ste23]). However, already with the analysis configuration available in the first half of 2021 it is possible to achieve many of the goals described above. Analyzing the data from the Vela pulsar firstly shows the time stamping to work correct and secondly underlines the instrument's capability to measure gamma-rays with energies well below 100 GeV. The phasogram is shown in Figure III.5 and shows a clear detection of the pulse matching previous results from [Abd18a]. Further, the analysis of PKS 0903-57 proofs that FC@CT5 is able to detect a strong point source ($> 80\sigma$ in this case) while no significant emission remains in the FoV after masking the source. Also a preliminary spectral analysis of the Crab Nebula data was conducted. While the flux calibration is pending in [Püh21] such that no final spectrum was produced, comparison of low level parameters of the Crab observations allows to conclude that the camera output is correct and the camera itself therefore works up to expectations.

Apart from the science verification and in particular since the observations dedicated to that are completed, FC@CT5 takes part in the normal science operations of the H.E.S.S. experiment. For example, the telescope with its new camera contributed in 2021 to the first detection of a recurrent nova in VHE gamma-rays ever ([Aha22b]). It obtained data between 100 GeV and 200 GeV, significantly reducing the gap between observations with CT1-4 (> 200 GeV) and Fermi-LAT (12.9 GeV). Further, the modern camera in combination with the large telescope allows to investigate new analysis approaches, e.g., the rejection of hadronic showers ([ON21], [ON22]). In conclusion, the operation of FC in the H.E.S.S. experiment is a proof that the camera is working as intended. While at the beginning some minor issues in the reconstruction needed to be resolved, FC is now well established as the camera instrument of the world's largest IACT.

III.3 Response to pulses of varying length

III.3.1 The FlashCam Two-Laser-Experiment

The reconstruction described in Section III.1.3 bases on laboratory measurements. In a dark room at the MPIK in Heidelberg, the camera that is now in use at the CT5 telescope of the H.E.S.S. experiment was illuminated homogeneously with a calibrated pulsed laser light source. The homogeneity is reached with a diffuser in front of the light source. Any deviations of the homogeneity are negligible such that the biases shown in Figure III.6 can be attributed to the camera. In that setup, the NSB is simulated by blueish LEDs at tuneable intensities. They induce an artificial NSB in the pixels of the camera of multiple 100 to 1000 MHz. Identical to when the camera is installed at a telescope, the camera temperature in the dark room setup is kept stable with the camera-internal cooling system. The values chosen to obtain the calibration parameters are an NSB of 300 MHz and a temperature of 30 °C. These values match very well those obtained later during the operation of FC@CT5.

To derive the reconstruction algorithm of FC (presented in Section III.1.3), data has been obtained with the setup described. Then, the algorithm was used to analyze newly obtained measurements and reconstruct the number of p.e.. As illustrated in Figure III.6, this worked with great success, which indicates that the camera response to a calibrated laser light source is stable and well understood. For each tested intensity between 1 p.e. and 3000 p.e., the reconstruction returned the correct value with an error $\leq \pm 1\%$ on the per-pixel average. Further, also the uncertainty by means of the standard deviation is for every tested intensity $< \pm 2\%$. Even the maximum outliers are mostly $\leq \pm 4\%$ and for no tested intensity larger than $\pm 6\%$. However, the setup ignores the long duration of a Cherenkov flash with respect to the pulsed laser. While simulations with CORSIKA and `sim_telarray` show that a typical Cherenkov flash illuminates each individual pixel for about 3 ns, the laser pulses have a full width at half maximum (FWHM) of ≈ 300 ps. As the sampling window of the pre-amplifier is 4 ns, it is a realistic assumption that the different shapes of a laser light pulse and a Cherenkov light pulse might lead to different reconstructed p.e., although the total number of photons in both pulses is equal.

To tackle this question an experiment was set up which approximates a pulse of finite length with two identical pulsed lasers, firing shortly after each other. The delay Δt between the two lasers is tunable from 0 to ~ 100 ns in steps of 0.5 ns. The laser heads are arranged orthogonal to each other. A beam splitter cube – a semi-reflective mirror at an angle of 45° to each of the laser beams – unifies the two pulses on a common optical path. The intensity of the lasers can be changed individually with optical filters in front of each laser or with a filter wheel in the common optical path. The laser output intensity is controlled via a graphical user interface (GUI), where different intensities can be set. However, changing the output intensity via the GUI is discouraged from experience, as it provides a smaller dynamic range and less fine gradations compared to the filter wheel. Further, it cannot be excluded that the pulse shape of the light pulses changes at different laser output intensities. Via a diffuser, the laser light is sent towards an FC PDP module as detector. The entire setup is located in a darkbox to allow measurements

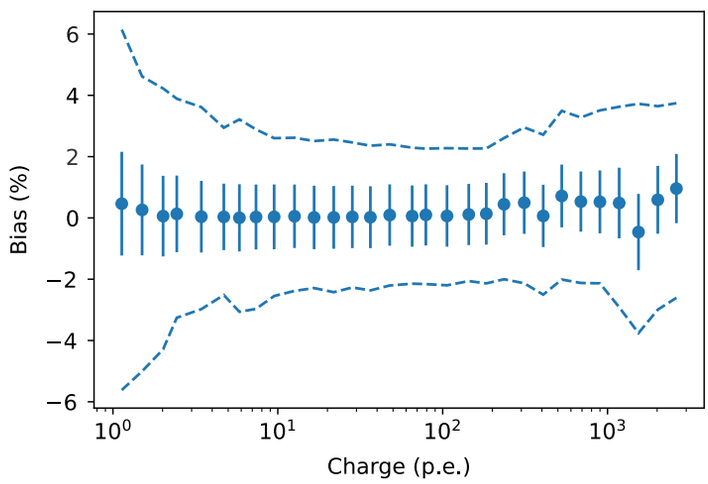

Figure III.6: Reconstruction bias of the FC reconstruction curve. The values are the averages obtained over all pixels, the error-bars represent the range covered by one standard deviation of these averages (1σ errors), and the dashed lines are the maximum outliers (the pixel with the highest and lowest value, respectively). The measurements were obtained with a calibrated laser light source at 30 °C and under artificial NSB illumination of 300 MHz in a laboratory at MPIK, Heidelberg. Data evaluation and image credit: Baiyang Bi, IAAT.

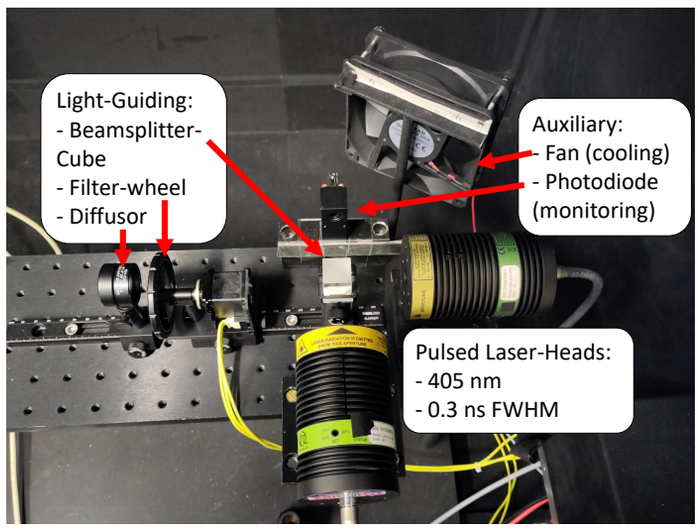

Figure III.7: Photograph of the FlashCam Two-Laser-Experiment. The laser heads are connected to a power-supply with trigger unit (outside the darkbox), which is controlled from a computer. Also the filter-wheel and the fan can be controlled without opening the darkbox. The NSB-LED is located to the left (outside of the picture), below the optical bench on which the setup is situated. Further to the left is the PDP module. In the picture, no additional optical filter is placed in front of any of the lasers.

down to individual photons and to protect the PMTs. A blue LED simulates NSB light. As auxiliary items, a fast rising photodiode is used to monitor the two pulses and Δt. Further, a fan cools the lasers to maintain a stable temperature. A photograph of the setup is shown in Figure III.7. The experiment was set up by the author of this work during his master's thesis ([Leu20]). There, a more ellaborative description of the setup can be found.

In [Leu20], measurements have been obtained with $\Delta t \in [0, 80]$ns in steps of ≥ 1 ns. In all three regimes of FC, three scenarios have been investigated: both pulses at the same intensity, one pulse at $\approx 50\%$ of the other pulse's intensity, and one pulse at $\approx 10\%$ of the other pulse's intensity. In the present work, these measurements are partially repeated. The delays in the range $0\,\text{ns} \leq \Delta t \leq 5\,\text{ns}$ are now fully covered in steps of 0.5 ns, larger delays are not considered. This is due to simulations by Baiyang Bi of two laser-pulses (each of negligible duration with respect to the camera response) with delay Δt, compared to one simulated Gaussian pulse (serving as a proxy for a Cherenkov shower) with a distinct FWHM. These simulations have shown that FC reconstructs the two laser-pulses with delay Δt like a Gaussian pulse of FWHM $\approx 1.4 \cdot \Delta t$. Of

course, this relation holds only for pulses sufficiently bright and Δt sufficiently small such that the FADC output drops in between the two laser pulses. Therefore, a pulse of FWHM = 3 ns can be simulated with the Two-Laser-Experiment at $\Delta t = 2.2$ ns and $\Delta t = 5$ ns corresponds to a shower of FWHM = 7 ns within one pixel. As the duration of an entire shower is ≈ 10 ns, this seems to be an adequate upper limit for the reconstruction to be tested against. Another finding from simulations is that a realistic pulse is best approximated with two pulses of equal intensity. So, no additional filters are placed in front of the individual lasers. The measurements are conducted in each of the three regimes of FC individually.

The general idea of the Two-Laser-Experiment is that two pulses arriving at the same time ($\Delta t < 0.5$ ns) are reconstructed as the sum of the two pulses when being measured separately. The aim is to test, whether or not small differences in arrival times ($0.5\,\text{ns} < \Delta t < 5\,\text{ns}$) change this behavior. An ideal result of the experiment would be that in each regime for $\Delta t \in [0.0, 5.0]$ns (or, at least, up to 2.5 ns, in order to account for the majority of Cherenkov photons, according to the simulations by Bi) all measurements give the same number of p.e.. Larger Δt are not necessary to be considered, as Cherenkov showers with durations of 7ns or more within a single pixel are not realistic for the use-case of FC.

III.3.2 Results

In Figure III.8, the results of the repeated Two-Laser-Experiment measurements are shown in the different intensity regimes for $\Delta t \leq 5$ ns.

For the linear regime, both reconstruction parameters introduced in Section III.1.3 – *pzmax* (blue) and *umax* (orange) – are shown. At reconstructed charges $\gtrsim 10$ p.e. equal results are derived with both parameters for light from a laser light source. However, it can be seen in Figure III.8 that within the Two-Laser-Setup the charge reconstructed with *pzmax* drops faster than the charge reconstructed with *umax*. Firstly, the orange curve is discussed, representing the reconstruction with *umax*. It shows a slight decrease of the reconstructed charge of about 2% at $\Delta t = 2.2$ ns and 5% at $\Delta t = 5$ ns. This is, because for low input intensities the pulses become separable already at $\Delta t \approx 1$ ns. In consequence, the peak of the upsampled trace broadens. *umax* then is slightly lower than it would be for a laser light pulse and following Equation III.1 a lower intensity is reconstructed. For an actual Cherenkov shower, with only one peak, the effect will be less drastic, and therefore the reconstruction of the charge reconstruction for pulses of realistic length with *umax* is considered verified within the defined accuracy. As discussed, the maximum of the pz-corrected trace is sharper (cf. Figure III.3), leading to a superior charge resolution of *pzmax* compared to *umax*. In reverse, this makes *umax* the more robust parameter, which is the reason why the curve reconstructed with *pzmax* drops faster than the one reconstructed with *umax*. As the experimental setup does not produce a single-peaked light pulse of varying length, but two light pulses of negligible length and with varying delay in between them, it is not suitable to test the behavior of *pzmax* for Cherenkov-like light pulses. However, as the reconstruction using *umax* is verified, and *pzmax* is known to behave alike *umax* (however, see Section IV.3.3), also the reconstruction using *pzmax* may be assumed to be verified.

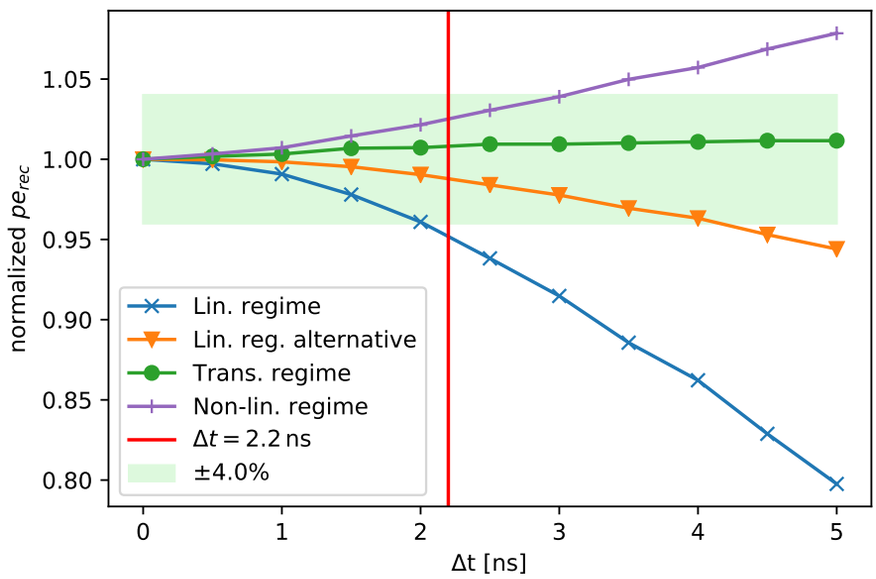

Figure III.8: Results of the FlashCam Two-Laser-Experiment as obtained during this work. The data points (with linear interpolation) show the ratio of reconstructed p.e. at given Δt over the reconstructed p.e. at $\Delta t = 0$. The green area is for comparison the $\pm 4\%$ area, in which maximum outliers are expected to occur.

The transition regime is reconstructed well, as can be seen from the green curve. The linearity of the parameter A_{1200} (see Figure III.4) proves to be stable for $\Delta t \leq 5\,\mathrm{ns}$. As already discussed in Section III.1.3, A_{1200} gets unstable and fails to properly reconstruct the charge when it approaches or exceeds 1000 p.e.. So, in the reconstruction algorithm currently applied for FC@CT5 the non-linear regime reconstruction (see Equation III.3 and Figure III.3, bottom panels) is necessary. However, for the MSTs of CTA-S it is discussed that only charges up to 1000 p.e. must be reconstructed.Therefore, investigations are ongoing, whether different settings of the preamplifier might allow to only use the linear and the transition regime, i.e., the parameters *pzmax* and A_{1200}.

One reason for these considerations can be seen in the purple curve, showing the results in the non-linear regime. It grows exponentially with Δt. For $\Delta t = 2.2\,\mathrm{ns}$, i.e., showers with FWHM of 3 ns, the bias is still tolerable ($\approx 3\%$). However, actual showers in the non-linear regime might last longer, as the analysis of simulations by Bi have not yet been conducted for exceptionally large numbers of p.e. For example, if a bright shower is distributed over 5 ns in an individual pixel, this would already induce a bias of 5%. The reason of this bias is understood: If an intense light pulse in a pixel is distributed in time, the clipping behavior of the pre-amplifier leads predictably to a longer duration of the maximum value (the plateau in the bottom-left panel of Figure III.3) and consequently to a longer time interval T_d between the (global) maximum and minimum of the differentiated trace (see the bottom-center panel of Figure III.3). As the correlation between T_d and pe_rec is exponential (see Equation III.3), also the relation between Δt and pe_rec is exponential. While it would be desirable to avoid the non-linear regime in the reconstruction of CTA parameters if feasible, it is in principle possible to correct for the bias introduced by the finite duration of pulses from Cherenkov showers. This would require more detailed experimental and simulation studies of the relationship between Δt and T_d, as well as the duration of a bright Cherenkov shower within a pixel.

IV

Towards an in-field calibration device for FlashCam in the Medium-Sized-Telescopes of CTA

IV.1 Flatfielding with IACTs

Flatfielding is a concept applied to all imaging telescopes recording optical light. It generally describes a calibration procedure to equalize different gain levels and sensitivities in the field of view. The typical approach is to obtain an image without sources, but a bit of illumination. For ground-based optical telescopes this can for example be realized by obtaining an image of the eastern sky at twilight, when the sky is bright enough to conceal all stars (and planets), but dark enough to not exceed the dynamic range of the pixels, or by obtaining an image of the telescope dome. The resulting image then is expected to show no features at all, i.e., to be "flat".

However, for IACTs with their single-photon resolving light detectors this is not feasible. The high sensitivity does not allow to switch the cameras on during twilight without risking temporal or permanent degradation of the detectors. Even the most recent cameras with SiPMs as detectors cannot obtain FF images during twilight, as the brightness of the sky would exceed the dynamic range. On the other hand, it is also not feasible to obtain FF-measurements by pointing to a dark spot in the night-sky. The large FoV, compared to other telescopes, does not allow to observe a field without any source bright enough to disturb the measurement.

Instead, the cameras are actively and homogeneously illuminated during (astronomical) darkness with the telescopes pointing to horizon, i.e., in a position where no strong sources are visible. This type of flatfielding omits correcting varying effectivities of the optics (e.g. due to vignetting), which must be covered in separate calibration procedures. It solely equalizes different gain levels of individual pixels by obtaining FF correction factors for every pixel. For pixel i, the FF factor F_i is calculated as the average amplitude $\bar{a} = \frac{\sum_i a_i}{n}$ over the entire n pixel camera divided by the amplitude a_i of the pixel:

$$F_i = \frac{\bar{a}}{a_i} \tag{IV.1}$$

F_i is multiplied to the measured amplitude of a pixel during the formation of camera images, i.e., the telescope raw-data.

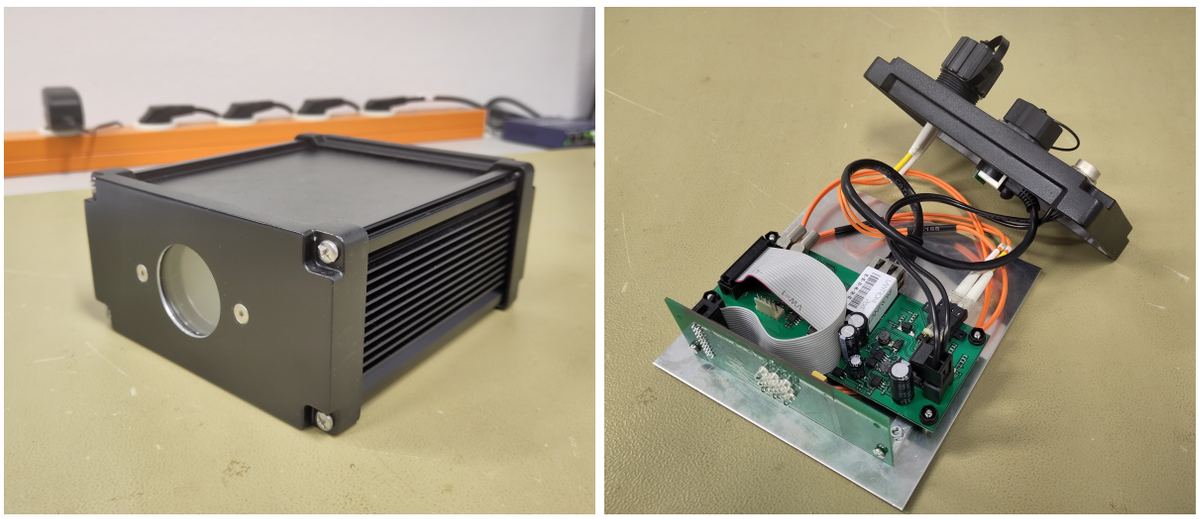

Figure IV.1: Photograph of an LUPM FF device as currently used in the H.E.S.S. experiment, obtained in the lab in Tübingen. Left panel: the box from the front with its milky glass diffusing exit window. Right panel: the interior PCB with the 13 LEDs, connected to the rear end of the box. The FF device and its control interface has been kindly provided by LUPM, France.

FF devices to generate such a homogenous illumination are also foreseen for the MSTs of CTA and currently applied in the H.E.S.S. experiment. They are situated centrally in the dish of the telescopes, with an opening angle of their light cone large enough to illuminate the entire camera but small enough to not disturb any other telescopes in the array. In this setup, it is possible to obtain proper FF measurements and eventually derive FF correction factors for all pixels.

In the course of this chapter, the FF devices currently used in the H.E.S.S. experiment are introduced. The extensive characterization study conducted during this work is presented (Section IV.2). This is followed by a simulation study for the flatfield measurements of FC@CT5 (Section IV.3). Simulations with `sim_telarray` allow to draw conclusions on the impact of different pulse shapes on the calibration of the linear regime, which in turn can be used to better understand the pulse shape of the FF device (see Section III.3). Section IV.4 outlines the requirements for an FF and calibration device that is planned to be installed in the MSTs of CTA-S that will be equipped with FC. Eventually, the chapter is summarized in Section IV.5.

IV.2 Characterization of the LUPM flatfield device

The FF devices currently in use in the H.E.S.S. experiment have originally been developed for the NectarCAM camera that will be used in the MSTs of CTA-N. The development has been led by G. Vasileiadis at the Laboratoire Univers et Particules de Montpellier (LUPM), France. LUPM kindly provided one of their FF devices to the IAAT to conduct investigations, whether the unit is suitable for usage with FC, in particular in the MSTs of CTA-S. The main difference to the usage with NectarCAM is that an FF device for FC is foreseen to conduct not only FF measurements, but a gain calibration over the full dynamic range. As the camera response depends on the pulse width (cf. Section III.3), the pulse width of the FF device must be determined. The LUPM FF

devices use up to thirteen LEDs that are pulsed with a frequency of 250 Hz and emit light pulses at 400 nm. One of the LEDs (#7) is weaker and slower than the others. It is foreseen for SPE measurements. In the H.E.S.S. experiment, it has never actually been used in this manner and it is neither foreseen to use it with FC. Therefore, it is ignored in the entire section. A frosted glass exit window serves as diffuser to create a homogeneous illumination and to equalize the pattern of the individual LEDs.

There are two possibilities to change the intensity of the device: either by changing the numbers of LEDs switched on (1 to 12), or by changing the voltage applied to them (-8 to -16 V) The duration of the pulses might vary between 3 to 5 ns. The quantities described here (which are summarized from an internal data-sheet) need to be quantified more precisely to allow a well based decision on the usage of the LUPM FF device as calibration device for the FC cameras of the CTA-S MSTs. In the following, a characterization process is described that addresses these points.

IV.2.1 Setup and measurement strategy

The characterization targets four questions:

- Can the FF device cover the necessary dynamic range of a FC when mounted in an MST, i.e., in a distance of 16 m?
- What is the pulse shape of the FF device and what are the implications for FC, regarding the dependence of the FC response on the pulse shape?
- Are there differences in the illumination depending on the LED(s) in use?
- Is the FF device stable over a time-span of several minutes to hours in operation and at different temperatures?

The first question can be answered from intensity sweep runs with FC@CT5. For these, various combinations of LEDs and voltages are used to create FF measurements at different illumination levels. E.g., in 2021 and 2022 the LEDs 1, 5, 9 & 13 were used at voltages of -8 to -16 V, with a step-size of 1 V. An earlier setting comprised the usage of 1 to 13 LEDs at -9 and -10 V. Under the assumption that the FF device output does not change over time and that the efficiency of the light guides (Winston cones) as well as the QE is stable, comparing the measured intensities with those from an earlier measurement allows to quantify the gain change.

To measure the pulse shape, an FF device is placed in a darkbox in a laboratory in Tübingen. In a distance of about 1 m, a Hamamatsu H10721 PMT is placed. It is capable of resolving pulses down to 0.6 ns duration. The PMT is read out at an 1 GHz oscilloscope (Agilent-Infiniium DSO8104A) in sampling mode, coupled with 50 Ω. It returns a voltage as function of time. From this curve, the pulse shape (FWHM, rise-time and fall-time of the pulse) and the intensity (amplitude) can be derived. An example of a recorded pulse is shown in Figure IV.2. In each measurement, ≥ 20000 samples are recorded. The variance of the measurements at this number of

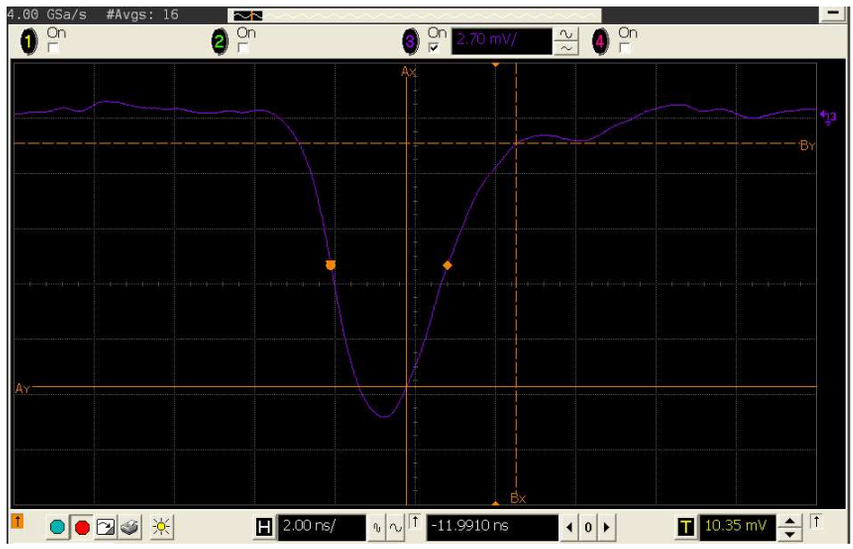

Figure IV.2: One pulse of the FF device measured with the Hamamatsu PMT in the darkbox and displayed at the oscilloscope. Note that the output of the PMT is negative, so the fall time of the signal is the rise time of the FF device pulse and vice versa. The orange lines denote the fall time (of the pulse), measured from 90% to 10% amplitude. The orange dots indicate where the FWHM is measured.

samples is $\approx 0.2\,\mathrm{ns}$ and does not change for higher numbers of samples. The statistical uncertainty of the individual measurement therefore is practically eliminated ($< 0.5\,\mathrm{ps}$).

The light of the FF device is attenuated with optical filters as the laboratory setting is different from an IACT: Most important, the distance between FF device and sensor is much smaller. In addition, the PMT device is more sensitive in timing than an IACT camera, at the cost of not being able to handle equally bright intensities. The filters by Thorlabs (model NDUV2R10A, -20A and -40A) nominally attenuate light in the spectrum of 200 to 1200 nm by 90%, 99%, and 99.99% corresponding to an optical density (od) of 1.0, 2.0, and 4.0, respectively. According to the manufacturer, the actual transmission rate at the wavelength of the FF device is slightly higher, especially for the filters with od of 1.0 and 2.0. However, to understand the timing and differences within the LEDs this is not of relevance.

Measurements are performed for each LED individually at $-8\,\mathrm{V}$, $-10\,\mathrm{V}$, $-12\,\mathrm{V}$, and $-16\,\mathrm{V}$ input voltage of the FF device. For two, exemplary LEDs (#1 and #5), step-sizes of $0.5\,\mathrm{V}$ are tested between $-8\,\mathrm{V}$ and $-12\,\mathrm{V}$ to understand the behavior at lower intensities. Another series of measurements investigates the behavior for all LEDs (except #7) together, in step-sizes of $2\,\mathrm{V}$ from -8 to $-16\,\mathrm{V}$.

In the same measurements, also differences in the apparent brightness of the LEDs are investigated. Differences in brightness can be derived from the measured intensities at the PMT, when the same optical filters are applied. This is the case for the majority of measurements, which are obtained using the od = 4.0 filter. Only four measurements (with LEDs 1, 2, 3, and 6) at the lowest intensity must be obtained using the od = 1.0 and od = 2.0 filters connected in series. These LEDs are tested against the others with higher input voltages. Therefore, no calibration of the transmissivity of the filters is needed.

The stability of the FF device with respect to time is easily tested by repeating individual measurements after an hour, a day, or up to several months. To verify the stability of the FF device with respect to temperature, a heat-up measurement is applied. If the FF device will be

used as calibration device for the FC cameras of the CTA-S MSTs, it may operate at different outside temperatures, reaching down to below 0 °C. In the laboratory, it may heat up to as much 32 °C when being switched on. Higher working temperatures of the FF device are not to be expected, as the desert-environment of CTA-S at night will be cooler than the laboratory. The heat-up measurement is necessary to ensure that within this temperature range, no significant changes in timing and intensity of the device appear.

To prepare the heat-up measurement, the FF device is frozen to slightly below 0 °C in a commercial fridge. Then, it is installed into the darkbox within less than five minutes and a dedicated, automated measurement protocol is started. The measurements described above are repeated, for all LEDs switched on and an input voltage of −12 V. Additionally, an internal temperature sensor is made use of to read the temperature at the end of each measurement. The results are FWHM, rise-time, fall-time and intensity as function of temperature, as well as temperature as function of time.

In this scheme, a measurement is defined as 45 s, delivering only ≈ 5400 instead of 20000 samples. This is necessary to have a sufficiently fine step-size in the tested temperatures. The statistical uncertainty then increases to ≈ 3 ps which is still negligible for the individual measurement.

IV.2.2 Results and Discussion

From the intensity sweep runs, it is known that the lowest possible setting, 1 LED at −8 V, induces about 60 p.e. for FC@CT5. The upper limit is unknown as it exceeds the dynamic range of the camera. Estimations based on the obtained measurements (with intensities up to ∼ 2500 p.e.) suggest that the charge of 3000 p.e. per pixel and pulse (former CTA maximum requirement) is exceeded either with twelve LEDs at −11 V or with six LEDs at −16 V. According to these estimations, the theoretically reachable maximum with the FF device is ≈ 7000 p.e.. In the MSTs, however, the FF device will be situated in the telescope dish, similarly to the usage in H.E.S.S. Therefore, the distance FF device – camera will be 16 m, compared to 32 m for CT5. As light intensity in photons/unit area changes $\propto \frac{1}{R^2}$ with R being the distance to the source, the intensities derived for FC@CT5 must be multiplied with 4 to obtain those for the MSTs. Then, the minimum intensity achievable is ≈ 240 p.e., which is too bright by at least a factor of 10, as the desired minimum intensity is ≈ 20 p.e. or less. The maximum intensity possible in this case would be ≈ 28 000 p.e., exceeding the necessary maximum by about a factor of 10. So, a simple solution is to place an optical filter of od = 1.0 right in front of the FF device. It would decrease the minimum to about 24 p.e. and the maximum to 2800 p.e..

The timing measurements show an increase of the pulse duration with increasing input voltage. Table IV.1 summarizes the results of the measurements with each LED individually. The results are given as average over all LEDs. The deviation of individual LEDs from the average is not larger than ±0.3 ns, except for one measurement with LED #6, for which the FWHM at −12 V input voltage is 0.4 ns larger than the average.

The FWHM as function of intensity (given in input voltage of the FF device) is shown in

Table IV.1: Results of the FF device characterization. The values are averages over all considered LEDs.

Voltage [V]	Rise-time [ns]	Fall-time [ns]	FWHM [ns]
8	1.9	2.9	3.2
10	2.0	3.3	3.5
12	2.1	3.7	3.7
16	2.2	3.7	3.9

Figure IV.3. The values are derived in measurements with LED #1 and LED #5, as well as with the series of measurements for all LEDs simultaneously. For comparison, also the averaged FWHM of the individual LEDs from Table IV.1 is visualized. The graph firstly shows that the trend one finds with the average values can be confirmed with individual LEDs: the FWHM increases, correlated with the input voltage. LEDs #1 and #5 are chosen for deeper investigations as they showed good properties, i.e., their pulse shape parameters at 8, 10, 12, and 16 V were smaller (or equal) and therefore more desirable than the average. This trend is evident when compared with the average values of the individual pixels. The data of these two LEDs is therefore a lower limit on the achievable timing performance of the FF device. In each of the four series of measurements shown in Figure IV.3, the FWHM increased from the lowest to the highest intensity by at least 6 ns. The statement holds also for the LEDs not displayed except for one outlier of only 0.4 ns FWHM difference between highest and lowest intensity. Using all pixels together increases the FWHM slightly at each intensity, with respect to measurements of individual LEDs. However, the increase of FWHM when adding one or multiple LEDs is smaller than it is when changing the intensity by increasing the input voltage of one individual LED. So, according to the timing measurements it would be favorable to change the intensity via different LEDs rather than via different input voltages, in order to have as low variations in the pulse duration as possible. Of course, this would in turn limit the dynamic range of the FF device, compared to the values presented above.

With the timing measurements, the FWHM, rise time, and fall time are determined. What can be concluded with these measurements is that the FWHM of an individual LED changes on average from 3.2 to 3.9 ns. When using all LEDs together, the FWHM increases to 4.0 ns at the highest output intensity. Interpolating the results of the Two-Laser-Experiment as presented in Section III.3 this corresponds to an increase of the reconstruction bias of 5-10%. While it would be possible to quantify and correct this additional bias, it would be preferable to avoid it or at least to further minimize it. What is still unknown is the exact pulse shape of the FF device and its impact on the FC pulse reconstruction in the linear regime. This can be answered with simulations, as will be discussed in Section IV.3.

The values for the intensity of the FF device presented above indicate that it is independent of the LED in use. However, a gradient can be seen in the image of FF measurements, which might be a hint to inhomogeneous behavior of the diffuser. The intensities measured in the laboratory, on the contrary, vary by a factor of 2.5 between the brightest and the faintest LED. Most likely, this

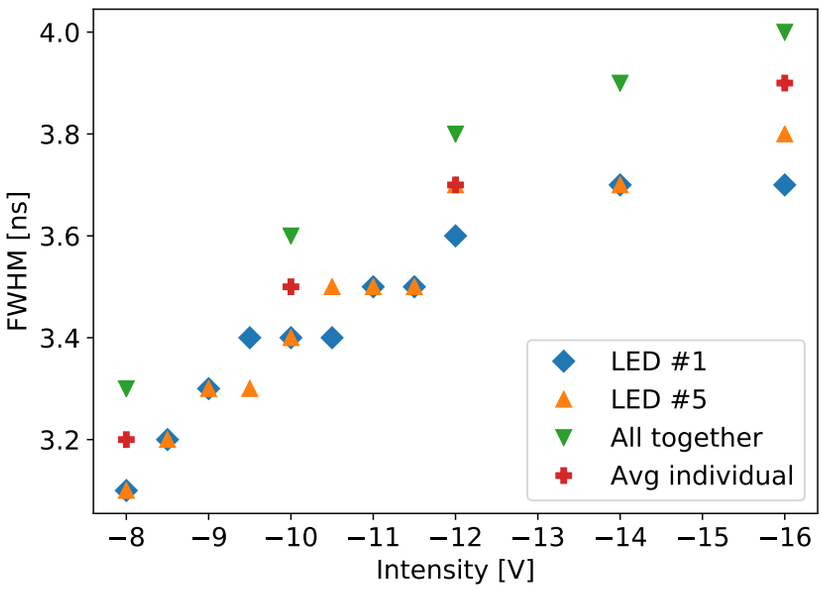

Figure IV.3: FWHM of the pulse over intensity (input voltage) of the FF device for LEDs #1 and #5, for all LEDs together, and for the average of all LEDs measured individually. #1 and #5 increase steadily between −8 V and −12 V and stabilize afterwards. In the other two series of measurements both, the increase and the stabilization are less significant, although clearly present.

is not due to the LEDs themselves but due to an inhomogeneous light distribution. When looking through the frozen glass exit window of the FF device, the individual LEDs are clearly visible at their respective positions. The different light amplitudes of the LEDs might therefore originate in different angles at which the PMT device is illuminated and correspondingly different amounts of photons being recorded. This is also potentially the reason for the gradient of illumination seen in FC@CT5. In conclusion, the obtained measurements do not allow to make a statement on the homogeneity of the LEDs. Anyways, the frozen glass exit window is to current knowledge insufficient to provide homogenous illumination of the MST cameras for arbitrary combinations of LEDs, down to the required accuracy of ∼percent level for FC. Implementation of another exit window / diffuser or a whole different solution (e.g., only one LED with a larger dynamic range) will also affect the conclusions drawn on the coverage of the FC dynamic range: While the current output will be sufficient when using an od=1.0 filter, a different exit window with different transparency would change the strength of the filter needed. A single-LED solution would require a different technological approach of one fast LED that is still capable to cover the entire dynamic range without changing its timing behavior.

The results of the heat-up measurements are shown in Figure IV.4, the development of the temperature is shown in Figure IV.5. Note that the temperatures of the six measurements $\leq 0\,°\mathrm{C}$ are interpolated, as the temperature sensor returns unrealistic values of $\sim -120\,°\mathrm{C}$. As can be seen, there are barely changes in the intensity and the rise time for different temperatures (lower panel of Figure IV.4). Also for the FWHM, the changes are within 0.1 ns for all data points above 0 °C. For the fall time, however, a clear and approximately linear change with the FF device temperature of about 0.2 ns is observed. The error bars describe the standard deviation of the mean of the individual measurements. As described above, this variance is very small, due to the high amount of samples per measurement. Nevertheless, the plots show larger variances between individual measurements than suggested by the variance of the mean which are in the order of 0.02 ns and 0.5 V, respectively, which corresponds to $\lesssim 1\%$ of the measured quantity. This

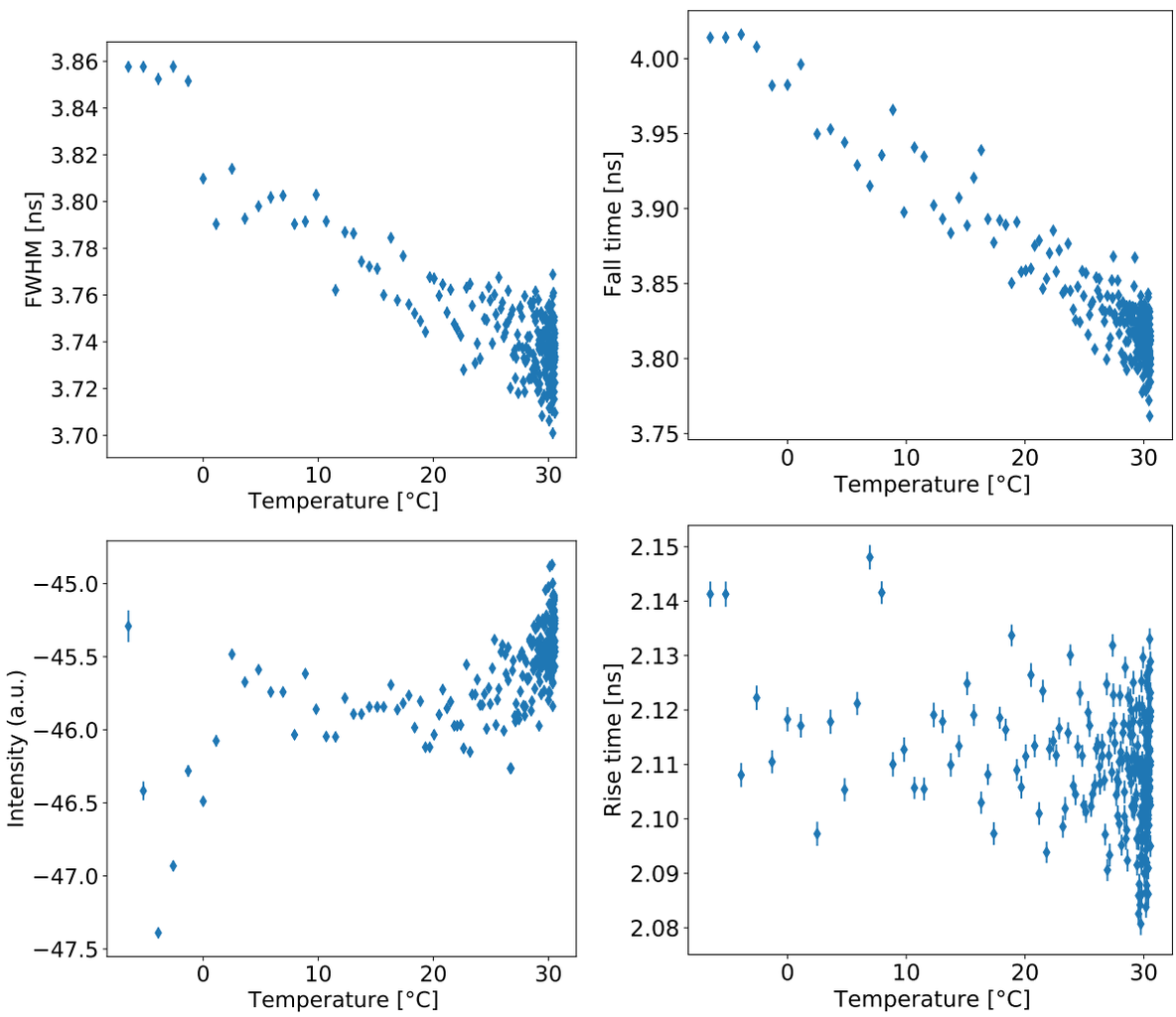

Figure IV.4: Results of the FF device heat-up measurement. The panels show different quantities of the FF device pulses with respect to the FF device temperature: FWHM (top left), fall time (top right), intensity as measured at the PMT (bottom left), and rise time (bottom right).

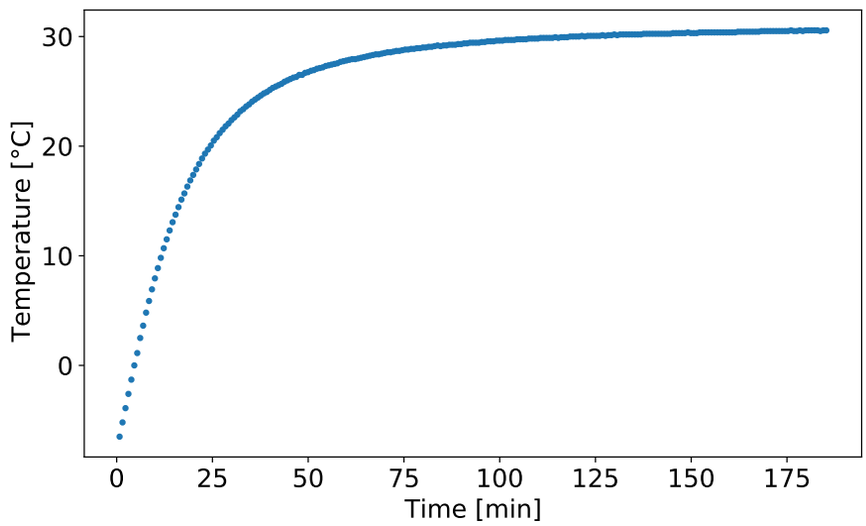

Figure IV.5: Development of the FF device temperature over time in the heat-up measurement. Note that all data points $\leq 0\,°C$ are interpolated. The curve saturates at $30.6\,°C$. Temperature of the laboratory is $\sim 20\,°C$. At varying environments, also the FF device stabilizes at different temperatures (observed: $\Delta T \approx \pm 2\,K$).

additional variance might represent the true dispersion of the system. It is deemed acceptable and is therefore not further investigated. In conclusion, the FF device is stable ($\pm 0.5\,ns$) when being operated at temperatures above $15\,°C$. In case that changes of $\pm 1\,ns$ in the fall time are accepted, stability is even given at any temperatures above $0\,°C$. These temperatures are reached after 5 min or 15 min of FF-device operation, respectively. After about 45 min, the temperature increase slows down significantly. Experience in the laboratory with the FF device has shown that it also warms up when no light is emitted, most likely due to the internal pulser-logic. Following the results of this work, it is therefore recommended to switch on the devices several minutes before intended usage, in the best case up to an hour ahead.

IV.3 Flatfield simulations for FlashCam in H.E.S.S. CT5

IV.3.1 Introduction

After installation of the fully functional advanced prototype of a FC to the CT5 telescope of H.E.S.S., the FF measurements were compared to laboratory measurements obtained during the calibration with a laser. The comparison found a deviation of 3.3% in $R_{u/pz}$[21] between the two measurements. This deviation can be explained with the results of the Two-Laser-Experiment (see Section III.3 and especially Figure III.8). However, it must be verified that it can be reproduced in simulations as well, in order to ensure that the response of FC to light pulses of varying length is implemented correctly. Initial simulations failed to reproduce the measurements and returned a change of $R_{u/pz} \approx 1\%$ at the expected pulse width of the FF device (FWHM=3.5 ns), compared to simulations with a laser light source. Suspected origin of the mismatch was that the pulse shape of the FF device might differ from a Gaussian and/or is broader than expected. It subsequently became a project within this thesis to investigate the reason for this mismatch.

This investigation contains two tasks: Firstly, to determine the pulse shape of the FF device

[21] The ratio between *umax* and *pzmax*, see Section III.1.3.

with direct measurements. The results of that are reported in Section IV.2. The second task is to implement this pulse shape into FF simulations and reproduce $R_{u/pz}$ correctly. It is reported in this section. The simulations are performed with `sim_telarray` [Ber08] and started via a bash-script. To manage the input parameters of the bash script and to run the subsequent evaluation routines a Python pipeline has been developed.

The initial mismatch between measurements and simulations, however, can be traced back to a bug in the simulation code. The function that calculates when to emit the photons in the simulation, in order to follow a Gaussian distribution of given width, expects as an input the FWHM of the distribution. In the documentation and the help text though, the standard deviation σ is requested. The bug has been reported and was resolved in the next release of `sim_telarray`.

Converting the input values accordingly with the factor $\frac{\mathrm{FWHM}}{\sigma} = \sqrt{8 \ln 2}$ immediately delivers results in the correct order of magnitude. However, now a 5% deviation between the simulations for a laser light source and those for the estimated FF device with a Gaussian of FWHM=3.5 ns is returned, being slightly too large. As the pulse shape cannot be ultimately determined with the measurements presented in Section IV.2, the implemented simulation chain now is used backwards: By matching simulations as close as possible to the measured 3.3% deviation, the pulse shape of the FF device can be determined with higher precision as with the measurements presented in Section IV.2.

IV.3.2 Simulating flatfield measurements

Flatfield measurements can be simulated with the program `sim_telarray`. It usually is used in conjunction with `CORSIKA` ([Hec98]) in IACT mode ([Ber08]) to simulate the detection of EAS with IACTs end-to-end: starting at a primary particle reaching the atmosphere down to the camera output of an IACT. In this framework, `CORSIKA` handles the simulation of the EAS and `sim_telarray` the response of an IACT to photons. However, as in a FF measurement no EAS is involved, `CORSIKA` is not needed for the respective simulations. They can be carried out in `sim_telarray` alone, using the LightEmission package to simulate a photon source. Here, `sim_telarray` and its LightEmission functionality are described. An overview of `CORSIKA` is given in Section V.1.

As mentioned above, `sim_telarray` simulates the response of IACTs to photons hitting the telescope. It is possible to simulate IACT arrays with multiple telescopes and also with different types of telescopes (e.g., H.E.S.S. II with CT1-4 and CT5 or a CTA array with LSTs, MSTs and SSTs). All telescopes are defined by a variety of properties, introduced in the manual for IACT simulations with `CORSIKA` and `sim_telarray` ([Ber22]) and summarized in the following. This summary only aims at introducing the methods needed to understand the FF simulations and the MC validation efforts (see Chapter V).

First to be defined is the central position on the ground of the observatory in question, which is necessary to be known in order to assume the correct magnetic field strength and orientation, as well as its altitude. Relative to this center, the telescopes are placed. The default alignment

is that the telescopes point to zenith and the azimuth orientation (in case a zenith angle $>0°$ is defined) equals 0°, which is defined as North. Then, a Cartesian system on the ground is oriented identically as the Cartesian system of an individual telescope, and the only variable is the pointing direction of a telescope, defined by its altitude and azimuth angle.

Within this geometry, the reflector is typically defined via the positions of the mirror facets and its focal length, as well as its mounting type. The mirror facets themselves are defined via their wavelength-dependent reflectivity, their diameter and their shape. A parameter introducing degradation will be discussed later. Final component of the geometrical setup of an IACT is the shadowing of the reflector(s) by masts, the camera, etc. This can be done explicitly via a file containing size and position of all masts and requesting full ray-tracing simulations of each photon approaching the primary reflector. As these are computationally very expensive they can be summarized with the `TELESCOPE_TRANSMISSION` parameter, being a factor in [0.0, 1.0] that defines the fraction of photons not being absorbed by telescope structures. This simplification is justified as IACT cameras only accept photons from a rather narrow angle, within which the shadowing is sufficiently homogenous.

Having defined the geometry of the IACT, its camera is next to be discussed. Cameras are defined via their (geometric) shape, including position, and if applicable the entrance window with its optical properties (e.g., the plexiglass window of FC). The implementation of the photo detectors is handled separately, including the pixels, the trigger-logic, the QE, response to and shape of SPE signals and random properties, accounting for statistical effects. Individual pixels are defined via an ID, position and deviations from nominal values such as PDE or gain (exclusively random fluctuations), as well as by a flag indicating whether the pixel is deactivated. Further, they can be assigned to an electronic board for more detailed simulations, as well as to a specific module to mimic, e.g., the behavior of FlashCam with its PDP modules. The pixel type defines the angular acceptance. Pixel types are a relict from an attempt to enable different types of pixels to be included within one camera. However, this was never fully implemented. The trigger logic can mimic both, analog and digital triggers and therefore represents the actual trigger conditions. It works, similar to actual cameras, with the (simulated) analog or digital signals, rather than with the actual number of p.e. recorded in the simulation.

Further parameters to be assigned to a camera are the QE as function of wavelength and the SPE response. The latter is given as the distribution of detected p.e. (at the anode) per induced p.e. at the cathode and therefore is a measure of the CE. QE and SPE response together account for the camera detection efficiency (DE), the probability of an incoming photon to be detected. Both distributions follow laboratory measurements. SPE simulations with additionally simulated NSB can reproduce the measured response distribution, proving the validity of the approach. For proper timing of signals, which is especially important for the trigger and small signal amplitudes, also the shape of a SPE pulse must be provided. Eventually, random variations of the QE, the gain, and the high voltage may be included to the definition of the camera, representing electronic noise and the uncertainty of or the variations in measurements of these quantities. In order to take into account aging effects of the pixels, which result in a lower overall detection efficiency but which cannot be attributed to individual components, a parameter

`CAMERA_DEGRADED_EFFICIENCY` $\in [0.0, 1.0]$ can be used. It is 1.0 by default, indicating that the camera is as efficient as defined with the quantities introduced. A lower value acts as a factor to be multiplied onto the nominal efficiency of the camera, decreasing the number of p.e. detected. A similar parameter, `MIRROR_DEGRADED_REFLECTION`, exists for the entire telescope. It is meant to depict the degradation of the mirrors, however, in practical application it is used instead of `CAMERA_DEGRADED_EFFICIENCY`, taking into account the lower detection efficiency of the pixels as well as the degradation of the mirrors. While `MIRROR_DEGRADED_REFLECTION` is used in MC shower simulations, only `CAMERA_DEGRADED_EFFICIENCY` must be used in FF measurement simulations. In these, a flag is set to ignore the ray-tracing / the optics, which speeds up the simulations and corresponds to reality where the FF device is located in the dish of the reflector, illuminating the whole camera. Consequently, the degradation of the mirrors must not be considered.

Aside of the telescopes, also the NSB is treated in `sim_telarray`. It is added via the flag `NIGHTSKY_BACKGROUND` as a rate of p.e. measured at each pixel in GHz. The degradation parameters introduced above scale the NSB frequency accordingly. Deviations for dedicated simulations can be introduced homogeneously across the camera with the `NSB_SCALING_FACTOR`, for example for bright sky regions such as Eta Carinae ([Ste23]). It in- or decreases the NSB level for all telescopes in the simulation by a given factor and therefore avoids extensive recalculations. This is of special interest for simulations of arrays with multiple telescope types like H.E.S.S. II or CTA.

Eventually, the atmospheric transmission is handled in `sim_telarray` as well. However, it does not have any impact on the FF simulations but plays an important role in the MC validation efforts described in Chapter V. Therefore, it will be discussed in that chapter.

The LightEmission Package is a feature within `sim_telarray` to obtain simulations with calibration light sources, bypassing the `CORSIKA` MC code. This makes simulations much faster and therefore more efficient, which is the reason why dedicated FF simulations are performed, rather than full shower simulations. In the framework of this thesis both, `sim_telarray` and the LightEmission Package are controlled via a bash-script. Additionally to the parameters already introduced, the script provides an interface to simulate a given number of pe/pixel coming from a light source with a Gaussian distribution and given FWHM. In the present work, the functionality to use a custom light distribution is added to that script. Custom light curves are given as files that list the time-steps and the corresponding intensities, normalized to a peak of 1 of a curve. The curves can be interpreted as probability density functions, re-normalized to peak at 1. The p.e. are then simulated randomly, and their times of emission are distributed such that it follows the defined probability densities.

The LightEmission package also allows the user to introduce a variance in the number of emitted photons, constituting another source of noise.

IV.3.3 Approaches and results

The simulations of FF measurements majorly contain two approaches to understand the behavior of $R_{u/pz}$. In the first approach, noise and comparable deviations from the nominal values are

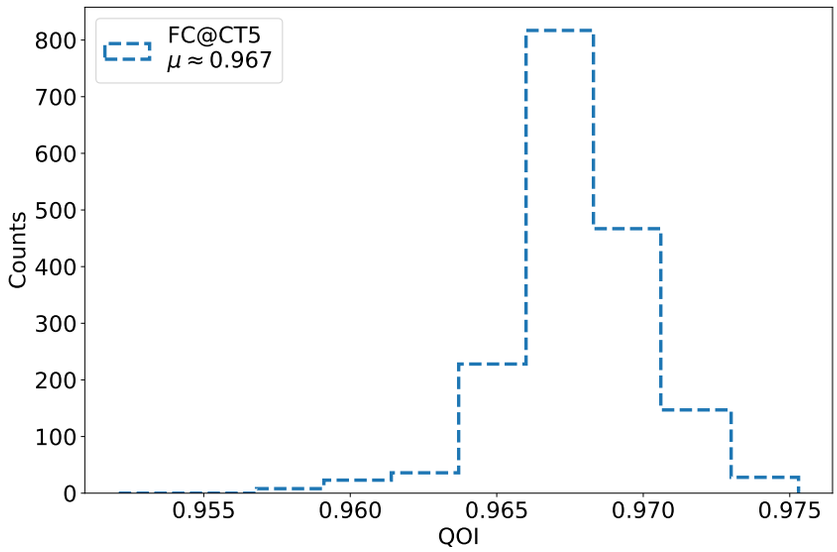

Figure IV.6: QOI as actually measured. The counts shown in the histogram depict averages over the individual pixels of FC. The FF measurements are obtained in Namibia with FC@CT5. Laser measurements are performed prior to camera shipping in the laboratory in Heidelberg during FC calibration. The plot is recreated from a figure by Baiyang Bi, using Webplotdigitizer ([Roh22]).

added to the simulations by defining in which fraction of the default value QE, gain and the number of pe may vary, the latter due to variances of the light source. The second approach is to vary the shape of the simulated FF device pulse, as outlined in Section IV.3.1. This approach is additionally used to investigate the behavior of $R_{u/pz}$ for different pulse shapes in detail. The quantity of interest (QOI) is the ratio between $R_{u/pz}$ for a laser light source (i.e., a Gaussian pulse with FWHM$= 0.3\,$ns, according to the laser manufacturer) and for the FF device (a pulse of uncertain, but somewhat Gaussian shape and with FWHM$\in [2.5, 4.0]\,$ns):

$$QOI = \frac{R_{u/pz}^{\text{laser}}}{R_{u/pz}^{\text{FF dev.}}} \tag{IV.2}$$

In Section IV.3.1, it was pointed out that a deviation in $R_{u/pz}$ of 3.3% between the laser calibration measurements and the FF measurements in Namibia has been found. Hence, if the simulations of the camera and of the light sources are correct, a result of $QOI = 0.967$ is expected from simulations. After resolving the bug as mentioned, the simulations deliver $QOI \approx 0.95$. Figure IV.6 shows the QOI distribution as measured with the FC installed in Namibia. These values already match well, however, the following investigations are conducted in order to obtain a better match of the measured and the simulated QOI In particular, this simulation study leads to new conclusions on the dependence of the FC response to pulses of varying length and it helps to characterize the LUPM FF unit more precise than the measurements presented in Section IV.2. Since the initial simulations are conducted without any electronic noise, its impact is tested first. It turns out that noise amplitudes of realistic scales ($\pm$2% of gain and QE, $\pm$3% for the number of p.e. emitted) do barely influence the QOI. The effect of the addition of noise is a slight increase of QOI, but only in the order of ~ 0.001 and therefore a factor of 10 smaller than what is needed to match the simulated with the measured QOI. More prominently, the noise smears out the histograms for the QOI, such that the two types of PMTs used in FC@CT5 cannot be disentangled. The introduced noise is kept in all forthcoming simulations.

Varying the pulse-shape and duration of the simulated FF device results in more significant changes of the *QOI*. The approaches for the pulse shapes are based on the results from the measurements of the FF device as presented in Section IV.2. However, possible systematic uncertainties are accounted for by allowing shorter durations than measured as well, if these lead to simulations matching the measured *QOI*. For that, rise time, fall time, and FWHM are varied separately. Pulse shapes other than pure Gaussians must be introduced to allow such independent modifications. As measured (see Section IV.2) the fall time in these simulations is longer than the rise time. This also matches the expectations for real electronic circuits, where the voltage needs longer to drop rather than to ramp up. Therefore, also the light pulse is expected to fall slower than to rise, which matches the measurements in the dark box.

Besides the default Gaussian two different distribution models are tested to describe the light pulse. The first is the Gaussx2-model. It consists of two Gaussian distributions with different standard deviations σ, both centered at the mean $t_0 = 0.0\,\text{ns}$. Each of them is re-normalized to peak at 1. To form the Gaussx2-model, the rising edge of the distribution with lower σ is combined with the falling edge of the other distribution with larger σ. In combination, this leads to a distribution with a faster rising edge and a slower falling edge, compared to a pure Gaussian distribution of identical FWHM. The Gaussx2-model is explicitly useful to test the influence of different rise- and fall times at a constant FWHM.

The other distribution model is named Gauss-Cauchy-model. Its rising edge is again defined by a Gaussian, the falling edge by a modified Cauchy distribution. The modification from a standard Cauchy distribution is the parameter α:

$$f_{s,\alpha}(t) = \frac{1}{\pi}\frac{s}{s^2 + (t^\alpha - t_0)^2} \tag{IV.3}$$

Both, the Gaussian as well as the modified Cauchy distribution peak at $t_0 = 0.0\,\text{ns}$. A sliding mean is used between 0 and 0.5 ns to ensure a smooth transition between the Gaussian and the Cauchy distribution, i.e., the rising and the falling edge. The Gauss-Cauchy-model allows to fix the rise time and to vary FWHM and fall time of the model pulse simultaneously. Compared to the Gaussx2-model, the main feature of pulses created with this model is a distinct time-span in which the amplitude is near maximal, due to the modified Cauchy distribution.

In Figure IV.7, the four pulses are shown, two of each model. The pulses in the image that are created with the same model have a similar FWHM. One pulse created with the Gaussx2-model is compared with a Gaussian pulse of identical FWHM but with different rise- and fall time. The two pulses created with the Gauss-Cauchy-model have similar FWHM and an identical rise time, but a different fall time, induced by variations in the parameters α and s. Simulations with the four model pulses shown in the figure are evaluated below exemplarily.

The evaluation of these simulations shows that the FF measurements of FC@CT5 can be reproduced well with both, the Gaussx2-model (including pure Gaussian pulse shapes) and the Gauss-Cauchy-model. Plotting the values for *QOI* of each pixel obtained in a simulation into a histogram returns the *QOI* distribution. The mean μ of this distribution can be found by fitting a Gaussian. Then, μ is the result for the *QOI* for this simulation. For the Gaussx2-model,

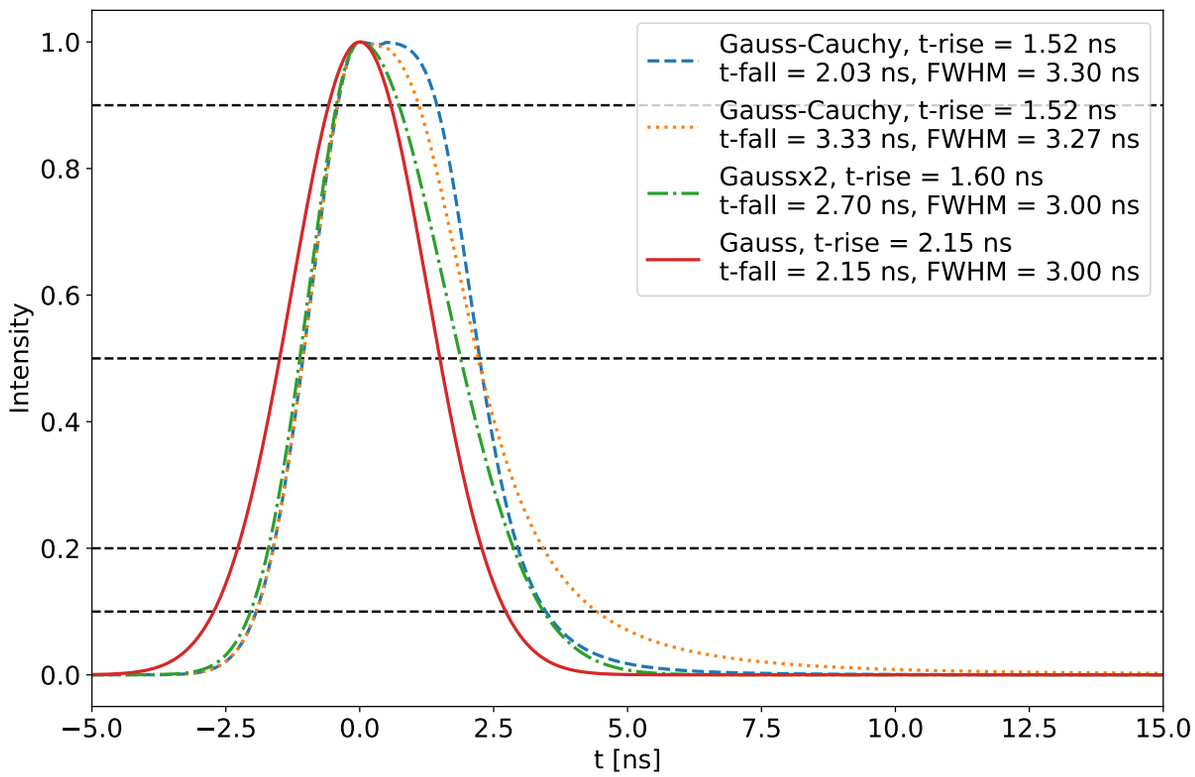

Figure IV.7: Some examples of artificial pulse-shapes. The two pulses created with the Gauss-Cauchy-model have an FWHM of $\approx 3.3\,\text{ns}$ and an identical rising edge with rise time of 1.52 ns. However, their fall time varies strongly with 2.03 ns and 3.33 ns, respectively. The two other pulses have an identical FWHM of 3.0 ns. The green, dashed-dotted curve has a rise time of 1.60 ns, a fall time of 2.70 ns, and was created with the Gaussx2-model. The red, solid curve, however, is a true Gaussian pulse with rise- and fall time of 2.15 ns, each. The intensity on the y-axis is normalized such that the peak of each curve is at 1.0. On the x-axis all curves are aligned such that their peak is at $t_0 = 0.0\,\text{ns}$. The black, dashed lines denote the values 0.1, 0.5 and 0.9, i.e., the 10%, 50% and 90% level of the light output, needed to measure rise- and fall time (both between 10% and 90%) and FWHM.

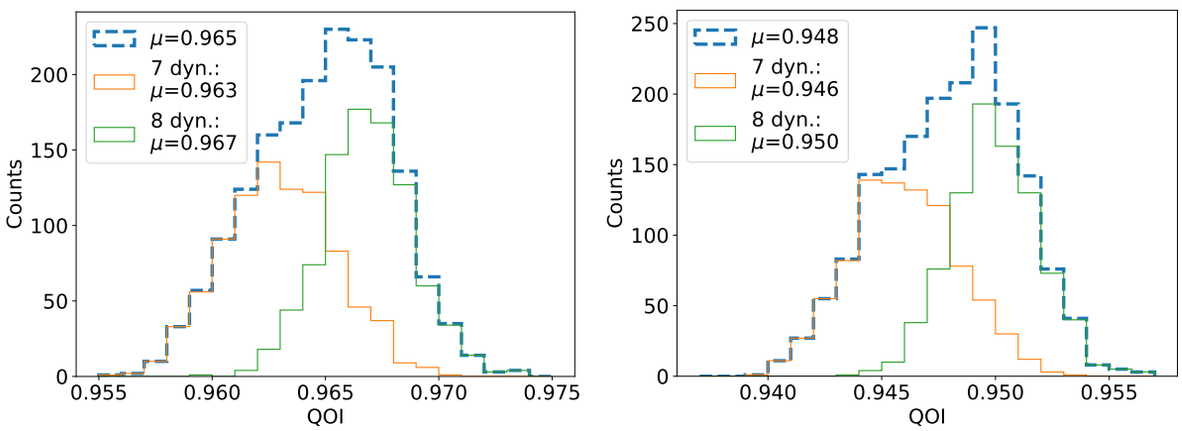

Figure IV.8: *QOI* histograms for two simulations with pulses created using the Gauss-Cauchy-model. The histograms in the left panel are created using the blue, dashed pulse shape shown in Figure IV.7. For the right panel histograms, the orange, dotted pulse shape is used. Only the in left panel the measured values for *QOI* are reproduced.

the pulse that returns a matching *QOI* distribution is the green, dashed-dotted one shown in Figure IV.7. It has a rise time of 1.6 ns, a fall time of 2.7 ns, and an FWHM of 3.0 ns. However, also a pure Gaussian pulse is tested at this FWHM (red, solid curve in Figure IV.7), delivering a similar result as the pulse created with the Gaussx2-model. The *QOI* distributions of both these pulses are shown in Figure IV.9.

From the pulses created with the Gauss-Cauchy-model, only the one sketched with the blue, dashed curve in Figure IV.7 reproduces the *QOI* result of the real measurements (Figure IV.8, left panel). The orange, dotted pulse shape delivers a *QOI* value that is too low (Figure IV.8, right panel). A lower *QOI* indicates that $R_{u/pz}$ decreases more than actually expected. This is a hint that the pulse in such simulations lasts longer than that of the FF device. Such behavior has been seen in the FF simulations when using a Gaussian pulse shape of FWHM 3.5 ns, as well as in the Two-Laser-Experiment.

To summarize the results of the FF measurement simulations:

- The measured *QOI* can be reproduced in simulations.
- For a fixed form of the pulse shape, it depends on the width (FWHM) of the pulse whether the *QOI* is reconstructed correctly or not.
- For different pulse shape forms, different widths are required to reconstruct the *QOI* correctly.

Comparing the pulse shapes with which the *QOI* is simulated successfully (blue dashed, green dashed-dotted and red solid curves in Figure IV.7) with others that do not (e.g., the orange dotted one) might explain the critical measure of the pulse shapes: All three successful pulses have a similar time span in which they are at more than 10% of their maximum intensity, as can be seen in Figure IV.7. On the other hand, the orange dotted pulse (which is assumed to last too long) is significantly longer brighter than 10% of its maximum intensity.

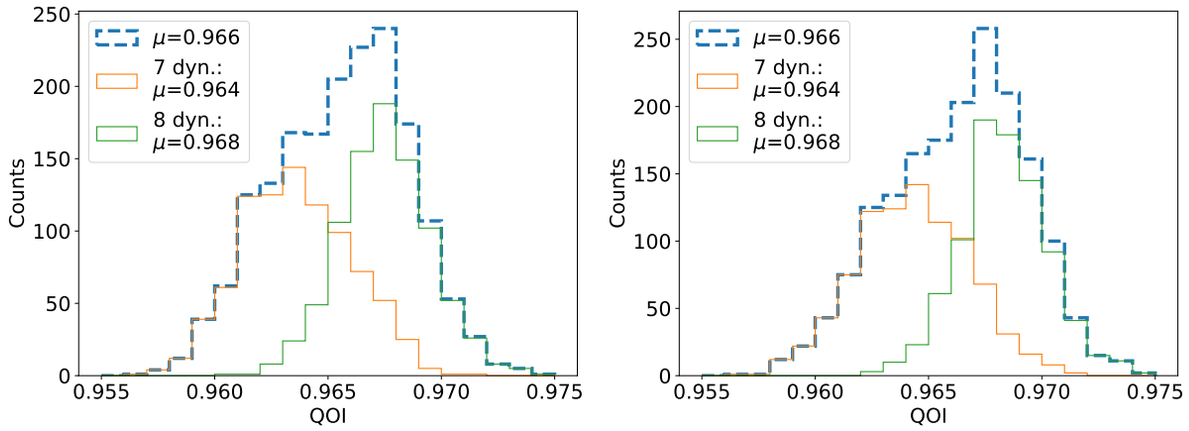

Figure IV.9: *QOI* histograms for two simulations returning similar values and reproducing the measurement for *QOI* correctly. The left histogram is created using the green, dashed-dotted pulse shape shown in Figure IV.7, which is created with the Gaussx2-model. For the right histogram, the red, solid pulse shape is used and therefore a pure Gaussian pulse shape.

Therefore, the FF simulations result in multiple pulse shapes that match the results from Section IV.2 within the assumed systematic uncertainties and that are capable of simulating the *QOI* correctly. Further, a new quantity must be introduced to determine the duration of a light pulse for FC calibration: the *bright time* $BT10$, defining the time span in which the intensity of the pulse is at least at 10% of its maximum intensity. For the present LUPM FF device, it is $BT10 \approx 5.5\,\text{ns}$, according to the FF simulations.

IV.4 Requirements for a flatfield device for the Medium-Sized-Telescopes of CTA

For the MSTs of CTA-S, which will be equipped with FCs, more than only an FF-device is planned. The device that will be installed in these telescopes must be usable additionally to its FF functionality for calibration over the whole dynamic range. Measurements like the intensity sweeps obtained with FC@CT5 are discussed, however, the final procedure is not yet agreed on. For such measurements, a device is needed that can illuminate every pixel of FC over the full dynamic range of the camera[22]. Further, the pulse shapes must be such that biases of the FC reconstruction are minimized. Section IV.2 argues that the current LUPM FF device is insufficient for this purpose, if only because of the inhomogeneous illumination. From the considerations presented there, together with the simulations of the influence of the pulse shape, requirements can be derived for a future *calibration device* for the FC cameras of the CTA-S MSTs. First, some basic properties the calibration device must fulfill are introduced. Then, its necessary dynamic range is calculated, before eventually timing requirements are presented.

[22] Except charges $< 10\,\text{p.e.}$, as such measurements would require a complete dark environment.

IV.4.1 Basic properties

First of all to be mentioned is the wavelength of the future device. As with the current FF device, the wavelength of the calibration device must be comparable to that of Cherenkov light. This is a necessary condition, as only such light is able to cross the plexiglass front window of the camera and can be detected by the PMTs at a reasonably high QE. For optimal results, the wavelength should be in the range 330 to 440 nm and ideally at 390 nm, where the QE of the PMTs peaks at 0.393.

To avoid a gradient across the camera as seen in FC@CT5, the illumination must be homogenous. The entire camera can be approximated with a circle of radius 1.2 m that must be illuminated at a distance of 16 m. This is achieved with a half-opening angle of the homogenous light cone of 4.3°. To rule out illumination of neighboring telescopes by the calibration device, its light cone should not be larger than the camera housing, which is a rectangle of $3 \times 3.1\,\mathrm{m}^2$. Therefore, the light cone should not be opened more than a circle of 1.5 m radius in the plane of the camera, resulting in a maximum half-opening angle of 5.4°. In this outer part of the light cone, homogeneity is not strictly required anymore. Nevertheless, it would be favorable if the entire light cone is as close to the 4.3° half-opening angle and in its entire extension as homogenous as possible, to loosen the constraints on the mounting. To achieve this, basically two solutions are conceivable: Either, a single LED (with sufficient dynamic range) is used and its output light cone is limited, e.g, by a tube. Or, multiple LEDs are used as in the existing FF-device, but with a diffuser or similar optics that guarantee homogenous illumination by smearing out the imprint of the individual LEDs.

Finally, the trigger output of the calibration device must be accurate and the device needs a sufficient pulse frequency. To avoid biases, the delay between the centroid of the light pulse and the leading edge of the trigger signal must not change by more than 0.1 ns over the whole dynamic range of the device. In the LUPM FF device, an optical trigger output is included (although not used) that is an excellent solution. The pulse frequency, however, needs to be more adjustable, from $\mathcal{O}(1\,\mathrm{Hz})$ to $\leq 5\,\mathrm{kHz}$. Especially fast pulsing is necessary in order to perform calibration measurements without consuming too much time.

IV.4.2 Dynamic range

The necessary dynamic range for the calibration device is already outlined in Section IV.2, defined in p.e.. Pulses of the calibration device should be able to illuminate every pixel of the camera in the range from $pe_{\mathrm{min}} = 10\,\mathrm{p.e.}$ to $pe_{\mathrm{max}} = 3000\,\mathrm{p.e.}$. This can be transformed with geometrical considerations into a photon or energy flux. For simplicity, the optimal wavelength of the calibration device, $\lambda = 390\,\mathrm{nm}$ is assumed. At this λ, the QE of the PMTs is 0.394, further losses due at the Winston cones and due to the limited CE are estimated to be 5%. These two together result in $DE = 0.3743$. In photons, the required output n_{phot} per pulse and pixel is then $n_{\mathrm{phot,min}} = pe_{\mathrm{min}}/DE = 26$ and $n_{\mathrm{phot,max}} = 8014$. Approximating the PDP as a regular hexagon with side length 1.2 m, the 1764 pixels (including posts and masked pixels) of FC are distributed over $3.741\,\mathrm{m}^2$. At 16 m distance, every pixel covers then a solid angle of $\Omega \approx 8.28 \times 10^{-6}\,\mathrm{sr}$. With

the given wavelength, one photon has an energy of 3.181 eV, so the necessary output energy per pulse of the calibration device under the described assumptions is $E_{\text{min}} = 1.03 \times 10^7 \frac{\text{eV}}{\text{sr}}$ and $E_{\text{max}} = 3.08 \times 10^9 \frac{\text{eV}}{\text{sr}}$.

In order to be safe and include, e.g., degradation of the device, a $\approx 10\%$ safety range is added to these numbers. Therefore, the required output energy range per pulse, under the given assumptions, is 9×10^6 to $3.5 \times 10^9 \frac{\text{eV}}{\text{sr}}$. Additionally, the requirement is defined that the pulse-to-pulse variation of the intensity may not be larger than $\pm 2\%$ over the entire dynamic range.

IV.4.3 Pulse width

As discussed already multiple times within this chapter as well as in Section III.3, the knowledge of the shape of pulses of the calibration device is crucial for proper understanding of the camera response. While the laboratory calibration is conducted with a laser light source of negligible width, the LEDs of the calibration device[23] will have a finite pulse length. The CTA FC project aims at a bias of the FC response to the calibration device of not more than $\pm 2\%$. For a Gaussian pulse shape, this would require an FWHM of 2.2 ns, following the results of the Two-Laser-Experiment for the non-linear regime (see Figure III.8). However, as found in Section IV.3 not the FWHM is the crucial quantity, but the bright time BT10. For a Gaussian pulse of 2.2 ns, the $BT10 = 4.0$ ns, which is the required upper limit for the LED pulse width for pulses in the non-linear regime of the camera. Typically, one expects a shorter pulse width at lower energies. This would not be an issue at all, as long as the shape is known such that biases can be corrected accordingly.

In case the non-linear regime is not used, this would ease the requirements for the FF device: in the linear regime, the tolerable FWHM for a $\pm 2\%$ bias is 3.4 ns, assuming that the reconstruction of the Two-Laser-Experiment with *umax* is representative for the reconstruction of Cherenkov showers in the linear regime (cf. Figure III.8). This Gaussian FWHM translates into a general requirement of $BT10 \leq 6.2$ ns, which is for example already fulfilled by the current LUPM FF device. In the case the non-linear regime is not used, intensities exceeding the linear regime would not be pulse width limited up to an FWHM of a Gaussian pulse of 6.9 ns, since the Two-Laser-Experiment shows no time dependence of the transition regime over the entire measurement (see Figure III.8).

Pulse-to-pulse variations of the pulse width, of course, are not tolerable. They would make it impossible to reconstruct the biases introduced by the finite pulse width with respect to the laser calibration source. Therefore, a strict upper limit of 0.1 ns is defined on variations of the $BT10$ pulse width.

IV.5 Summary

The chapter discusses what FF measurements are, why they are obtained and how they are technically implemented in the H.E.S.S. telescopes. Section IV.2 presents the characterization

[23] A laser light source for the in-field calibration devices is ruled out for maintenance and economical reasons.

of the LUPM FF device. Its pulse shape (rise time, fall time and FWHM) are measured for individual and combinations of LEDs. A clear rise in all parameters, especially the fall time and the FWHM is recorded. The temperature dependence of the FF device pulse shape and intensity is tested as well. Clear temperature dependencies in the fall time and the FWHM are visible, however, their effect is rather small. Further, the dynamic range of the device is extrapolated from measurements of FC@CT5. While the dynamic range itself is sufficient to cover the dynamic range of FC, the absolute illumination levels are about a factor 20 too high for an FC mounted in an MST. This issue could simply be resolved with an optical filter. The homogeneity of the FF device is also investigated using measurements of FC@CT5. It can be concluded that the frozen glass diffuser of the device is insufficient to smear out the individual LEDs. A gradient in the illumination levels of FF measurements is present in FC@CT5. This finding is supported by the large differences in the intensities of individual LEDs of the FF device measured in the laboratory.

In Section IV.3, a simulation study for FF measurements with FC@CT5 is described. The initial purpose of the simulations, understanding a deviation of $> 3\%$ in $R_{u/pz}$, is reached by finding and resolving a bug in the `sim_telarray` simulation code. The simulation framework is then further used to understand the influence of varying pulse forms on the response of FC in the linear regime and to characterize the pulse form of the LUPM FF device in more detail. It is shown that multiple pulse forms are capable of reconstructing the measurements correctly, depending on their respective FWHM. While the FWHM of the successfully reconstructing pulse forms is is not equal, their bright time BT10 is, defining the time span during which intensity of the pulse is at more than 10% of its maximum intensity. This BT10 is subsequently identified as the measure that is crucial for describing the response of FC in the linear regime to an incoming pulse. The BT10 of the LUPM FF device with the settings used for FF measurements is $(5.5 \pm 0.1)\,\mathrm{ns}$, according to the simulations.

Section IV.4 derives requirements for a calibration device for MSTs equipped with FC, based on the results of the previous sections and additional considerations. It is discussed that the available LUPM FF device is insufficient. Therefore, a new device must be developed. This process is already started but beyond the scope of this thesis.

V

Validation of Monte Carlo simulations for an analysis chain in H.E.S.S.

V.1 Introduction

In Chapter II the role of MC simulations for the analysis of IACT data is outlined: They are required to train algorithms, e.g., neuronal networks, for gamma-hadron separation and further to create the lookup tables for correct energy reconstruction of individual events. A correct energy reconstruction of individual events is necessary to obtain spectra and reconstruct the flux of astrophysical sources properly. Thus, MC simulations are crucial for TeV astronomy with IACTs. At the same time, they feature a complex interplay of measurements and approximations. The actual MC simulations are shower simulations, in which the development of an EAS induced by a photon or a hadron through the atmosphere is simulated. In H.E.S.S., and at least partially also in CTA, this part will be covered with the `CORSIKA` software ([Hec98]) that is described in Section V.1.2. The results of these MC simulations are then piped into another software describing the telescopes and their response to photons. Together with `CORSIKA`, typically `sim_telarray` is used ([Ber08]), as described in Section IV.3.2.

When exchanging parts of the telescopes (e.g., a camera) it is necessary to adapt the simulations in order to obtain consistent and correct scientific results. In the context of the installation of FC@CT5 in 2019, it was decided to validate the entire simulation chain of the HAP analysis framework of H.E.S.S. for self-consistency and correctness. For this effort, the HAP MC validation team was formed, consisting of Johannes Schäfer (lead), Tim Lukas Holch, Simon Steinmassl and the author of this thesis.

A measure for the success of a MC validation in IACT astronomy is whether the spectrum of the standard candle in VHE astronomy, the Crab Nebula, can be reconstructed consistently with a reference spectrum (see Section V.1.1). A lower level parameter to understand whether the assumptions made in the simulations are correct are the telescope trigger rates, i.e., using the CR flux as standard candle. Trigger rates are automatically measured in all observations, hence, a large bandwidth of different observing conditions is available. This means that the trigger rate is an intrinsic measure of an IACT (array). Thus, when the simulated conditions match the obser-

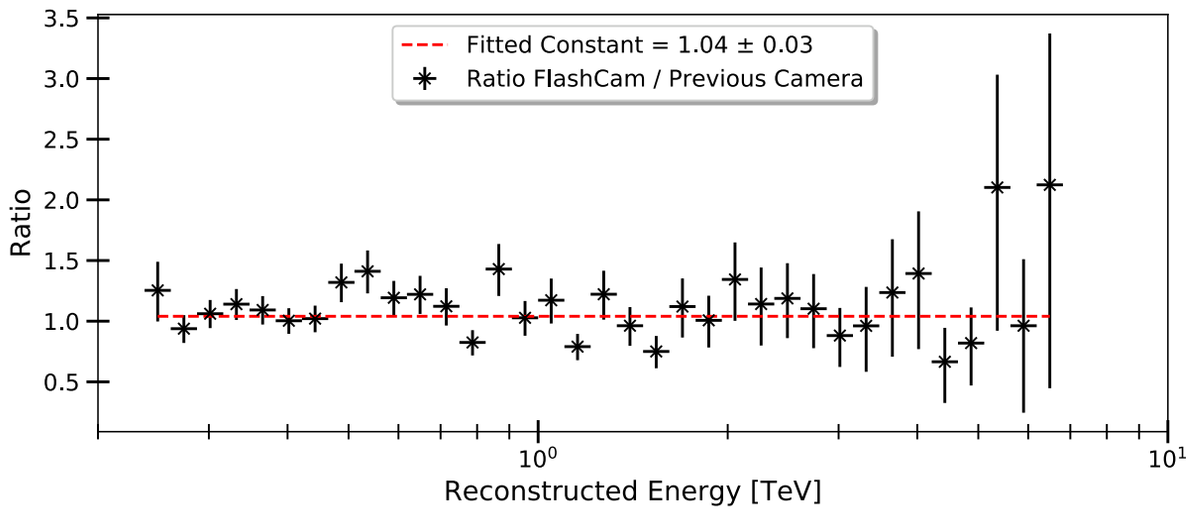

Figure V.1: Comparison of spectra of the Crab Nebula, as measured with the original CT5 camera and with FC@CT5. Image taken from [Püh21].

vation conditions, the simulated and the measured trigger rates must match. It is not necessary to take any external reference into account. Critical measures are the CT5 monoscopic trigger rate and the stereoscopic participation rate of CT1-4. Contrary to the spectrum of the Crab Nebula, which is formed by photon induced EAS, the trigger rates are dominated by hadronic events coming homogeneously from every direction. Due to the steepness of the cosmic ray spectrum, the majority of events is close to the trigger threshold. This implies that small deviations in the simulations from reality in general cause measurable effects. In consequence, the trigger rate is an excellent measure for the correctness of the simulations and any deviation from reality must be physically explained.

In this chapter, the results of the MC validation conducted in 2021 and 2022 are presented. Section V.2 describes checks in which the simulation processes themselves are verified, such as simulated photon intensities and the telescope optics. This section is independent of the analysis chain. The validation of the simulation configuration of individual telescopes is described in Section V.3. Special focus is laid on topics for which the author has had the main responsibility, being the simulation of pedestal widths and – tied to that – the estimation of the NSB level (Section V.3.1), as well as the simulation of the raw amplitudes (Section V.3.2). Eventually, in Section V.4 the validation of high level parameters is presented, as well as the final results of the MC validation for the HAP analysis chain. More details on other results of the MC validation efforts can be found in Holch et al. 2023 ([Hol22]), Leuschner et al. 2023 ([Leu23]), and the doctoral theses of Johannes Schäfer (Schäfer 2023, [Sch23]) and Simon Steinmassl (Steinmassl 2023, [Ste23]).

V.1.1 Motivation

With the installation of FC@CT5, the hardware of the H.E.S.S. experiment changed drastically and the new camera had to be incorporated to the system. The camera description in

`sim_telarray` was validated beforehand for CTA and is not subject to change. Leaving the rest of the telescope description untouched, measurements with FC@CT5 agreed with those obtained with the previous camera, as shown in Figure V.1 for the Crab Nebula and further described in [Püh21]. However, already before exchange of the cameras, the measurements of CT5 did not match those of CT1-4. The consistency of measurements with FC and the previous camera shows that the telescope description must have been incorrect. For example, the spectrum of the Crab Nebula (see Figure V.2) deviates from the formerly published H.E.S.S. result ([Aha06b]) as well as from the widely accepted reference spectrum of Meyer et al. that combines multiple measurements ([Mey10]). To quantify this deviation: the flux normalization at 1 TeV was 46% too high, with $\phi_{1\,\mathrm{TeV}} = (5.04 \pm 0.08) \times 10^{-11}\,\frac{1}{\mathrm{TeV\,cm^2\,s}}$, compared to the reference value of $(3.45 \pm 0.05) \times 10^{-11}\,\frac{1}{\mathrm{TeV\,cm^2\,s}}$ and the derived spectral slope of 2.33 ± 0.02 was 11% too hard / 0.3 too low with respect to the H.E.S.S. reference value of 2.63 ± 0.01 ([Ste23]). Both these deviations cannot be explained with the systematic uncertainty, which is given as ±20% on the flux and ±0.2 on the spectral index for the reference values ([Aha06b]). It must be mentioned that these reference values have been obtained with CT1-4, which cannot be directly compared to CT5. The systematic uncertainty of a CT5 mono analysis is expected to be slightly higher, especially in the high energy end. Nevertheless, a fit on the obtained data should be consistent within systematic uncertainties of the CT1-4 analysis. Thus, the analysis of the telescopes CT1-4 was not consistent with the new FC@CT5 analysis, which excluded the (unlikely) possibility of an elsewhere unnoticed, temporary change of the Crab Nebula luminosity and spectrum. The high level analysis itself appeared to work as intended, so the deviations most likely originated in the IRFs and lookup tables. In order to correct these, the bottom-up approach of the MC validation was initiated.

The time span for which the MC validation is valid without any restrictions is from June 6th, 2020 (gain adaption in CT1-4) to August 28th, 2020 (Winston cone cleaning of the HESS1U cameras), reaching over the H.E.S.S. runs 160051 to 162824. For further usage, however, only the parameter describing the optical throughput (`MIRROR_DEGRADED_REFLECTION`) must be adapted. Then, the obtained configuration can be applied until the change of the HESS1U trigger boards (March 2022) for CT1-4 and for the entire time span since installation of FC until at least January 2024[24] for CT5.

V.1.2 MC simulations with CORSIKA

As outlined above and in Section IV.3.2, the end-to-end simulation of EAS can be conducted with `CORSIKA` in conjunction with `sim_telarray`. A description on the usage of `sim_telarray` is given in Section IV.3.2, a brief description of `CORSIKA` according to its user manual ([Ber22]) follows here.

The `CORSIKA` particle interaction MC simulation program ([Hec98]) can be used in various scenarios. Here, the version compiled with the options `ATMEXT` (for treatment of pre-calculated model atmospheres), `CERENKOV` (for generation of Cherenkov light), `IACT` (for the interface to

[24] Time of writing of this thesis. The time span in which no hardware in CT5 is changed may and probably will be longer.

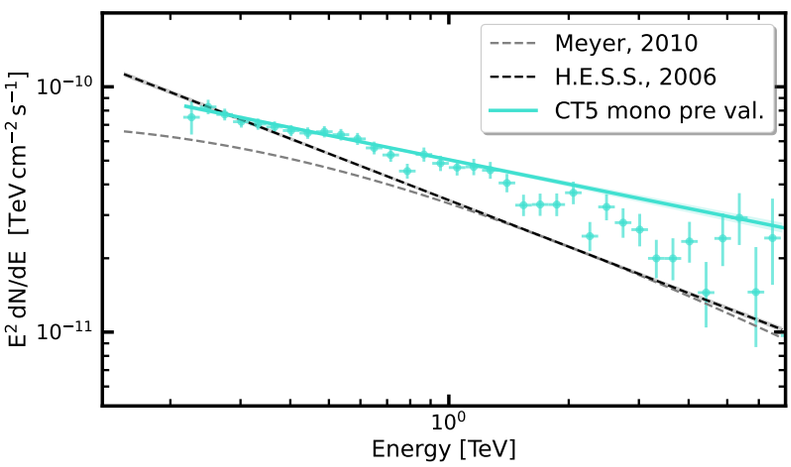

Figure V.2: Spectrum of the Crab nebula derived from $\sim$ 10 h of observations with FC@CT5. The analysis is performed based on the simulation configuration prior to the validation efforts. There was an evident discrepancy between the newly obtained spectrum and previous results of the H.E.S.S. collaboration ([Aha06b]), as well as with the generally accepted reference work of Meyer et al. ([Mey10]). Image credit: [Ste23].

`sim_telarray`), and `VIEWCONE` (for primaries coming from a cone around zenith and azimuth angle, rather than from the exact direction defined by these angles) is discussed. The input parameters to `CORSIKA` contain an integer code defining the type of the primary particle (can be protons, photons, diffuse emission, leptons, or heavier nuclei), a slope for the primary energy spectrum (by default as a powerlaw), the energy range in which primaries are simulated, the direction from which primaries should come, the opening angle of the view cone around that direction, and the number of showers to be generated. Further input defines the observatory: its height above sea level, the magnetic field, its orientation, and a model of the atmospheric profile at the location of the array. The telescopes are defined by their positions with respect to the array center and a radius on the ground that fully contains the telescope. As the majority of computation time is needed for the shower creation with `CORSIKA`, the showers are used multiple times with random (horizontal) displacements of the telescope array. This allows effective simulation of similar showers S_i with different shower cores, $S_i = (a, E, \vec{\Omega}, \vec{r_i})$. Crucial is also provision of four seeds for the pseudo-random number generator. In the described approach this is by default handled via `sim_telarray`, providing pseudo-random numbers as seeds and avoiding the same simulation to be run again and again. Also parameters defining the nuclear interactions, such as a defined first interaction height or energy cuts for particles are provided. However, these are typically kept at default values implying no restrictions / forced interactions. Only the energy cuts are such that particles not contributing to the generation of Cherenkov light are taken out of the simulation. Eventually, the Cherenkov emission parameters are defined, being the wavelength range (typically: 200 to 700 nm) and the photon bunch size.

Photon bunches are one among a couple of concepts to increase the efficiency of the simulations by approximating the physical processes. Instead of tracing each Cherenkov photon individually, they are collected in photon bunches from the moment they are created. Each photon bunch is treated like an individual photon in calculations for atmospheric absorption, ray-tracing and detection. The usage of photon bunches, by default containing 10 photons, decreases the computing time needed to trace these photons by a factor as large as the number of photons in the bunch.

However, it also lowers the precision and consequently increases the systematic uncertainty of the simulations, especially for events with few photons only. Compared to the systematic uncertainty of an MC IACT simulation, this increase in systematic uncertainty is marginally, though. Thus, using photon bunches with ≈ 10 photons per bunch is usually considered worth it. Further CPU time is saved by considering only such bunches that could possibly be detected, i.e., contribute to a telescope trigger. A first discrimination can be done with the keyword `MIN_PHOTONS`: it probes the sum of Cherenkov photons in all bunches, that is, the number of photons produced in a shower. If this sum – calculated before atmospheric absorption and losses at the mirror/detector level – is lower than a threshold (e.g., 200) defined by the keyword, the telescopes will impossibly trigger and the shower does not need to be followed up. Another feature to save CPU time makes use of the radius specified for every telescope that was introduced above, by approximating each telescope as a sphere of that radius. Photon bunches must fulfill two criteria to be recorded: firstly, they must hit the shadow of this telescope sphere that is created by projecting it to the ground[25] and secondly, they must intersect with the telescope sphere itself. With these criteria, photon bunches are excluded that would miss the telescope cameras. In particular, the shadow criterion prevents photons bunches to be recorded that would hit the reflector, but in an angle that would not lead to reflection into the detector.

As mentioned above, a model atmosphere is provided for the simulations. It consists of two models, one describing the atmospheric profile, its density, temperature, vapor content, etc. as a function of altitude. The other is the atmospheric transmission (also: extinction) model, describing the optical density of the atmosphere as a function of altitude and wavelength. The atmospheric profile is of great importance for the simulation of interactions in the EAS. Especially the density of the atmosphere determines the interaction probability of particles in an EAS. The atmospheric transmission model, on the other hand, is crucial to describe the transmission of photon bunches through the atmosphere. It consists of two parts, firstly the absorption by molecules in the atmosphere, and secondly by aerosols. Due to the limited atmospheric transmission, mostly due to aerosols, only a fraction of the Cherenkov photons produced in an EAS reach the ground. The probability of a photon bunch to be absorbed and therefore to be removed from the simulation is derived from the transmission model, based on the altitude of emission, the wavelength and the distance to the detector (sphere). The validation of the atmospheric model, especially the transmission model, is covered in Section V.2.

Already at compile time, the user must select a nuclear interaction model. `CORSIKA` offers a wide range of models, each with its own strengths and weaknesses. For simulations of the H.E.S.S. experiment, the model QGSJET-II-4 ([Ost11]) is used by default. Within the MC validation, the impact of changing this model to EPOS LHC ([Pie09]) or SIBYLL ([Ahn09]) is investigated (see Section V.4.1). Main difference of the models is the extrapolation towards highest energies and the number of modeled processes ([Sch23]).

Given a shower passes the criteria on `MIN_PHOTONS` and on hitting the telescope spheres and their shadows, the resulting photon bunches are directly inserted into the telescope simulation

[25] For computational reasons, the ground is divided in cells. So, the photon bunches must only hit a cell which is (partly) covered by the shadow, not necessarily the actual shadow.

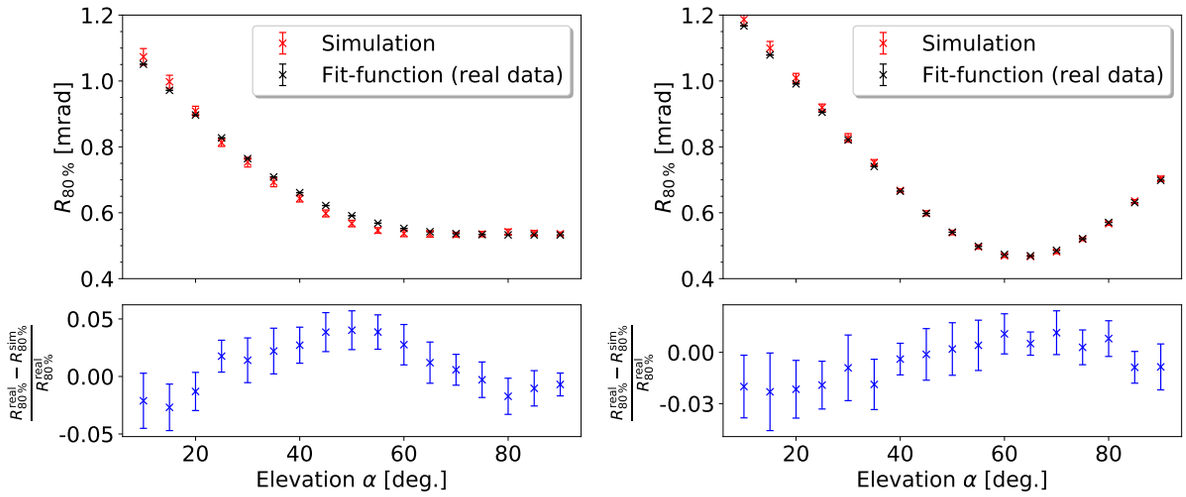

Figure V.3: Optical PSF of CT1 (left, similar for CT2-4) and CT5 (right) after adjustments during the MC validation effort, together with the measured values for comparison. The remaining deviation of $< \pm 5\% \approx 4\,\mathrm{mm}$ (in the focal plane, see lower panels) is acceptable. Image credits: [Sch23].

with `sim_telarray`. There, their extinction probability is calculated following the atmospheric transmission model and their impact on the telescope is simulated. Only necessary metadata of a shower, such as its origin, energy, number of produced photons, etc. is typically written to file, not the exact simulation results. This saves both, CPU time and memory space. To match metadata and simulation output, each event is assigned a per-simulation unique number.

The simulations with `CORSIKA` are the basis of the MC simulation chain validated in the following sections. However, the vast majority of adaptions during the validation effort concerns the detector simulation with `sim_telarray`.

V.2 Self-consistency of Monte Carlo simulations

In the first step, the self-consistency of the simulations is validated. That is, whether simulated light pulses are processed as expected and whether the results of these simulations match corresponding measurements. This section is intended to be an overview only, as the author of this thesis did not conduct the efforts himself. In [Ste23], the verification of basic pulse properties is described. The behavior for different intensities and temporal offsets is verified with simulated *laser events*. Nanosecond pulses of a given intensity (in photons) are simulated to hit the pixels directly and without temporal offset between the pixels. No issues have been identified in this part. Further, photon-induced EAS are simulated with different intensities but at identical impact positions to verify the correct dependence of the pulse amplitude on these intensities. Again, there have been no issues. Therefore, it can be concluded that simulated pulses are reconstructed as expected.

The p.e. *definition* is checked for consistency using laser simulations as well, to ensure that the computation of the detection efficiency is consistent. The intensities defined for these simulations

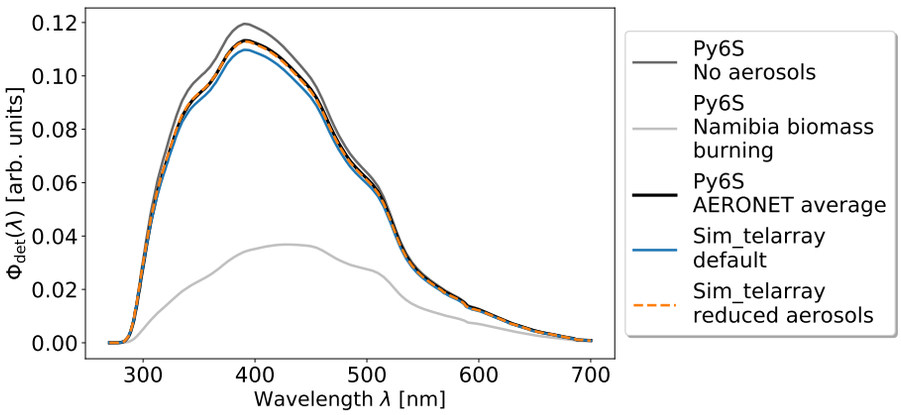

Figure V.4: Comparison of different transmission models. The curves show the flux of Cherenkov photons originating at 15 km above sea level that would be detected by CT5. Image credit: Tim Lukas Holch, DESY Zeuthen.

are reconstructed as a pixel-wise mean value within ±1%. This result is valid for both, the simulation-internal analysis tool and after applying the HAP MC conversion application ([Ste23]).

Another step in the basic validation process is to verify consistency between the simulated and the real *telescope optics*. This work is presented in detail in [Sch23]. The aim is to match the simulated optical PSF with real measurements. The optical PSF describes the radius of a circle containing 80% of the light from a point source, R_{80}. It depends on the telescope elevation, as the telescope structure is bend by its own weight. In-field, the optical PSF is measured by pointing the telescope to a star, with the camera lid closed. The light spot of this star is then recorded by an optical CCD camera and its size is extracted. Simulations with `sim_telarray` allow to mimic such measurements by creating a star at infinite distance that provides parallel light. Following [Got18], the PSF is parametrized by

$$R_{80}(\alpha) = \sqrt{R_{\text{min}}^2 + d_1^2 \cdot [\sin(\alpha) - \sin(\alpha_0)]^2 + d_2^2 \cdot [\cos(\alpha) - \cos(\alpha_0)]^2}. \tag{V.1}$$

Here, R_{min} is the empirically found minimum of the PSF and α_0 is the corresponding elevation angle, i.e., $R_{80}(\alpha = \alpha_0) = R_{\text{min}}$ The parameters d_1 and d_2 are pure scaling factors. d_2 is necessary to account for the larger and heavier dish of CT5, compared to CT1-4 ([Got18]). Therefore, for CT1-4 $d_2 = 0$ and Equation V.1 simplifies to that given in [Cor03]. Alike the measurements, simulations are conducted for different elevations in steps of 5°. During the validation of the PSF, the initial mismatch between simulations and real measurements is reduced from up to 20% to less than 5% for each telescope. In the focal plane, this corresponds to a mismatch of $R_{80} \leq 4\,\text{mm}$Changing the PSF had little effect on the telescope trigger rates, most likely because both the pre- and post-validation values are much smaller than one pixel of the Cherenkov cameras. Thus, the remaining mismatch is deemed acceptable. A comparison of the adapted simulated PSF with real measurements is shown in Figure V.3. The shown images are for CT1 and for CT5. The lower panels contain the deviation between simulations and real measurements. As CT1-4 are similar telescopes, in most figures only one of them is shown exemplarily.

The last major point to be discussed in this section is the validation of the *atmospheric model*, which was mainly conducted by Tim Lukas Holch. It is also discussed in [Sch23] and [Ste23], additional results can be found in [Hol22]. The atmospheric density profile is compared to publicly

available sources, which confirm the assumptions made in `sim_telarray` for the H.E.S.S. site. Validating the atmospheric transmission profile is more challenging. A resource for this is data from the AERONET[26] network ([Hol98]), of which a station is deployed at the H.E.S.S. site since 2016. The network consists of photometers, measuring either the sun- or the moonlight, the latter only while the moon is more than 3/4 full. From these measurements, the properties of atmospheric transmission are measured, especially the optical depth as a function of wavelength. While the molecular optical depth turned out to be stable and the assumptions in the default simulation configuration are correct, the aerosol content in the troposphere and consequently the aerosol optical depth (AOD) is highly variable on a scale of hours ([Hol22]). This is mainly during the biomass burning season in South-Western Africa, mainly in September and October ([For18]) and within the H.E.S.S. collaboration known as "Thomas-Lohse-Effect[27]". Especially in this time, the AOD in the wavelength band of Cherenkov light can exceed 1.0, implying that less than 10% of all Cherenkov photons which are produced on average in an altitude of 15 km can reach the ground. However, comparison of the default atmospheric transmission table with the values provided by AERONET shows that the default table features an AOD that is about 50% higher than the yearly average. This causes two effects: firstly, the observed average trigger rates are higher than the simulated ones. The higher opacity of the simulated atmosphere compared to the real one leads to more Cherenkov photons getting extinct in simulations than in reality. Thus, showers that are close to the trigger threshold but would trigger the telescopes in reality do not exceed the trigger threshold in simulations. As denoted above, many showers that actually do trigger the telescopes are close to the threshold, due to the steepness of the CR spectrum. Therefore, such an artificial increase of the effective trigger threshold by some p.e. leads to significantly lower trigger rates. Secondly, the energy reconstruction is systematically too high. Again due to the higher opacity, showers with given properties $S = (a, E, \vec{\Omega}, \vec{r})$ get simulated with a smaller Hillas Size as they would have in observations with the average atmosphere. In turn, photon-induced showers with given $\vec{\Omega}$, $\vec{r}$, and Size are written to the lookup tables with higher reconstructed energy E than if the average atmospheric transmission was simulated. Consequently, the atmospheric transmission table has been changed such that the AOD is reduced by 50%, now matching the yearly average. The newly generated atmospheric transmission model is internally referred to as *mixed atmosphere*, as it is less pessimistic than the previously used model but still contains aerosols[28]. Figure V.4 shows simulations of detected Cherenkov light spectra after transmission through model atmospheres with different aerosol content. Although the difference between the (old) default transmission model and the (new) mixed atmosphere seems marginal, it affects the trigger rates of all telescopes by about 10% ([Leu23]).

However, it is obvious that the atmospheric transmission is still a source of large uncertainty due to its variability. Significant variations of the AOD are also possible outside the biomass burning season, as shown in Figure V.5. Whenever an observation is conducted under an at-

[26] AErosol RObotic NETwork. See https://aeronet.gsfc.nasa.gov/, accessed on January 15th, 2024.

[27] This name goes back to Prof. Thomas Lohse who used to conduct on-site shifts for many years during September/October.

[28] At an intermediate stage, it was discussed to use an atmospheric transmission model without any aerosols at all.

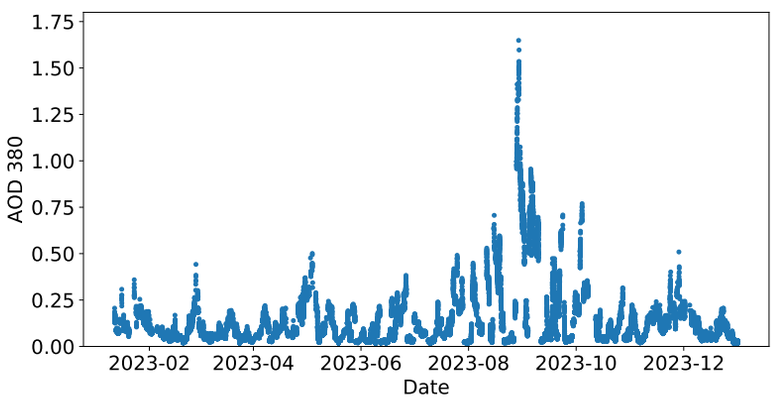

Figure V.5: Aerosol optical density at the H.E.S.S. site in the 380 nm band over the course of the year 2023. Most prominent is the peak in September, caused by the biomass burning season. However, also other peaks of unidentified origin can be seen. Figure created using data from AERONET ([Hol98]) and the H.E.S.S. internal AERONET data wrapper by Tim Lukas Holch, DESY Zeuthen.

mosphere different than the model atmosphere used in the simulations, events are reconstructed either with too high or too low energies and the effective energy threshold of the system is different than assumed. Currently, the strategy to obtain reliable scientific results is to produce spectra and lightcurves only from observations under "good" atmospheric conditions, mainly quantified by trigger rates within a certain range. However, this firstly leads to observations under "bad" or "too good" conditions being rejected, i.e., ignored. Secondly, within the specified range of "good" conditions, the variations in atmospheric transparency are still large, causing the systematic errors described above. To tackle this problem, the MC validation team has proposed a correction scheme that accounts for varying atmospheric transmission profiles by introducing an AOD dependent correction factor. As H.E.S.S. mostly operates during times with no or only little moonlight, no direct AOD measurements with AERONET are available for most observations. However, H.E.S.S. internally computes a transparency coefficient (TC) that is mainly based on the trigger rate and directly linked to the atmospheric transparency. The comparison of observation runs conducted at times of sufficiently bright moonlight with the AERONET measurements allows to derive the relation AOD(TC). The approach of the MC validation team is to calculate a correction factor for the reconstructed energy of an event and the corresponding IRFs. This has the potential to recover many observations that are currently deemed unusable due to insufficient atmospheric conditions. The approach has been presented at the 2022 AtmoHEAD conference ([Hol22]) and was successfully applied in the analysis of the recurrent Nova RS Ophiuchi ([Aha22b]).

V.3 Single telescope consistency

The next level within the verification process is to understand whether low-level parameters of individual telescopes match between simulations and real data. The author of this thesis was responsible for validation of the pedestal width and, directly tied to that, the NSB level. Further, he verified that the raw amplitudes match between simulations and measurements. the results of these activities are described in detail in Section V.3.1 and in Section V.3.2. Further efforts, such

as the validation of the individual telescope trigger thresholds are summarized in Section V.3.3.

V.3.1 Night Sky Background and pedestal width

Introduction and background

The NSB is the main contributor to the photon background of an IACT camera. According to [Pre02], main contributor to the NSB is night airglow, arising in photochemical processes in the stratosphere and above. Short after sunset and close to sunrise, zodiacal light – sunlight scattered in the atmosphere – is prominent in the West or East, respectively. NSB is defined as a diffuse background, therefore, bright stars are not considered contributors. However, unresolved and very faint stars contribute to NSB, as well as diffuse galactic light, that is star light scattered by interstellar dust. A minor role plays extragalactic light from unresolved galaxies or scattered in intergalactic space. At high geographic latitudes ($> 40°$, [Ben98]), the aurora borealis may not be neglected. For IACT astronomy, this does not play a role as telescopes are typically located close to the northern or southern tropic. In absence of moonlight, NSB leads to a rate of $\gtrsim 10$ to 100 MHz of p.e. in each pixel of an IACT camera, depending on the size of the telescope, the pixels themselves, etc.

The NSB rate, denoting the rate of NSB p.e. being recorded by each pixel, is in theory given by

$$f_{\mathrm{pix}} = \int F(\lambda)\Omega_{\mathrm{pix}} A_{\mathrm{mirr}} R_{\mathrm{mirr}}(\lambda)\epsilon_{\mathrm{cone}}(\lambda)\epsilon_{\mathrm{pmt}}(\lambda)\mathrm{d}\lambda \tag{V.2}$$

In this equation, $F(\lambda)$ is the spectral flux of NSB photons reaching the ground, Ω_{pix} the FoV of a single pixel, A_{mirr} and $R_{\mathrm{mirr}}(\lambda)$ the area and the reflectivity of the reflector, $\epsilon_{\mathrm{cone}}(\lambda)$ is the efficiency of the Winston cones and $\epsilon_{\mathrm{pmt}}(\lambda)$ the QE of the PMTs. In particular the NSB spectrum and the QE of the PMTs change drastically with the wavelength. While the QE reaches its maximum between 300 and 400 nm (see Paragraph II.1.2), the first relevant line of the NSB spectrum is at 557.7 nm ([Ben98]). The interaction of PMT QE and NSB spectrum will be investigated below in more detail. For $R_{\mathrm{mirr}}(\lambda)$ and $\epsilon_{\mathrm{cone}}(\lambda)$, on the other hand, it is sufficient to use mean values as the wavelength dependency is minor.

NSB has two effects on observations with IACTs. Firstly, it decreases the effective trigger threshold of the telescope, compared to a theoretical scenario without NSB: As the NSB p.e. rate is in the same order as the trigger rate or higher, one or multiple NSB p.e. are in each trigger window, decreasing the number of Cherenkov photon induced p.e. necessary to trigger the telescope. Secondly, NSB is a major source of noise as it is the largest contributor to the *pedestal width*.

The pedestal width and the influence of NSB to it is described in [Aha04b]. Pedestal denotes the mean ADC value of each readout channel (i.e., each pixel), recorded in absence of Cherenkov photons. In the absolute dark, e.g., when the camera lid is closed, it varies slightly due to electronic noise and forms a narrow Gaussian distribution when considering all pixels (see Figure V.6, "without NSB"). In the presence of NSB, this distribution broadens significantly. The width of

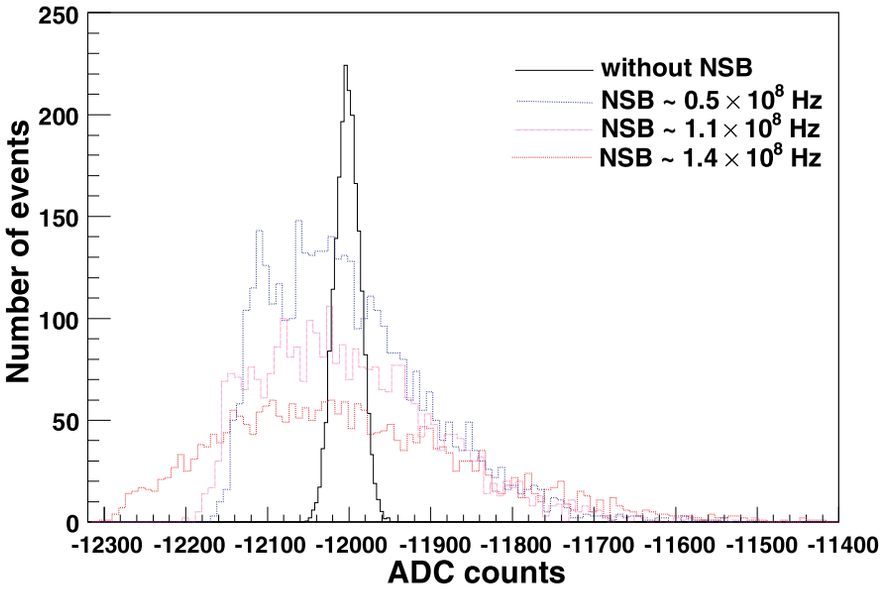

Figure V.6: Pedestal distributions of one pixel at different NSB levels, measured with one of the telescopes CT1-4 and its original camera. Image source: [Aha04b]. Reprinted with kind permission of Elsevier.

this Gaussian distribution is labeled pedestal width. When reconstructing the number of p.e. in an event from the ADC counts, the mean pedestal is subtracted. As the width of the pedestal distribution in Figure V.6 suggests, this mean can vary from the actual pedestal due to the NSB by several hundred ADC counts, corresponding to multiple p.e.. This is a source of noise that can not be corrected for. For high level analysis, the impact is negligible as the effects cancel out on average. Events close to threshold that are more affected and might be possibly biased are usually ignored due to the typically applied analysis cuts prior to gamma-hadron separation. In the low level parameters, especially the trigger rates, NSB and pedestal width make a well measurable impact ([Leu23]). Therefore, simulations must use a correct NSB rate in order to reproduce the measured pedestal width and to simulate the trigger rates correctly.

During observations, the pedestal and its width are derived as follows, according to [Aha04b]: during each observation run the pedestal of each pixel is estimated multiple times. For that, triggered camera images are used. Pixels containing Cherenkov light are not considered. The ADC counts in all other pixels are inserted into a pedestal histogram. Once this histogram has enough entries, the mean and the width of it are derived, being the current pedestal mean and width of that pixel. With the original H.E.S.S. I cameras, the pedestal mean and width were updated approximately once a minute. With the higher trigger rates of the HESS1U cameras and of FC, this happens predictably more often. The most accessible result of this procedure is the mean pedestal (width) that is written to file for each pixel and each observation run. The measured pedestal width is the mean value of the pedestal width of all observation runs and of every pixel in the specified range of the MC validation.

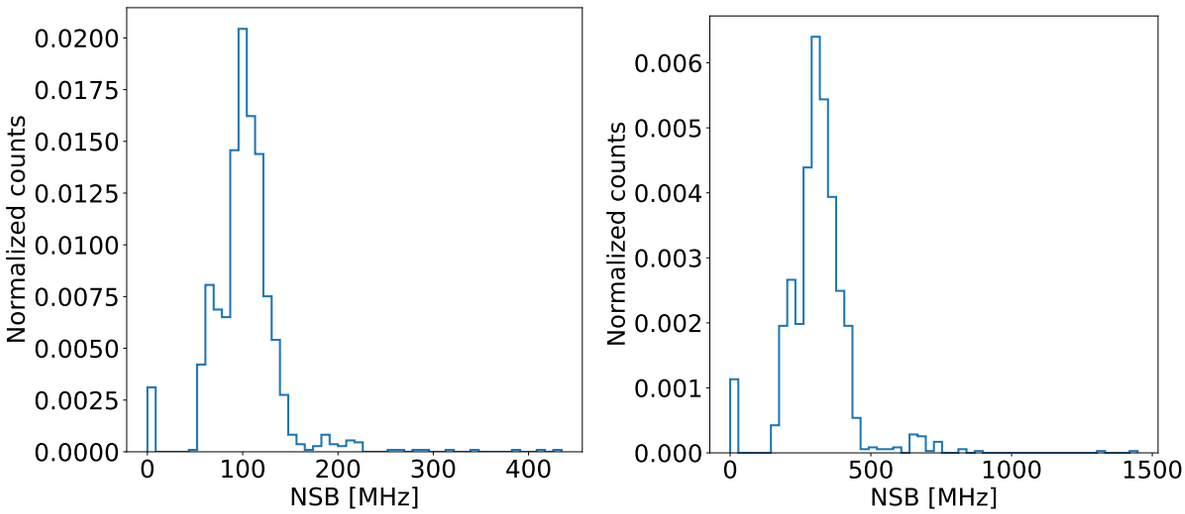

Figure V.7: Telescope averaged NSB rates of all runs in the validation period as read from the H.E.S.S. database. Left: CT1, CT2-4 are similar. Right: CT5.

Derivation of the NSB for H.E.S.S. simulations

There are three possibilities to determine the appropriate NSB rate for MC simulations. The first and most simple is to adapt the NSB rate such that the result of the pedestal simulations matches the measured pedestal width by trial and error. However, this is not the approach the MC validation aims for. As the defined goal is not only to match simulations and measurements, but to understand the simulations in detail such a trial and error method is not favorable. Nevertheless, the two remaining approaches are assessed according to their effect, i.e., whether simulations of the pedestal width return the measured value or not.

Another possibility is to use the H.E.S.S. database. For every observation run and every telescope, an estimated NSB rate is written to the database, computed during data calibration. Possible estimation methods for the HESS1U cameras are described in Section 5 of [Aha04b], showing well agreement with each other. As mentioned in Section III.1.2, FC pixel signals are DC-coupled. So, the NSB can directly be estimated from changes in the baseline current.

The values obtained from the database are presented as histograms, exemplary for CT1 and CT5 in Figure V.7. As can be seen, there are several outliers that probably falsify the mean. Firstly, a couple of entries appear to have an NSB rate of 0. These runs can be identified as FF runs, for which no NSB is calculated, and which are therefore not considered. Further, the distributions yield a tail with a small peak around 200 MHz (CT1-4) and between 600 and 800 MHz (CT5), respectively. This tail consists of 47 runs that can mostly be identified as moonlight observation runs that were conducted with a higher trigger threshold and under comparably bright moonlight. Those runs in the tail that are not moonlight runs face either very high (and sometimes unstable) trigger rates, or are truncated or otherwise very short runs. Therefore, they are excluded from the derivation of the mean NSB rate from the database. From the remaining distributions of NSB rates the mean is derived as shown in Figure V.8 by fitting a Gaussian to the histograms. For each telescope, this mean must be divided by the `MIRROR_DEGRADED_REFLECTION`

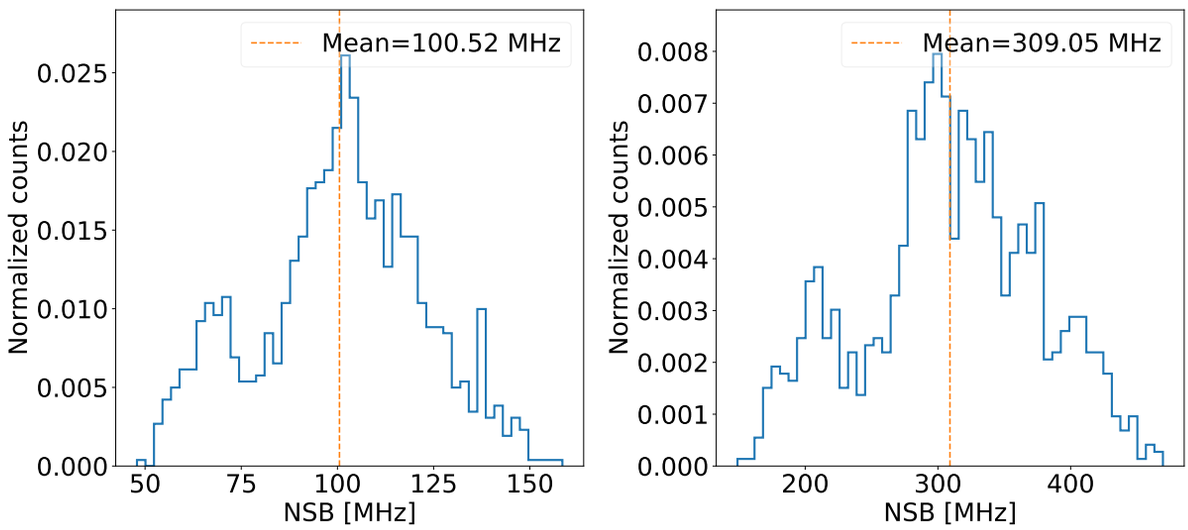

Figure V.8: NSB rates from the H.E.S.S. database after removal of the tail and of runs without NSB. The median measured NSB rate is fitted with a Gaussian. Left: CT1, CT2-4 are similar. Right: CT5.

(see Section IV.3.2), as this parameter is multiplied in `sim_telarray` to the provided NSB rates to account for a degraded optical efficiency with respect to the nominal configuration values. `MIRROR_DEGRADED_REFLECTION` is a period-wise correction parameter, also referred to as optical efficiency of a telescope. Within one period, the optical efficiency is assumed to be stable. The NSB rates derived from the DB already include the optical efficiency, since the rates are derived from camera data after passing through the telescope optics. Then, the derived rates are 138.85 MHz for CT1-4 and 391.21 MHz for CT5.

The other possibility is to following Equation V.2 to calculate an NSB rate. For practical use, the equation is slightly adapted to a preliminary form of:

$$f_{\text{pix}} = \phi_{\text{NSB}} \cdot \Omega_{\text{pix}} \cdot A_{\text{mirr}} \cdot R_{\text{mirr,avg}} \cdot \epsilon_{\text{cone,avg}} \cdot \epsilon_{\text{pmt, NSB}} \tag{V.3}$$

Now, ϕ_{NSB} is the average photon rate for $300\,\text{nm} \leq \lambda \leq 650\,\text{nm}$. At the H.E.S.S. site it is $\phi_{\text{NSB}} = (2.21 \pm 0.22) \times 10^{12}\,\frac{\text{ph}}{\text{sr s m}^2}$, as derived in [Pre02] for a sky field away from the galaxy and without any stars brighter than 6 mag. The wavelength range is sufficient, since at shorter wavelengths the NSB level is negligible and at longer wavelengths the QE of PMTs is practically 0 ([Pre02]). The values of the other parameters are summarized in Table V.1.

Ω_{pix} can be found in [Bol14] for the HESS1U cameras and has been derived for FC by H. Salzmann, IAAT, in his master's thesis ([Sal20]). The mirror areas and reflectivities are obtained from the `sim_telarray` configuration files. The former have been derived by K. Bernlöhr, MPIK, from the construction drawings of the telescopes and have been evaluated by him with the ray-tracing functionality of `sim_telarray` ([Ber02]). The latter is derived from measurements of mirrors for the CT1-4 telescopes straight from the factory. The reliability of these mirror reflectivities is limited by aging effects due to environmental influences and not least by the recoating of the CT1-4 mirrors. However, the values in use are the best available ([Ber24]) and deviations are constantly

Table V.1: Necessary parameters to derive the NSB rate for CT1-4 and CT5, respectively. Note that the pixel FoV is given in degree rather than steradian, following the references. For usage in the formula, it is converted taking the focal length of the telescopes into account.

Parameter	CT1-4/HESS1U	CT5/FC
Ω_{pix}	0.16°	0.08°
A_{mirr}	94 m^2	561.2 m^2
$R_{\text{mirr, avg}}$	0.84	0.84
$\epsilon_{\text{cone, avg}}$	0.9	0.8
$\epsilon_{\text{pmt, NSB}}$	0.098	0.1478

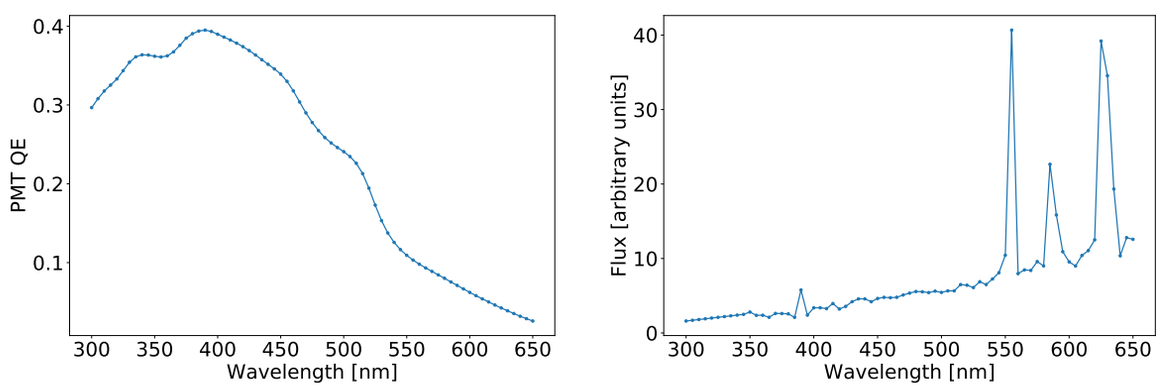

Figure V.9: Left: QE of FC, as used in simulations. Right: NSB spectrum, with a resolution matching the QE. The original values are extracted from [Ben98], values between 300 and 350 nm are interpolated.

corrected for (see the discussion of the muon chain in Section V.3.3). For the HESS1U cameras, also the efficiency of the Winston cones is obtained from `sim_telarray` configuration files. It is based on calculations by H. Krawczynski, MPIK ([Kra00]). For FC, $\epsilon_{\text{cone,avg}}$ is estimated from [Pür19]. Eventually, $\epsilon_{\text{pmt, NSB}}$ is the average QE of the PMTs for NSB light. It is derived by folding the spectral QE of the PMTs with the NSB spectrum. As the HESS1U cameras use the same PMTs as the original HESS1 cameras, the value given in [Pre02] can be used. For FC, this has been done in the course of this work and is presented in the following.

The QE of the FC PMTs is available in wavelength steps of 5 nm as a configuration file of `sim_telarray` that is based on measurements by O. Kalekin, ECAP/FAU Erlangen-Nürnberg. Figure V.9 displays the QE of the FC PMTs in the left panel. The NSB spectrum can be extracted from [Ben98], using the Webplotdigitizer software ([Roh22]). This spectrum starts at 350 nm and extends to > 800 nm. To also cover the necessary range of 300 to 350 nm, the mean values from 350 to 450 nm are linearly extrapolated. Values above 650 nm are ignored for further considerations. By means of a floating mean, the spectrum is modified such that only one average value for each step of 5 nm remains. The final spectrum is shown in Figure V.9. It is then used to calculate the weighted average of the QE, being 0.1478 as reported in Table V.1.

Another effect that must be taken into account is the reflection of NSB light from the ground.

Table V.2: Parameters to derive the ground area for derivation of the NSB rate for CT1-4 and CT5, respectively.

Parameter	CT1-4/HESS1U	CT5/FC
acc_{cone}	28°	27°
f	15 m	36 m
h_{mount}	10 m	24 m
r_{mirr}	6	14

The Winston cones' angular acceptance exceeds the area covered by the reflector. The soil at the H.E.S.S. site can be described as a dry savanna with ground albedo of $\alpha \approx 0.2$ ([Li22]). The area on the ground seen by the camera (when the telescopes point to zenith), A_{gr}, can be calculated with basic properties of the telescopes:

$$A_{\text{gr}} = \underbrace{(\tan(acc_{\text{cone}}) \cdot (f + h_{\text{mount}}))^2 \cdot \pi}_{\text{total area covered by camera}} - \underbrace{\left(\frac{r_{\text{mirr}}}{f} \cdot (f + h_{\text{mount}})\right)^2 \cdot \pi}_{\text{area shadowed by reflector}} \tag{V.4}$$

acc_{cone} is the maximum acceptance angle of the Winston cones. A simplification is made, such that on average, the angular acceptances from Table V.1 can be used. f is the focal length of the camera, and h_{mount} the altitude of the rotational axis of the mirrors, i.e., the altitude in which the mirrors are mounted. Together, $f + h_{\text{mount}}$ are the altitude above ground in which the camera is situated when the telescope points to zenith. r_{mirr} denotes the radius of the reflector. The values used are summarized in Table V.2. The maximum acceptance angles are derived from the same sources as the angular acceptances themselves: the `sim_telarray` configuration file (based on [Kra00]) for CT1-4 and [Pür19] for CT5. All other parameters can be found on the public H.E.S.S. website[29]. Then, the ground area that must be taken into account is 1225.8 m^2 for CT5 and 241.0 m^2 for CT1-4.

In order to account for the ground albedo, a corresponding term must be added to Equation V.3:

$$f_{\text{pix}} = \phi_{\text{NSB}} \cdot \Omega_{\text{pix}} \cdot \epsilon_{\text{cone, avg}} \cdot \epsilon_{\text{pmt, NSB}} \cdot (A_{\text{mirr}} \cdot R_{\text{mirr, avg}} + A_{\text{gr}} \cdot \alpha) \tag{V.5}$$

This delivers 134.93 MHz for CT1-4 and 322.54 MHz for CT5[30], respectively.

While the results for CT1-4 match very well between the database (computed during calibration) and the calculations as shown above ($\frac{\text{NSB}_{\text{calc}}}{\text{NSB}_{\text{db}}} < 3\%$), the values for CT5 do not agree ($\frac{\text{NSB}_{\text{calc}}}{\text{NSB}_{\text{db}}} \approx 20\%$). As discussed above, pedestal width simulations are run with both NSB rates in question to decide which of them reproduces the measured pedestal width better. For CT1-4, simulations are run as well to ensure that simulations with the NSB rates reproduce the measured pedestal width correctly. In Figure V.10, the results of these simulations are shown, compared to the measured pedestal width. For CT1-4, the NSB rate obtained from the database

[29] https://www.mpi-hd.mpg.de/HESS/pages/about/HESS_I_II/, accessed on January 24th, 2024.

[30] Initially, an NSB rate of 316.01 MHz has been reported for CT5 at the end of the MC validation. All results reported in the following are based on that value. The deviation of $\approx 2\%$ to the rate reported here is expected to change the pedestal width by $\leq 2\%$ and further quantities by $\sim 0.1\%$ or less (see, e.g., Table V.3).

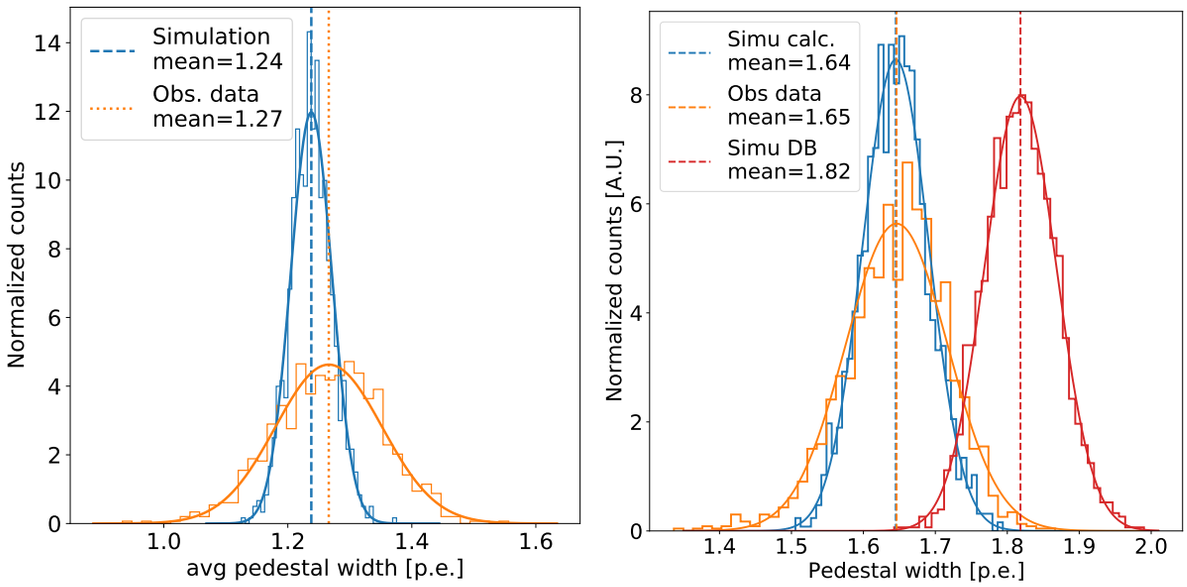

Figure V.10: Pedestal width simulations of CT1 (left panel, exemplary for CT1-4) and CT5 (right panel). The pedestal width distribution among all pixels is shown for a simulation, conducted with the new NSB rates (blue), and in form of the mean of all observation runs considered in the MC validation (orange). For CT5, also the distribution obtained with the NSB rate derived from the database is displayed in red. By fitting a Gaussian to the distributions, the respective mean is derived.

(138.85 MHz) reproduces the pedestal width slightly better in simulations and should be applied in future MC simulations. The results for CT5 show that the simulation with the calculated NSB rate matches the measured pedestal width perfectly, while the rate obtained from the database creates a pedestal width about 10% too high. Therefore, the NSB rate for simulations of CT5 should be the calculated NSB rate of 322.54 MHz. These findings conclude the validation of the pedestal width, that now can well be reconstructed as Figure V.10 shows.

Discussion

One might ask whether it is inconsistent to use the NSB rate obtained from the database for one telescope type and the calculated rate for the other. This might be resolved with the following considerations: Measuring the NSB rate directly while obtaining the data with the methods described in [Aha04b] is a straightforward method and should always be preferred if possible, e.g., for CT1-4 where the rate computed from observational data reproduces in simulations the measured pedestal width. However, for CT5 this is not possible, as either the estimation of the NSB rates or of the pedestal width does not work properly as of now. As the NSB rate is derived with a different method than for CT1-4, while the pedestal width is not, it is a fair assumption that the derivation of the NSB rate is the source of this error. Therefore, the calculated rate can be used if it returns the correct pedestal width in simulations.

However, there are many uncertainties in calculating the NSB rate. The reflections from ground contribute about 1/3 of the entire NSB rate. As they scale linear with the albedo, a

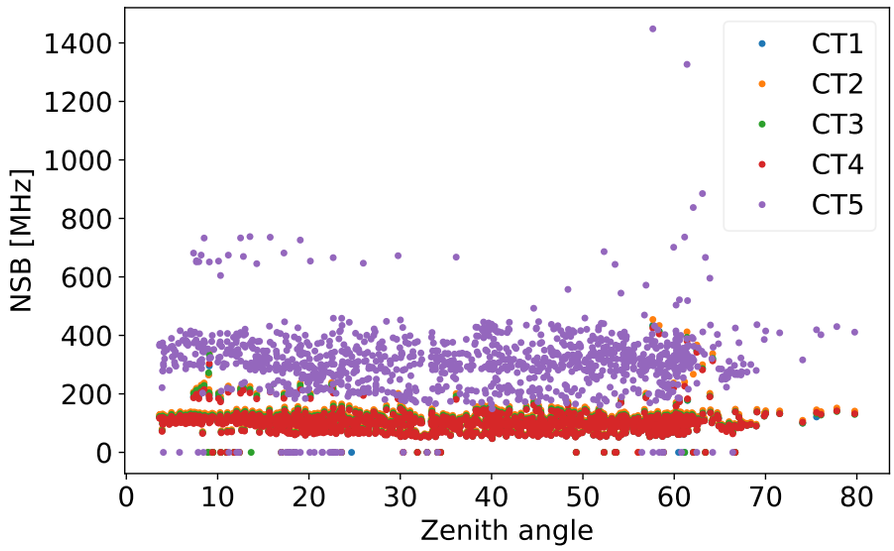

Figure V.11: NSB rates as derived from the H.E.S.S. database over zenith angle of the respective observation. Note that the CT5 rate is believed to be systematically too high, as explained in the text. Any relative changes of the NSB rate as a function of zenith should appear in this plot, though.

slight difference in the albedo would change results massively. For example, about 0.4 is the albedo in a desert ([Cor21]), which is a reasonable approximation in sufficiently dry years. Also, no spectral investigation of the albedo has been done. A further source of uncertainty for the entire calculation is the NSB photon rate ϕ_{NSB} that has been derived more than 20 years ago and the measurements where never repeated. During this time, the contribution from the city of Windhoek to the NSB has certainly raised, due to a population growth of more than 100%. The NSB spectrum on which the derivation of $\epsilon_{\mathrm{pmt,\,NSB}}$ relies is not certain as well: it has been derived on the Canary Island of La Palma, more than 25 years ago. It is questionable, whether the results obtained on the top of a mountain on an island in the Atlantic Ocean with a city comparably close can be 1:1 applied to the H.E.S.S. site in the flat, continental savanna, about 100 km apart from the next city. Measurements of the NSB spectrum at the H.E.S.S. site are currently under consideration, but not yet started at the time of writing.

Another point to be addressed is the dependence of the NSB on the zenith angle. In general, the NSB depends on the zenith angle, as pointed out in [Ben98] and also found for measurements on La Palma in [Pre02]. However, for the measurements in Namibia, [Pre02] reports that there is no such dependency. Figure V.11 verifies this statement, by plotting the NSB rate derived from the H.E.S.S. database over the zenith angle of the respective observation. Although the NSB rates in the database for CT5 are assumed to be too high, any zenith angle dependency should be visible if present. For CT1-4, this holds even more. However, except for few outliers due to the reasons explained above, the NSB rates are stable for all runs. Therefore, it is sufficient to describe the NSB rates with one value for all zenith angles. Investigations of the mechanism that leads to this behavior are not within the scope of this thesis.

NSB under moonlight conditions

Preferably, IACT observations are conducted with no or only little moonlight. During full moon and phases close to it, no observations are possible with PMT-based cameras as the background

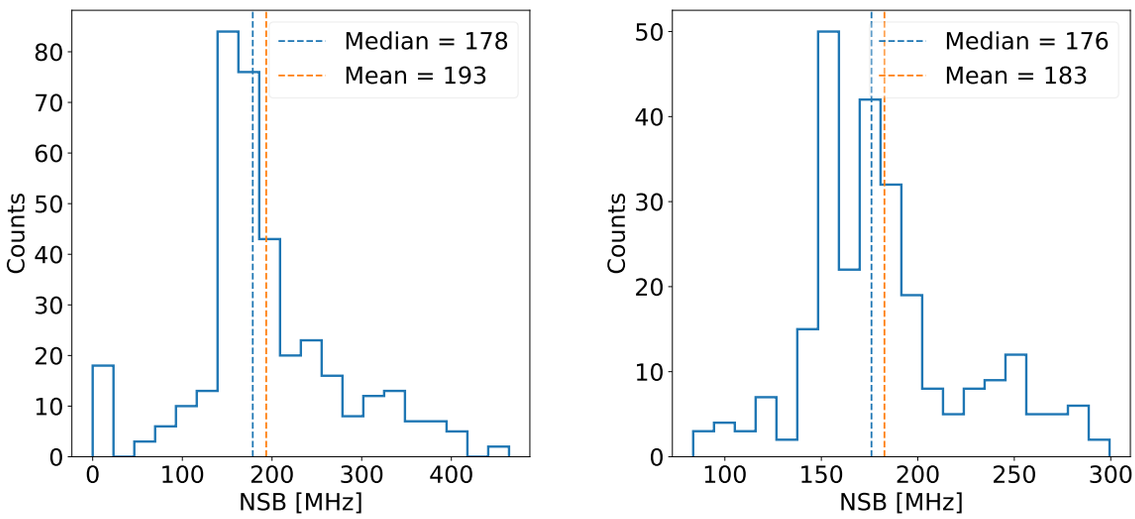

Figure V.12: Distributions of measured NSB rates during moonlight observation runs before (left) and after (right) applying the selection steps described in the text. The plots show distributions for CT1, CT2-4 are similar.

light is too bright and would possible lead to a persistent degradation of the detectors. In the past years, H.E.S.S. exploited observations under intermediate moonlight that is remarkably brighter than the usual optical background but dim enough to not damage the PMTs. For these observations, a dedicated hardware configuration is used that in particular yields a higher trigger threshold. The *moonlight observation configuration* ensures that the DAQ remains capable of handling the trigger rates. This requires also dedicated MC simulations in order to derive IRFs and lookup tables matching the configuration. Although moonlight is not normally considered a contribution to the NSB ([Ben98], [Pre02]), the practical effect of moonlight is to increase the NSB rate. In the following, the derivation of an NSB rate for simulations to analyze data obtained with the moonlight observation configuration is discussed.

To implement the NSB rate for moonlight simulations, the parameter `NSB_SCALING_FACTOR` is used. It is a factor that is multiplied to the nominal NSB rate in moonlight simulations, rather than hard-coding an NSB rate independently. The moonlight observation configuration is used for moonlight of varying brightness, and also when observing bright galactic fields during phases of low moonlight. Therefore, a consistent calculation of the `NSB_SCALING_FACTOR` is not feasible. Consequently, it must be derived from the database, which does not allow to derive conclusions on the rate of CT5, as discussed above. So, the `NSB_SCALING_FACTOR` is given as the ratio [CT1-4 Moonlight NSB] / [CT1-4 Normal NSB] and will be used for CT1-4 as well as for CT5. This is a consistent approach, as the `NSB_SCALING_FACTOR` is applied to ϕ_{NSB} in Equation V.5 and is therefore telescope-independent.

Since there are not enough runs in the period when the MC validation is fully valid for adequate statistics, all runs from the FC installation to the start of the investigation are used (H.E.S.S. run number 172672, obtained on February 4th, 2022). Within these runs, initially all moonlight

observations are selected. Figure V.12 shows the NSB values measured in all moonlight observation runs in the left panel. It can be seen that for a few runs the NSB estimation has not been successful and a rate of 0 is displayed. Consequently, these runs are filtered out. Also, some of the runs are rather short, so a minimum duration of 750 s is chosen. From the remaining runs, all those are filtered out of which the transparency coefficient is lower than 0.9 or higher than 1.2. After verifying that no unusual amount of pixels is switched off in any of the telescopes in each run left, histograms of NSB distributions are plotted. They show a clear peak and a large tail, extending beyond NSB rates of 400 MHz.

It is not meaningful to include these outstanding high intensities in the derivation of the NSB rate for moonlight observations, as they shift the mean and even the median of the distributions to higher values than the distribution peak. It has therefore been decided to ignore runs with NSB rates of more than 300 MHz (as written in the database) in these considerations, and rather make them subject of dedicated simulations that match the corresponding target. The resulting distribution is shown for CT1 exemplarily in Figure V.12, right panel. The remaining runs deliver an `NSB_SCALING_FACTOR` of ≈ 1.7 which is subsequently adapted for moonlight simulation runs.

Summary

In this section, the NSB rate to be inserted into the telescope simulation has been derived. The results are rates of 138.85 MHz for CT1-4 and 322.54 MHz for CT5. With these rates, the measured pedestal width can be reproduced in simulations with $\leq 2\%$ deviation. For moonlight simulations, an `NSB_SCALING_FACTOR` of 1.7 must be applied. So, the validation of the pedestal widths is successful.

A secondary result of the presented investigations is that the estimation of the NSB rate with the baseline, as done for FC@CT5 is inconsistent with the measurement/simulation of the pedestal width, as well as with the calculations of the NSB rate presented here. Most likely, this is because the NSB rate measured and written to the database is too high, on average by about 20%. However, a miscalculation of the pedestal width in real measurements and simulations, as well as of the NSB rate, cannot be excluded, given the large uncertainties in the calculations of the NSB rate in particular. The issue has been reported to the CTA FlashCam project team for further investigations, as it is beyond the scope of this work.

The validation of the NSB rates has a measurable effect on the simulated trigger rates. They increased by 3-6%, as reported in Table V.3. This improves the match between the simulated and measured trigger rates substantially.

Finally, it has been verified that there is no zenith angle dependency of the NSB rate for IACTs at the H.E.S.S. site.

V.3.2 Raw amplitude simulation

To verify the correct handling of background photon counts in simulations, the raw amplitudes are compared. Raw amplitudes are the charges of the pixels remaining in an only slightly cleaned image. A slightly cleaned image is a for example an image on which the *Extended0704* algorithm

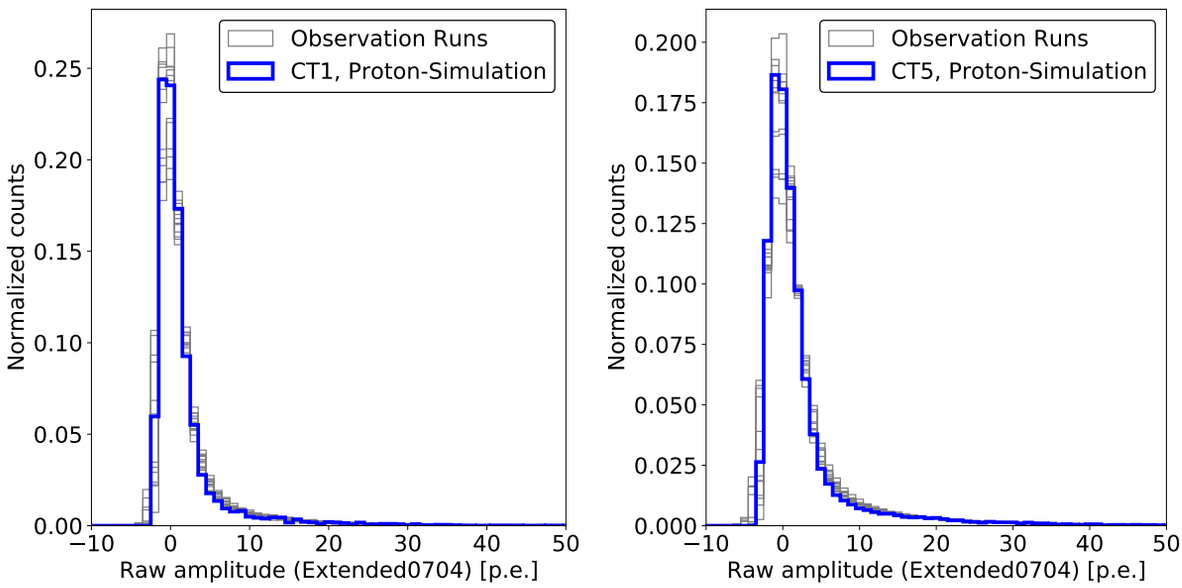

Figure V.13: Normalized count histograms of raw amplitudes for one simulation and multiple comparable observation runs. The simulation uses protons only and the telescopes point to North at 20° zenith angle. The observation runs point to various directions at $20° \pm 5°$ zenith angle, and have been conducted under atmospheric conditions close to those simulated. Left panel: CT1, CT2-4 are similar. Right panel: CT5.

has been applied. "0704" denotes the cleaning strategy, that each pixel with at least 4 p.e. needs a neighboring pixel with at least 7 p.e. and vice versa (cf. Section II.2.1). "Extended" means that around every pixel surviving this cleaning a ring with a thickness of 2 pixels is kept, additionally. The resulting distribution of pixels with respect to their charge amplitude is dominated by pixels not containing Cherenkov light and therefore varying by few p.e. around 0 p.e. If the peak of the simulated distribution matches those of observation runs, the simulation and handling of background photons such as NSB represents that of the real system. The tail of the distribution towards larger charges can be neglected here, as it contains the actual Cherenkov signals. These are validated separately during the high level validation of the Hillas parameters, by means of the Size. This is discussed in Section V.4.

The simulated raw amplitudes are shown for CT1 and CT5 together with the raw amplitudes of multiple observation runs in Figure V.13. The simulation uses protons as primary particles and is conducted once all necessary adaptions that have been found during the MC validation effort are implemented. For computational efficiency, the simulations assume a CR proton spectrum following a simple powerlaw with index $\Gamma = 2.0$. Although the noise peak should be independent of the simulated Cherenkov events, the simulated distribution is weighted with a correction factor of $E^{-0.7}$, in order to transform the simulated CR proton powerlaw into an approximated, actual powerlaw of $\Gamma = 2.7$ ([Hai04]). The telescopes have been simulated to point to North at 20° zenith angle. The observation runs for comparison have been selected such that they are comparable to the simulated conditions. This comprises in particular the atmospheric transparency and the zenith angles of the observations which are all $\in [15°, 25°]$. Further, in order to be comparable to

pure proton simulations, the observation runs may not have a strong gamma-ray source like the Crab Nebula in their FoV.

As can be seen in Figure V.13, the noise peak and its position are well reproduced in the simulations, for the CT1-4 telescopes as well as for CT5. Thus, the raw amplitudes of pixels during triggered events are similar in simulations and observations. This verifies that low level pixel amplitudes in the simulations are handled identical as in the actual observations. It consequently confirms that image cleaning procedures should and can be applied similar to simulated data and to observations.

V.3.3 Further efforts

After discussing intensively the investigations on the raw amplitudes and especially on the NSB and the pedestal widths, this paragraph summarizes the single telescope validation efforts to which the author of this thesis only contributed little. The verification of individual telescopes further comprises the *optical efficiency*. As discussed in the introduction to `sim_telarray` in Section IV.3.2, all components of the optical system of a telescope yield a defined optical efficiency in simulations, e.g., the reflectivity of the mirrors or the QE of the pixels. These do degrade on the long term (e.g., the photo-cathode of the PMTs) and sometimes change on shorter timescales (e.g., mirrors getting dusty due to heavy wind and cleaned at a rain shower in the rainy season). It is not feasible to adjust these parameters constantly in the simulation configuration and therefore not meaningful to validate each of the optical components within the MC validation effort. However, what is adjusted regularly is the parameter `MIRROR_DEGRADED_REFLECTION`. As explained in Section IV.3.2, it states how good is the optical throughput of the system, compared to the reference values defined in the reflector and camera configuration. Summarizing the optical throughput efficiency in this parameter is sufficient, as it is irrelevant which exact component degrades, as long as the overall level of degradation is known ([Ber22]).

The reflectivity of an IACT can be measured using muon efficiencies following [Mit16]. Muons are generated in hadron-induced air showers and penetrate the atmosphere deeply. They might emit Cherenkov light only few hundred meters above an IACT, resulting in a ring-like image in the camera. It is possible to analytically calculate the brightness of such a ring based on its radius, which corresponds to the opening angle of the Cherenkov cone. The muon efficiency of the telescope is then given by the ratio of the measured intensity to the calculated intensity. The same procedure can be applied in dedicated muon simulations, returning the muon efficiency of the telescope as configured in simulations. Finally, a correction factor can be derived as ratio of the simulated muon efficiency to the measured muon efficiency. This correction factor is the `MIRROR_DEGRADED_REFLECTION`.

The validation of the muon chain has been led by Tim Lukas Holch. Two main points are identified in the investigations. Firstly, the systematic uncertainty of the trigger rate due to the optical throughput estimation with muon efficiencies has been quantified. The muon efficiency derived from observations varies on the scale of days. Analyzing these deviations allows to derive a systematic uncertainty of $\pm 5\%$ on the measured muon efficiency that propagates through the

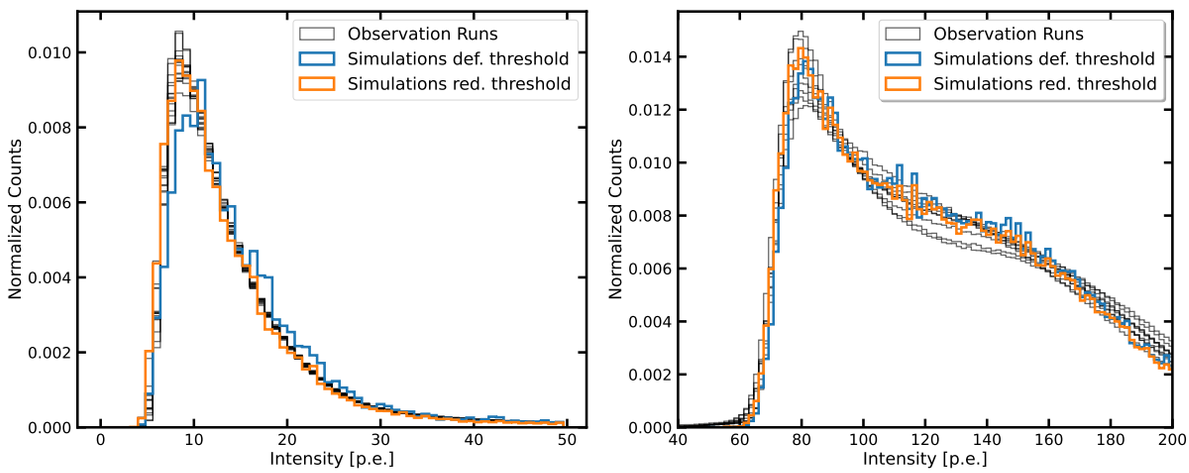

Figure V.14: Right: intensity distribution of the third-brightest pixel of events recorded with CT1 (CT2-4 similar). Shown are observation runs (grey), simulation runs with the default, pre-validation threshold (blue) and simulation runs with the validated, reduced threshold (orange). Left: intensity distribution of the brightest sector of events recorded with CT5. Again, observation runs (grey) are shown together with simulations with default threshold (blue) and reduced threshold (orange), respectively. Image credits [Ste23].

analysis chain to the degraded mirror efficiencies. Secondly, the analysis chain for simulations with CT5 has been upgraded with the installation of FC@CT5. Especially the introduction of proper handling of the pedestal and the pedestal width (implemented by Simon Steinmassl) is a new concept compared to the old CT5 camera that represents how the FC camera works. When replacing the default values with those found after validating the pedestal width (cf. Section V.3.1), the simulated muon efficiency distribution is off by $\approx 8\%$, compared to the measurements ([Ste23]). To match the distributions again, the `MIRROR_DEGRADED_REFLECTION` must be increased by 8% ([Leu23]). For CT1-4, the parameter has been decreased by 2.4%.

Due to the steepness of the CR spectrum, simulating the *trigger threshold* of all telescopes correctly is crucial to eventually match the simulated with the observed trigger rates. For CT1-4, this investigation has been conducted by Johannes Schäfer and for CT5 by Simon Steinmassl. Detailed descriptions of their efforts can be found in [Sch23] and [Ste23], respectively. For the verification, observation runs with no strong gamma-ray source in the field of view are compared to proton simulations, to take into account that the majority of triggered events are induced by hadrons. The observation runs are chosen such that the zenith angle and the atmosphere are consistent with the simulations at 20° zenith angle and with the validated atmospheric model (see Section V.2).

The trigger criterion for the CT1-4 cameras is that three pixels must a exceed an adjustable threshold in order to trigger the camera. The trigger of CT1-4 is fully analog, using a dedicated signal channel to form the trigger decisions ([Ash19]). To simulate this trigger behavior as close to reality as possible, the unitless `DISCRIMINATOR_THRESHOLD` variable is used in `sim_telarray` ([Ber08], [Ber22]). To verify whether the simulation matches the observations, the intensity distribution of third-brightest pixels is compared. Schäfer's investigation shows that the default

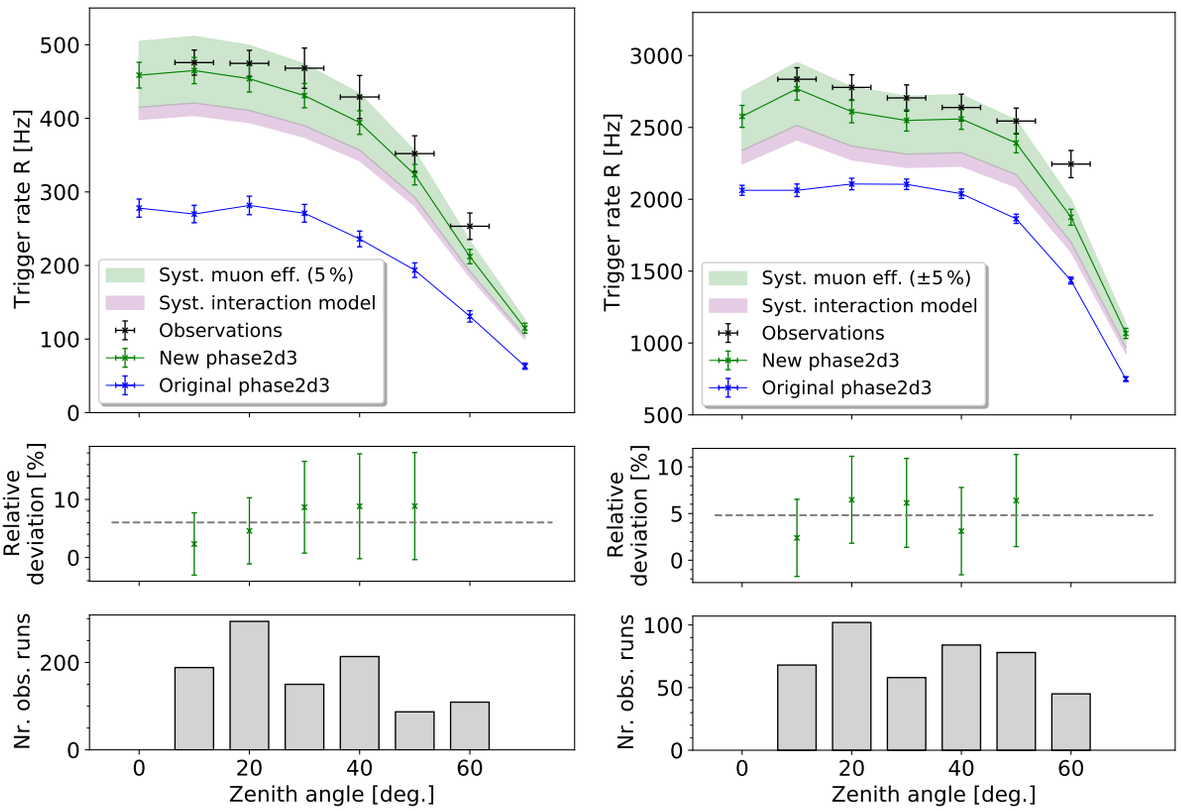

Figure V.15: Stereo trigger participation rate of CT1 (left, CT2-4 similar) and trigger rate CT5 (right) over zenith angle. The top panels show in black the rates of comparable observation, in green the rates from simulations with the validated configuration, and in blue the rates from simulations with the pre-validation configuration. The rates with the validated configuration show additionally systematic uncertainty bands due to the muon efficiency and due to the hadronic interaction model. The center panels yield the deviations of each zenith angle step between 10° and 50°, together with the mean (dashed grey). The bottom panel shows the number of observation runs used to derive each data point for the observations data. Plots taken from [Sch23].

(def., that is, pre-validation) value of the `DISCRIMINATOR_THRESHOLD` results in a distribution of third-brightest pixels shifted to higher values compared to observations, i.e., that the threshold is too high. He then reduced the threshold by on average 17% until the distributions match as shown in Figure V.14, left panel.

The CT5 trigger is digital, requiring one of FC's 588 overlapping nine-pixel trigger sectors to exceed a given threshold (see Section III.1.2). In Figure V.14, right panel, it can be seen that also for FC@CT5, a slight decrease of the simulated trigger threshold of 3.7% has been necessary. Then, only a 1% uncertainty remains which is attributed to the finite bin width ([Ste23]).

Parameter	Change CT1-4	Impact CT1-4	Change CT5	Impact CT5
Optical PSF	+20%	+1%	+9%	<+1%
Aerosol level	-50%	+10%	-50%	+12%
NSB	+67%	+3-6%	+55%	+6%
Optical Efficiency	-2.4%	-15%	+8%	+23%
Trigger Threshold	-17%	+41%	-4%	+6%

Table V.3: Overview of changed parameters for CT1-4 (mean) and CT5, together with the respective impact on the stereo participation trigger rate. The parameters are listed according to their appearance in the main text.

V.4 Results and summary

V.4.1 Trigger rates

As discussed in the introduction of this chapter, the trigger rates (stereoscopic participation rate for CT1-4, mono trigger rates for CT5) are good measures to verify that simulations and real data match at the low level. The task to calculate the trigger rates and to determine the uncertainties has been led by Johannes Schäfer. This is a summary of the efforts, more detailed descriptions of each step can be found in [Sch23]. Before the MC validation, i.e., with the original simulation configuration, there has been a mismatch of up to 66% for CT1-4 and of 29% for CT5. After implementation of all changes discussed, the trigger rates match within 6% for all telescopes, as is shown in Figure V.15. Table V.3 lists the individual changes in the simulation configuration discussed in the previous section and their impact on the simulated trigger rates.

Additionally, the systematic uncertainties are much better understood. Until the investigations of the MC validation team, a general ±10% uncertainty in the simulations has been assumed. Now, the two main contributors have been identified of which the uncertainty cannot be further reduced. Firstly, there is the uncertainty in the derived muon efficiency of ±5%, as discussed above. This uncertainty propagates to a systematic uncertainty in the trigger rates of $\Delta^{\text{sys.}}_{\mu-\text{eff}} = ^{+10.1\%}_{-9.5\%}$ for CT1-4 and $\Delta^{\text{sys.}}_{\mu-\text{eff}} = ^{+6.6\%}_{-9.2\%}$ for CT5 ([Sch23]). The other contributor is the choice of the interaction model, as introduced in Section V.1.2. By default QGSJET-II is used for IACT simulations with `CORSIKA` and `sim_telarray` ([Ber22]). Using other, in principle suitable models results in up to 4% lower trigger rates (with EPOS-LHC, [Pie09]) which is consequently assumed as systematic uncertainty of $\Delta^{\text{sys.}}_{\text{mod}} = ^{+0\%}_{-4\%}$ ([Sch23]). The stated uncertainties are shown as error bands of the validated simulation in Figure V.15.

To calculate the trigger rates of each telescope, the effective area derived from the simulations is folded with the cosmic ray proton flux, multiplied by a correction for nuclei heavier than atomar hydrogen. For the proton spectrum, the Global Spline Fit (GSF) spectrum introduced in [Dem17] is used. Compared to the powerlaw approximation used before, the GSF yields more features and is therefore more precise. The correction factor has been validated separately and remains at the value used for H.E.S.S. simulations of 1.34. In order to further increase the precision, the simulated energy range has been extended. While in earlier simulations the lower limit for

proton simulations has been the lower limit of the H.E.S.S. energy range, 30 GeV, a lower limit of 14 GeV is derived below which showers do not contribute to the trigger rate at all. This simulation adaption increases the total trigger rate by $7.8 \pm 0.3\%$ ([Sch23]). Also, the simulated viewcone has been revisited which defines the maximum allowed distance of the shower impact point to the array center. As a larger viewcone increases the computation time of the simulations, it should not be too large, although this bears the risk of losing some showers. However, the previous viewcone of 5° contains 92.2% of all showers only. It is adapted to 8°, now containing 99.1% of all showers, which is deemed a good compromise between shower loss and computation time[31] ([Sch23]).

V.4.2 High level validation

Once the trigger rates obtained in simulations match the observed ones, it is meaningful to verify that higher level analysis products are consistent. For that, Steinmassl compared among other parameters the distribution of the Size of shower images from proton simulations with those from observation runs at similar zenith angle and without a strong gamma-ray source in the FoV (see [Ste23]). Matching distributions of the Size are an indicator for consistent assumptions of all parameters that influence the measured intensity, in particular the atmospheric model, the optical throughput efficiency, and the handling of background. For all telescopes, the distributions derived from simulations match those from observation runs.

Finally, a full set of IRFs and lookup tables is derived, with which the FC@CT5 data mentioned at the beginning of this chapter for the Crab Nebula is analyzed. Additionally, also the CT1-4 data obtained in the same observations are analyzed. For both analyses, a power law is fitted to the data. The results of this are shown in Figure V.16 and have originally been presented in [Ste23]. As can be seen in the figure, the data analyzed using the validated simulations matches the references clearly better than the pre-validation approach. The spectral parameters of the powerlaw model for the FC dataset are an index $\alpha = 2.472 \pm 0.012$ and a normalization at 1 TeV of $\phi_0 = (3.87 \pm 0.05) \times 10^{-11} \frac{1}{\mathrm{TeV\,cm^2\,s}}$. For CT1-4, it is $\alpha = 2.496 \pm 0.012$ and $\phi_0 = (3.66 \pm 0.04) \times 10^{-11} \frac{1}{\mathrm{TeV\,cm^2\,s}}$ at 1 TeV. Both these values match the formerly published H.E.S.S. result within the systematic uncertainty of the analysis given there ([Aha06b], see Section V.1.1). With this result, a correct reconstruction of data from the standard candle in TeV astronomy, the HAP MC validation is considered successfully completed.

The IRFs and lookup tables produced with the simulation configuration for CT5 are used in the analysis presented in Chapter VI in all parts where CT5 is involved. In that chapter, the capabilities of FC@CT5 to spectrally and morphologically resolve an extended source are demonstrated. A good match between the FC@CT5 data, older CT1-4 data that has not been target of this validation, and published data emphasizes the accuracy of the final configuration. Furthermore, the HAP MC validation is a well documented end-to-end approach that can be used to validate earlier phases of the H.E.S.S. experiment and might in future prove useful for CTA as well.

[31] Note that these containment values have been derived with the previous lower limit on the shower energy of 30 GeV and might have slightly changed. The 8° viewcone is however kept.

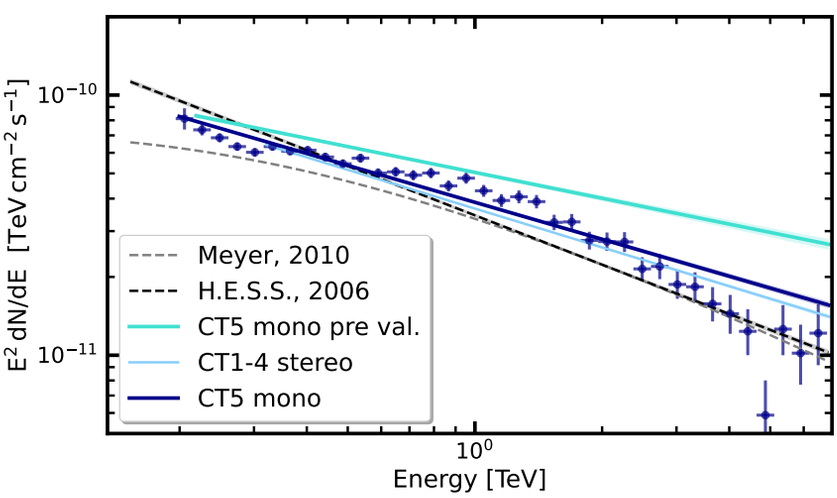

Figure V.16: Spectra of the Crab Nebula from different analyses. A powerlaw model is fitted to CT1-4 stereo and CT5 mono data from 2020. They are compared to the CT5 mono analysis before the MC validation effort on the same dataset. The published spectra of the H.E.S.S. collaboration ([Aha06b]) and of Meyer et al. are given for reference ([Mey10]). Image credit [Ste23].

VI

Analysis of HESS J1731-347 and HESS J1729-345: Performance of FlashCam@CT5 for extended sources and an energy dependence study

VI.1 Introduction

The shells of young and middle aged SNRs were expected to accelerate cosmic rays to $\geq 100\,\mathrm{TeV}$ and therefore to emit VHE gamma-rays, already before the first of these sources was detected ([Dru94]). However, it took until 2001 to detect the first SNR in TeV gamma-rays, being Cassiopeia A, observed by the HEGRA Collaboration ([Aha01]). In 2004, the shell structure of an extended SNR has been resolved for the first time, which was accomplished by the H.E.S.S. collaboration on the example of SNR RX J1713.7-3946 ([Aha04c]).

A central scientific goal of the H.E.S.S. experiment has been to perform the first survey of the galactic plane in VHE gamma-rays. This resulted in a first scan of the inner galaxy ([Aha06a]) and later in a survey of the entire galactic plane ([Abd18b]). During the scan of the inner galaxy, eight sources have been found which at the time did not yet have an unambiguous counterpart in any other wavelength ([Aha08c]) One of these sources – HESS J1731-347 – yields a tail extending to the west. The resulting irregular morphology has been interpreted as an indication of multiple sources ([Aha08c]). In the same year, further attention was drawn on HESS J1731-347 when Tian et al. detected a shell-type SNR in radio and X-rays in spatial coincidence with the main part of this source (so, not the westward-extending tail) ([Tia08]). While an almost perfect circular shell structure has been found in the radio image, the X-ray emission can only be traced back to the eastern half of the remnant ([Tia08]). Since the shape of the emission regions matches, Tian et al. assume a physical association. They explain the lack of X-ray emission from half the SNR with absorption blocking these X-rays. ^{12}CO maps of the SNR and its surrounding indicate increasing column density to the west, supporting the statement ([Tia08]). Already in their 2008 paper, Tian et al. mentioned the possibility that the gas absorbing the X-rays might be bound in molecular clouds interacting with the SNR. However, the resolution of the available radio data as well as the total amount of gamma-ray-data was not sufficient at that time to draw any further conclusion.

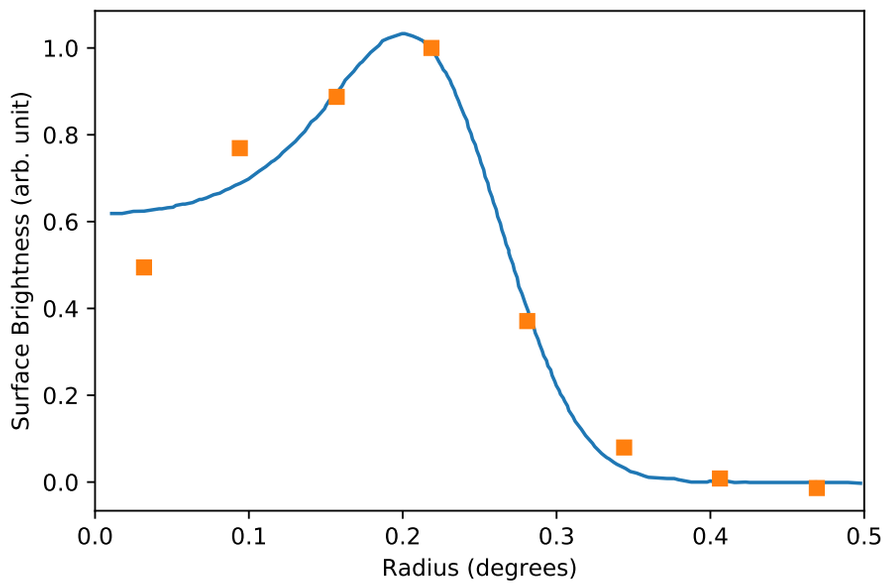

Figure VI.1: Radial profile of HESS J1731-347 from the 2011 H.E.S.S. paper (orange squares) and the best-fit shell model (blue line). Figure recreated from [Abr11] using WebPlotDigitizer version 4.6 ([Roh22]).

In the following years, further H.E.S.S. observations were triggered. In 2011, they resulted in the detection of a shell structure, spatially coincident with the radio SNR. This confirmed the association assumed by Tian et al. ([Abr11]). In that work, the H.E.S.S. collaboration announced to have found two distinct sources of gamma-ray emission in the formerly discovered HESS J1731-347 region: one is the SNR itself, the second is named HESS J1729-345. The nature of the latter remained unclear.

Within [Abr11], extensive modeling of the spatial and spectral properties of HESS J1731-347 is presented. After confirming the homogeneity of the emission with respect to the position angle, a radial profile was produced (see Figure VI.1) to derive a model of the morphology. Statistically favored is a shell with a best-fit radius of $0.27° \pm 0.02°$ ([Abr11]). Note that this radius is not the outermost radius as can be seen in Figure VI.1, but it is somewhere on the falling edge of the emission. The thickness of the shell cannot be fully constrained. However, the observed emission can be described with a thin but unresolved shell. For the thickness, an upper limit of 0.12° had been derived ([Abr11]). This establishes HESS J1731-347 as the fourth ever discovered SNR with a spatially resolved shell structure in TeV gamma-rays.

To derive a spectrum of HESS J1731-347 a circular region of $r = 0.3°$ is used. As a center, the CCO position is chosen ($\alpha_{\mathrm{J2000}} = 17^{\mathrm{h}}32^{\mathrm{m}}03^{\mathrm{s}}$, $\delta_{\mathrm{J2000}} = -34°45'18''$) ([Abr11]). After gamma-ray background estimation with the multiple reflected regions technique (see Section II.2.2), a power-law spectral model (see Paragraph VI.3.3) is fitted on the data in the energy range from 0.26 to 30 TeV. They obtain a photon index of $\Gamma = 2.32 \pm 0.06$, a decorrelation energy of $E_0 = 0.783\,\mathrm{TeV}$ and a normalization of $(4.67 \pm 0.19) \times 10^{-12}\,\frac{1}{\mathrm{TeV\,cm^2\,s}}$ at $E = E_0$. This results in an integrated flux of $(6.91 \pm 0.75) \times 10^{-12}\,\frac{\mathrm{erg}}{\mathrm{cm^2\,s}}$ in the energy range from 1 to 10 TeV.

The H.E.S.S. collaboration also derives a distance of $\sim$ 3.2 kpc to the ^{12}CO region that is thought to be responsible for the partial absorption of the shell's X-ray emission. This is adopted as lower limit for the distance of the SNR. HESS J1731-347 is the remnant of a core collapse SN with the CCO XMMU J173203.3-344518 ([Klo13]), which implies that the SNR is located in a star forming region and therefore in one of the galaxy's spiral arms. Possible distances would then be close to the lower limit of 3.2 kpc (Scutum-Crux arm), a medium distance of 4.5 kpc (Norma-Cygnus arm), close to the galactic center (3 kpc Expanding arm) or far-distance solutions, like the Sagittarius arm at 12 kpc.

Fukuda et al. suggest a localization of HESS J1731-347 in the 3 kpc arm, close to the galactic center ([Fuk14]). They base their conclusion on observations of hydrogen, traced with ^{12}CO and H I observations. They study the abundance of gas by comparing various velocity channels in the ranges from -90 to -70 $\frac{\text{km}}{\text{s}}$ and -40 to 0 $\frac{\text{km}}{\text{s}}$ (four channels per range, each with a width of 5 $\frac{\text{km}}{\text{s}}$). Apparently by visual inspection, they identify "an H I hole toward the SNR which shows a good correspondence with the outer boundary of the SNR shell" [Fuk14] in the channel -80 to -75 $\frac{\text{km}}{\text{s}}$. In the CO maps of the channels from -90 to -80 $\frac{\text{km}}{\text{s}}$, they identify two peaks that might correspond to the regions of highest excess in the northeast and west of the gamma-ray image ([Fuk14]). In the velocity channel maps from -40 to 0 $\frac{\text{km}}{\text{s}}$, no peculiarity in the H I distribution can be seen. The ^{12}CO map from -20 to -10 $\frac{\text{km}}{\text{s}}$ shows a dense structure that was at the time the paper was written supposed to cause the absorption of X-rays from the SNR shell, a suspicion that got confirmed in 2017 by Doroshenko et al. ([Dor17]). Apart from that, no obvious connection to the SNR shell itself can be drawn. From their analysis, they derive a distance of HESS J1731-347 of 5.2 to 6 kpc ([Fuk14]).

However, when looking from today's perspective at the wider picture, this conclusion cannot hold. Firstly, the hole in the H I velocity maps might be by pure chance, as similar sized holes can be found in the direct vicinity without an SNR being observed there (cf. Figure 3, top in [Fuk14]). Secondly, while the H I hole admittedly matches the SNR shape mostly, there is significant H I abundance in the northeast of the projected SNR that extends to the SNR center well beyond the PSF of the H.E.S.S. analysis (cf. Figure 1, top, third panel from left in [Fuk14]). Regarding the CO maps, the reported peaks exist in spatial coincidence with the gamma-ray peaks. However, similar peaks that might explain the emission from HESS J1729-345 are not visible in the specified velocity range, but in the range from -20 to -10 $\frac{\text{km}}{\text{s}}$ (cf. Figure 1 and Figure 2, bottom panels in [Fuk14]). This contradicts multiple hints suggesting a connection between HESS J1731-347 and HESS J1729-345 (presented below). Also, further evidence for such a connection will be presented in Section VI.4.

So do physical properties of the SNR that are directly derived from the distance to the SNR. For example, a distance of about 5 kpc would imply a physical size of HESS J1731-347 of about 50 pc (compared to $\sim$ 15 pc of other SNRs) and a luminosity that is about a factor ten higher in magnitude than RX J1713.7-3946, making HESS J1731-347 the brightest shell SNR in TeV gamma-rays ([Abr11]). While the large size would be easily compatible with a higher age, this would constrain the expected gamma-ray luminosity way below such values (see e.g. [Ptu05]), in particular leptonic emission which in the model of Fukuda et al. should contribute about

20% of the gamma-ray flux ([Fuk14]). Therefore, the assumption from [Abr11] appears more realistic, where the distance to HESS J1731-347 is expected to be around the lower limit of 3.2 kpc. Modeling the spectrum of the neutron star in the center of HESS J1731-347, commonly believed to be the central compact object of the SNR, Klochkov et al. disfavored a distance of more than 4.5 kpc as well ([Klo13]).

Also Doroshenko studied HESS J1731-347 with varying collaborators ([Dor17], [Dor22]). In [Dor17], they use a larger dataset in radio and X-rays, compared to those of [Tia08], [Abr11] and [Fuk14]. They unambiguously confirm the spatial coincidence of absorbed X-ray emission and ^{12}CO containing regions at 3.2 kpc, and therefore the lower limit on the distance to HESS J1731-347. Additionally, they connect observations in the infrared and optical extinction maps with the known SNR-shell. In multiple positions of the western edge of the SNR, they find structures which are aligned with the western edge of the SNR ([Dor17]). This leaves only two possible scenarios: either, the structures are only in the projection well aligned with the SNR, but still lay in the foreground([Dor17]). Therefore, they tend towards the other possibility: the structures are part of a molecular cloud interacting with the SNR. In this case, the SNR-shock would have developed into the molecular cloud, its impact causing the structures observed. The fact that no distortion of the circular shapes of the radio and the TeV shells is observed, indicates that such an interaction can only have started recently ([Dor17]). Eventually, Doroshenko et al. solved the puzzle of the distance of HESS J1731-347 in favor of the low distance solution ([Dor22]). As the CCO of the SNR is most likely part of a binary system ([Dor16]), they use the companion to constrain its distance with to (2.5 ± 0.3) kpc, using Gaia parallax measurements ([Dor22]). This is then also the distance to the CCO and thus to the entire SNR. Within uncertainties, the distance agrees with the most recent study on the gas clouds forming the lower limit ([Max18]) and is therefore taken as the actual distance to HESS J1731-347.

In MC simulations, Cui et al. investigate possible interactions of the SNR with the surrounding molecular clouds, assuming a distance of 3.2 kpc ([Cui16]). In particular, they discuss whether a scenario is plausible that the unidentified TeV-source HESS J1729-345 consists of molecular clouds, illuminated by CRs from HESS J1731-347.

Following the model of CR injection to the vicinity of SNRs by Ptuskin and Zirakashvili ([Ptu05] [Ptu08]), CR can escape SNRs dependent on their momentum p. The spectrum in the direct vicinity follows (during the adiabatic/Sedov stage of SNR evolution) a power-law of the form p^{-4}, for particles in the energy range between ~ 10 GeV and the maximum momentum $p_{\mathrm{max}}(t)$. The maximum momentum is the momentum a particle can gain before it inevitably escapes the shock front and therefore is correlated to the velocity of the shock. This implies that the most energetic particles leave the shock first, while with growing age (and decreasing shock velocity) only less energetic particles get injected into the surrounding. However, as the overall particle spectrum is very steep in momentum, at later times the number of injected particles increases.

Cui et al. modeled the surrounding of HESS J1731-347 in three dimensions by assuming a molecular cloud (*MC J1729*[32]) very close to the SNR, at 30.7 pc, and a second, smaller but

[32]Note that Cui et al. use the abbreviation "MC" for "Molecular Cloud", rather than "Monte Carlo" as it is done in this thesis. However, the names of the molecular clouds are kept here as introduced in [Cui16] and [Cui19]

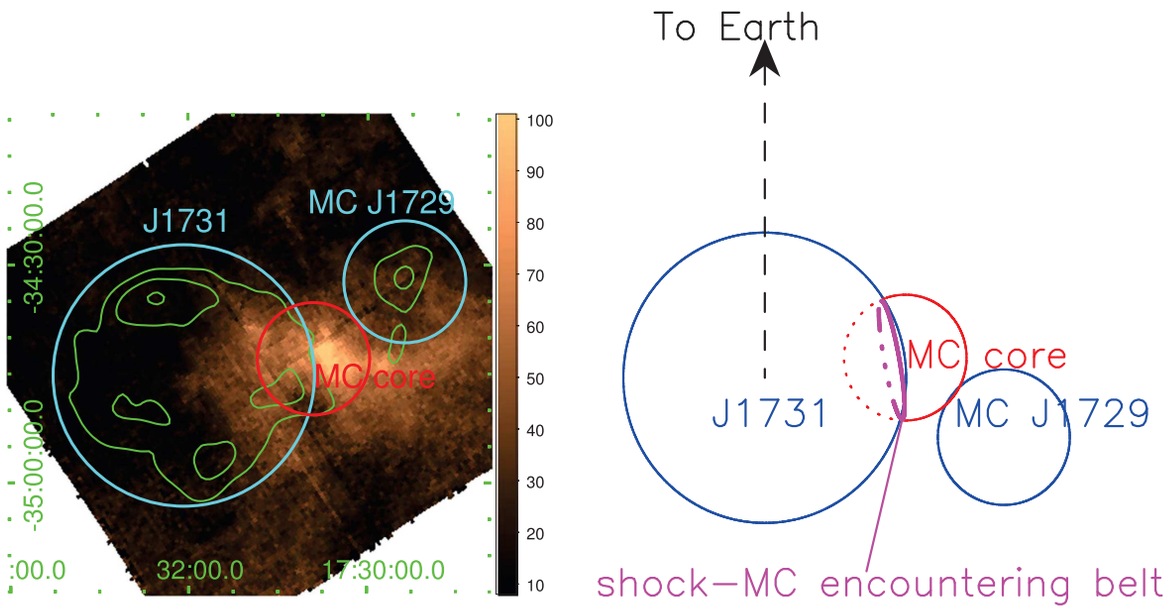

Figure VI.2: Left: Model of the HESS J1731-347 and HESS J1729-345 region as modeled by [Cui19], plotted on a CO map in the velocity range $V = -5$ to $-25\,\frac{\mathrm{km}}{\mathrm{s}}$ by [Max18] and with the TeV contours (green) from [Abr11]. The velocity range corresponds to gas in the Scutum-Crux arm. The color bar describes the CO line intensity in units of $\frac{\mathrm{K\,km}}{\mathrm{s}}$. Right panel: sketch of the applied model looked at from bottom. The line of sight towards Earth is indicated by the arrow. Image source: [Cui19].

denser cloud (*MC core*) in the foreground at 100 pc distance to the SNR ([Cui16], cf. Figure 1 in [Cui16] for illustration). Figure VI.2 shows a slightly different model (developed afterwards) in which MC core is located closer to HESS J1731-347. The simplest solution to explain the observational results with their model is a progenitor star of about $20\,M_\odot$ with the SNR residing still inside the main sequence bubble of the progenitor star. This scenario allows high shock velocities ($\geq 1000\,\frac{\mathrm{km}}{\mathrm{s}}$) until present, necessary to fulfill a dominantly leptonic emission scenario suggested by upper limits on GeV emission reported by [Ace15b]. Further, the localization of the molecular clouds close to the SNR and at 100 pc distance, respectively, deliver the observational result of a bright HESS J1729-345 region and a dimmer emission region at the position of MC core between HESS J1731-347 and HESS J1729-345 ([Cui16]).

In a follow-up work on his 2016 paper, Cui et al. tried to understand the emission from the HESS J1729-345 region based on more recent data from the Fermi satellite ([Cui19]). Based on a possible GeV point source at the western edge of the SNR shell they suggest MC core to be much closer to the shell than modeled in [Cui16]. Actually, they suggest the SNR might have collided with that cloud, immediately releasing the CR hadrons confined in the shock. The geometry of this model system is shown in Figure VI.2, together with the shape of HESS J1731-347 and HESS J1729-345 following to [Abr11]. The figure yields also the integrated CO map from [Max18] that matches the close distance solution, i.e., in the Scutum-Crux arm. The modified scenario would lead to illumination of MC core close to the SNR shell by these freshly released CRs in the

for consistency.

GeV band, while MC J1729 as well as the parts of MC core farther away from the shell would only be illuminated by very high energetic CRs that have diffused from the SNR at earlier times. In their favored scenario, the TeV-spectra both of MC core and MC J1729 peak at about 2 TeV with similar amplitudes before ending in an exponential cutoff, with the MC core spectrum dropping slightly faster than that of MC J1729.

Note that in both models, the one described in [Cui16] and the one from [Cui19], the explanations for the expected emission from MC J1729 and from MC core are not mutually dependent: if one of the predictions is falsified this does not necessarily allow to make a statement on the other assumption. Further note that the existence and position of MC J1729 is only based on the estimated source HESS J1729-345 as introduced by the H.E.S.S. collaboration in [Abr11].

In his PhD thesis [Cap19], Capasso presents investigations whether the TeV gamma-ray emission seen in the west of HESS J1731-347 and farther outwards, up to HESS J1729-345 is correlated to the density of molecular clouds (traced with updated ^{12}CO maps by [Max18]) in spatial coincidence. Two contradicting scenarios are tested. The emission might solely originate from the molecular clouds at a fixed distance (tested: 3.2 kpc, 4.5 kpc and 5-6 kpc). In particular the 3.2 kpc solution supports the theory proposed in [Cui16] (and the later [Cui19]) of hadrons escaping from the SNR interacting with the nearby molecular clouds (*active scenario*, [Cap19]). The other scenario is that TeV gamma-rays outside HESS J1731-347 are the cumulative emission from molecular clouds along the line of sight, interacting with background CRs (*passive scenario*). While the correlation study alone favors the passive scenario (r=0.54, p=1.5×10^{-5}), diffuse CR fluxes much higher than the one observed at earth's position would be required to explain the gamma-ray flux. Among the fixed distance solutions, the 3.2 kpc one is favored, though being less correlated than the passive scenario (r=0.40, p=2.4×10^{-3}). However, it is known from [Cui16] and [Cui19] that this scenario is capable of producing gamma-ray fluxes in the observed order of magnitude. Capasso himself admits that the observed VHE gamma-rays which seem to originate from the SNR region might be contaminated by emission from the molecular cloud ([Cap19]). This might be a reason why the passive scenario in that correlation study is statistically favored over the physically more plausible active scenario. He concludes that his analysis is not capable of confirming any of the two scenarios ([Cap19]).

In the following, Section VI.2 introduces the datasets used for the analyses presented further on in the chapter. These analyses contain firstly the science verification of FlashCam@CT5 for extended sources in Section VI.3. It is shown that the CT5-telescope, equipped with a new FlashCam-camera (see Chapter III), is capable of reproducing the results of morphological and spectral analyses of the H.E.S.S. collaboration, as published in [Abr11]. As the analysis is performed with Gammapy, using updated calibration procedures and a different analysis algorithm compared to that used in [Abr11], also the archival CT1-4 data is analyzed in Section VI.3 for reference. Section VI.4 contains a study that investigates energy dependence of the TeV emission in HESS J1729-345. It disentangles HESS J1729-345 into two distinct sources, separated spatially and with different spectra. In that section, also the position of HESS J1731-347 can be fixed in the Scutum-Crux arm, for the first time by using TeV data only. The results will further be discussed with regard to the origins of the gamma-ray emission from HESS J1729-345 and in particular the

results of [Cui16], [Cui19] and [Cap19]. Eventually, Section VI.5 briefly summarizes the content of this chapter.

VI.2 Data selection

The vast majority of VHE observations on HESS J1731-347 was made during the H.E.S.S. I era before the installation of CT5, and the early H.E.S.S. II era before the camera upgrade of CT1-4. This is also the dataset on which [Abr11], [Cui16] and [Cap19] based their results. Additional data was obtained in 2020 and 2021, after the installation of FC to CT5. For the science verification of FC (see Section VI.3), obviously the FC data is used. Additionally, the CT1-4 data prior to the camera upgrade is re-analyzed. This serves firstly as proof of principle for the science verification. Since the analysis algorithms have improved since the publication of [Abr11] and the time of creating this work, this re-analysis will also give more precise uncertainty estimates on the properties of HESS J1731-347. However, in the course of this chapter also new results are presented. The data obtained with CT1-4 and the upgraded cameras has not been available for analysis with Gammapy at the time the analyses have been conducted and is therefore excluded.

Further, it is important to ensure a good quality of the data. The time when HESS J1731-347 was observed with FC coincides with the biomass-burning season ([For18]) in south western Africa. The aerosols from these bush-fires lead to an increased opaqueness of the lower troposphere, reducing the amount of Cherenkov light reaching the telescopes at the H.E.S.S. site (see Section V.2 and [Hol22]). While algorithms to account for this are in development, they are not ready for wide use at the time of writing this thesis. Therefore, the FC data set is selected such that the atmospheric conditions the observations were conducted under match those assumed in the MC detector simulations. This allows to obtain reasonable results without correcting for the varying, actual conditions as these remaining variations are small compared to systematic uncertainties and can therefore be neglected.

The CT1-4 observations were conducted during different times and over a range of eight years. However, to exclude possible uncertainties due to changes in the atmosphere and to ensure comparability of the two datasets, the same criteria as for the FC data are applied.

In H.E.S.S., a dedicated software tool (`haptools.runselector`) can assist with the selection of observations fulfilling dedicated criteria. Using this tool all runs are selected that

- were pointed on a position within 2° around 262.5500° right ascension and −34.5933° declination, the center of HESS J1731-347 as reported within the software tool.
- were conducted before 2016 (CT1-4 with old cameras) or after November 1st, 2019 (FC@CT5), respectively.
- contain at least three of the small telescopes (CT1-4 with old cameras) / contain CT5 (FC@CT5).
- fulfill the HAP *spectral* criteria. These ensure the aforementioned good atmospheric conditions as well as very stable operation of the system.

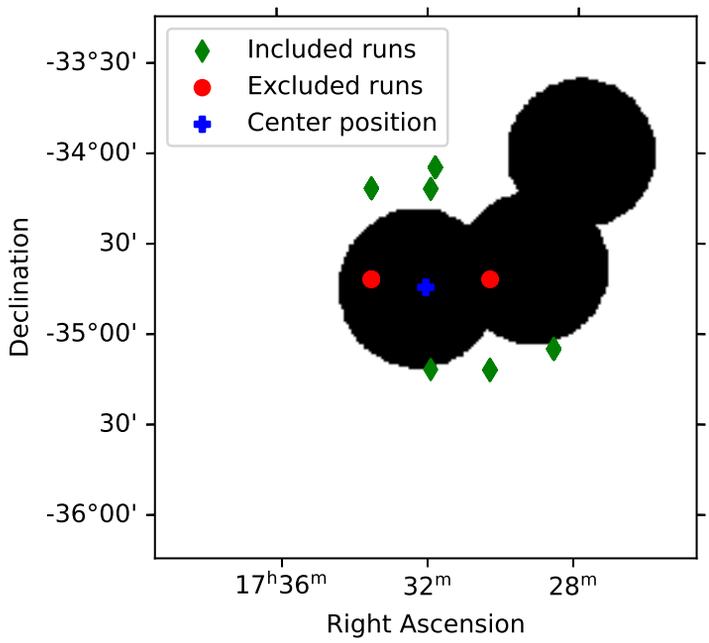

Figure VI.3: Exclusion regions used for the FC science verification. The red points show pointing positions of runs that are excluded for the spectral analysis as described in the text, the green diamonds show the pointing positions of those runs which are used in both, the spectral and the spatial analysis. The blue plus indicates the center of HESS J1731-347 assumed for the science verification.

This software assisted run-selection results in 140 runs for CT1-4 with a livetime of 231 443 s or ≈ 64.3 h and 57 runs for FC, resulting in a livetime of 94 177 s or ≈ 26.2 h.

However, for the spectral analysis of FC data the number of usable runs is reduced: eight runs were pointed to regions very close to HESS J1731-347. Therefore, no OFF-regions laying outside the exclusion regions defined for the analysis (see Paragraph VI.3.3 for details) could be found to create the reflected-regions background, making these runs unusable for spectral analysis. Figure VI.3 shows the exclusion regions applied in the FC science verification together with the pointing positions of the observation runs and an indication whether they are used in the spectral analysis or not. Gammapy excludes these runs automatically. This leads to 49 runs taken into account for the spectral analysis, with a total livetime of 81 554.0 s, corresponding to ≈ 22.7 h.

All analyses presented in this chapter are conducted using Gammapy (version 0.20) [Dei17, Don22], an open-source tool for the high level analysis of gamma-ray astronomy. This requires the data to be stored in the FITS data-format. For the CT1-4 dataset the FITS files are ready-to-use available on the Heidelberg computing cluster. As FC data analysis is still in a preliminary state, the FITS files must be produced manually for each individual analysis. Additionally, background model files must be included which are for FC@CT5 data currently produced and provided on request only[33], following the approach presented in [Moh19].

[33]Thanks at this point to Andreas Specovius for providing the background models.

Table VI.1: Position and size of the exclusion regions used for the background estimation. The values are taken from the current H.E.S.S. standard analysis. Contrary to the analysis presented in Section VI.4, no adjustments have been made to maintain the best possible comparability of the results.

Region	Center	Radius
A	RA: 17h32m16s DEC: $-34°45'44''$	0.44°
B	RA: 17h29m11s DEC: $-34°38'57''$	0.42°
C	RA: 17h27m55s DEC: $-34°0'53''$	0.41°

VI.3 Science verification of FlashCam for extended sources

VI.3.1 Motivation and approach

Following the installation of the advanced FC prototype into CT5 in 2019, multiple steps were taken to verify the functionality of the camera. Already before the validation of Monte Carlo simulations (see Chapter V) was finalized, the conclusion was drawn that the camera works up to expectations (see Chapter III and [Püh21]). However, a pending step in this science verification is the analysis of an extended source and the proof that key parameters such as flux, spectrum and morphology of such a source could be reproduced.

Due to its morphology, HESS J1731-347 is a suitable target for such a verification study. On the one hand, the extension of the SNR exceeds the PSF of CT5 with FC and is structured with its shell-type morphology ([Abr11]). On the other hand, the source is still small enough to be confined well in the FoV of the instrument, hence it is possible to observe and resolve the entire structure within a reasonable amount of observing time (compared to, e.g., the galactic center). For this, observations of HESS J1731-347 were conducted in 2020 and 2021 with the H.E.S.S. experiment. As explained in Section VI.2, the CT1-4 data taken prior to the camera upgrade are re-analyzed using the same configuration in order to have comparable results as well as a crosscheck of the high level analysis.

In the following sections the science verification and its results are presented. Section VI.3.2 covers the spatial analysis and Section VI.3.3 the spectral analysis. In each section, the respective data reduction process is described as well as the model to be fitted at the data. Finally, Section VI.3.4 summarizes this science verification.

VI.3.2 Spatial analysis

Data reduction

Data reduction in Gammapy comprises the reading and processing of FITS files before the individual science products are created. For the spatial analysis, the events are binned on maps with dimensions of $3° \times 3°$ and a binsize of 0.01°. Center of the maps is the CCO of HESS J1731-347

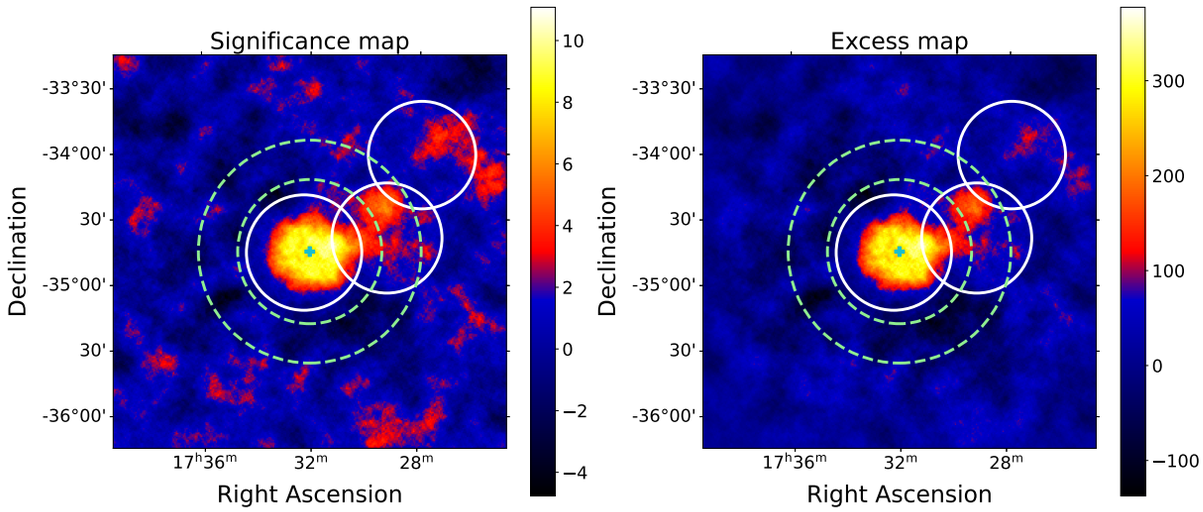

Figure VI.4: Significance (left) and excess map (right) for the CT1-4 dataset. The cyan cross in the center of each map denotes the central position of HESS J1731-347. The white circles are the edges of the exclusion regions for the background estimator, the green dashed lines indicate the edges of the ring exclusion region.

at (RA: 17h32m03s, DEC: $-34°45'18''$). This geometry follows [Abr11] to obtain comparability of the results. For the FC data, all events with a reconstructed energy from 0.1 to 10 TeV are taken into account. The CT1-4 data uses all events from 0.25 to 30 TeV as was done in [Abr11]. While the energy range for the CT1-4 data is taken from [Abr11], the FC energy range was chosen after an iterative process, maximizing the signal-to-noise ratio of the analysis and the maximum significance over background of the resulting significance maps. Binsize is 0.01° for both, the CT1-4 and the FC dataset.

Once the events are binned on the maps, the background must be estimated and consecutively subtracted. As described in Section II.2.2, the ring background method is used in a spatial analysis. Here, a ring of inner radius 0.55° and width 0.3° is applied around the center as OFF-region. Three exclusion regions are extracted from the H.E.S.S.-internal analysis configuration and comprise three circles. Their coordinates are given in Table VI.1.

After removal of the background, sky maps are produced from the counts maps showing spatially resolved significance and excess. These maps are shown in Figure VI.5 for the FC dataset and in Figure VI.4 for the CT1-4 dataset, respectively.

To be able to derive meaningful conclusions from the visual inspections of sky maps, it is crucial to take the gamma-ray acceptance into account. The gamma-ray acceptance, i.e., the probability to detect a signal event, varies within the FoV of the camera. Without corrections, there would always be an excess close to the center of the FoV and a lack of events at the edges, even without a gamma-ray source within the FoV. However, the background model files that are incorporated in the data reduction employ a model for the gamma-ray acceptance based on archival H.E.S.S. data ([Moh19]). Therefore, the gamma-ray acceptance must not be further considered.

To allow a reasonable comparison of the spatial analysis with [Abr11], masking of the sky-maps is necessary. To avoid contamination of their results on HESS J1731-347 from the HESS J1729-

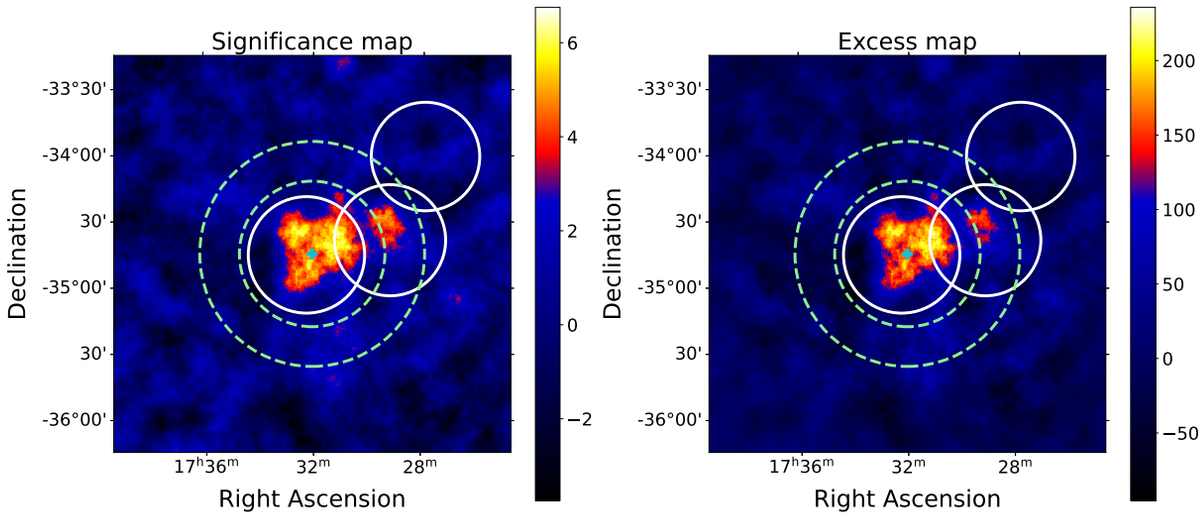

Figure VI.5: Significance (left) and excess map (right) for the FC dataset. The colorbar is stretched proportional to the square-root of the value of each bin in order to obtain a good visibility of regions with high significance/excess. The cyan cross in the center of each map denotes the central position of HESS J1731-347. The white circles are the edges of the exclusion regions for the background estimator, the green dashed lines indicate the edges of the ring exclusion region.

345-region, a triangle-shaped area is excluded from the analysis in [Abr11]. This is recreated following the reported description: One corner of the triangle is located in the center of the map, i.e., the center of HESS J1731-347, one arm points horizontal to east and the second arm is directed to the north-east, with an opening-angle of 40° between them. For illustration, significance and excess map of the CT1-4 dataset after application of this mask are shown in Figure VI.6. The FC sky-maps are treated equally. Then, both datasets are ready for further analysis.

Spatial model

In the 2011 paper, the spatial fit is performed by extracting a radial profile from the (masked) counts map and fitting a shell model to it. The shell emits uniformly, and is defined by an outer radius r_{out} and a width. It is projected on the sky and folded with the gamma-ray PSF, which has been derived to be $r_{68\%} = 0.06°$ for that analysis ([Abr11]). In Gammapy, two spatial models describing such a shell are predefined in the user interface. They both refer to the same backend model, describing a projected, uniformly radiating shell. This shell is defined by Equation VI.1[34] where the parameters r_{in} define the inner and r_{out} the outer radius of the emission region. Further, $\vec{p}$ is a point to be evaluated on the projected shell. It is defined in spherical coordinates as $\vec{p} = \vec{p}(lon, lat)$. θ is the sky separation between the center of the shell, $\vec{p_0}$ (defined by the two model parameters lon_0 and lat_0: $\vec{p_0} = \vec{p}(lon_0, lat_0)$), and $\vec{p}$.

[34] A typo in [Gam22] was corrected in Equation VI.1: For the second case, the documentation states "for $r_{\text{in}} \leq \theta < r_{\text{out}}$". However, the source code evaluates to "≤" twice.

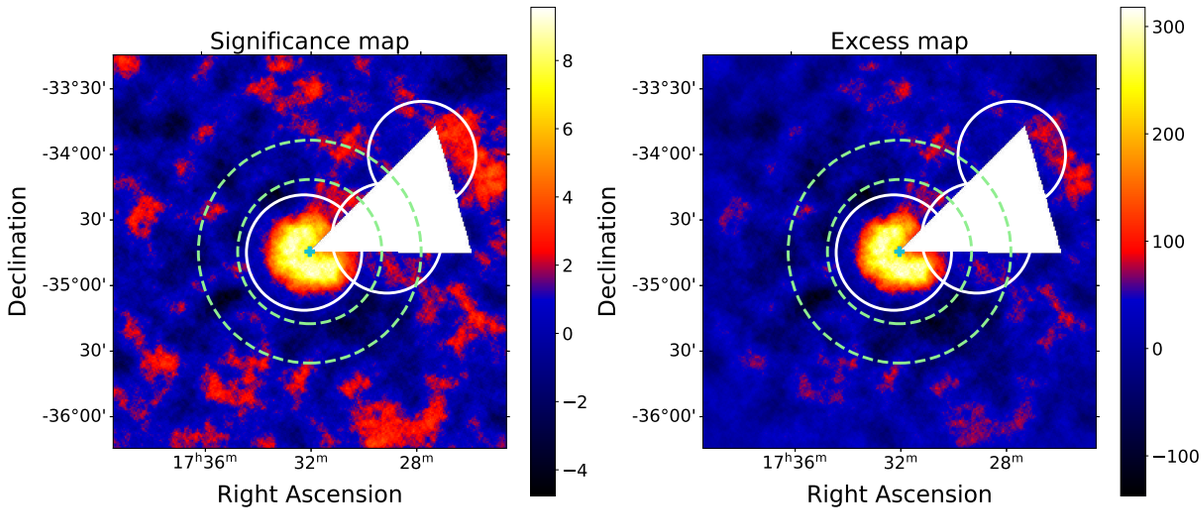

Figure VI.6: Significance (left) and excess map (right) for the CT1-4 dataset after application of a mask (white triangle) to exclude contamination of the image from HESS J1729-345. As in Figure VI.4, the cyan cross denotes the center of HESS J1731-347, the white circles are the edges of the exclusion regions for the background estimator and the green dashed lines indicate the edges of the ring exclusion region.

$$\phi(\vec{p}) = \frac{3}{2\pi\left(r_{\text{out}}^3 - r_{\text{in}}^3\right)} \cdot \begin{cases} \sqrt{r_{\text{out}}^2 - \theta^2} - \sqrt{r_{\text{in}}^2 - \theta^2} & \text{for } \theta < r_{\text{in}} \\ \sqrt{r_{\text{out}}^2 - \theta^2} & \text{for } r_{\text{in}} \leq \theta \leq r_{\text{out}} \\ 0 & \text{for } \theta > r_{\text{out}} \end{cases} \tag{VI.1}$$

The parametrization of r_{in} and r_{out} is the only difference between the two models available (named `ShellSpatialModel` and `Shell2SpatialModel`). In `ShellSpatialModel` the free parameters are r_{in} (named `radius`) and `width`. r_{out} is then defined as $r_{\text{in}} + $ `width`. Contrary, in `Shell2SpatialModel` the parameter describing the radius is r_{out} (named `r_0`) and the shell width is defined via the relative width parameter $\eta \in (0, 1]$. It is given by

$$\eta = 1 - \frac{r_{\text{in}}}{r_{\text{out}}}. \tag{VI.2}$$

Vice versa, r_{in} can be retrieved as

$$r_{\text{in}} = (1 - \eta) r_{\text{out}} \tag{VI.3}$$

In [Abr11], the used parameters are a radius, most consistent but not identical with r_{out} and the (absolute) width. While the former is well constrained, the latter is given as an upper limit only. To allow easier comparison of the results, `Shell2SpatialModel` was therefore chosen for the spatial description of HESS J1731-347 within this work.

However, the upper limit of the shell width must be transformed into an upper limit for η to allow a comparison in the following.

Table VI.2: Results of the spatial analysis of the FC science verification. The values are parameters of the spatial model of an uniformly emitting shell, as given by Equation VI.1 for the respective dataset. The values of the FC and the CT1-4 dataset are derived in this work, those of [Abr11] are given for comparison.

Dataset	r_0 or r_{out}	`width`	η
FC	$0.314° \pm 0.014°$	$0.12° \pm 0.06°$	0.39 ± 0.17
CT1-4	$0.300° \pm 0.006°$	$0.14° \pm 0.02°$	0.45 ± 0.07
[Abr11]	$0.27° \pm 0.02°$	$\leq 0.12°$	≤ 0.44

$$\eta = 1 - \frac{r_{\text{in}}}{r_{\text{out}}} = \frac{width}{r_{\text{out}}} \xrightarrow[r_{\text{out}} = 0.27°]{width \leq 0.12°} \eta \leq 0.44 \tag{VI.4}$$

When fitting the shell model to the data, lon_0 and lat_0 are fixed to the center position used in [Abr11]. This mirrors the 2011 approach, as deriving the shell parameters via a radial profile implies a fixed center. The parameters r_0 and η remain free to be fitted to the data.

Results

When fitting the model described by Equation VI.1 to the CT1-4 data, the obtained best fit result is $r_{\text{out}} = 0.300° \pm 0.006°$ and $\eta = 0.45 \pm 0.07$. Converting η leads to a shell-width in units of degrees of $0.14° \pm 0.02°$. Fitting the shell model to the FC data returns an outer radius of $r_0 = 0.314° \pm 0.014°$ and a relative width of the shell of $\eta = 0.39 \pm 0.17$. This corresponds to an absolute width of $0.12° \pm 0.06°$. Therefore, the FC data matches the re-analyzed CT1-4 data well within the respective uncertainties.

Comparing the results obtained in this work with the values reported in [Abr11], one finds that the outer radius of the shell does not match within uncertainties. However, as elaborated in Section VI.1, the radius given in the 2011 H.E.S.S. paper does not correspond to the outer radius as defined in Equation VI.1. It is actually slightly smaller than it would be if defined similarly. Deriving an outer radius beyond which no emission remains from Figure VI.1 yields a comparable value as derived in the present analyses. The width of the shell derived with the FC data and the re-analysis of the CT1-4 data matches the upper limit stated in [Abr11] within the uncertainties. This applies to both, the absolute value in units of degrees and the relative width η. Consequently, this part of the verification is considered successful.

The relationship of the two fitted parameters r_0 and η is visualized in their joint confidence surface plots in Figure VI.7. Plotted onto the $\sqrt{TS}$-surfaces are the 1σ, 2σ and 3σ contours of the respective analysis, visualizing the already mentioned correlation between r_0 and η. For interpretation of these contours, it must be taken into account that in two dimensions, 1σ has a probability coverage of 39.3%, 2σ of 86.5% and 3σ of 98.9%.

In the plots, the best fit values for FC (red) and CT1-4 (cyan) are marked together with the statistical uncertainties of the corresponding fit. In orange, the upper limit of η together with the best fit radius and its statistical uncertainty from [Abr11] is plotted. The left plot in Figure VI.7 shows the $\sqrt{TS}$-surface of the CT1-4 analysis, on the right is the $\sqrt{TS}$-surface of the FC analysis.

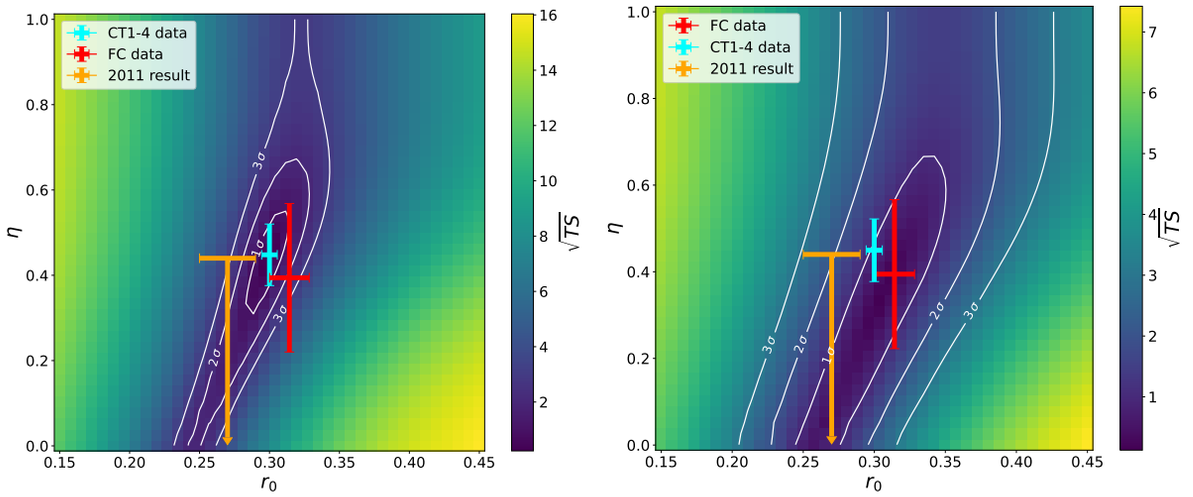

Figure VI.7: Confidence contour plots of the spatial model parameters for the CT1-4 dataset (left) and the FC dataset (right). On the x-axis are outer radii r_{out} of the shell model from 0.15° to 0.45°, on the y-axis is the parameter η in its whole possible range from 0 to 1. The best fit result and the statistical uncertainties of the fit of the CT1-4 data is marked in cyan, those of the FC data in red. The white lines denote the two-dimensional confidence contours of the respective analysis. In orange, the derived upper limit of η is shown for the results from [Abr11] at the best fit value of the radius.

FC@CT5 has an intrinsically worse PSF than the four stereoscopically operating telescopes CT1-4 together, and additionally, the total livetime of the FC dataset is only about 40% that of the CT1-4 dataset. Therefore, it is not surprising that the contour lines are broader the uncertainties larger.

Common in both confidence contour plots is the trend that η is less constrained towards lower values and in particular less constrained than r_{out}. This underlines the conclusion of [Abr11] that the observations suggest a spatially unresolved but thin emitting SNR shell.

VI.3.3 Spectral analysis

Data reduction

For the spectral analysis, the data reduction is carried out differently than for the spatial analysis. Focus is laid on reconstructing the energy of all events within the predefined ON-region. No sky maps are produced. All data outside the ON-region is ignored, except for background estimation. Following [Abr11] for comparability, the ON-region is centered at the position of the CCO and has a radius of 0.3°. The CT1-4 dataset uses events with reconstructed energies from 0.26 to 30 TeV, following [Abr11]. The FC dataset is analyzed from 0.16 to 7 TeV, taking into account the different effective areas of CT1-4 and CT5, respectively.

To estimate the background, the reflected regions background method is applied (see Section II.2.2 and [Ber07]). The same three exclusion regions as for the spatial analysis are applied, given in Table VI.1. No further masking is necessary following [Abr11], as they assume all events within the innermost 0.3° to come directly from HESS J1731-347. As will be shown in Figure VI.9

in the results section of the science verification (Section VI.3.4), this assumption is reasonable and will therefore be adapted here.

Within a region of such an extension, the IRF (in particular, the effective area) changes. Therefore, in the definition of the `SpectrumDatasetMaker`, the flag `use_region_center` must be set to `False`. This has the effect that IRF will be averaged over the entire On-region and the average value is considered. Otherwise, in the analysis of a point-like source, the IRF of the center of the On-region is applied to the entire On-region.

Model

The model used by the H.E.S.S. Collaboration for the spectrum of HESS J1731-347 is a power-law spectral model of the form

$$\frac{\mathrm{d}N}{\mathrm{d}E} = N_0 \left(\frac{E}{E_0}\right)^{-\Gamma} \tag{VI.5}$$

Γ is called the photon index of the spectrum, E_0 is the reference energy and N_0 the normalization or amplitude. An identical model is pre-defined as `PowerLawSpectralModel` in Gammapy as well ([Gam22]).

N_0 is given in units of $1\,/\,(\text{energy}\cdot\text{area}\cdot\text{time})$. Therefore, it is the energy flux at $E = E_0$. Classically, E_0 is the decorrelation energy, where the correlation between slope and normalization vanishes. However, from a mathematical point of view, it can be chosen freely in the used model. To facilitate the comparison of the amplitude N_0 derived within this work with that reported by the H.E.S.S. collaboration, E_0 is fixed to 0.783 TeV, the same value as was used in [Abr11]. Subsequently, all values of N_0 given in this section refer to $E = E_0 = 0.783\,\text{TeV}$.

The analysis carried out here relies on FITS files produced with updated calibration procedures compared to those used in [Abr11]. Further, the analysis software used for event building and gamma-hadron separation is different than the one used in the 2011 paper (HAP in this work vs. M++ in the 2011 work). Therefore, not only the statistical uncertainties of the fitted parameters must be taken into account when comparing the results, but also the systematic uncertainties. For spectral analyses of powerlaw-like sources with H.E.S.S., typically a systematic uncertainty of 0.2 on the powerlaw index Γ and 20% on the normalization N_0 is assumed (see, e.g., [Aha22b]). Those are also the systematics stated in [Abr11]. In the present work, no further investigation of the systematic uncertainties is conducted; the values given above are applied.

Due to the differences in calibration and software between this work and the analysis applied in [Abr11], a model deviating from a powerlaw might be possible. However, the analyses do not show any hint in this direction. So, the powerlaw model described in Equation VI.5 is considered satisfactory and applied here.

Results

Fitting the power-law model as described previously in Paragraph VI.3.3 to the two datasets delivers overall well comparable results which are listed in table Table VI.3. The photon indices

Table VI.3: Derived spectral parameters and integrated fluxes for HESS J1731-347 with the FC dataset as well as with the CT1-4 dataset. For comparison, also the values derived in [Abr11] are given. The integrated fluxes are given in the energy ranges from 1 to 10 TeV and from 0.5 to 5 TeV. Additionally to the statistical uncertainties, a systematic uncertainty of 20% on N_0 and 0.2 on Γ must be assumed

Dataset	Γ	N_0 $\left[10^{-12}\frac{1}{\mathrm{TeV\,cm^2\,s}}\right]$	$F_{1-10\,\mathrm{TeV}}$ $\left[10^{-12}\frac{\mathrm{erg}}{\mathrm{cm^2\,s}}\right]$	$F_{0.5-5\,\mathrm{TeV}}$ $\left[10^{-12}\frac{\mathrm{erg}}{\mathrm{cm^2\,s}}\right]$
FC	2.27 ± 0.14	3.75 ± 0.44	5.9 ± 1.5	7.1 ± 1.2
CT1-4	2.25 ± 0.04	3.91 ± 0.19	6.29 ± 0.36	7.50 ± 0.34
[Abr11]	2.32 ± 0.06	4.67 ± 0.19	6.91 ± 0.59	8.63 ± 0.46

derived within this work match well among each other and are also consistent with the result published in 2011 when taking the statistical uncertainty into account. For the CT1-4 and the FC dataset the derived amplitudes agree with each other as well. However, the result reported by [Abr11] is off by 16.3% and 19.7% to CT1-4 and FC data, respectively. This is outside the statistical uncertainty range, but well within the systematic uncertainty of 20%.

Confidence contour plots of the fitted parameters are shown in Figure VI.8, left for the CT1-4 dataset and right for the FC dataset. They underline the statement that the two spectra derived in this work agree. Again, the higher confidence in the CT1-4 dataset is due stereoscopic configuration with four telescopes and not due to the camera. While the photon indices match, it can be ruled out at more than 3σ confidence (corresponding to more than 98.9%) that the different amplitudes of the spectrum derived in 2011 and the one derived from the CT1-4 dataset are due to statistical fluctuations. For the FC dataset, the confidence for this statement in more than 2σ (>86.5%). Though, it must be emphasized again that the mismatch lays within the systematic uncertainty of the analysis. Therefore, the difference can be accounted to the different calibration and analysis algorithms used for this work compared to [Abr11].

Additionally to the spectral parameters, Table VI.3 lists the integrated fluxes derived from the three different spectra together with their statistical errors. The integrated fluxes are given in the energy range 1 to 10 TeV that was stated originally by the H.E.S.S. collaboration. Integrated fluxes in the energy range 0.5 to 5 TeV are also given, as this range is fully covered by FC data, unlike the former energy range. As the spectral parameters match within uncertainty, the integrated fluxes match as well between the CT1-4 and the FC dataset. The integrated fluxes derived with the spectrum from [Abr11] are higher, corresponding to the higher amplitude of the spectrum. However, they still match within statistical and systematic uncertainties, in some cases even within statistical uncertainties, only.

VI.3.4 Summary of the FC science verification for extended sources

Having performed a spatial and a spectral analysis of the SNR HESS J1731-347 with FlashCam@CT5 in mono mode, one can state that the science verification in that aspect is successful.

In the spatial analysis (see Section VI.3.2), all parameters of the applied model match with those derived in a parallel analysis of CT1-4 data. As elaborated in Section VI.1 and Paragraph VI.3.2,

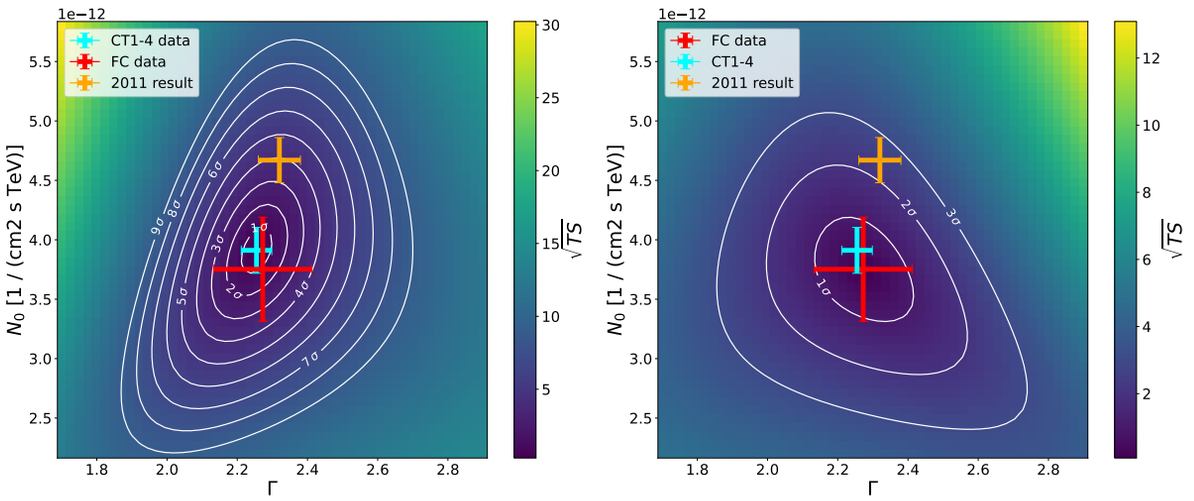

Figure VI.8: Confidence contour plots of the spectral model parameters for the CT1-4 dataset (left) and the FC dataset (right). The best fit result and the statistical uncertainties of the fit of the CT1-4 data is marked (cyan) as well as those of the FC data (red) and the values reported in [Abr11] (orange). The white lines denote two-dimensional confidence contours of the respective analysis. An additional systematic uncertainty of 0.2 on Γ and 20% on N_0 is stated in [Abr11] on their results.

the SNR shell radius is defined differently in the reference paper [Abr11] and in the applied model. This is the reason, why the derived radius of the shell is larger than that published in the paper. Unfortunately, there is no information how the radius is derived in [Abr11], so it is not possible to investigate this further.

As a final proof of the quality of the fitted model, Figure VI.9 displays the CT1-4 (left) and FC (right) significance maps after subtraction of the model. The model regions are indicated with white circles of their respective radius. The only remaining regions of high significance are around the source HESS J1729-345. It can clearly be seen that they show a different morphology in the two images. The statistical significance of which and the astrophysical implications will be further investigated in Section VI.4.

The spectral analysis yields comparable results: the spectra derived with the FC dataset and with the CT1-4 dataset are consistent. Furthermore, the derived photon index matches that published in 2011. However, the derived flux amplitude of this work differs from that reported in [Abr11]. This can be attributed to systematic effects coming from the different calibration and analysis methods applied. Finally, Figure VI.10 shows the two spectra derived in this work with their respective flux points as well as the spectrum published in 2011 by the H.E.S.S. collaboration. Flux points here and also later in Section VI.4.3 are derived with the `FluxPointsEstimator` of Gammapy. It fits the amplitude of the chosen spectral model individually for each energy bin within the energy limits set by the respective energy bin[35]. Within this work, all flux points are derived under the assumption of a powerlaw spectral model (Equation VI.5), fitted to the respective dataset. The method is as well described in [Ace15a] and [Abd18b]. In all spectra

[35]For details, see https://gamma-astro-data-formats.readthedocs.io/en/latest/spectra/binned_likelihoods/index.html, accessed on February 19th, 2024.

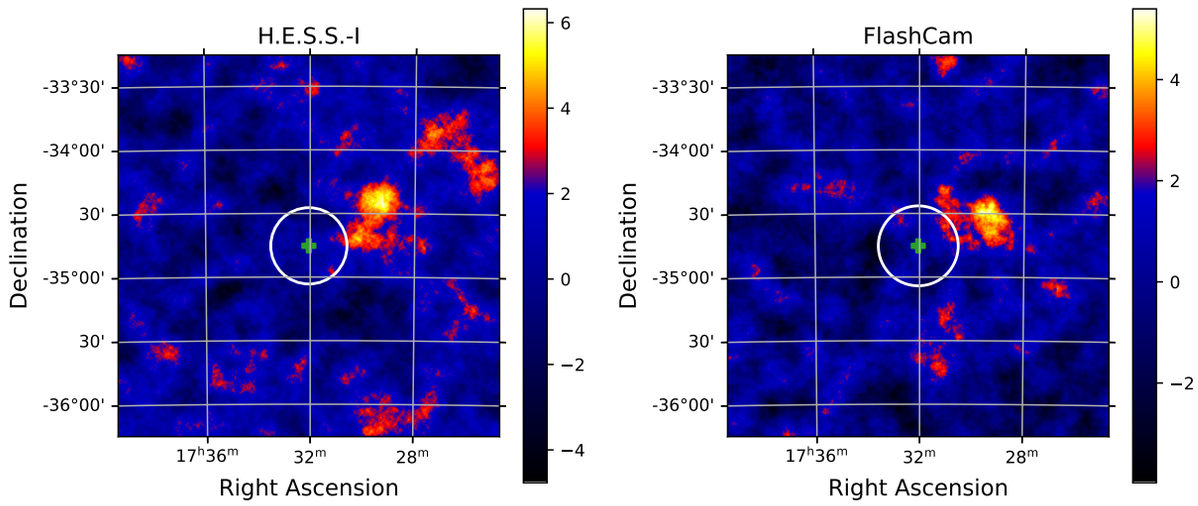

Figure VI.9: The significance maps after subtraction of the shell model for the CT1-4 data (left) and for the FC data (right). The respective colorbars are stretched proportional to the square-root of the value of each bin in order to obtain a good visibility of regions with high significance.

shown, the same number of flux points is tried to be derived as bins are used for the generation of the spectra. However, if the excess count statistics is too low, no sufficiently certain (1σ) flux points can be derived. In such cases, `FluxPointsEstimator` returns upper limits at 2σ rather than flux points.

With the FC analysis, two additional flux points have been derived that extend the low energy end of the spectrum to about 100 GeV. There is no evidence for any deviation of the spectrum of HESS J1731-347 from the chosen powerlaw model. To investigate possible modifications, perhaps below the current energy threshold of 100 GeV, more data with FC@CT5 would be necessary than those evaluated in the present work.

VI.4 Energy dependence of HESS J1729-345

VI.4.1 Motivation

Looking at Figure VI.9 raises the question why the HESS J1729-345 region is shaped differently in the FC and the CT1-4 image. The most obvious reason would be the different PSF of the telescopes. However, this would only explain a larger extension of HESS J1729-345 in the FC image, due to the worse PSF of the CT5 telescope. What is actually seen instead is a clear shift of HESS J1729-345 and its center when comparing the two images. This behavior cannot alone be explained by the PSF. Another reason may be the different energy ranges in which the maps are produced: 0.1 to 10 TeV for the FC data and 0.25 to 30 TeV for the CT1-4 data. Consequently, the different spatial appearance of HESS J1729-345 in the CT1-4 and the FC@CT5 image can be seen as a hint towards an energy dependence in this region. This is of great interest given the still unsolved puzzle of the nature of HESS J1729-345. Energy dependence in the emission from HESS J1729-345 might deliver further evidence in support of any of the models presented

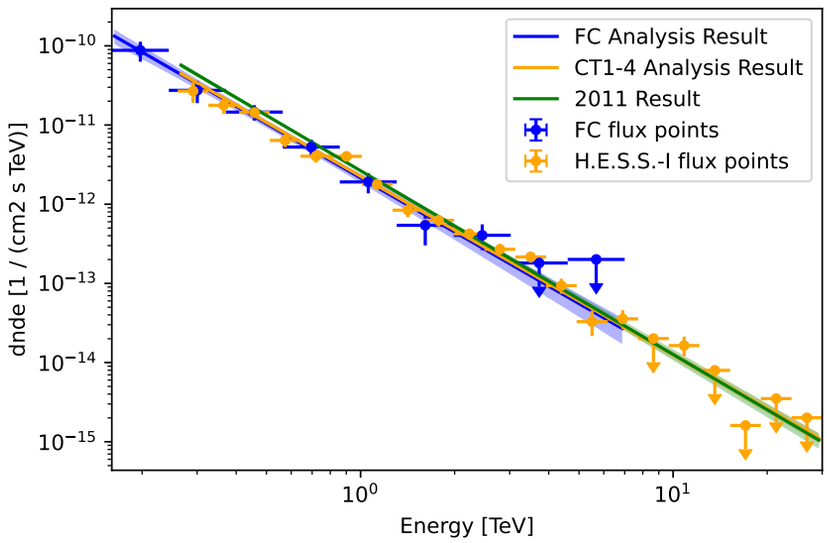

Figure VI.10: Spectra of HESS J1731-347 as derived from the FC dataset (blue), the CT1-4 dataset (orange) and as reported in [Abr11] (green). The fit range is indicated by the length of the respective model line. Additionally, flux points and upper limits have been derived from the datasets under the assumption of the respective model, following the usual Gammapy convention.

in Section VI.1.

In this section, a study is presented that spatially models HESS J1731-347, HESS J1729-345 and the surrounding in two different energy bands: a low energy band, covering energies up to 1 TeV and a high energy band, covering everything up to 40 TeV. The spatial modeling leads to the separation of HESS J1729-345 into two distinct sources: the high energy band emission region (HE emission region) and the low energy band emission region (LE emission region). In a second step, spectra are extracted and modeled from the two regions. The statistics of the FC dataset turns out to be not sufficient to standalone detect any of the two regions, due to the limited livetime. However, it can and is used to cross-check the results obtained in the LE emission region.

Beside the different treatment of the energies, the data reduction remains mostly the same as described in Paragraph VI.3.2 and will not be elaborated here again. The only point to be mentioned is that the radius of exclusion region b is increased to 0.55°. This is, because preliminary analysis with the old radius has shown possible emission from outside the excluded region (i.e., inside the area used for background determination). For the science verification, however, such an adjustment seemed inappropriate in order to ensure comparability between the analyses.

Unfortunately, the livetime of the datasets is further reduced for spectral analysis of the HE and the LE emission regions, as no reflected Off-regions can be found outside the exclusion regions for multiple observations. Most drastically, the CT1-4 dataset available for spectral analysis of the HE emission region contains only 118 runs with a total livetime of 196 478 s, corresponding to 54.6 h. In the LE emission region, the CT1-4 dataset consists of 121 runs with a livetime of 200 356 s (55.7 h). The FC dataset in that region, on the other hand, has a livetime of 89 513 s (24.9 h) for spectral analysis as more runs can be accounted for here, compared to the spectral analysis of HESS J1731-347. For the spatial analysis, the full datasets described in Section VI.2 remain applicable.

Table VI.4: Spatial properties of the SNR shell as fitted in the different energy bands. The 0.25-30 TeV band is that obtained in Section VI.3.2.

Energy range	r_0	η	width
0.25-1 TeV	$0.314° \pm 0.017°$	0.42 ± 0.13	$0.13° \pm 0.04°$
1-40 TeV	$0.285° \pm 0.001°$	0.44 ± 0.08	$0.13° \pm 0.02°$
0.25-30 TeV	$0.300° \pm 0.006°$	0.45 ± 0.07	$0.14° \pm 0.02°$

VI.4.2 Spatial Modeling

To investigate potential energy dependence in HESS J1729-345, firstly the spatial appearance of the SNR shell must be determined in the different energy bands, as the model derived in Section VI.3.2 covers the whole range and deviations in any of the regimes cannot be excluded. For that, the HESS J1731-347 SNR shell is modeled according to Equation VI.1 in the low and high energy band separately. The obtained properties are listed in Table VI.4.

As can be seen, the width of the shell is constant with respect to the different energy bands. However, the outer radii r_0 (i.e., the radii beyond which no more emission is detected in the respective energy band) do not agree within the 1σ uncertainty range of the fits. In particular, it is remarkable that the HE band yields a smaller outer radius than the LE band. Identical to the approach in Section VI.3.2 and in [Abr11], a triangle mask has been used to exclude contamination of the SNR model by HESS J1729-345, ruling out any influence from this source to the fit. Therefore, the smaller radius in the HE band than in the LE band might be assumed to be an intrinsic feature of the SNR shell itself. This result is in contradiction to common models of SNR development (e.g., [Ptu08]). A conclusion from these models is that higher energetic particles escape the SNR shock front faster than particles of lower energy. This leads to the expectation that r_0 in the HE band should be larger than in the LE band. However, the opposite might be the case. Anyways, this does not necessarily mean that [Ptu08] are wrong: While the outer radii seem to be well defined, the shell widths are not, leaving uncertainties due to the correlation of shell width and r_0 (cf. Figure VI.7). Further, the stated uncertainties represent one standard deviation, only. Hence, significantly more data would be necessary in order to draw a reliable conclusion on the radii of HESS J1731-347 in different energy bands and, if necessary, to be in a position to question the existing models of SNR evolution.

After subtracting that model from the maps, no significant emission is left inside the modeled shell as can be seen from the respective significance maps in Figure VI.11. However, to the west of the shell, one emission region per energy band is detected at an estimated peak significance level of $\sim 6\sigma$. These regions are centered at different positions, correlating with the highest excess. Furthermore, the two regions are differently shaped. To describe the shape of the emission regions in their respective energy band, two different spatial models are fitted to the data.

In the low energy band from 0.25 to 1 TeV (left panel in Figure VI.11) a uniformly emitting disk with a smooth transition to the outside is applied (`DiskSpatialModel`, as defined in [Gam22]). The disk is completely described by its radius r_0 and the `edge_width`. `edge_width` is defined such that the intensity drops from 95% to 5% in $[r_0 - 0.5 \cdot \texttt{edge\_width},\ r_0 + 0.5 \cdot \texttt{edge\_width}]$,

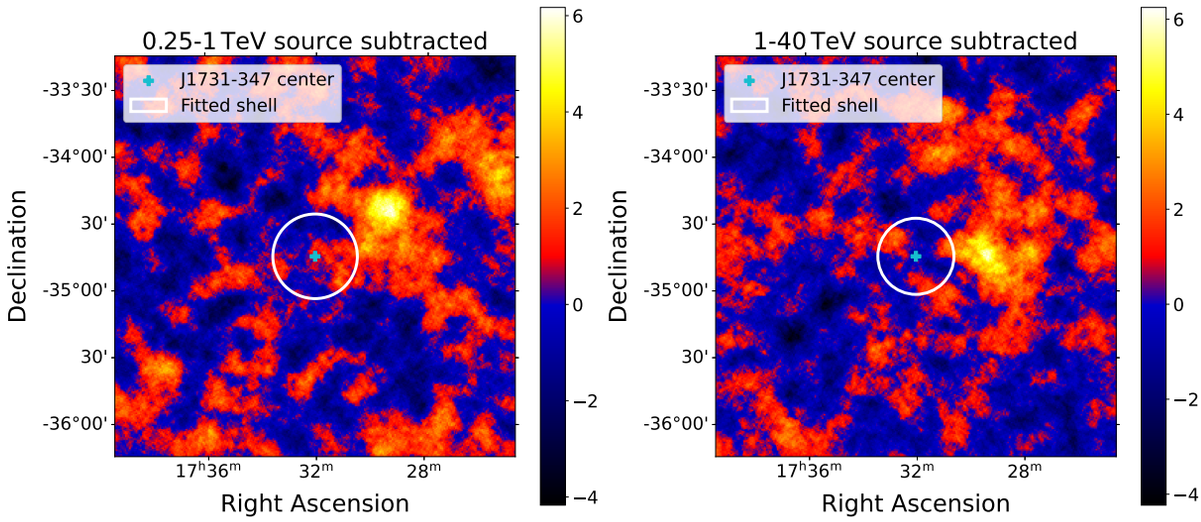

Figure VI.11: CT1-4 significance maps of the low energy (left) and high energy band (right) after subtraction of the fitted models for HESS J1731-347. The size of the respective SNR shell is marked with a white circle, the center (identical in both) with a cyan cross.

Table VI.5: Model parameters for the two significant excess regions of HESS J1729-345. For e and φ in the low energy band, the default values are used.

Energy band	Position	r_0 [deg]	e	φ [deg]	`edge_width`
Low E	RA: 17h29m32.16s DEC: $-34°25'48''$	0.179 ± 0.025	0	0	0.4
High E	RA: 17h29m10.26s DEC: $-34°47'0''$	0.366 ± 0.052	0.848 ± 0.087	67 ± 11	0.5

with smooth transitions from 100% and to 0%, respectively. The parameter r_0 denotes the radius at which the intensity is exactly 50% of the maximum.

For the high energy band from 1 to 40 TeV (right panel in Figure VI.11), the same model is used as a basis. Additional to the parameters explained above $e \in [0, 1]$ and an angle φ are given, converting the circular disk into an ellipse with eccentricity e and with r_0 being the length of the major semi-axis. The disk is rotated counter-clockwise by φ, where $\varphi = 0°$ indicates that the major semi-axis faces north. This elongated disk model is tested for the low energy data as well, but modeling results in an eccentricity of 0, so the approach is abandoned.

As at the same time the center position $\vec{p}$ and the shape of the spatial models need to be defined, fitting follows an iterative process. First, $\vec{p}$ is estimated by eye from Figure VI.11. For that position, radius, eccentricity and rotation angle are fitted. Next, the obtained parameters are fixed and the position is fitted, resulting in small deviations ($\lesssim 0.05°$) from the first guess. Fixing the newly derived position again, the other parameters once more are left free to be fitted. Since another iteration of free $\vec{p}$ and fixed other parameters does not lead to any changes, these values are considered final.

The parameters found from this procedure are listed in Table VI.5. Figure VI.12 shows the combined models for HESS J1731-347 and HESS J1729-345 in both energy regimes. There, the

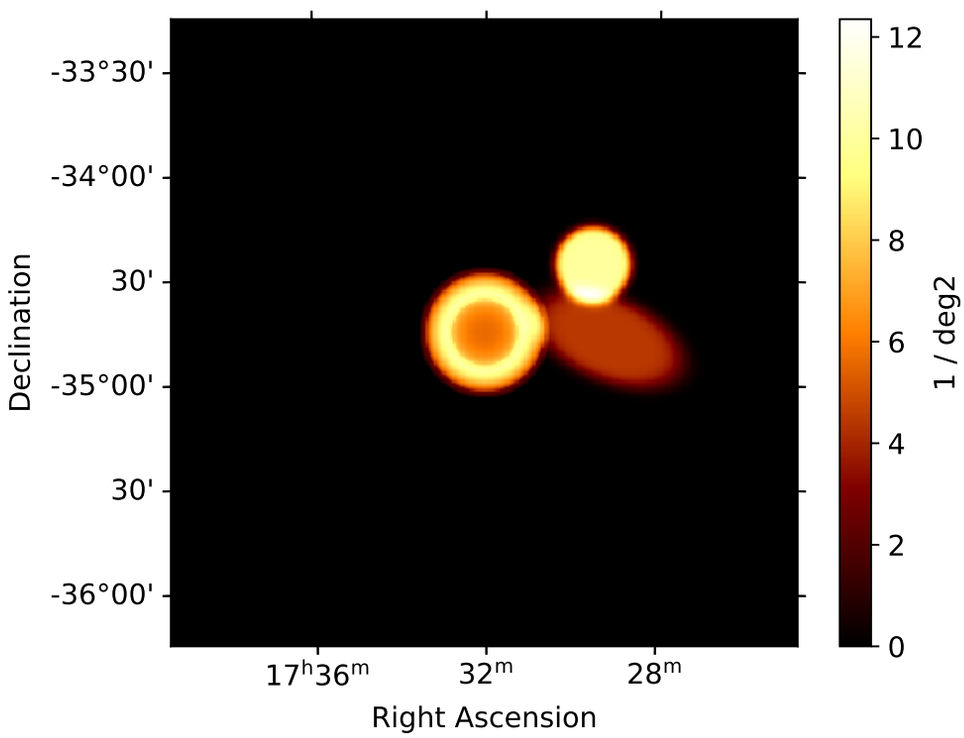

Figure VI.12: Combined model of HESS J1731-347 and HESS J1729-345 from 0.25 to 40 TeV. The SNR shell is a sum of the expected counts from the models of both energy bands. The bright, circular disk is modeled exclusively at energies below 1 TeV, while the fainter ellipse only appears at energies above 1 TeV.

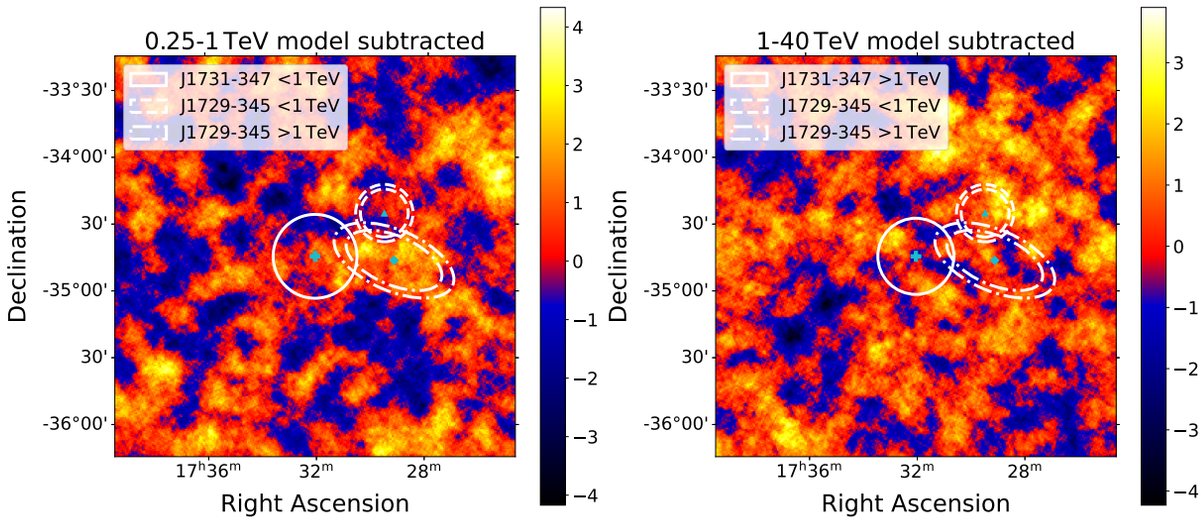

Figure VI.13: Significance maps of the low energy band (left) and the high energy band (right) after subtraction of the fitted source models for HESS J1731-347 and HESS J1729-345. The respective SNR shell model (solid) and the contours (at distance r_0 and $r_0 + 0.5 \cdot \text{edge\_width}$) of the LE (dashed) and HE (dashed-dotted) emission regions are outlined in both maps. In the left (right) map, only the low (high) energy emission region source model is subtracted.

shell structure of the SNR is seen bright in the center, modeled in both energy regimes. The two structures of which HESS J1729-345 consists are located west of that. Round and more to the north is the disk found to describe the emission in the low energy band, the LE emission region. Below that, fainter, the ellipse describing the emission of the high energy band $\geq 1\,\text{TeV}$ (HE emission region) can be seen.

To evaluate whether these two models are sufficient to describe the emission from HESS J1729-345 they were subtracted from the respective sky-map. The resulting significance maps are shown in Figure VI.13. On the left is the map in the low energy band. The solid line is the SNR shell in that energy regime, the dashed line denotes the modeled disk in which counts were subtracted from the map. For comparison, the dashed-dotted ellipse outlines the modeled HE emission region. However, no counts from this region were subtracted in the left image. Opposite, in the right image of Figure VI.13 the high energy band emission after subtraction of the relevant models is shown. Again, the circle outlined with a solid line is the SNR reconstructed in that energy band. The dashed and dashed-dotted structures denote the LE and HE emission regions of HESS J1729-345, respectively. In this map, only counts from the modeled HE emission region (i.e., the dashed-dotted ellipse) were subtracted, the LE emission region is shown for comparison, only.

After subtracting the models mentioned before from the respective maps, no significant emission is left in either of the energy bands as can be seen in Figure VI.13. Therefore, it can be concluded that the significant emission in the HESS J1729-345 region originates in two distinct regions. The centers of these regions are separated by 0.36°. The main feature to distinguish the two regions is the energy in which their emission is significant over the background.

Figure VI.14 shows the identified source regions plotted onto the CS density maps from [Max18].

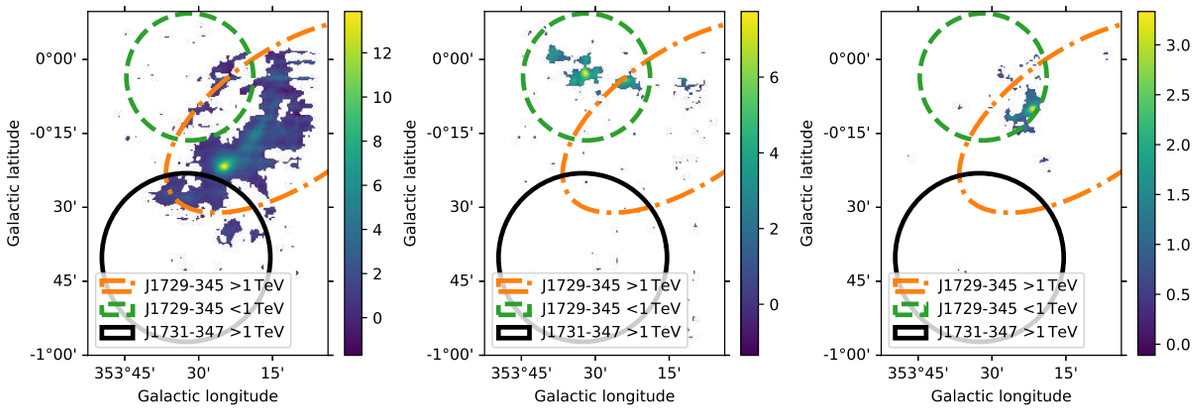

Figure VI.14: Spatial models of HESS J1731-347 (black circle) and the HESS J1729-345 region (green dashed circle and orange dash-dotted ellipse) placed on the CS density maps from [Max18]. Left: Velocity range $V = -23.5$ to $-7.0\,\frac{\mathrm{km}}{\mathrm{h}}$, corresponding to the Scutum-Crux arm. Middle: $V = -30$ to $-60\,\frac{\mathrm{km}}{\mathrm{h}}$, corresponding to the Norma-Cygnus arm. Right: $V = -85.5$ to $-78.0\,\frac{\mathrm{km}}{\mathrm{h}}$, corresponding to the 3 kpc Expanding arm. Colorbars are in units of $\left[\frac{\mathrm{K\,km}}{\mathrm{s}}\right]$.

The three maps correspond (from left to right) to gas in the Scutum-Crux arm, the Norma-Cygnus arm and the 3 kpc Expanding arm. The gas in the Scutum-Crux arm is aligned well with the most significant/intense gamma-ray emission in the HE band emission region. Contrary, the LE band emission region is barely covered with gas from the Scutum-Crux arm, but its center is well aligned with the densest spot of gas in the Norma-Cygnus arm. The gas contribution from the 3 kpc Expanding arm is located in the overlap zone of the low and the high energy band emission region. No significant excess can be clearly attributed to this excerpt.

VI.4.3 Spectral modeling

In order to further characterize the two emission regions found above, spectra are extracted from both of them. The LE emission region is modeled in the entire energy range from 0.25 to 30 TeV. For the HE emission region, this turned out not to be feasible, as the low count statistics from this faint region does not allow to draw reliable conclusions at the low energy end. Spectral modeling of the HE emission region therefore is conducted from 0.4 to 30 TeV. As On-regions, the entire regions defined in Table VI.5 are used initially, meaning a circle / an ellipsis with radius / major semi-axis of length $r_0 + 0.5 \cdot$ `edge_width`. As can be seen in Figure VI.13, the high energy emission region overlaps partially with the SNR and with the low energy emission region. Further, in Figure VI.12 it can be seen that the high energy emission region is the faintest of the three distinct regions. Therefore, the spectrum might be contaminated by emission from the SNR shell and the LE emission region. To tackle this, two further On-regions inside the full HE emission region (from here on, referred to as 'all' region of the HE emission region) are defined and tested. One is the 'safe' region, avoiding almost any interference with the SNR and the LE emission region; the other is the 'inner' region, defining all points within the HE emission region ellipse where the emission is at least 50% (i.e., an ellipse as given for the HE region in Table VI.5, but with `edge_width` = 0.0). The different regions are summarized in Figure VI.15

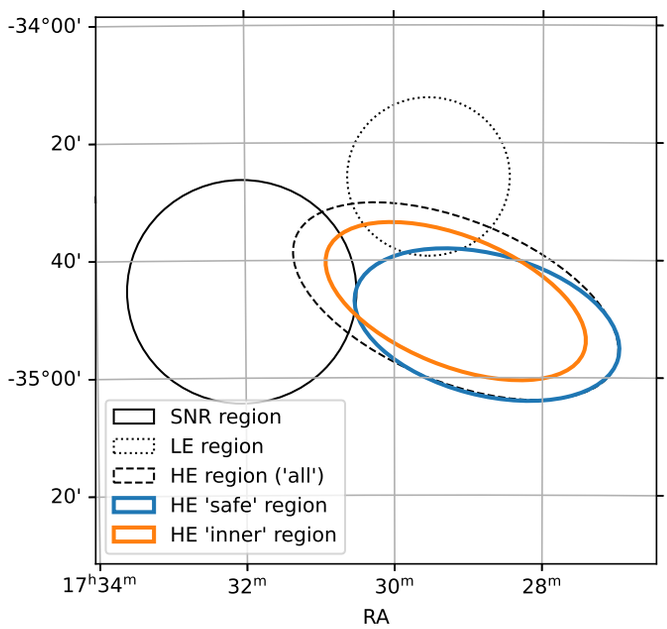

Figure VI.15: Different On-regions for the spectrum of the HE emission region of HESS J1729-345. The 'all' region is the complete, spatially fitted emission region (black dashed contour). The 'safe' region is the elliptical sub-region of the all region that does not interfere with the SNR and almost not with the LE emission region (blue contour). The 'inner' region includes all points of the HE emission region where the modeled emission is at least 50% of the maximum (orange contour). For reference, also the contour of the LE emission region (black dotted contour, corresponding to the all region of HE) and the contour of the SNR (in 0.25 to 1 TeV) is given.

Table VI.6: Spectral parameters of the low energy band emission region (CT1-4 and FC data). The amplitude N_0 is evaluated at the reference energy E_0.

Region	$\Gamma 1$	N_0 $\left[10^{-12}\frac{1}{\mathrm{TeV\,cm^2\,s}}\right]$	E_0 [TeV]	$F_{1-10\,\mathrm{TeV}}$ $\left[10^{-12}\frac{\mathrm{TeV}}{\mathrm{cm^2\,s}}\right]$	$F_{0.5-5\,\mathrm{TeV}}$ $\left[10^{-12}\frac{\mathrm{TeV}}{\mathrm{cm^2\,s}}\right]$
Low E	2.68 ± 0.14	1.45 ± 0.17	0.774	0.77 ± 0.16	1.22 ± 0.17
Low E FC	2.39 ± 0.30	1.34 ± 0.36	0.775	1.10 ± 0.64	1.45 ± 0.56

The energy range of all regions is divided in 10 bins. Further, a powerlaw is used to model the spectrum as a first attempt in all regions. For the low energy emission region this assumption turns out to describe the data well, as can be seen in Figure VI.16, left panel. The powerlaw with $\Gamma = 2.68 \pm 0.15$ matches the derived flux points. To confirm this result, a spectral analysis with a powerlaw model is also attempted on the FlashCam data for the low energy emission region. While the low number of counts (due to the shorter livetime of the FC dataset) only allows to apply two energy bins in the range from 0.16 to 7 TeV, the spectrum obtained matches that of the CT1-4 analysis within the statistical errors ($\Gamma = 2.39 \pm 0.30$). The detailed spectral parameters are given in Table VI.6 together with the expected integral energy fluxes according to the models in the energy ranges from 1 to 10 $\frac{\mathrm{TeV}}{\mathrm{cm^2\,s}}$ and from 0.5 to 5 $\frac{\mathrm{TeV}}{\mathrm{cm^2\,s}}$. The On-region of the low energy emission region is detected in the CT1-4 analysis with a significance of 8.4σ. For the smaller FC dataset, the significance is 4.6σ.

Fitting a spectrum in the high energy emission region is more complex. The fitted powerlaw spectrum with a photon index of $\Gamma = 2.51 \pm 0.12$ does not seem to match the data well, as can be seen in Figure VI.16, right panel. Suggested by the derived flux points, a broken powerlaw is fitted as competing model. It behaves like a normal powerlaw of the form $\mathrm{d}N/\mathrm{d}E = N_0 \cdot \left(\frac{E}{E_{\mathrm{break}}}\right)^{-\Gamma}$

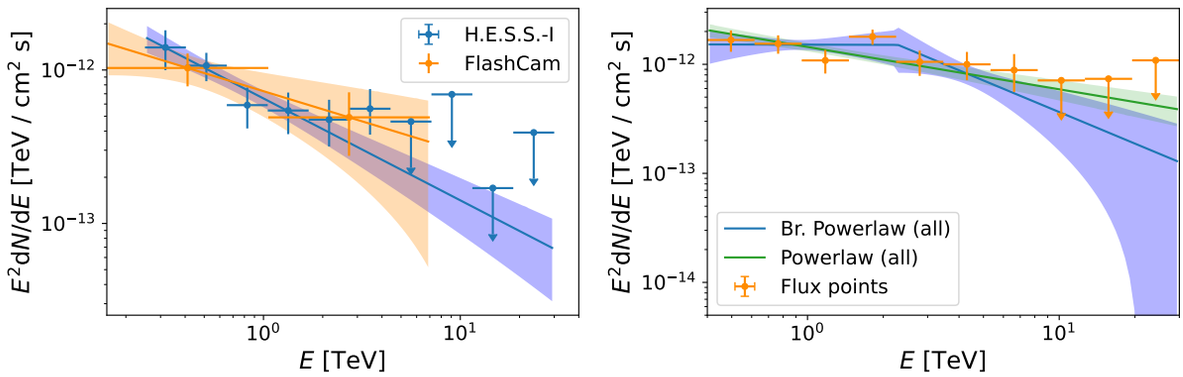

Figure VI.16: Spectra of the HESS J1729-345 region. Left: emission from the LE region is fitted with a powerlaw. The results obtained with the CT1-4 dataset and the FC dataset match within the statistical errors. Right: emission from the entire HE region (flux points in orange) is fitted with a broken powerlaw (blue) and with a normal powerlaw (green). No spectrum with FlashCam has been obtained.

with $\Gamma = \Gamma 1$ for $E < E_{\text{break}}$ and $\Gamma = \Gamma 2$ for $E \geq E_{\text{break}}$. Following [Gam22], the broken powerlaw is described by

$$\frac{\mathrm{d}N}{\mathrm{d}E} = N_0 \cdot \begin{cases} \left(\frac{E}{E_{\text{break}}}\right)^{-\Gamma 1} & \text{if } E < E_{\text{break}} \\ \left(\frac{E}{E_{\text{break}}}\right)^{-\Gamma 2} & \text{otherwise} \end{cases} \tag{VI.6}$$

The fitted photon indices are $\Gamma 1 = 2.00 \pm 0.30$ before the spectrum breaks and $\Gamma 2 = 2.96 \pm 0.48$ afterwards. In the range from 1 to 10 TeV, the integral energy flux [36] is $(2.44 \pm 0.29) \times 10^{-12}\ \frac{\text{TeV}}{\text{cm}^2\,\text{s}}$. The χ^2/d.o.f. values are 10.816/8 for the powerlaw and 6.202/6 for the broken powerlaw. A χ^2-difference test ([SE03]) to compare the two models then delivers χ^2/d.o.f. = 4.6139/2, allowing to prefer the broken powerlaw model over the powerlaw model at 90% certainty level. The obtained broken powerlaw spectrum is plotted in the right panel of Figure VI.16 as well. The detailed spectral parameters for both, powerlaw and broken powerlaw are listed in the upper two rows of Table VI.7. The fitted amplitude N_0 of the broken powerlaw (evaluated at E_{break}) has a large uncertainty, which is due to the correlation of N_0 and E_{break} and is also suggested by the shadowed uncertainty area in Figure VI.16. In rows three to six of that table are the spectral parameters obtained from the safe and the inner region for the two models, respectively.

For the safe region, the high fluctuation in the flux points does not allow to prefer the broken powerlaw model over the normal powerlaw model. The χ^2/d.o.f. values are 10.0776/6 and 14.2631/8 for the broken powerlaw and the powerlaw, respectively, leading to a difference χ^2/d.o.f. of 4.1855/2. Therefore, in this region the best fit spectrum is a powerlaw of index $\Gamma = 2.46 \pm 0.14$ and an integral flux from 1 to 10 TeV of $(1.13 \pm 0.20) \times 10^{-12}\ \frac{\text{TeV}}{\text{cm}^2\,\text{s}}$, according to the data available. Note that the spectral indices of the powerlaw models fitted to the three On-regions defined

[36] Note that in Gammapy, the uncertainty of the energy flux of a model is calculated via an error propagation that takes the correlation of model parameters into account. Therefore, high uncertainties in the individual parameters do not automatically lead to a high uncertainty in the energy flux, if the parameters are highly (anti-)correlated. This is for example the case for E_{break} and N_0.

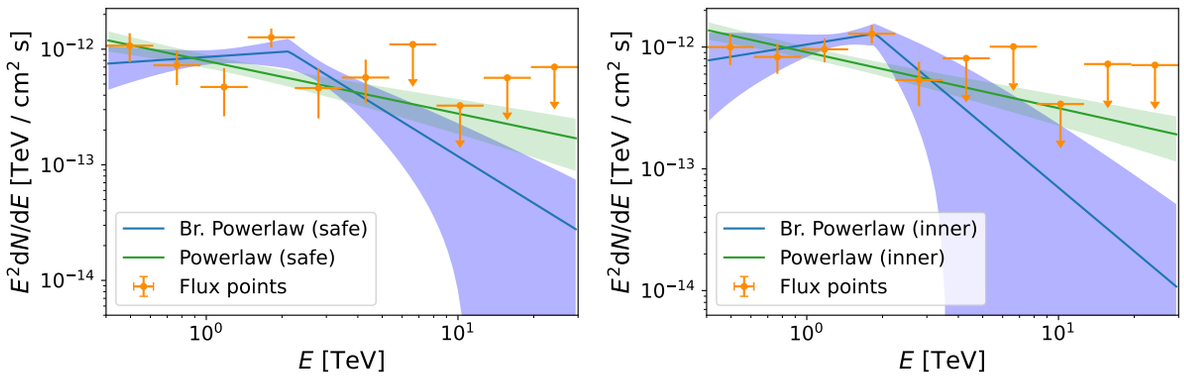

Figure VI.17: Spectra of the safe (left panel) and the inner (right panel) On-region of the HE emission region. In both panels, a powerlaw (green) and a broken powerlaw (blue) is fitted to the flux points (orange). The spectral parameters are listed in Table VI.7.

within the HE emission region are in very good agreement. Furthermore, for the safe and the inner region, also the integral fluxes match well.

Eventually, in the inner On-region the broken powerlaw is preferred over the normal powerlaw at the 97.5% certainty level (χ^2/d.o.f. = 8.3755/2, with χ^2/d.o.f. = 4.1340/6 for the broken powerlaw and χ^2/d.o.f. = 12.5096/8 for the unbroken powerlaw). The indices obtained are $\Gamma 1 = 1.67 \pm 0.56$ and $\Gamma 2 = 3.74 \pm 1.32$. From 1 to 10 TeV, the flux from the inner region is $(1.43 \pm 0.55) \times 10^{-12} \frac{\text{TeV}}{\text{cm}^2\,\text{s}}$, according to the broken powerlaw model. The resulting spectra for the safe and the inner region are plotted in Figure VI.17. More observational data would be needed to further constrain the true shape of the spectrum and to obtain more robust flux results.

Independent of which of the three On-regions evaluated and which of the spectral models is chosen, agreement with the model fitted to the LE region can be ruled out within statistical uncertainties. This implies that the spectra of the two regions of HESS J1729-345 differ, regardless whether the break in the powerlaw for the HE region will be confirmed in future observations or not, and that the HE emission region is no kind of "extension" of the SNR shell. Further to be noted is that there is an independent, spectral detection of the HE emission region in the all, safe and inner On-region with 11.0σ, 7.5σ and 8.8σ, respectively. The detection of the inner and the safe On-region, with little or no overlap with the SNR and the LE emission region, combined with the different spectra, allows the LE and the HE emission regions to be established as two independent sources. Their underlying emission processes are of different nature, which is discussed in the next section.

VI.4.4 Interpretation

As pointed out in the previous two sections, the HESS J1729-345 region is formed by two independent emission regions: A fainter one of elliptical shape that emits a significantly detected flux only at energies $\gtrsim 1$ TeV and a brighter one of circular shape that emits a significantly detectable flux only at energies $\lesssim 1$ TeV. In this work, the former is referred to as *the high energy band emission region* and the latter is referred to as the *the low energy band emission region* of

Table VI.7: Spectral parameters of the three regions defined within the high energy band emission region. For each region, a broken powerlaw and a powerlaw are fitted, respectively. In the all and the inner region, the broken powerlaw is significantly (at the 90% and the 97.5% level, respectively) better than the powerlaw. In the safe region, the broken powerlaw does not significantly improve the fit and is therefore not preferred.

Region	$\Gamma 1$	$\Gamma 2$	N_0 $\left[10^{-13}\frac{1}{\mathrm{TeV\,cm^2\,s}}\right]$	E_0 [TeV] or E_{break} [TeV]	$F_{1-10\,\mathrm{TeV}}$ $\left[10^{-12}\frac{\mathrm{TeV}}{\mathrm{cm^2\,s}}\right]$
All br. Pwl	2.00 ± 0.30	2.96 ± 0.48	2.9 ± 4.1	2.3 ± 1.3	2.44 ± 0.29
All Pwl	2.39 ± 0.09	—	8.26 ± 0.73	1.26	2.20 ± 0.25
Safe br. Pwl	1.85 ± 0.39	3.35 ± 0.71	2.12 ± 0.62	2.12 ± 0.03	1.30 ± 0.22
Safe Pwl	2.46 ± 0.14	—	5.56 ± 0.73	1.16	1.13 ± 0.20
Inner br. Pwl	1.67 ± 0.56	3.74 ± 1.32	3.71 ± 0.78	1.865 ± 0.011	1.43 ± 0.55
Inner Pwl	2.46 ± 0.12	—	6.64 ± 0.74	1.135	1.29 ± 0.19

HESS J1729-345, short: the HE and the LE emission regions.

The first question to be posed when interpreting the HE emission region is, which of the derived spectra should be investigated. The obvious advantage of the all spectrum is that it covers the entire HE emission region found in the spatial analysis. However, it also is contaminated from the SNR shell and/or the LE emission region. This can be seen, as its 1-10TeV flux is about twice as high as that of the inner region, which should according to the spatial modeling contain the majority of the flux from the source. On the other hand, the fact that the safe and the inner regions have similar fluxes shows that the excess flux must originate from the overlap of the all region with the SNR shell and the LE emission region not covered by the inner region. From the same argument, the inner region should be preferred over the safe region, as it is not significantly contaminated from the SNR shell or the LE emission region. This is corroborated by the fact that the fluxes from the two regions in question are similar. However, the inner region includes the bright spot in the CS map of [Max18] (cf. Figure VI.14, left panel), which the safe region doesn't. Therefore, the interpretation of the HE emission region is based on the results of the spatial analysis and of the spectral analysis conducted in the inner region. Spatially, the inner region covers more than half of the molecular cloud MC core and the lower $\sim$ third of the molecular cloud MC J1729, as introduced by Cui et al. ([Cui19], cf. Figure VI.2). Especially, the entire part of MC core outside the SNR shell is covered. For the spectrum of both molecular clouds, Cui et al. expect a broken powerlaw with $E_{\mathrm{break}} \gtrsim 2\,\mathrm{TeV}$, $\Gamma 1 \leq 2$, $\Gamma 2 > 2$, and an exponential cutoff beyond 10 TeV. The spectral parameters of the (inner) HE emission region match these requirements, in case the broken powerlaw model is applied. The unbroken powerlaw cannot be supported following the findings of this work. Firstly, the broken powerlaw is preferred at the 97.5% significance level over the unbroken solution. Secondly, the peak significance of the spatially resolved map is $\approx 6\sigma$ at energies $\geq 1\,\mathrm{TeV}$ and only $\lesssim 4\sigma$ at energies $\leq 1\,\mathrm{TeV}$, which is not expected for an unbroken powerlaw. Only the cutoff can neither be confirmed nor rejected with the data available. Additionally, also the amplitude of the fitted spectrum is in the same order of magnitude as shown in Figure 6 from [Cui19]. The scenario of passive illumination of all

molecular clouds along the line of sight can be rejected, since this would require the illumination to originate mainly in the Scutum Crux arm. However, the LE emission region is brighter (see Figure VI.12), but does barely cover the densest parts of the gas cloud in the Scutum Crux arm. Therefore, the HE emission region can be identified as a molecular cloud in the Scutum Crux arm, illuminated by the nearby SNR HESS J1731-347. This model scenario which is supported by the data places the SNR at the cloud distance in the Scutum Crux arm. Although [Dor22] had found this result before, it is the first time that such a conclusion can be drawn from TeV data and molecular clouds alone. This is noteworthy, as these two tracers were originally used to discover the source and to derive the initial lower limit on its distance.

An interpretation of the LE emission region is less straight forward. As it is north-east of the originally published center-position of HESS J1729-345 (most likely due to a different analysis method), it does not exactly match the position of the cloud MC J1729 as assumed by Cui et al. However, their assumption has been based on the previous available H.E.S.S. result on HESS J1729-345. The model might in future be adapted according to the improved results. Moreover, the spectrum in TeV of the LE emission region does not match the expected broken powerlaw: from 0.16 to 3 TeV, it is a normal powerlaw with $\Gamma \approx 2.6$ and there is no evidence for a cutoff at any energy. This is a strong hint to reject the models proposed in [Cui16] and [Cui19] for this region. Instead, the main contributor to this emission could be in the Norma-Cygnus arm, according to the gas maps from [Max18], i.e., at a different location than the SNR. The center of the LE emission region coincides with the center of the dense CS-traced gas of the Norma-Cygnus arm, which is believed to be a star forming region ([Max18]). Star forming regions show an increased rate of supernovae taking place ([Acc09a]), resulting in a higher density of SNRs and PWN ([Str20]), both being well established source classes for VHE gamma-rays ([H. 18]). It is therefore a natural assumption that the LE emission region might consist of unresolved sources in this star forming region in the Norma-Cygnus arm. Additionally to the Norma-Cygnus arm, also illumination of less dense gas by hadrons from the galactic CR sea in the Scutum-Crux arm and even in the 3 kpc Expanding arm might play a (minor) role. However, the addition of all these gas contributions still does not lead to the large extension of the emission region, which therefore remains unexplained. Note also that in the LE emission region, no flux points beyond 3 TeV can be confined. This can be interpreted as an indication of a sharp cutoff in the spectrum. However, this cannot be confirmed nor refuted with the available data. Such a cut-off could be a hint towards one or multiple unresolved PWN in the Norma-Cygnus arm as origin of the VHE gamma-rays from the LE emission region.

VI.5 Summary

The chapter reports on analyses of the SNR HESS J1731-347 and its neighboring source HESS J1729-345. In the first part, data obtained with the 2019 installed FlashCam camera at CT5 is analyzed. The camera and the software as implemented in H.E.S.S. are capable to spatially resolve a source that is well extended beyond the PSF and to obtain a spectrum of the entire source region. To exclude systematic effects due to changes in analysis methods, also the archive CT1-4 data is

re-analyzed. The results obtained from the two datasets are in good agreement with each other, taken the different energy ranges into account. Further, they are also consistent with the reference values published in [Abr11]. In the spectral analysis, the usage of FlashCam@CT5 allowed to extend the spectrum down to 160 GeV, compared to about 260 GeV in the CT1-4 analysis. This establishes FlashCam@CT5 as an capable instrument to investigate TeV gamma-ray-emission even from comparably faint, widely extended sources well below 200 GeV.

The second analysis of the chapter investigates energy dependence in the region west of HESS J1731-347. Initially, the TeV excess found in this area was interpreted as a single source named HESS J1729-345. However, in the course of this work it was found that the region in question actually consists of two independent sources: the high and the low energy band emission region of HESS J1729-345. The HE emission region is found to be most likely originating from a molecular cloud in the Scutum Crux arm being illuminated by CRs escaping the SNR HESS J1731-347. This fixes the position of the SNR into the Scutum Crux arm using TeV observations, consistent with Doroshenko et al. who did this for the CCO which is associated with the SNR ([Dor22]). Additionally, this is evidence in support of parts of the model Cui et al. proposed ([Cui19]). Namely, the interaction of escaping super-TeV CRs with surrounding molecular clouds is found. The best-fit spectrum of that interaction region is consistent with the simulated spectrum by [Cui19]. Therefore, the most probable explanation for the TeV gamma-ray emission seen is that the dense molecular cloud MC core gets penetrated and in consequence illuminated by escaping super-TeV CRs from the SNR.

The origin of the LE emission region cannot be determined with absolute certainty. Its center is consistent with dense gas believed to be a star forming region and located in the Norma-Cygnus arm of the galaxy, at a distance of about 4.5 kpc ([Max18]). The emission might therefore originate from multiple, undetected sources of VHE gamma-rays in this star forming region. Additional contributions from molecular clouds in the Scutum-Crux arm and the 3 kpc arm might be present as well. However, disentangling these possible contributions in more detail is not feasible with the data available. Note also that the spatial extent of the emission region is larger than expected from the traced gas alone, discouraging the theory of a background-illuminated cloud. The physical mechanism causing the TeV gamma-ray emission in the LE emission region therefore remains unknown.

Bibliography

[Aab17] Aab, A. et al. (Pierre Auger Collaboration), 2017. *Observation of a large-scale anisotropy in the arrival directions of cosmic rays above* 8×10^{18} eV. Science 357(6357), 1266. doi:10.1126/science.aan4338.

[Aar17] Aartsen, M. et al. (Icecube Collaboration), 2017. *Astrophysical neutrinos and cosmic rays observed by IceCube.* Advances in Space Research 62(10), 2902. doi:10.1016/j.asr.2017.05.030.

[Abb23] Abbasi, R. et al. (Icecube Collaboration), 2023. *Observation of high-energy neutrinos from the Galactic plane.* Science 380(6652), 1338. doi:10.1126/science.adc9818.

[Abd17a] Abdalla, H. et al. (The H.E.S.S. Collaboration), 2017. *Characterizing the γ-ray long-term variability of PKS 2155-304 with H.E.S.S. and Fermi-LAT.* A&A 598. doi:10.1051/0004-6361/201629419.

[Abd17b] Abdalla, H. et al. (The H.E.S.S. Collaboration), 2017. *Measurement of the EBL spectral energy distribution using the VHE γ-ray spectra of H.E.S.S. blazars.* A&A 606, A59. doi:10.1051/0004-6361/201731200.

[Abd18a] Abdalla, H. et al. (The H.E.S.S. Collaboration), 2018. *First ground-based measurements of sub-20 GeV to 100 GeV γ-Rays from the Vela pulsar with H.E.S.S.II.* A&A 620, A66. doi:10.1051/0004-6361/201732153.

[Abd18b] Abdalla, H. et al. (The H.E.S.S. Collaboration), 2018. *The H.E.S.S. Galactic plane survey.* A&A 612, A1. doi:10.1051/0004-6361/201732098.

[Abd19] Abdalla, H. et al. (The H.E.S.S. Collaboration), 2019. *A very-high-energy component deep in the γ-ray burst afterglow.* Nature 575(7783), 464. doi:10.1038/s41586-019-1743-9.

[Abd20] Abdalla, H. et al. (The H.E.S.S. Collaboration), 2020. *Detection of very-high-energy γ-ray emission from the colliding wind binary η Car with H.E.S.S..* A&A 635, A167. doi:10.1051/0004-6361/201936761.

[Abe18] Abeysekara, A.U. et al. (VERITAS Collaboration), 2018. *A Very High Energy γ-Ray Survey toward the Cygnus Region of the Galaxy.* ApJ 861(2), 134. doi:10.3847/1538-4357/aac4a2.

[Abe20] Abeysekara, A.U. et al., 2020. *Demonstration of stellar intensity interferometry with the four VERITAS telescopes.* Nat. Astron. 4, 1164. doi:10.1038/s41550-020-1143-y.

[Abr11] Abramowski, A. et al. (The H.E.S.S. Collaboration), 2011. *A new SNR with TeV shell-type morphology: HESS J1731-347.* A&A 531, A81. doi:10.1051/0004-6361/201016425.

[Acc09a] Acciari, V.A. et al. (VERITAS Collaboration), 2009. *A connection between star formation activity and cosmic rays in the starburst galaxy M82.* Nature 462(7274), 770. doi:710.1038/nature08557.

[Acc09b] Acciari, V.A. et al. (VERITAS Collaboration and VLBA 43 GHz M87 Monitoring Team and H.E.S.S. Collaboration and MAGIC Collaboration), 2009. *Radio Imaging of the Very-High-Energy γ-Ray Emission Region in the Central Engine of a Radio Galaxy.* Science 325(5939), 444. doi:10.1126/science.1175406.

[Ace15a] Acero, F. et al. (Fermi-LAT Collaboration), 2015. *Fermi Large Area Telescope Third Source Catalog.* Astrophys. J. 218(2), 23. doi:10.1088/0067-0049/218/2/23.

[Ace15b] Acero, F. et al., 2015. *Study of TeV shell supernova remnants at gamma-ray energies.* A&A 580, A74. doi:10.1051/0004-6361/201525932.

[Ack13] Ackermann, M. et al., 2013. *Detection of the Characteristic Pion-Decay Signature in Supernova Remnants.* Science 339(6121), 807. doi:10.1126/science.1231160.

[Ada21] Adams, C.B. et al., 2021. *Detection of the Crab Nebula with the 9.7 m prototype Schwarzschild-Couder telescope.* Astroparticle Physics 128, 102562. doi:10.1016/j.astropartphys.2021.102562.

[Aha97] Aharonian, F. et al., 1997. *The potential of ground based arrays of imaging atmospheric Cherenkov telescopes. I. Determination of shower parameters.* Astropart. Phys. 6, 343. doi:10.1016/S0927-6505(96)00069-2.

[Aha01] Aharonian, F. et al. (HEGRA Collaboration), 2001. *Evidence for TeV gamma ray emission from Cassiopeia A.* A&A 370, 112. doi:10.1051/0004-6361:20010243.

[Aha04a] Aharonian, F., 2004. Very high cosmic gamma radiation: a crucial window on the extreme Universe. World Scientific Publishing Co. Pte. Ltd., Singapore. doi:10.1142/4657.

[Aha04b] Aharonian, F. et al. (The H.E.S.S. Collaboration), 2004. *Calibration of the cameras of the H.E.S.S. detector.* Astropart. Phys. 22(2), 109. doi:10.1016/j.astropartphys.2004.06.006.

[Aha04c] Aharonian, F.A. et al. (The H.E.S.S. Collaboration), 2004. *High-energy particle acceleration in the shell of a supernova remnant.* Nature 432(7013), 75. doi:10.1038/nature02960.

[Aha06a] Aharonian, F. et al. (The H.E.S.S. Collaboration), 2006. *The H.E.S.S. Survey of the Inner Galaxy in Very High Energy Gamma Rays.* ApJ 636(2), 777. doi:10.1086/498013.

[Aha06b] Aharonian, F. et al. (The H.E.S.S. Collaboration), 2006. *Observations of the Crab nebula with HESS.* A&A 457(3), 899. doi:10.1051/0004-6361:20065351.

[Aha08a] Aharonian, F. et al. (The H.E.S.S. Collaboration), 2008. *Discovery of very high energy gamma-ray emission coincident with molecular clouds in the W 28 (G6.4-0.1) field.* A&A 481(2), 401. doi:10.1051/0004-6361:20077765.

[Aha08b] Aharonian, F. et al., 2008. *High energy astrophysics with ground-based gamma ray detectors.* Rep. Prog. Phys. 71(9), 096901. doi:10.1088/0034-4885/71/9/096901.

[Aha08c] Aharonian, F. et al. (The H.E.S.S. Collaboration), 2008. *HESS very-high-energy gamma-ray sources without identified counterparts.* A&A 477(1), 353. doi:10.1051/0004-6361:20078516.

[Aha22a] Aharonian, F. et al. (The H.E.S.S. Collaboration), 2022. *Evidence for γ-ray emission from the remnant of Kepler's supernova based on deep H.E.S.S. observations.* A&A 662, A65. doi:10.1051/0004-6361/202243096.

[Aha22b] Aharonian, F. et al. (The H.E.S.S. Collaboration), 2022. *Time-resolved hadronic particle acceleration in the recurrent nova RS Ophiuchi.* Science 376(6588), 77. doi:10.1126/science.abn0567.

[Aha24] Aharonian, F. et al. (The H.E.S.S. Collaboration), 2024. *Acceleration and transport of relativistic electrons in the jets of the microquasar SS 433.* Science 383(6681), 402. doi:10.1126/science.adi2048.

[Ahn09] Ahn, E.J. et al., 2009. *Cosmic ray interaction event generator SIBYLL 2.1.* Phys. Rev. D. 80, 094003. doi:10.1103/PhysRevD.80.094003.

[Ahn16] Ahnen, M.L. et al. (MAGIC Collaboration), 2016. *Long-term multi-wavelength variability and correlation study of Markarian 421 from 2007 to 2009.* A&A 593, A91. doi:10.1051/0004-6361/201628447.

[Ale16a] Aleksić, J. et al., 2016. *The major upgrade of the MAGIC telescopes, Part I: The hardware improvements and the commissioning of the system.* Astropart. Phys. 72, 61. doi:10.1016/j.astropartphys.2015.04.004.

[Ale16b] Aleksić, J. et al., 2016. *The major upgrade of the MAGIC telescopes, Part II: A performance study using observations of the Crab Nebula.* Astropart. Phys. 72, 76. doi:10.1016/j.astropartphys.2015.02.005.

[Ant93] Antonucci, R., 1993. *Unified models for active galactic nuclei and quasars.* Ann. Rev. Astron. Astrophys. 31, 473. doi:10.1146/annurev.aa.31.090193.002353.

[Arc21] Arcaro, C. (CTA ASTRI project), 2021. *The ASTRI-Horn Dual-Mirror Small-Size Cherenkov Telescope: recent updates, first results and outlook.* PoS HEASA2019, 46. doi:10.22323/1.371.0046.

[Ash19] Ashton, T. et al., 2019. *A NECTAr-based upgrade for the Cherenkov cameras of the H.E.S.S. 12-meter telescopes.* Astropart. Phys. 118, 102425. doi:10.1016/j.astropartphys.2019.102425.

[Bel78] Bell, A.R., 1978. *The acceleration of cosmic rays in shock fronts – I.* MNRAS 182, 147. doi:10.1093/mnras/182.2.147.

[Bel93] Bellamy, E. et al., 1993. *Absolute calibration and monitoring of a spectrometric channel using a photomultiplier.* NIM-A 339(3), 468. doi:10.1016/0168-9002(94)90183-X.

[Bel13] Bell, A.R., 2013. *Cosmic ray acceleration.* Astropart. Phys. 43, 56. doi:10.1016/j.astropartphys.2012.05.022.

[Ben98] Benn, C. et al., 1998. *Brightness of the night sky over La Palma.* New Astronomy Reviews 42, 503. doi:10.1016/S1387-6473(98)00062-1.

[Ber02] Bernlöhr, K., 2002. *CORSIKA and sim_hessarray – Simulation of the imaging atmospheric Cherenkov technique for the H.E.S.S. experiment.* H.E.S.S. internal note 02/05.

[Ber03] Bernlöhr, K. et al., 2003. *The optical system of the H.E.S.S. imaging atmospheric Cherenkov telescopes. Part I: layout and components of the system.* Astroparticle Physics 20(2), 111. doi:10.1016/S0927-6505(03)00171-3.

[Ber07] Berge, D. et al., 2007. *Background modelling in very-high-energy γ-ray astronomy.* A&A 466(3), 1219. doi:10.1051/0004-6361:20066674.

[Ber08] Bernlöhr, K., 2008. *Simulation of atmospheric Cherenkov telescopes with CORSIKA and sim_telarray.* Astroparticle Physics 30, 149. doi:10.1016/j.astropartphys.2008.07.009.

[Ber22] Bernlöhr, K., 2022. CORSIKA and sim_telarray – Simulation of the imaging atmospheric Cherenkov technique. Accessed: November 11th, 2022, URL `https://www.mpi-hd.mpg.de/hfm/~bernlohr/sim_telarray/Documentation/sim_telarray.pdf`.

[Ber24] Bernlöhr, K., 2024. *Personal correspondence.*

[Bi22] Bi, B. et al., 2022. *Performance of the new FlashCam-based camera in the 28m telescope of H.E.S.S.* PoS ICRC2021, 743. doi:10.22323/1.395.0743.

[Bi24] Bi, B. et al., 2024. *Study and Verification of the Charge Reconstruction Algorithm for the FlashCam Camera* In preparation.

[Bol14] Bolmont, J. et al., 2014. *The camera of the fifth H.E.S.S. telescope. Part I: System description.* NIM-A 761, 46. doi:10.1016/j.nima.2014.05.093.

[Bos22] Bose, D. et al., 2022. *Galactic and extragalactic sources of very high energy gamma rays.* EPJST 231, 27. doi:10.1140/epjs/s11734-022-00434-8.

[Bra23] Bradascio, F. (CTA MST Project), 2023. *Status of the Medium-Sized Telescopes for the Cherenkov Telescope Array Observatory.* PoS ICRC2023, 859. doi:10.22323/1.444.0859.

[Buz09] Buzhan, P. et al., 2009. *The cross-talk problem in SiPMs and their use as light sensors for imaging atmospheric Cherenkov telescopes.* NIM-A 610, 131. doi:https://doi.org/10.1016/j.nima.2009.05.150.

[Cap19] Capasso, M., 2019. Study of supernova remnants with H.E.S.S. and analysis of prototype data of the FlashCam Cherenkov Camera. Ph.D. thesis, Eberhard Karls Universiät Tübingen. doi:10.15496/publikation-32687.

[Che19] Chesi, G. et al., 2019. *Optimizing Silicon photomultipliers for Quantum Optics.* Sci. Rep. 9, 7433. doi:10.1038/s41598-019-43742-1.

[Con19] Consortium, T.C., 2019. Science with the Cherenkov Telescope Array. World Scientific Co. Pte. Ltd. doi:10.1142/10986.

[Cor03] Cornils, R. et al., 2003. *The optical system of the H.E.S.S. imaging atmospheric Cherenkov telescopes. Part II: mirror alignment and point spread function.* Astropart. Phys. 20(2), 129. doi:10.1016/S0927-6505(03)00172-5.

[Cor19] Cortina, J. (CTA LST project), 2019. *Status of the Large Size Telescopes of the Cherenkov Telescope Array.* PoS ICRC2019, 653. doi:10.22323/1.358.0653.

[Cor21] Cordero, R.R. et al., 2021. *Evaluation of MEDIS-derived estimates of the albedo over the Atacama Desert using ground-based spectral measurements.* Scientific Reports 11, 19822. doi:10.1038/s41598-021-98622-4.

[Cui16] Cui, Y. et al., 2016. *A young supernova remnant illuminating nearby molecular clouds with cosmic rays.* A&A 591, A68. doi:10.1051/0004-6361/201628505.

[Cui19] Cui, Y. et al., 2019. *Is the SNR HESS J1731-347 Colliding with Molecular Clouds?* ApJ 887, 47. doi:10.3847/1538-4357/ab4ea0.

[Dav57] Davies, J.M. et al., 1957. *Design of the quartermaster solar furnace.* Solar Energy 1(2), 16. doi:10.1016/0038-092X(57)90116-0.

[de 21] de Naurois, M., 2021. *The Making of Catalogues for Very-High-Energy γ-ray Sources.* Universe 7(11), 421. doi:10.3390/universe7110421.

[Dei17] Deil, C. et al., 2017. *Gammapy - A prototype for CTA science tools.* PoS ICRC2017, 766. doi:10.22323/1.301.0766.

[Dem17] Dembinski, H. et al., 2017. *Data-driven model of the cosmic-ray flux and mass composition from 10 GeV to* 10^{11} *GeV.* PoS ICRC2017, 533. doi:10.22323/1.301.0533.

[Dem20] Dembinski, H. et al., 2020. *scikit-hep/iminuit.* doi:10.5281/zenodo.3949207. Published on Zenodo.

[dN09] de Naurois, M. et al., 2009. *A high performance likelihood reconstruction of γ-rays for imaging atmospheric Cherenkov telescopes.* Astropart. Phys. 32(5), 231. doi:10.1016/j.astropartphys.2009.09.001.

[Don22] Donath, A. et al., 2022. *Gammapy: Python toolbox for gamma-ray astronomy.* doi:10.5281/zenodo.6552377. Version 0.20, published on Zenodo.

[Dor16] Doroshenko, V. et al., 2016. *Evidence for a binary origin of a central compact object.* MNRAS 458(3), 2565. doi:10.1093/mnras/stw499.

[Dor17] Doroshenko, V. et al., 2017. *XMM-Newton observations of the non-thermal supernova remnant HESS J1731-347 (G353.6-0.7).* A&A 608, A23. doi:10.1051/0004-6361/201730983.

[Dor22] Doroshenko, V. et al., 2022. *A strangely light neutron star within a supernova remnant.* Nat. Astron. 6, 1444. doi:10.1038/s41550-022-01800-1.

[Dru94] Drury, L.O. et al., 1994. *The gamma-ray visibility of supernova remnants. A test of cosmic ray origin.* A&A 287, 959. doi:10.48550/arXiv.astro-ph/9305037.

[Fer49] Fermi, E., 1949. *On the Origin of Cosmic Radiation.* Phys. Rev. 75(8), 1169. doi:10.1103/PhysRev.75.1169.

[For18] Formenti, P. et al., 2018. *Three years of measurements of light-absorbing aerosols over coastal Namibia: seasonality, origin, and transport.* Atmospheric Chem. Phys. 18(23), 17003. doi:10.5194/acp-18-17003-2018.

[Fuk14] Fukuda, T. et al., 2014. *Interstellar protons in the TeV γ-ray SNR HESS J1731-347: Possible evidence for the coexistence of hadronic and leptonic γ-rays.* ApJ 788(1), 94. doi:10.1088/0004-637X/788/1/94.

[Gam22] The Gammapy developers, 2022. *Gammapy v0.20 Model Gallery.* Accessed: May 31st, 2023, URL `https://docs.gammapy.org/0.20.1/user-guide/model-gallery/index.html`.

[Gia68] Giacconi, R. et al., 1968. *Observational Techniques in X-Ray Astronomy.* Annual Review of Astronomy and Astrophysics 6, 373. doi:10.1146/annurev.aa.06.090168.002105.

[Gia17] Giavitto, G. et al., 2017. *The upgrade of the H.E.S.S. cameras.* NIM-A 876, 35. doi:10.1016/j.nima.2016.12.057.

[Gli16] Glicenstein, J.F. et al. (CTA Consortium), 2016. *NectarCAM: a camera for the medium size telescopes of the Cherenkov Telescope Array.* PoS ICRC2015, 937. doi:10.22323/1.236.0937.

[Got18] Gotschall, D., 2018. The Mirror Alignment and Control System of H.E.S.S. Phase II, and Observational Studies of TeV Shell Candidates and of the Nova Sgr 2015 No. 2 with H.E.S.S.. Ph.D. thesis, Eberhard Karls Universiät Tübingen. doi:10.15496/publikation-24840.

[Gre66] Greisen, K., 1966. *End to the Cosmic-Ray Spectrum?* Phys. Rev. Let. 16(17), 748. doi:10.1103/PhysRevLett.16.748.

[H. 18] H. E. S. S. Collaboration et al. (The H.E.S.S. Collaboration), 2018. *The population of TeV pulsar wind nebulae in the H.E.S.S. Galactic Plane Survey.* A&A 612, A2. doi:10.1051/0004-6361/201629377.

[Hai04] Haino, S. et al., 2004. *Measurements of primary and atmospheric cosmic-ray spectra with the BESS-TeV spectrometer.* Phys. Lett. B 594(1-2), 35. doi:10.1016/j.physletb.2004.05.019.

[Ham17] Hamamatsu Photonics K.K., 2017. *PHOTOMULTIPLIER TUBES Basics and Applications.* https://www.hamamatsu.com/content/dam/hamamatsu-photonics/sites/documents/99_SALES_LIBRARY/etd/PMT_handbook_v4E.pdf. Accessed: 28th. August, 2023.

[Han24] Hanna, D. et al., 2024. *The Very Energetic Radiation Imaging Telescope Array System (VERITAS).* In: Handbook of X-ray and Gamma-ray Astrophysics (edited by C. Bambi & A. Santangelo). Springer Nature, Singapore. doi:10.1007/978-981-19-6960-7_68.

[HB67] Hanburry Brown, J. et al., 1967. *The Stellar Interferometer At Narrabri Observatory – I: A Description of the Instrument and the Observational Procedure.* MNRAS 137, 375. doi:10.1093/mnras/137.4.375.

[Hec98] Heck, D. et al., 1998. *CORSIKA: A Monte Carlo code to simulate extensive air showers.* Tech. rep., Forschungszentrum Karlsruhe. doi:10.5445/IR/270043064.

[Her08] Hermann, G. et al., 2008. *A Trigger And Readout Scheme For Future Cherenkov Telescope Arrays.* In: Proceedings of the 4th International Meeting on High Energy Gamma-Ray Astronomy, vol. 1085, 898–901. AIP Conference Proceedings. doi:10.48550/arXiv.0812.0762.

[Hes26] Hess, V., 1926. *Die elektrische Leitfähigkeit der Atmosphäre und ihre Ursachen.* In: Sammlung Vieweg: Agen aus den Gebieten Naturwissenschaften und Technik (edited

by K. Scheel), vol. 84-85. Springer Fachmedien Wiesbaden GmbH. doi:10.1007/978-3-663-06995-9. In German.

[Hes08] Hester, J.J., 2008. *The Crab Nebula: an astrophysical chimera.* Ann. Rev. Astron. Astrophys. 46, 127. doi:10.1146/annurev.astro.45.051806.110608.

[Hil85] Hillas, A.M., 1985. *Cerenkov Light Images of EAS Produced by Primary Gamma Rays and by Nuclei.* In: 19th International Cosmic Ray Conference (ICRC19), vol. 3, 445. URL https://ui.adsabs.harvard.edu/abs/1985ICRC....3..445H.

[Hin09] Hinton, J.A. et al., 2009. *Teraelectronvolt Astronomy.* Ann. Rev. A&A 47, 523. doi:10.1146/annurev-astro-082708-101816.

[Hof00] Hofmann, W. et al. (HEGRA Collaboration), 2000. *On the optimum spacing of stereoscopic imaging atmospheric Cherenkov telescopes.* Astropart. Phys. 13(4), 253. doi:10.1016/S0927-6505(99)00126-7.

[Hof22] Hofmann, W., 2022. Source of the Month, vol. 2, 488–490. DESY for the H.E.S.S. Collaboration, Zeuthen. Accessed: October 31st, 2023, URL https://www.mpi-hd.mpg.de/HESS/pages/home/som/2020/10/.

[Hof24] Hofmann, W. et al., 2024. *The Cherenkov Telescope Array.* In: Handbook of X-ray and Gamma-ray Astrophysics (edited by C. Bambi & A. Santangelo). Springer Nature, Singapore. doi:10.1007/978-981-19-6960-7_70.

[Hol98] Holben, B. et al., 1998. *AERONET—A Federated Instrument Network and Data Archive for Aerosol Characterization.* Remote Sensing of Environment 66(1), 1. doi:10.1016/S0034-4257(98)00031-5.

[Hol06] Holder, J. et al. (VERITAS Collaboration), 2006. *The first VERITAS telescope.* Astropart. Phys. 25(6), 391. doi:10.1016/j.astropartphys.2006.04.002.

[Hol22] Holch, T.L. et al., 2022. *Assessing aerosol induced errors in Monte Carlo based air-shower reconstruction for atmospheric Cherenkov detectors.* J. Phys.: Conf. Ser. 2398, 012017. doi:10.1088/1742-6596/2398/1/012017.

[Jam75] James, F. et al., 1975. *Minuit: A System for Function Minimization and Analysis of the Parameter Errors and Correlations.* Comp. Phys. Commun. 10, 343. doi:10.1016/0010-4655(75)90039-9.

[Kla19] Klanner, R., 2019. *Characterisatoin of SiPMs.* NIM-A 926, 36. doi:10.1016/j.nima.2018.11.083.

[Klo13] Klochkov, D. et al., 2013. *A non-pulsating neutron star in the supernova remnant HESS J1731-347/G353.6-0.7 with a carbon atmosphere.* A&A 556, A41. doi:10.1051/0004-6361/201321740.

[Kno99] Knoll, G.F., 1999. Radiation Detection and Measurement. John Wiley & Sons Inc., New York, 3rd edn.

[Koh96] Kohnle, A. et al., 1996. *Stereoscopic imaging of air showers with the first two HEGRA Cherenkov telescopes.* Astropart. Phys. 5(2), 119. doi:10.1016/0927-6505(96)00011-4.

[Kon99] Konopelko, A. et al. (HEGRA Collaboration), 1999. *Performance of the stereoscopic system of the HEGRA imaging air Čerenkov telescopes: Monte Carlo simulations and observations.* Astroparticle Physics 10(4), 275. doi:10.1016/S0927-6505(98)00062-0.

[Kra00] Krawczynski, H., 2000. *Study of several Winston cone geometries.* H.E.S.S. internal note 00/03.

[Lem06] Lemoine-Goumard, M. et al., 2006. *Selection and 3D-reconstruction of gamma-ray-induced air showers with a stereoscopic system of atmospheric Cherenkov telescopes.* Astroparticle Physics 25(3), 195. doi:10.1016/j.astropartphys.2006.01.005.

[Leu20] Leuschner, F., 2020. A Two-Laser-Experiment for CTA FlashCam. Master's thesis, Eberhard Karls Universiät Tübingen. URL `http://astro.uni-tuebingen.de/publications/diplom/leuschner-master.pdf`.

[Leu23] Leuschner, F. et al., 2023. *Validation of Monte Carlo Simulations for an analysis chain in H.E.S.S.*. PoS Gamma2022, 231. doi:10.22323/1.417.0231.

[Li83] Li, T.P. et al., 1983. *Analysis methods for results in gamma-ray astronomy.* ApJ 272, 317. doi:10.1086/161295.

[Li22] Li, H. et al., 2022. *Comparison of the green-to-desert Sahara transitions between the Holocene and the last interglacial.* Climate of the Past 18(10), 2303. doi:10.5194/cp-18-2303-2022.

[Lom20] Lombardi, S. et al., 2020. *First detection of the Crab Nebula at TeV energies with a Cherenkov telescope in a dual-mirror Schwarzschild-Couder configuration: the ASTRI-Horn telescope.* A&A 634, A22. doi:10.1051/0004-6361/201936791.

[Lon11] Longair, M.S., 2011. High Energy Astrophysics. Cambridge University Press, Cambridge, 3rd edn. doi:10.1017/CBO9780511778346.

[Max18] Maxted, N. et al., 2018. *Probing the local environment of the supernova remnant HESS J1731-347 with CO and CS observations.* MNRAS 474, 662. doi:10.1093/mnras/stx2727.

[Maz22] Mazin, D. (CTA LST project), 2022. *Status and results of the prototype LST of CTA.* PoS ICRC2021, 872. doi:10.22323/1.395.0872.

[Mey10] Meyer, M. et al., 2010. *The Crab Nebula as a standard candle in very high-energy astrophysics.* A&A 523, A2. doi:10.1051/0004-6361/201014108.

[Mit16] Mitchell, A. et al., 2016. *A Generic Algorithm for IACT Optical Efficiency Calibration using Muons.* PoS ICRC2015, 756. doi:10.22323/1.236.0756.

[Moh19] Mohrmann, L. et al., 2019. *Validation of open-source science tools and background model construction in γ-ray astronomy.* A&A 632, A72. doi:10.1051/0004-6361/201936452.

[Mur16] Murach, T. et al., 2016. *A Neural Network-based Reconstruction Algorithm for monoscopically detected Air Showers observed with the H.E.S.S. Experiment.* PoS ICRC2015, 1022. doi:10.22323/1.236.1022.

[Mur17] Murach, T., 2017. Monoscopic Analysis of H.E.S.S. Phase II Data on PSR B1259–63/LS 2883. Ph.D. thesis, Humboldt-Universität zu Berlin, Mathematisch-Naturwissenschaftliche Fakultät. doi:10.18452/18484.

[Nau12] Naumann, C.L. et al., 2012. *New electronics for the Cherenkov Telescope Array (NECTAr).* NIM-A 695, 44. doi:10.1016/j.nima.2011.11.008.

[Nig21] Nigro, C. et al., 2021. *Evolution of Data Formats in Very-High-Energy Gamma-Ray Astronomy.* Universe 7(10), 374. doi:10.3390/universe7100374.

[Ohm09] Ohm, S. et al., 2009. *γ-hadron separation in very-high-energy γ-ray astronomy using a multivariate analysis method.* Astropart. Phys. 31(5), 383. doi:10.1016/j.astropartphys.2009.04.001.

[ON21] Olivera-Nieto, L. et al., 2021. *Muons as a tool for background rejection in imaging atmospheric Cherenkov telescope arrays.* Eur. Phys. J. C 81, 1101. doi:10.1140/epjc/s10052-021-09869-0.

[ON22] Oliver-Nieto, L. et al., 2022. *Background rejection using image residuals from large telescopes in imaging atmospheric Cherenkov telescope arrays.* Eur. Phys. J. C 82, 1118. doi:10.1140/epjc/s10052-022-11067-5.

[Ost11] Ostapchenko, S., 2011. *Monte Carlo treatment of hadronic interactions in enhanced Pomeron scheme: QGSJET-II model.* Phys. Rev. D 83, 014018. doi:10.1103/PhysRevD.83.014018.

[Pan23] Pantaleo, F. R. for the CTA SCT project, 2023. *The prototype Schwarzschild Couder Telescope: a Medium-Sized Telescope for the Cherenkov Telescope Array.* J. Phys.: Conf. Ser. 2429, 012021. doi:10.1088/1742-6596/2429/1/012021.

[Pie09] Pierog, T. et al., 2009. *EPOS Model and Ultra High Energy Cosmic Rays.* Nuc. Phys. B - Proc. Supp. 196, 102. doi:10.1016/j.nuclphysbps.2009.09.017.

[Pre02] Preuss, S. et al., 2002. *Study of the photon flux from the night sky at La Palma and Namibia, in the wavelength region relevant for imaging atmospheric Cherenkov telescopes.* NIM-A 481, 229. doi:10.1016/S0168-9002(01)01264-5.

[Ptu05] Ptuskin, V.S. et al., 2005. *On the spectrum of high-energy cosmic rays produced by supernova remnants in the presence of strong cosmic-ray streaming instability and wave dissipation.* A&A 429(3), 755. doi:10.1051/0004-6361:20041517.

[Ptu08] Ptuskin, V.S. et al., 2008. *Diffusive Shock Acceleration with Magnetic Amplification by Nonresonant Streaming Instability in Supernova Remnants.* ApJ 678(2), 939. doi:10.1086/529580.

[Püh15] Pühlhofer, G. et al., 2015. *FlashCam: a fully-digital camera for the medium-sized telescopes of the Cherenkov Telescope Array.* PoS ICRC2015, 1039. doi:10.22323/1.236.1039.

[Püh17] Pühlhofer, G. et al., 2017. *The medium sized telescopes of the Cherenkov telescope array.* In: 6th International Symposium on High Energy Gamma-Ray Astronomy, vol. 1792 of *American Institute of Physics Conference series*, 080002. doi:10.1063/1.4969023.

[Püh19] Pühlhofer, G. et al., 2019. *FlashCam: a fully digital camera for the Cherenkov telescope array medium-sized telescopes.* In: Optics for EUV, X-Ray, and Gamma-Ray Astronomy IX (edited by S.L. O'Dell & G. Pareschi), vol. 11119, 111191V. International Society for Optics and Photonics, SPIE. doi:10.1117/12.2531025.

[Püh21] Pühlhofer, G. et al., 2021. *Science verification of the new FlashCam-based camera in the 28m telescope of H.E.S.S..* PoS ICRC2021, 764. doi:10.22323/1.395.0764.

[Püh24] Pühlhofer, G. et al., 2024. *H.E.S.S.: The High Energy Stereoscopic System.* In: Handbook of X-ray and Gamma-ray Astrophysics (edited by C. Bambi & A. Santangelo). Springer Nature, Singapore. doi:10.1007/978-981-19-6960-7_68.

[Pür19] Pürckhauer, S. et al., 2019. *Comparison between light concentrator measurements at MPIK and IPAG.* CTA internal note.

[Roh22] Rohatgi, A., 2022. *Webplotdigitizer: Version 4.6.* URL https://automeris.io/WebPlotDigitizer.

[Ryb04] Rybicki, G.B. et al., 2004. Radiative Processes in Astrophysics. Wiley-Vch Verlag GmbH & Co. KGaA, Weinheim. doi:10.1002/9783527618170.

[Sal20] Salzmann, H., 2020. Investigation of the Optical and Gamma-Ray Point Spread Functions of H.E.S.S. CT5 after the Installation of NamCam. Master's thesis, Eberhard Karls Universiät Tübingen. URL http://astro.uni-tuebingen.de/publications/diplom/salzmann-master.pdf.

[Sch23] Schäfer, J., 2023. Simulation of IceACT With TARGET, Validation of the H.E.S.S. Simulation Chain, and a New H.E.S.S. 3D Analysis of the Crab Using the ABRIR Method for Improved Background Rejection. Ph.D. thesis, Friedrich-Alexander-Universität Erlangen-Nürnberg. URL https://nbn-resolving.org/urn:nbn:de:bvb:29-opus4-237057.

[Scu22] Scuderi, S. et al., 2022. *The ASTRI Mini-Array of Cherenkov telescopes at the Observatorio del Teide.* JHEAp 35, 52. doi:10.1016/j.jheap.2022.05.001.

[SE03] Schermelleh-Engel, K. et al., 2003. *Evaluating the Fit of Structural Equation Models: Tests of Significance and Descriptive Goodness-of-Fit Measures.* Methods of Psychological Research Online 8, 23–74.

[Ste23] Steinmassl, S., 2023. Probing particle acceleration in stellar binary systems using gamma-ray observations. Ph.D. thesis, Universiät Heidelberg. doi:10.11588/heidok.00033375.

[Str20] Straal, S.M. et al., 2020. *A dispersion excess from pulsar wind nebulae and supernova remnants: Implications for pulsars and FRBs.* A&A 634, A105. doi:10.1051/0004-6361/201833376.

[Tia08] Tian, W.W. et al., 2008. *Discovery of the Radio and X-Ray Counterpart of TeV γ-Ray Source HESS J1731–347.* ApJ 679(2), L85. doi:10.1086/589506.

[Tju20] Tjus, J.B. et al., 2020. *Closing in on the origin of Galactic cosmic rays using multimessenger information.* Phys. Rep. 872, 1. doi:10.1016/j.physrep.2020.05.002.

[Toy13] Toyama, T. et al., 2013. *Novel Photo Multiplier Tubes for the Cherenkov Telescope Array Project.* In: 33rd International Cosmic Ray Conference, vol. 2, 1178–1181. doi:10.48550/arXiv.1307.5463.

[Vie22] Vieu, T. et al., 2022. *Cosmic ray production in superbubbles.* MNRAS 512, 1275. doi:10.1093/mnras/stac543.

[Wee89] Weekes, T.C. et al., 1989. *Observation of TeV Gamma Rays from the Crab Nebula Using the Atmospheric Cerenkov Imaging Technique.* ApJ 342, 379. doi:10.1086/167599.

[Wer17] Werner, F. et al., 2017. *Performance Verification of the FlashCam Prototype Camera for the Cherenkov Telescope Array.* NIM-A 876, 31. doi:10.1016/j.nima.2016.12.056.

[Whi22] White, R. (CTA SST Collaboration), 2022. *The Small-Sized Telescopes for the Southern Site of the Cherenkov Telescope Array.* PoS ICRC2021, 728. doi:10.22323/1.395.0728.

[Zor19] Zorn, J. (CTA GCT project), 2019. *CHEC – A compact high energy camera for the Cherenkov Telescope Array.* NIM-A 936, 229. doi:10.1016/j.nima.2018.09.138.

A

Runlists for the H.E.S.S. analyses

In this appendix, the runs used for the H.E.S.S. analyses are listed, sorted according to the respective analysis.

A.1 Spatial analysis of HESS J1731-347

A.1.1 CT1-4 runs

20901, 20941, 20957, 20960, 20962, 21218, 21239, 21240, 21241, 21243, 21271, 21344, 21375, 21393, 21406, 25089, 25090, 25099, 25100, 25107, 25108, 25215, 25216, 25217, 25583, 25584, 25992, 33108, 33109, 33112, 33139, 33140, 33141, 33158, 33163, 33164, 33165, 33166, 33189, 33191, 33192, 33193, 33228, 33230, 40078, 40079, 40094, 40095, 40096, 40097, 40118, 40135, 40136, 40137, 40138, 40164, 40180, 40181, 40182, 40183, 40224, 40257, 40258, 40259, 40260, 40261, 40292, 40320, 40321, 40322, 40354, 40355, 40356, 40379, 40380, 40381, 40409, 40410, 40440, 40441, 40464, 40465, 52030, 52085, 52108, 52128, 52129, 52130, 52149, 52150, 52151, 52152, 52164, 52357, 52373, 52374, 52375, 52389, 52390, 52410, 52411, 52467, 52469, 52491, 52492, 52523, 52524, 52525, 52547, 52548, 52549, 52572, 52573, 52574, 52596, 52597, 52623, 52624, 52625, 52649, 52650, 52965, 52966, 52967, 53004, 53005, 53006, 53007, 53023, 53024, 53025, 53122, 53124, 53143, 53144, 53145, 53172, 53173, 53174, 53205

A.1.2 CT5 runs

161733, 161734, 161735, 161755, 161756, 161757, 161758, 161781, 161782, 161784, 161785, 161837, 161838, 161861, 161862, 161863, 161864, 161888, 161889, 161890, 161891, 161915, 161919, 162304, 162305, 162322, 162344, 162346, 162373, 162375, 162402, 162457, 162458, 162485, 162486, 162513, 162514, 162540, 162541, 162892, 169949, 169950, 170002, 170003, 170004, 170055, 170091, 170110, 170111, 170136, 170137, 170163, 170164, 170188, 170189, 170213, 170214

A.2 Spectral analysis for HESS J1731-347

A.2.1 CT1-4 runs

For the CT1-4 analysis, the same runs as given in Section A.1.1 are used.

A.2.2 FC runs

For the FC@CT5 analysis, the same runs as given in Section A.1.2 are used, except for the runs 162304, 162322, 162344, 162373, 162402, 162457, 162514 and 162540 (see Section VI.2 for the reasons of this reduction).

A.3 Spatial analysis of HESS J1729-345

A.3.1 CT1-4 runs

For the CT1-4 analysis, the same runs as given in Section A.1.1 are used for both, the LE and the HE emission region.

A.3.2 FC runs

No spatial analysis of the HESS J1729-345 region has been conducted with FC@CT5.

A.4 Spectral analysis of HESS J1729-345

A.4.1 CT1-4 runs

Initially, the same runs are used for the CT1-4 analysis as given in Section A.1.1. However, of these runs the following were excluded, as no Off-regions could be found for the target positions:

For the LE emission region: 20960, 33112, 33158, 33166, 33192, 52108, 52128, 52150, 52375, 52410, 52492, 52549, 52596, 52624, 52966, 53006, 53024, 53143, 53173

For the HE emission region: all the above and additionally runs 25090, 25108, 25217

A.4.2 CT5 runs

Initially, the same runs are used for the CT5 analysis as given in Section A.1.2. However, of these runs the following were excluded, as no Off-regions could be found for the target position in the LE emission region: 162322, 162344, 162402

For the HE emission region, no analysis has been conducted with FC@CT5.

A.5 Further information

Further information, including all produced files, are stored in the Gitlab instance of the IAAT. For access, approach the person responsible for the H.E.S.S. experiment at the IAAT[37] or the professor for High Energy Astrophysics[38]. For further questions, you may at any reach out to the author of this thesis.

[37] At the time of writing: Dr. Gerd Pühlhofer
[38] At the time of writing: Prof. Andrea Santangelo

B

List of Abbreviations

ABRIR	Algorithm for Background Rejection using Image Residuals
AGN	Active Galactic Nuclei
AOD	Aerosol Optical Depth
CE	Collection Efficiency
CMB	Cosmic Microwave Background
CR	Cosmic Ray
CTA	Cherenkov Telescope Array
DAQ	Data Aquisition
DC	Davies-Cotton
DSA	Diffuse Shock Acceleration
EAS	Extended Air Showers
EBL	Extragalactic Background Light
FADC	Flash Analog-to-Digital Converter
FC	FlashCam
FC@CT5	FC mounted to the CT5 telescope of H.E.S.S.
FF	Flatfield
FITS	Flexible Image Transport System
FoV	Field of View
FPGA	Field Programmable Gate Array
FWHM	Full Width at Half Maximum
GRB	Gamma-ray Burst
GSF	Global Spline Fit
GUI	Graphical User Interface
GZK	Greisen-Zatsepin-Kusmin
HE	High Energy
HEGRA	High Energy Gamma Ray Astronomy
H.E.S.S.	High Energetic Stereoscopic System
HV	High Voltage

IACT	Imaging Air Cherenkov Telescope
IC	Inverse Compton
IGM	Intergalactic Medium
IRF	Instrument Response Function
ISM	Interstellar Medium
LE	Low Energy
LHC	Large Hadron Collider
LMC	Large Magellanic Cloud
LUPM	Laboratoire Univers et Particules de Montpellier
LST	Large-Sized Telescope
MAGIC	Major Atmospheric Gamma Imaging Cherenkov(-Telescope)
MC	Monte-Carlo (as in *Monte-Carlo Simulation*)
MRSL	Mean Reduced Scaled Length
MRSLO	Mean Reduced Scaled Length Off
MRSW	Mean Reduced Scaled Width
MRSWO	Mean Reduced Scaled Width Off
MST	Medium-Sized Telescope
NSB	Night-Sky Background
od	Optical Density
PDP	Photon Detector Plane
pe	Photo-Electron(s)
p.e.	Photo-Electron(s), as a unit
PMT	Photoelectron-Multiplier Tube
PSF	Point Spread Function
PWN	Pulsar Wind Nebulae
QE	Quantum Efficiency
QOI	Quantity of Interest
ROS	Readout Electronics
SC(T)	Schwarzschild-Couder (Telescope)
SCW	Scaled Width
SiPM	Silicon-Photomultiplier
SNR	Supernova Remnant
SPE	Single pe
SST	Small-Sized Telescope
TC	Transparency Coefficient
VERITAS	Very Energetic Radiation Imaging Telescope Array System
VHE	Very High Energy/Energetic

Note that an "s" at the end indicates the plural of the abbreviated word/term.

List of Figures

Acknowledgments

Obtaining a doctoral degree is an achievement of a single person, but to make it happen it takes a good network in academia, private life, and everything between. This holds even more true, when the intrinsic hard time of being a grad student gets struck by a supernova-like shock caused by a global pandemic. Covid-19 hit Germany and the Tübingen University the exact day I started: March 16^{th}, 2020, and I'm incredible thankful to everyone who helped me stay (mostly) sane during the $\approx 3\,\text{yr}$ it lasted and the following year I needed to finish up.

However, some individuals deserve to be named in particular. Firstly, I thank Prof. Andrea Santangelo for the possibility to work in the High-Energy-Astrophysics group. I want to express my gratitude to my supervisor Dr. Gerd Pühlhofer for his open door, his ideas, explanations and his support throughout the whole time I worked in Cherenkov astronomy with CTA and H.E.S.S., for making my shift at the H.E.S.S. telescopes in Namibia possible and for proofreading the manuscript. In that context I also thank Dr. Regine Ehmann for helping me with the translation of the Abstract. I thank my office mates Baiyang and Heiko for the spirit we kept in our too hot, too cold, and sometimes rainy room. I miss the discussions about astrophysics, languages and the German bureaucracy with you guys.

The project I grew most on during the past years has for sure been the validation of the MC simulations. Here, I'm thankful for the always fun, productive and encouraging collaboration I had with Johannes, Simon and Tim as part of the MC validation team. My shift at the H.E.S.S. site in Namibia in August/September 2022 has been an unique experience that I'll never forget. I thank the whole local crew and in particular my co-shifters Kai and Sennea for the great atmosphere, for teaching me how to operate some of worlds largest telescopes, and for the trust they put into me. In general, I want to thank the whole H.E.S.S. collaboration for the support in the past years. No matter whether we met remotely in an animated castle or in-person in an Irish resort, it was always a pleasure.

Fortunately, being a doctoral student is not all intense, hard work (although it sometimes feels like it). Thus, I thank the whole IAAT and in particular my fellow grad students for all the great times we had. Thanks for the lunches and journal clubs outside, in heat and cold. Thanks for the sometimes fruitful, sometimes crazy coffee breaks. And of course thanks for all our integration hours, dinners and fun evenings. Talking about IAAT, I want to emphasize how much the vintage A112 connection means to me - thanks Inga, Christi and Heiko for the strong bond we build over

the years! Another highlight in my PhD time has been the ISAPP school in early 2022 in Paris. Thanks to all the cool kids for making this an exceptional experience. Thanks for the hiking adventures, for discovering Paris and its cellars, for the Italian I learned but dare not cite here, and for the enthusiasm about science that I needed at that time more than I knew back then.

I also thank all the friends outside of academia that helped me keeping a balance and showing me that there is more in life than astroparticle physics. Without my amazing flatmates, the pandemic would have been so much harder than it was - thanks to all of you; in particular to Jule and Lea. It's been often only the three of us in Kingersheimer Straße and I enjoy remembering the time we spent and the trips we made. Further, big thanks goes to my Handball mates at Tuebingen University team and in Hagelloch, for keeping me grounded and offering a place to get a free head.

Finally, my biggest thanks go to my family: thanks to my parents, for supporting me all my life and helping me to become who I am. And most of all thanks to Steffi, for being the best, for going through life's ups and downs with me, and for always having my back.